

6. SITE 796¹

Shipboard Scientific Party²

HOLE 796A

Date occupied: 22 July 1989
Date departed: 24 July 1989
Time on hole: 2 days, 1 hr, 45 min
Position: 42.894°N, 139.411°E
Bottom felt (rig floor; m; drill pipe measurement): 2581.8
Distance between rig floor and sea level (m): 11.2
Water depth (drill pipe measurement from sea level, m): 2570.6
Total depth (rig floor; m): 2761.7
Penetration (m): 242.9
Number of cores (including cores with no recovery): 2.7
Total length of cored section (m): 242.9
Total core recovered (m): 155.25
Core recovery (%): 63.9
Oldest sediment cored:
Depth sub-bottom (m): 242.9
Nature: claystone
Age: late Miocene or older
Measured velocity (km/s): not measured

HOLE 796B

Date occupied: 24 July 1989
Date departed: 29 July 1989
Time on hole: 4 days, 21 hr, 30 min
Position: 42°84900N, 139°41400E
Bottom felt (rig floor; m; drill pipe measurement): 2633.8
Distance between rig floor and sea level (m): 11.2
Water depth (drill pipe measurement from sea level, m): 2622.6
Total depth (rig floor; m): 3098.7
Penetration (m): 464.9
Number of cores (including cores with no recovery): 33
Total length of cored section (m): 293.8
Total core recovered (m): 85.31
Core recovery (%): 29
Oldest sediment cored:
Depth sub-bottom (m): 464.9
Nature: claystone
Age: late or middle Miocene
Measured velocity (km/s): 2.1

Principal results: The specific objectives of Site 796, located on Okushiri Ridge in the eastern margin of Japan Basin were: (1) to deter-

mine the age and history of uplift of the ridge; (2) to measure the direction of the present stress field; (3) to determine the age and nature of the basement; and (4) to characterize the sedimentation and oceanographic evolution of the area.

Unfortunately the penetration into the basement was not attained (total depth 465 mbsf, 110 m above basement) because of unstable hole conditions caused by shallow coarse sand beds and fractured rocks in the lower levels. As a result objectives (2) and (3) were not achieved. The results at Site 796 are summarized below and in Figures 1A to -D. The principal results at Site 796 are as follows:

1. The age of initiation of uplift of Okushiri Ridge was deduced by the shallowest appearance of a sand bed as originally anticipated. The age of the shallowest sand bed is estimated to be 1.8 Ma by diatom stratigraphy. This observation suggests that Okushiri Ridge (water depth 2300 m) uplifted 1300 m above the Japan Basin floor (water depth 3600 m) in 1.8 Ma at a rate of 0.7 mm/yr. As the uplift of Okushiri Ridge is caused by thrust activity along the eastern margin of the Japan Sea (a possible new Eurasia-North America plate boundary), these results provide the first exact age data to address the initiation of the convergence along this margin and the tectonics along this new plate boundary.

2. The lithology at Site 796 below the uppermost Pliocene is quite different from the previous two sites and is characterized by abundant input of coarse-grained clastic and pyroclastic detritus as sediment gravity flow deposits, suggesting the marginal facies of a basin. Paleooceanographic conditions that are suggested by the sedimentary sequences and paleontological data, however, are approximately similar to those inferred at Sites 794 and 795. The calcium carbonate abundance in the sediments and the microfossil preservation show that the site was above the carbonate compensation depth (CCD) during the middle(?) Miocene and below it through the late Miocene to the Quaternary. The ubiquitous bioturbation observed throughout the sedimentary column shows that the sediments at Site 796 accumulated under oxic conditions. Interstitial water geochemistry shows elemental depth variation but these variations are well explained when correlated with lithology, especially ash beds and sand beds. No vertical fluid transport was suggested by the interstitial water geochemical data, whereas physical property data may suggest occurrence of some vertical fluid flux.

3. The highest heat flow ever obtained in the Japan Sea, 156 mW/m², was measured at Hole 796B. The associated high temperature gradient (178°C/km) is quite consistent with the shallow, indistinct opal-A/opal-CT transition zone (215 mbsf, 40°C). Frictional heating along the thrust faults is one potential source of excess heat, but frictional heat alone is probably not of a great enough magnitude to account for this high heat flow. A mechanism to concentrate the heat flow, such as fluid flow along faults, is required to match the magnitude of the anomaly.

Location and Approach

Site 796 is located on the eastward-dipping slope of Okushiri Ridge in the eastern margin of the Japan Sea, 1 mi northward and downslope of proposed location J3b-1. The slope is estimated to have been formed by a westward-dipping thrust fault. Two *JOIDES Resolution* seismic lines, one bearing east-west, the other north-south, were obtained. The east-west line is parallel to a pre-existing multichannel line. The site was located over relatively smooth topography with fewer side echoes on the 12 kHz PDR profile than in surrounding areas. The beacon was launched on the third pass of the site after reconfirming the location in order to avoid any possible closures. Hole 796B was shifted 250 m downslope from Hole 796A to avoid coarse sand beds (51.7–146.2 mbsf) which caused hole problems, with the hope that these beds in Hole 796A represented only the fill of a local channel.

¹ Tamaki, K., Pisciotta, K., Allan, J., et al., 1990. *Proc. ODP, Init. Repts.*, 127: College Station, TX (Ocean Drilling Program).

² Shipboard Scientific Party is as given in the list of participants preceding the contents.

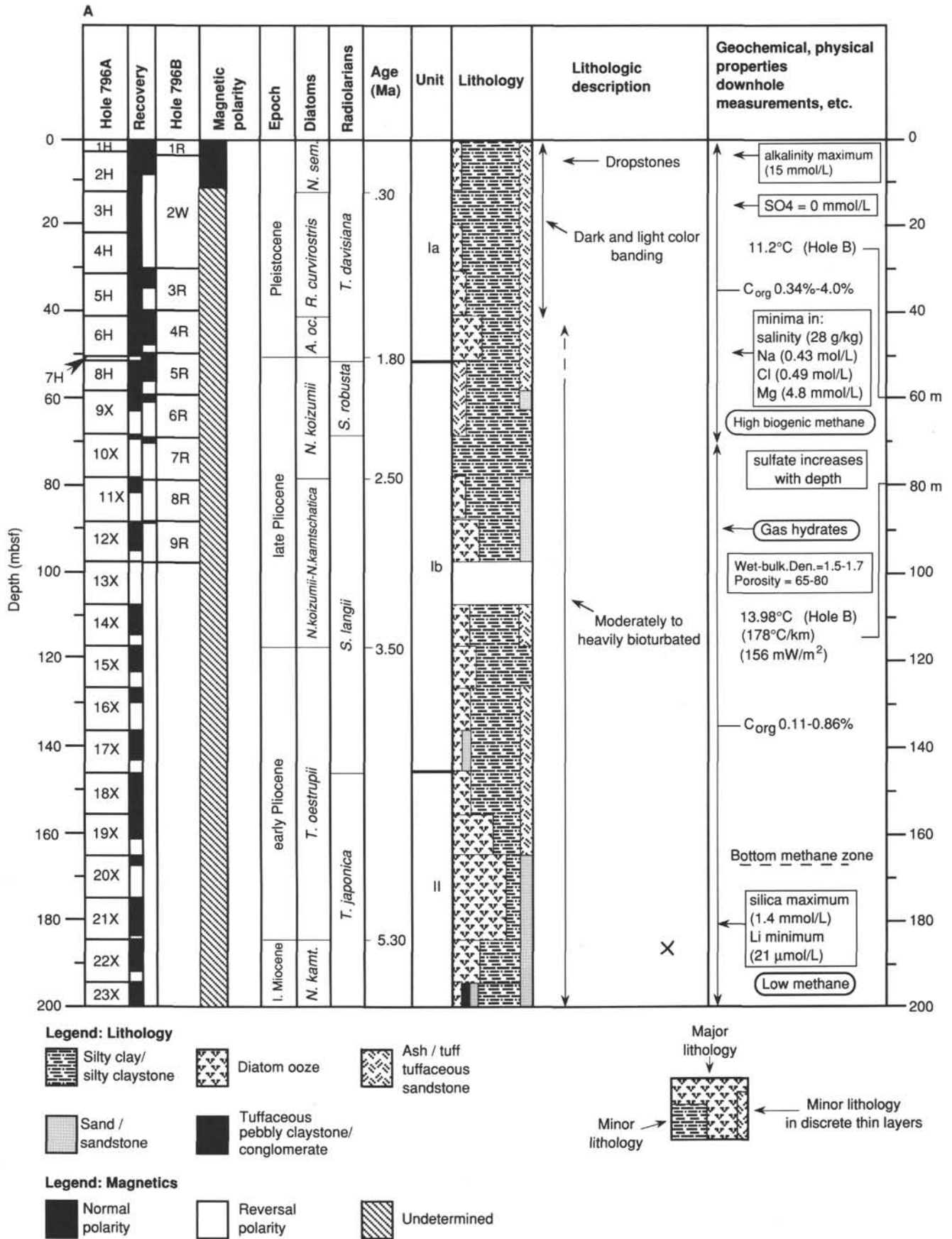


Figure 1. Stratigraphic summary column for Site 796.

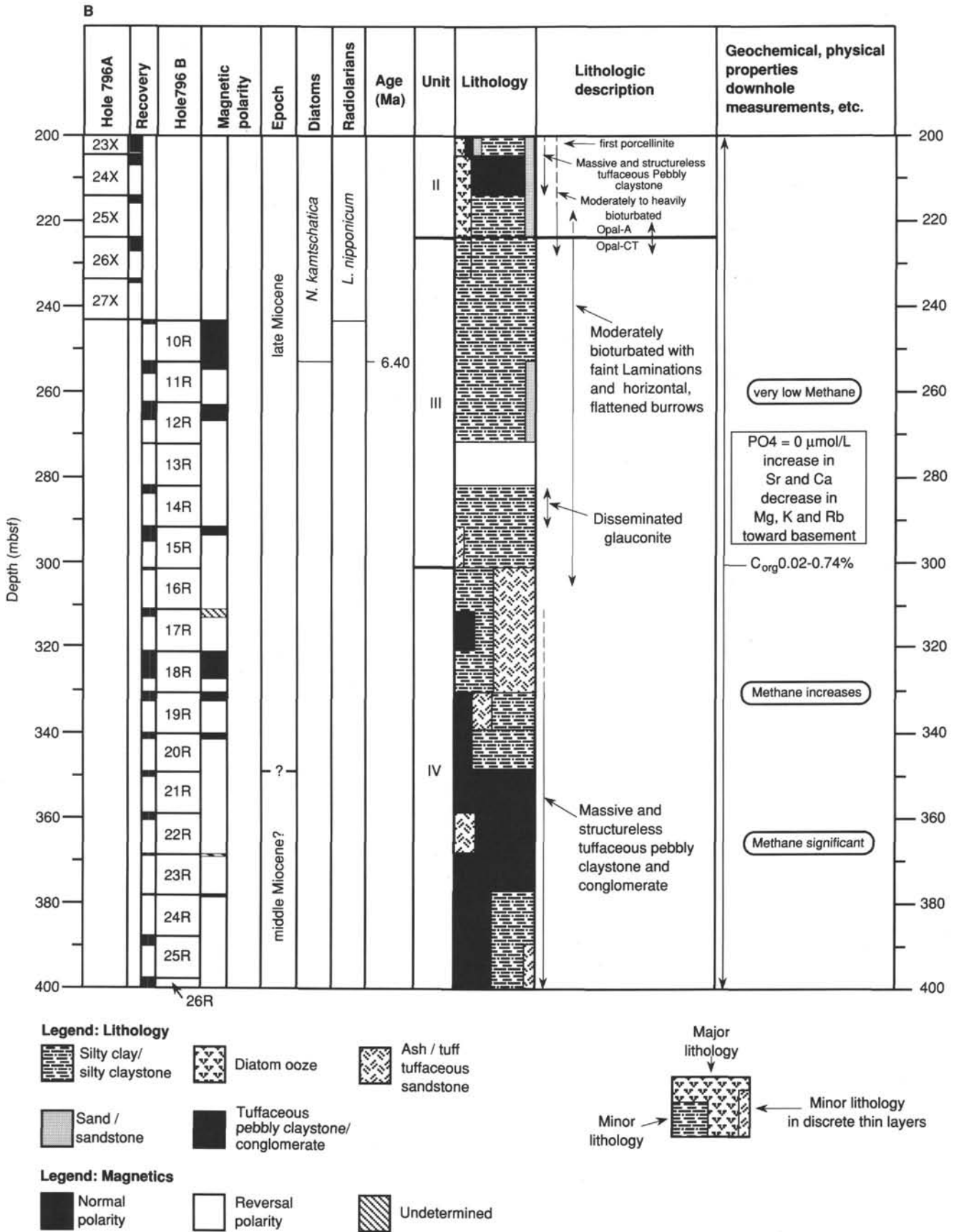


Figure 1 (continued).

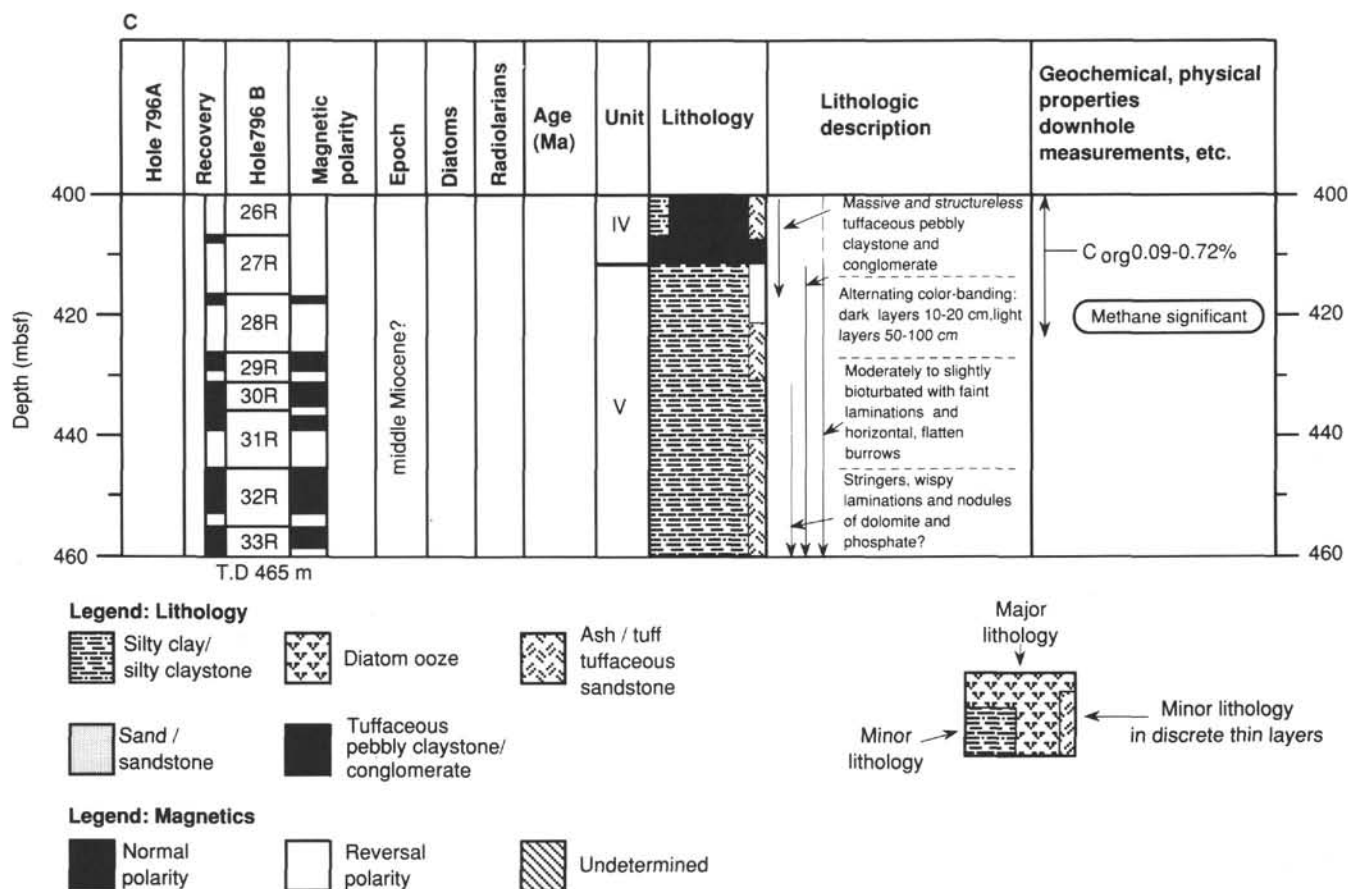


Figure 1 (continued).

Lithology

The sedimentary section cored in Holes 796A and 796B differs from those of Sites 794 and 795 by exhibiting a remarkable input of terrigenous components during the late Miocene to Quaternary. Sand is first observed in Core 127-796A-9X at Hole 796A (63 mbsf) and in Core 127-796B-7R at Hole 796B (70 mbsf). In both holes, the shallowest sand appears in the uppermost part of the uppermost Pliocene strata (1.8–2.5 Ma). In Hole 796B, the age of the shallowest sand is constrained by special additional sampling of diatoms to be 1.8 Ma. The opal-A/opal-CT transition was observed at 225 mbsf by XRD analyses. The division of units is as follows:

Subunit IA: 0–51.7 mbsf; Quaternary

Clay and silty clay without sand. The unit is moderately to highly bioturbated, and associated with soft sediment deformation by slumping and microfaults.

Subunit IB: 51.7–146.2 mbsf; Pliocene

Clay and silty clay with frequent sand beds. The frequency of soft-sediment deformation features decreases when compared to Subunit IA. Sand beds occur throughout the subunit as scattered thin beds (typically 1–10 cm thick, thickest 65 cm) that have sharp basal contacts. The sands are dominated by volcanic lithic fragments and pumice of fine- to medium-grain size.

Unit II: 146.2–223.5 mbsf; early Pliocene–late Miocene

Clayey diatom ooze and diatom claystone. The detrital input increases toward the base of unit with sandstone and pebbly claystone. Sandstone beds occur as thin (2–10 cm) graded units with sharp basal contacts and are dominantly composed of volcanic lithic fragments and glass or pumice.

Unit III: 223.5–301.0 mbsf; late Miocene

Siliceous claystone, claystone, and sandstone. Claystone units are moderately to highly bioturbated. Sandstone and siltstone interbeds are abundant in the middle part. Sandstones (a few centimeters to 60 cm) are graded and medium- to coarse-grained with volcanic lithic detritus and glass shards. Scattered glauconite is observed.

Unit IV: 301.0–416.5 mbsf; late Miocene?

Siliceous claystone, pebbly claystone, tuffaceous sandstone, and tuff. This unit is characterized by siliceous claystone interbedded with coarse-grained pyroclastic deposits which consist of sandstone and pebbly claystone with abundant volcanic detritus and discrete tuff beds. The opal-CT/quartz diagenetic boundary is observed at 301–330 mbsf. The claystone is well bioturbated. Pebbly claystone commonly occurs through this unit and is matrix-supported, coarse-grain sand to pebble-size volcanic detritus that includes pumice, tuff, and other volcanic lithic fragments. Laminated tuffaceous sandstone is present as thin beds throughout the unit, and laminated, graded tuff beds (some exceeding 2 m in thickness) also occur.

Unit V: 416.5–464.9 mbsf; late-middle(?) Miocene

Siliceous claystone and silty claystone. This unit is distinguished from overlying strata by the paucity of coarse clastic/pyroclastic deposits and by an increase in dolomite and Mg-calcite. Siliceous claystones are generally bioturbated.

Age and Sediment Accumulation Rates

Sediment ages are well constrained by diatom zones in Unit I, Unit II, and the uppermost part of Unit III (0–253 mbsf). Below this level, all diatoms have been dissolved. The paleomagnetic data as well as the other paleontological data were sparse and not usable to identify da-

tums or to be used for age determination. The oldest age determined is 6.4 Ma at 253 mbsf by the first appearance datum of *Neodenticula kamtschatica*, a diatom. The age of Units IV and V was estimated solely by the simple extrapolation of the sediment accumulation curve. The minimum estimated age of the bottom of the hole (465 mbsf) is 9.7 Ma based on this extrapolation. Uncompacted sedimentation rates are: 62 m/m.y. for the late Miocene, 29–42 m/m.y. for the Pliocene, and 48–74 m/m.y. for the Quaternary. A period of slow sedimentation (9 m/m.y.) occurred at about the Pliocene-Quaternary boundary.

Magnetics

The average intensity of magnetization of the sediments at Site 796 was stronger than at the previous two sites, falling regularly below 5 mA/m only on the lowermost portion of Hole 796B. Nevertheless, a coherent magnetic stratigraphy was not established at Site 796, due to problems of sediment disruption by gas, remagnetization, poor recovery, and limited paleontological data.

Geochemistry

High methane concentrations were observed at 10–140 mbsf, with the concentrations ranging from 7,300 to 830,000 ppm in the vacutainer samples. C_1/C_2 ratios in this interval were constantly above 1000, suggesting a biogenic source of this gas. Gas-hydrate was observed in Core 127-796A-12X (approximately 90 mbsf) and sampled. The results of the analysis of the clathrate shows that the pore-water chemistry (salinity, NaCl, sulfate) at Site 796 is influenced by the presence of methane-clathrates and that clathrates are probably present throughout the upper 120 m of this site. Below 200 mbsf, the methane concentration decreases to less than 100 ppm, and below 340 mbsf methane increases again to 1500 to 8200 ppm with only small amounts of ethane (1–16 ppm), suggesting a minor influx of thermogenic methane. No serious safety problem concerning gas was encountered at the bottom of the hole.

The Quaternary sediments above 70 mbsf vary in organic carbon content, with the concentration ranging between 0.34% and 4.0% and suggesting a rather prominent variation in paleo-environment. The low organic carbon contents (<1.0%) below 70 mbsf indicate sediment deposition under highly oxygenated bottom water conditions. The base of the sulfate reduction zone occurs at 14 mbsf, much shallower than at the previous site (80 mbsf at Site 795). Sulfate increases again below 62 mbsf and attains a value of 20 mmol/L at 206 mbsf. Abundant ash layers in the upper 150 m apparently controlled the behavior of alkaline earth elements (in particular the extreme depletion of Mg in this horizon) at this site. Preliminary examination of the pore-water chemistry does not show any positive evidence of fluid-transport along possible active faults.

Seismic Stratigraphy

The acoustic character of the sediments at Site 796 is mostly opaque except for a lowermost thin interval. No clear bottom-simulating reflector associated with gas-hydrate is observed at Site 796. A weak opal-A/opal-CT reflector is observed at 0.27 s bsf. The acoustically opaque interval represents abundant input of coarse materials into the sedimentary section. The top of Unit IV makes a strong reflector in correlation with the alternation of tuff and pebbly claystone. Five seismic intervals overlying acoustic basement were identified and correlated to the lithostratigraphic units. The unconformity between Interval 1 and Interval 2 which correlates to the boundary between Units IA and IB is well observed in seismic profiles. The bottom of Hole 796B (465 mbsf) is estimated to be 110 m above the acoustic basement.

Heat Flow and Temperature

Temperature measurements were made using the Uyeda probe at five horizons down to 127.1 mbsf in Hole 796A and at three horizons down to 79.8 mbsf in Hole 796B. The measurements in Hole 796A yielded spurious data because of an encounter with coarse sediments at several horizons. The measurements in Hole 796B yielded valid data with a temperature gradient of 178°C/km and a heat flow value of 156 mW/m², the highest heat flow that has ever been measured in the Japan Sea. Preliminary calculations show that frictional heating along thrust faults could possibly account for this high heat flow, although it is probably too low in magnitude unless transcurrent faulting is occurring as well. Another source of heat is fluid flow along faults.

Logging and Physical Properties

Four successful logging runs were completed between 100 and 340 mbsf in Hole 796B (Combination Sonic/Lithodensity/Temperature/DIT,

Geochem, FMS, and BHTV). The resistivity, velocity, and bulk density profiles characterize the sedimentary section well. As the total recovery of cores is poor at this site, the logging data represent indispensable data needed to complete the description of the lithologic column. The opal-A/opal-CT transition is recognized at 215 mbsf on logs and is different from the depth of identification by the XRD analyses (225 mbsf). This difference may come from poor recovery at the corresponding horizons, and logging data may provide a better estimate of the level of this transition. Sand beds and tuff beds are well identified by the resistivity, velocity, and bulk density profiles. The FMS data display frequent, mostly horizontal layers with thicknesses ranging from 5 to 30 cm. A BHTV run was executed in the sediment section because some sandstone layers have high sonic velocity (>4000 m/s). Some small-scale fractures were observed but no prominent breakouts were present on the preliminary BHTV images.

Most of the physical properties show variations correlated to lithologic variations. Some parts of the water content data may be correlated to fluid circulation along faults.

BACKGROUND AND OBJECTIVES

Background

Location and Bathymetry

Site 796 lies in the northeastern Japan Sea about 42 km off the western coast of Hokkaido (Fig. 2). It is situated in about 2600 m of water on the eastern flank of one of the ridges of the Okushiri Ridge complex. This complex is part of the extensive system of north-trending ridges, escarpments, and closed basins which runs the length of western Hokkaido and northwestern Honshu (Tamaki and Honza, 1985). The ridge on which Site 796 is located is a kinked, doubly culminating, linear feature with up to 1500 m of vertical relief and extending continuously for about 90 km in a north-south direction. The eastern flank of this ridge is steep and the seafloor is scarred with irregular, hummocky features indicative of slumping and mass wasting (see Fig. 11). The western flank is gentler and the seafloor more even except near the base of the slope where disruptive folding is common. This flank also contains several spur ridges which plunge westward from the main north-south ridge much like the feature observed near Site 795. The kink in the trend of the ridge occurs just north of the site and trends northeast-southwest.

To the north, the Okushiri Ridge extends in a series of generally right-stepping en echelon ridges, although a consistent offset pattern is not well developed. The two large, isolated highs lying to the west of these ridges are not part of this trend. East of the ridge are small, deep, and closed or silled basins, the largest of which is the Shiribeshi Trough (Fig. 2). These basins are elongate in the north-south direction and have extremely steep, sharp edges and flat bottoms. Further to the east is the steep slope leading to the shelf which borders western Hokkaido. Several northwest-trending lineaments punctuate this slope, the most striking of which is the northwest-trending Suttu Canyon.

To the south, Okushiri Ridge steps eastward where it forms a north-south spur leading to the platform containing Okushiri Island. A narrow bathymetric sill separates this island platform from western Hokkaido. West and southwest of Okushiri Ridge in this area lies the deep, flat floor of the Japan Basin.

Crustal Structure

The crustal structure in the vicinity of Site 796 is poorly constrained. The closest refraction data come from the central Japan Basin (Ludwig et al., 1975) and from an area north of the site (Gnibidenko, 1979; also see "Site 795" chapter, this volume). Based on these results, the estimated crustal thickness in the Okushiri Ridge area near Site 796 is approximately 13–17 km. This estimate is intermediate between the 11–12 km value for the Japan Basin and the greater values of 30–35 km for the

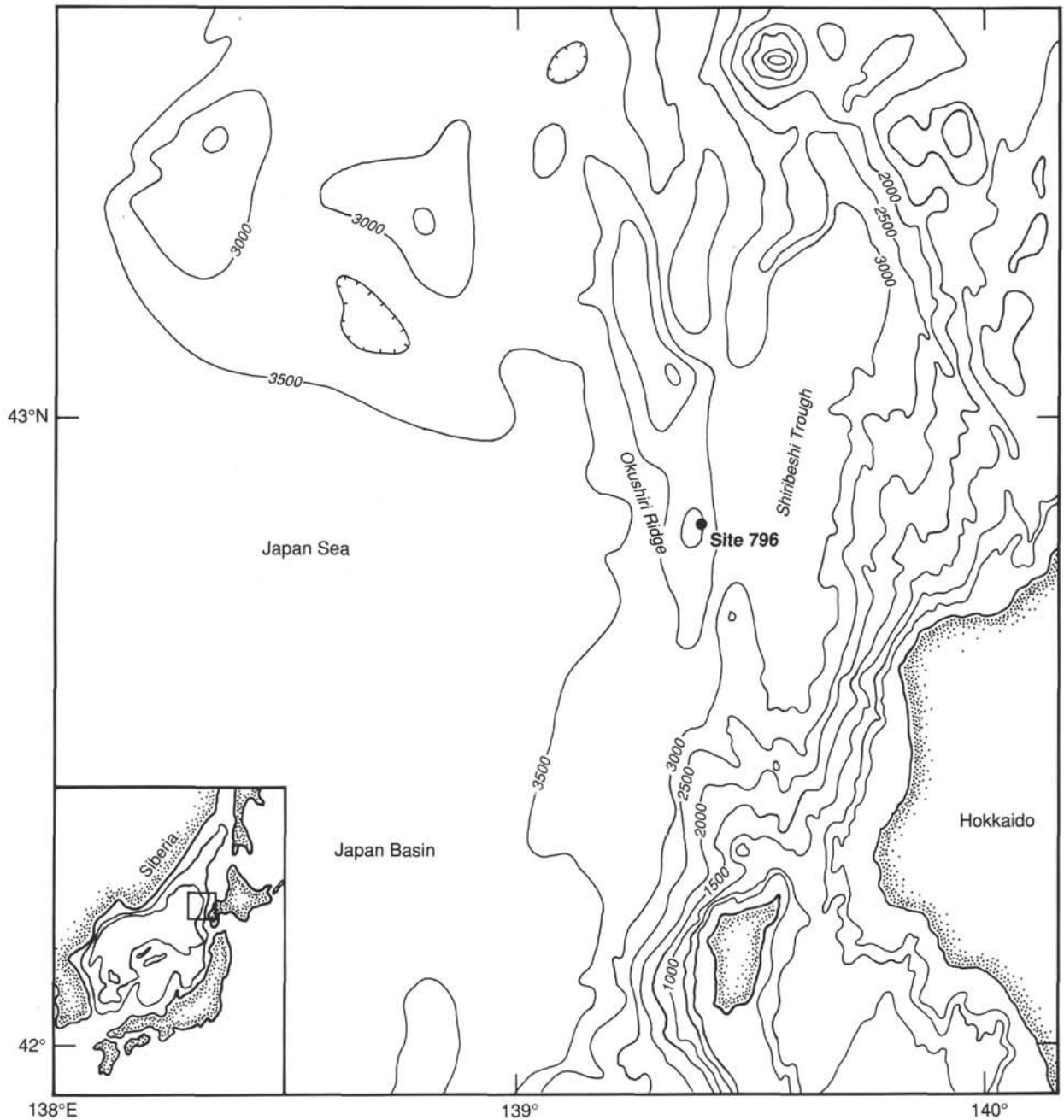


Figure 2. Location map of the area surrounding Site 796 showing bathymetric features and the site location. The bathymetric contour interval is 500 m.

continental areas. Based on the cross section by Gribidenko (1979) which lies north of the site, the inferred thicknesses for the intervals equivalent to oceanic Layers 2 and 3 are about 7 and 9 km, respectively.

Heat Flow

The measured heat flow values in the area surrounding Site 796 fall in the range of 82–119 mW/m² (Fig. 3). The average of values closest to the site is 94 mW/m², which is somewhat less than the average value for the Japan Basin but about the same as the Yamato Basin (Yoshii and Yamano, 1983; Tamaki, 1986). We have not used this value to provide a first approximation of basement age as at the previous two sites because recent uplift and tectonism has likely perturbed heat flow in this area.

Magnetics and Gravity

Magnetic anomaly profiles near Site 796 have peak to peak amplitudes in the range of 150–300 nT and wavelengths on the order of 50 km (Fig. 4). In map view, these anomalies form irregular blocky patterns much like those near Site 795 to the north, suggesting that the area around Site 796 is underlain by discrete basement blocks (Isezaki, 1986). This magnetic anomaly pattern changes to the south near the southwestern tip of Hokkaido where amplitudes increase, and to the northeast where both amplitudes and frequencies increase. These differing signatures probably reflect laterally variable volcanic terranes underlying the sedimentary cover. To the west and southwest in the Japan Basin, short, disrupted linear patterns similar to those

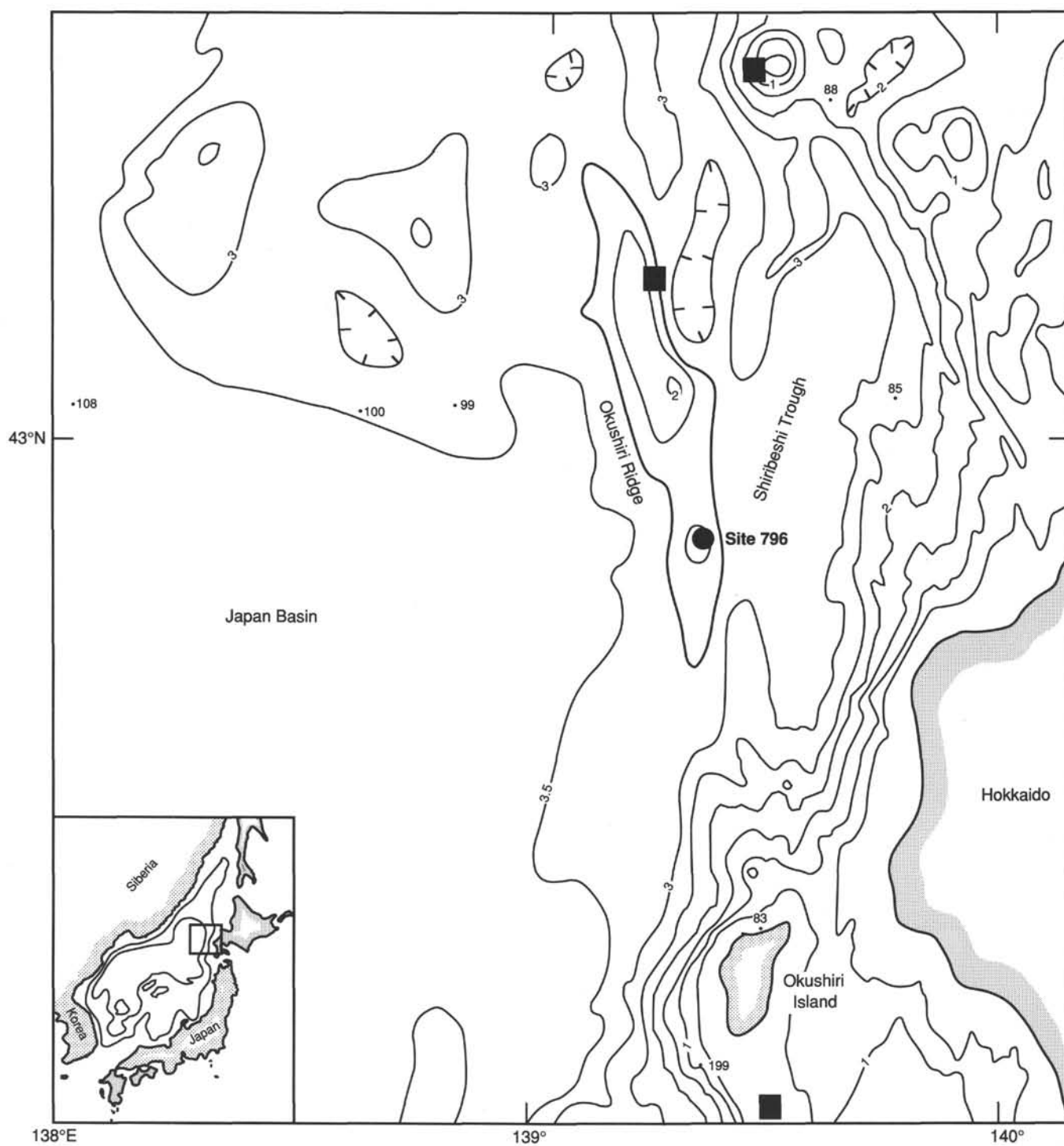


Figure 3. Location of heat flow values and dredge samples. Heat flow values are represented by small dots; units are in mW/m^2 , and data are from Yoshi and Yamano (1983). Dredge samples are represented by solid squares. See text for descriptions. The bathymetric contour interval is 500 m.

found in areas of propagating spreading ridges characterize the magnetic anomalies (Tamaki et al., 1988a, 1988b).

Free-air gravity anomalies in the site area range from -50 to 60 mgal (Fig. 5). As with the previous sites, the gravity anomalies faithfully mirror the bathymetry. Accordingly, a gravity high of about 38 mgal overlies the Okushiri Ridge, while the adjacent Shiribeshi Trough which lies just east of the site, has a corresponding gravity low of -50 mgal (Figs. 5 and 6). The rela-

tively high gravity over the ridge reflects the shallow basement there; the adjacent low delineates a significant thickness of sediment in the Shiribeshi Trough.

Basement Rocks

Information regarding possible basement rock types in the vicinity of Site 796 is sparse. Only three dredge operations have been carried out in the immediate area and only two of these

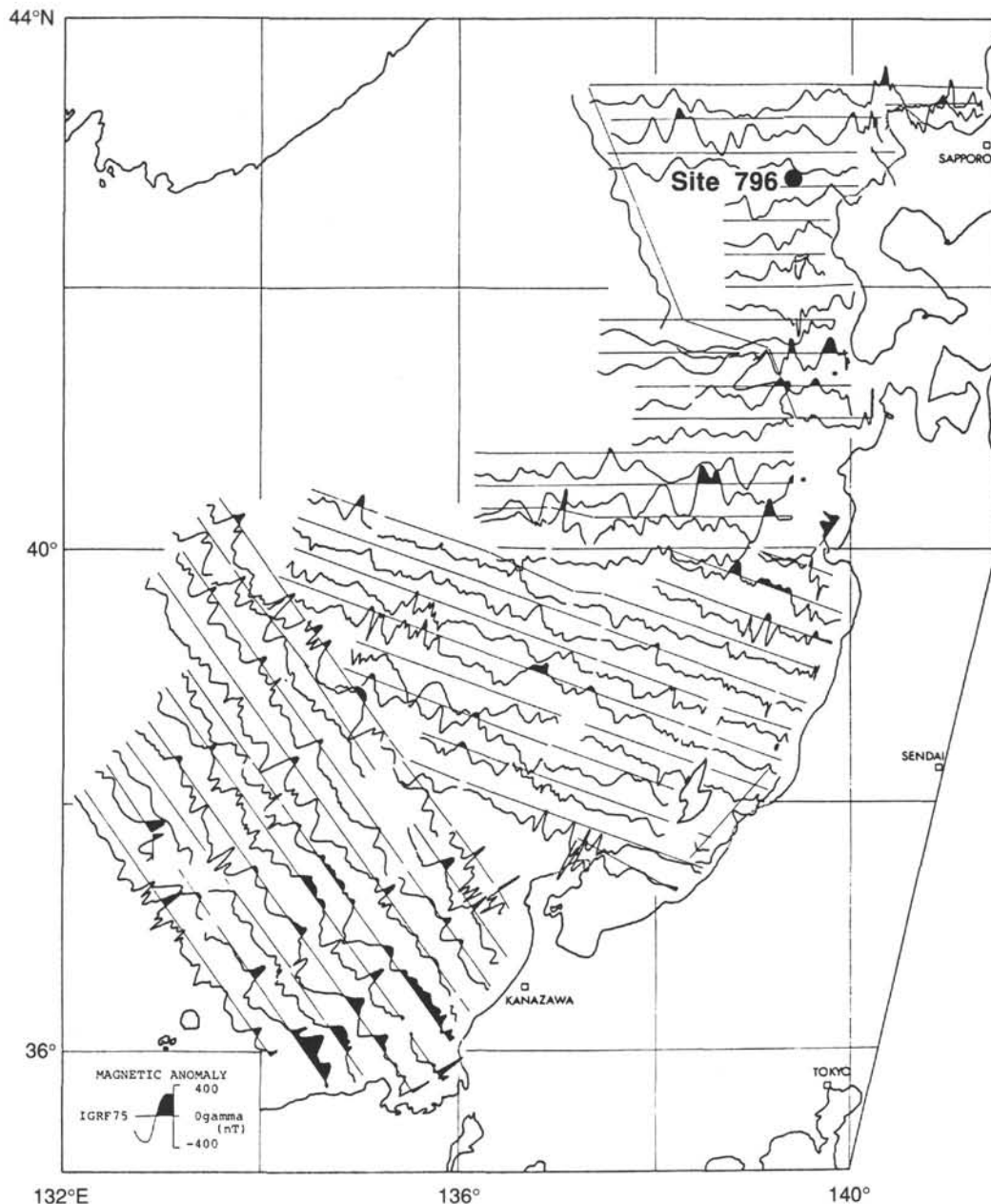


Figure 4. Magnetic anomaly profiles along ship tracks around Site 796. Data from Honza (1979).

were successful (Fig. 3). The dredging of Okushiri Ridge, at $43^{\circ}15.0'N$, $139^{\circ}18.8'E$, recovered no materials. The other two efforts recovered mostly *in situ* Neogene silty and sandy sediments with some shell fragments, and small volcanic pebbles which either were not in place or comprise components of the sands (Honza, 1979). Thus, no samples which may be representative of acoustic basement have been recovered by dredging operations in the area surrounding Site 796. Further north, east of Site 795, basaltic rocks have been dredged from the northern end of Okushiri Ridge and these provide the only direct information on nature of acoustic basement of this ridge.

In contrast with the dredging results, onshore outcrops provide the best clues as to the identity of acoustic basement near Site 796. A variety of volcanic, plutonic, and metasedimentary suites crop out in southwestern Hokkaido and on Okushiri Island some 40–50 km to the south-southeast (Geological Survey of Japan, 1982). The volcanic rocks include Quaternary andes-

ites and Miocene andesites and basalts. Plutonic rocks are mostly Lower Cretaceous granitic rocks. The metasedimentary suite consists of Paleozoic and Mesozoic limestones, chert, basalts, mudstones, and sandstones. These occurrences provide some perspective on the kinds of rocks which may comprise acoustic basement offshore, but it is not possible to tie any of them directly to Site 796 using seismic data.

Tectonic Setting

Site 796 lies within the active tectonic zone of the eastern Japan Sea (Tamaki and Honza, 1985). This zone is characterized by fault-bounded, north-trending ridges, escarpments, and closed basins, a morphology commonly found along transcurrent fault systems. Based on this distinctive morphology and on regional structural analyses (Kimura et al., 1983; Lallemand and Jolivet, 1985), Jolivet et al. (in press) suggested that many of the faults in this system were once right-slip faults which formed during a

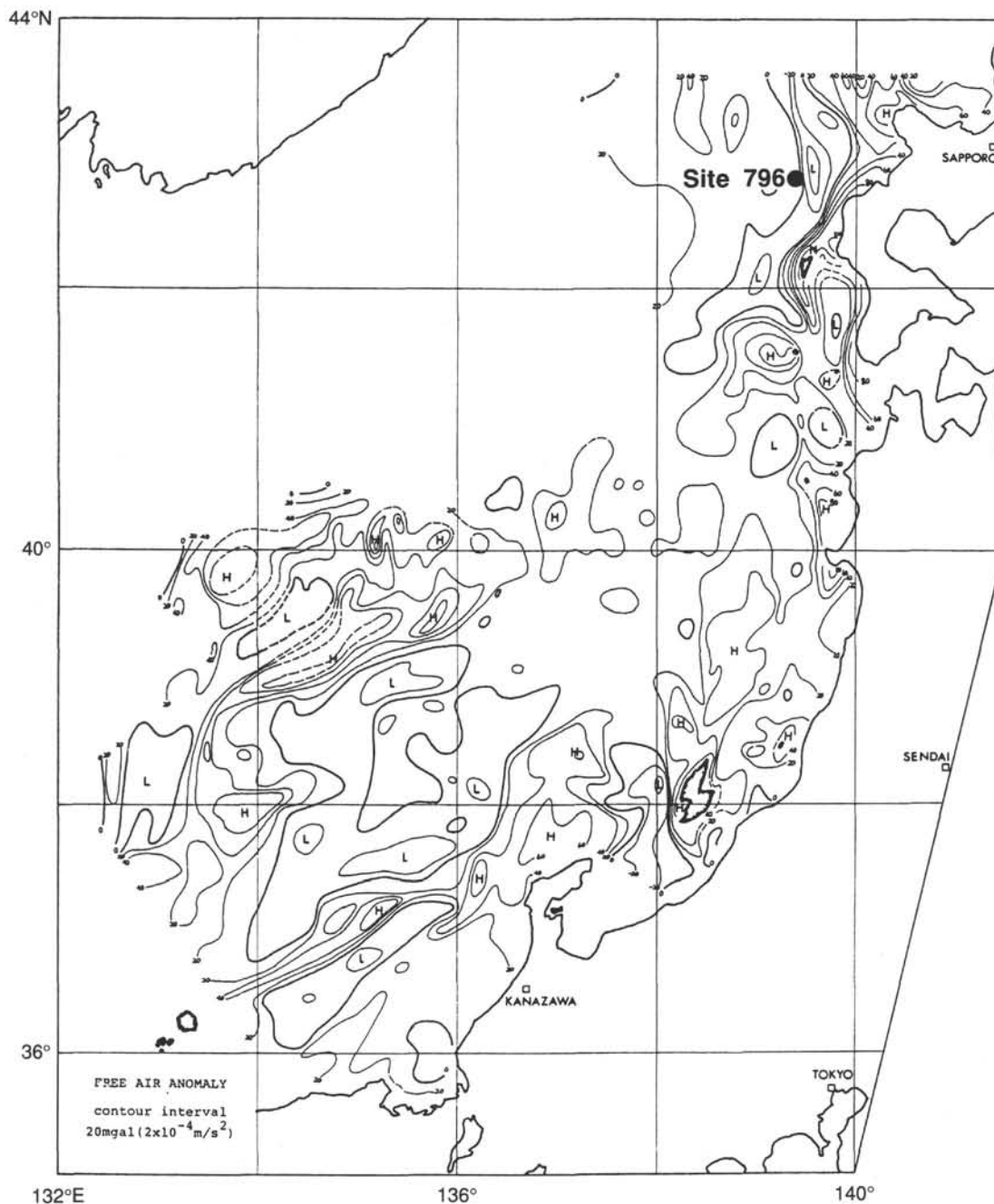


Figure 5. Free-air gravity anomaly map in the vicinity of Site 796. Contour interval is 20 mgal. Data from Honza (1979).

Neogene episode of transcurrent motion and which have been recently reactivated as thrust faults.

Presently, most of the faults within the east Japan Sea tectonic zone are steep thrust or reverse faults and the region is characterized by large earthquakes having compressional focal mechanisms. Several of these faults bound Okushiri Ridge near Site 796 (Figs. 7 and 8) and similar reverse faults occur along en echelon ridges further to the north and south. Although no large earthquakes have been associated with these local faults, several recent shocks of very large magnitude ($M = 6.4-7.7$) have occurred on similar faults to the north and south within the tectonic zone (Ichikawa, 1971; Fukao and Furumoto, 1975; Ishikawa et al., 1984; Tamaki and Honza, 1985). The focal depths for these earthquakes range from 14 to 33 km and focal

mechanism solutions indicate east-west and northwest-southeast compression. Based on these data and on an estimate of 30 km for the thickness of the lithosphere in the Japan Sea (Abe and Kanamori, 1970), Tamaki and Honza (1985) have suggested that some of these reverse faults cut the entire lithosphere and that the east Japan Sea tectonic zone may now be an area of incipient subduction. In this scenario, the Okushiri Ridge near Site 796 represents an active obducted block; ongoing compression of this ridge is supported by folding and thrust fault deformation of Quaternary sediments in the adjacent Shiribeshi Trough (Figs. 6 and 8).

Associated with the faulting in the area surrounding Site 796 and the Okushiri Ridge are at least two styles of folding. Simple folds have developed in Quaternary strata which are adjacent to

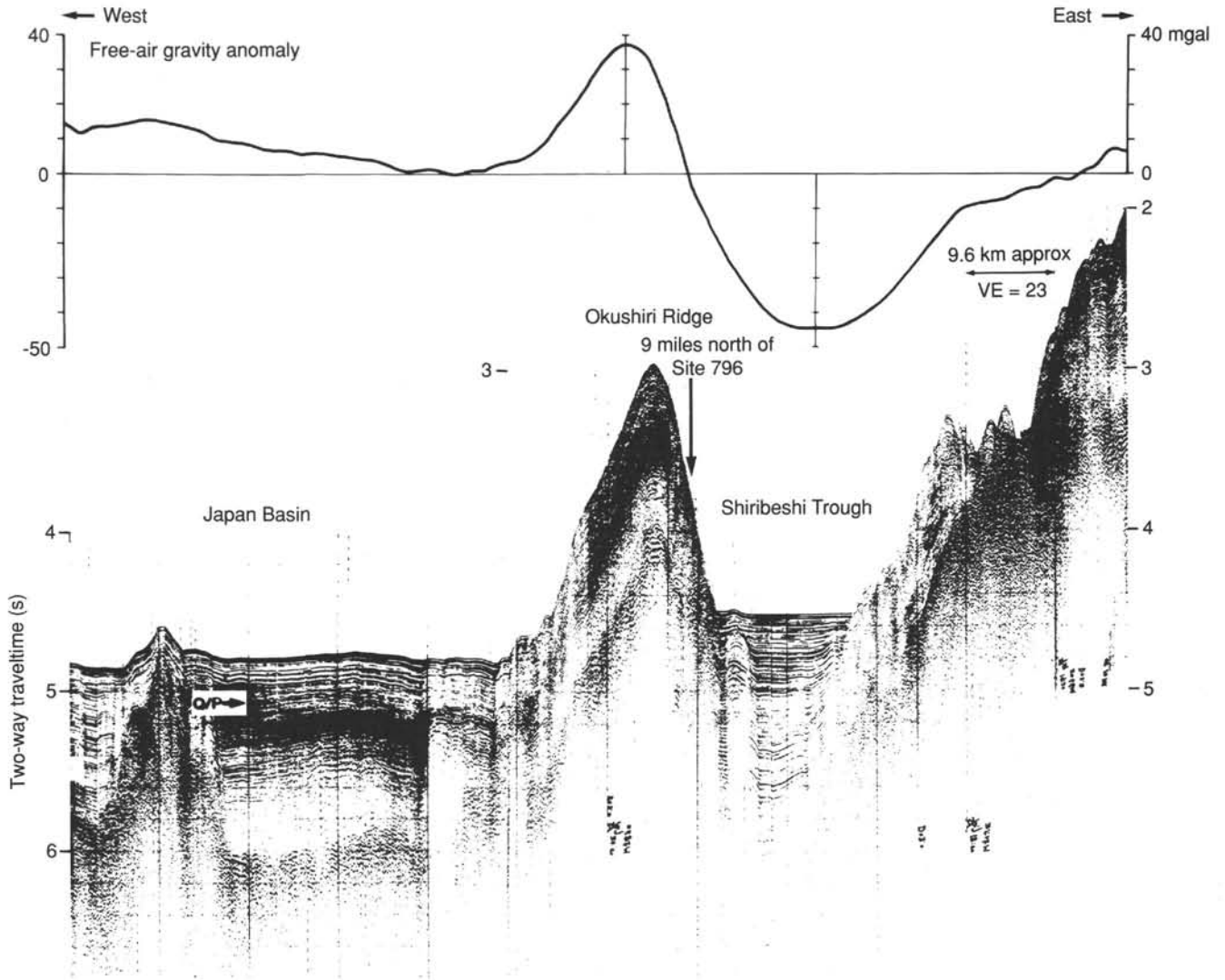


Figure 6. East-west single channel seismic reflection Line J12 and free-air gravity profile north of Site 796. Note the extreme vertical exaggeration of the seismic section. See Figure 7 for location.

uplifted linear ridges such as in the western Shiribeshi Trough (Figs. 6 and 8). The folds are sometimes cut by eastward-verging and propagating thrust faults which apparently root in decollements at the base of the Quaternary section (Fig. 8). Folds and faults of this type are formed by east-west compression of the Quaternary sediments caught between uplifted highs such as the Okushiri Ridge.

In addition to these structures, asymmetric folds occur whose axes are coincident with the ridge crests. These may not represent true folds but rather are erosional or collapsed edges of the uplifted blocks (Figs. 6 and 8). Such an origin is supported by the thinner stratigraphic section present on these steep limbs relative to the more gently-dipping limbs and by the hummocky surface of the seafloor.

Folds also occur associated with the trailing edges of some of the uplifted blocks (Figs. 6 and 8; also see Figs. 10 and 11, and seismic sections in Tamaki, 1988). These folds are relatively short wavelength features which occur at the break in slope between the Japan Basin and the uplifted blocks. They are active features because they disrupt the seafloor and because they show little evidence of erosion. As yet, no systematic analysis of the faulting associated with these folds has been done.

Sedimentation

The sedimentary section which overlies acoustic basement in the vicinity of Site 796 shows considerable lateral variation. On the gentle western limb of Okushiri Ridge, the sedimentary thickness is on the order of about 800 m and the seismic character is similar to that at Sites 794 and 795 (Figs. 6 and 8). At least four seismic intervals occur within this section, including: (1) an upper moderately to weakly stratified interval; (2) an upper weakly stratified to transparent interval; (3) a middle moderately well stratified interval; and, (4) a lower weakly to moderately stratified interval. These intervals can be traced to the crest of the ridge where the reflection character deteriorates. On the eastern limb, the same seismic intervals are present but the sedimentary thickness is only about 500–600 m and the reflector definition and continuity are poor. In addition, the seafloor shows rather hummocky relief indicating significant slumping and mass wasting. East of the Okushiri Ridge, the Neogene hemipelagic section presumably lies buried beneath a rapidly deposited, westward-thickening wedge of mostly Quaternary clastic sediments which partially fill the Shiribeshi Trough. Seismic and gravity data show that the greatest thickness of this fill,

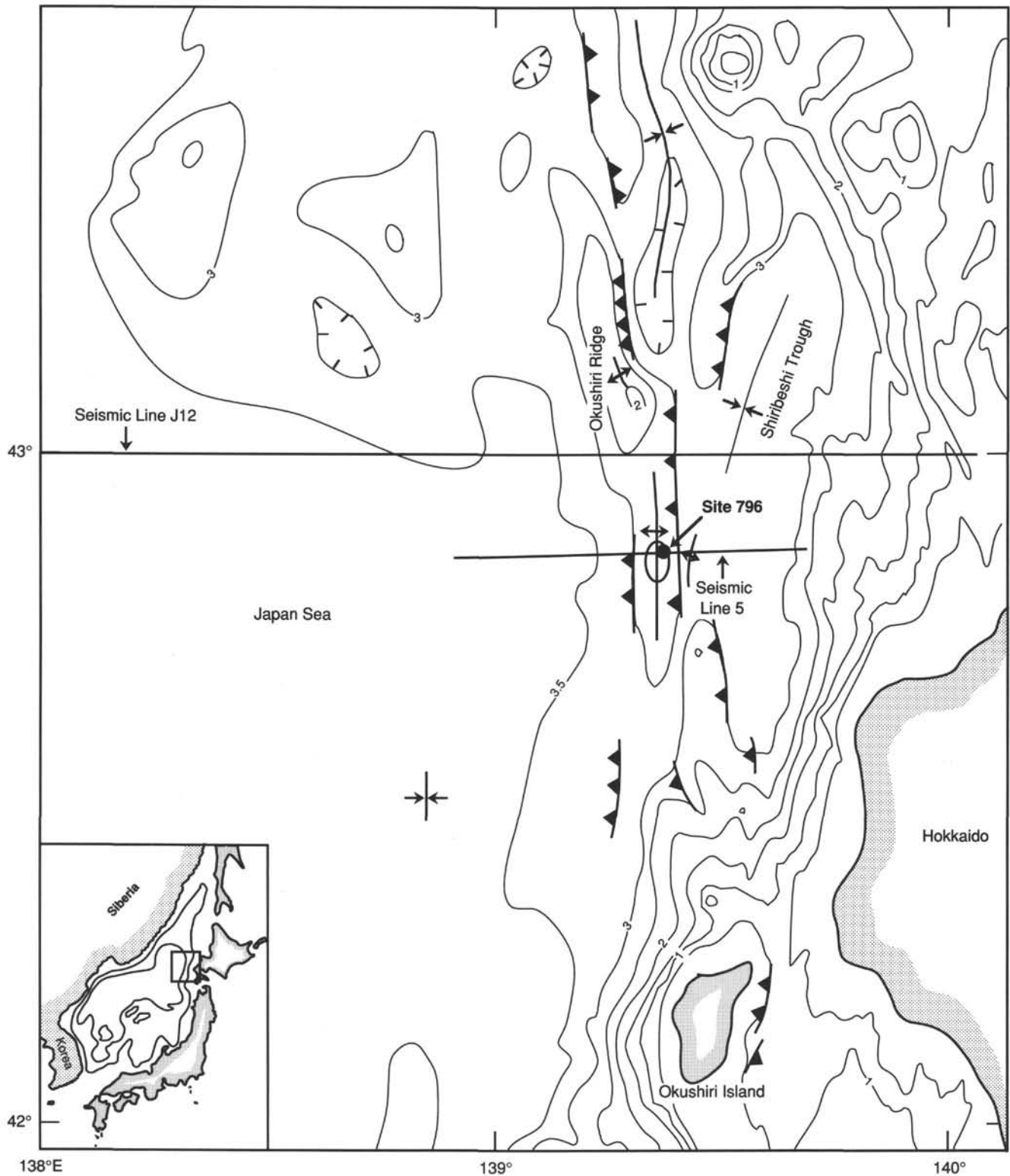


Figure 7. Tectonic map of the area surrounding Site 796 showing recognized faults and fold axes. The location of seismic Line J12 shown in Figure 6 is noted. The bathymetric contour interval is 500 m.

about 1800 m, lies at the base of the steep eastern flank of Okushiri Ridge (Figs. 5, 6, and 8). Further to the east, at the feather-edge of this Quaternary fill, the Neogene and Quaternary hemipelagic section appears again on an uplifted, eroded high.

Prior to drilling, the estimated thickness of the sedimentary section at Site 796 was 570 m. Because of intervening structures, direct seismic ties to other drill sites were not possible and only general character ties could be made. Even this comparison is tenuous because structural disruption and slumping have af-

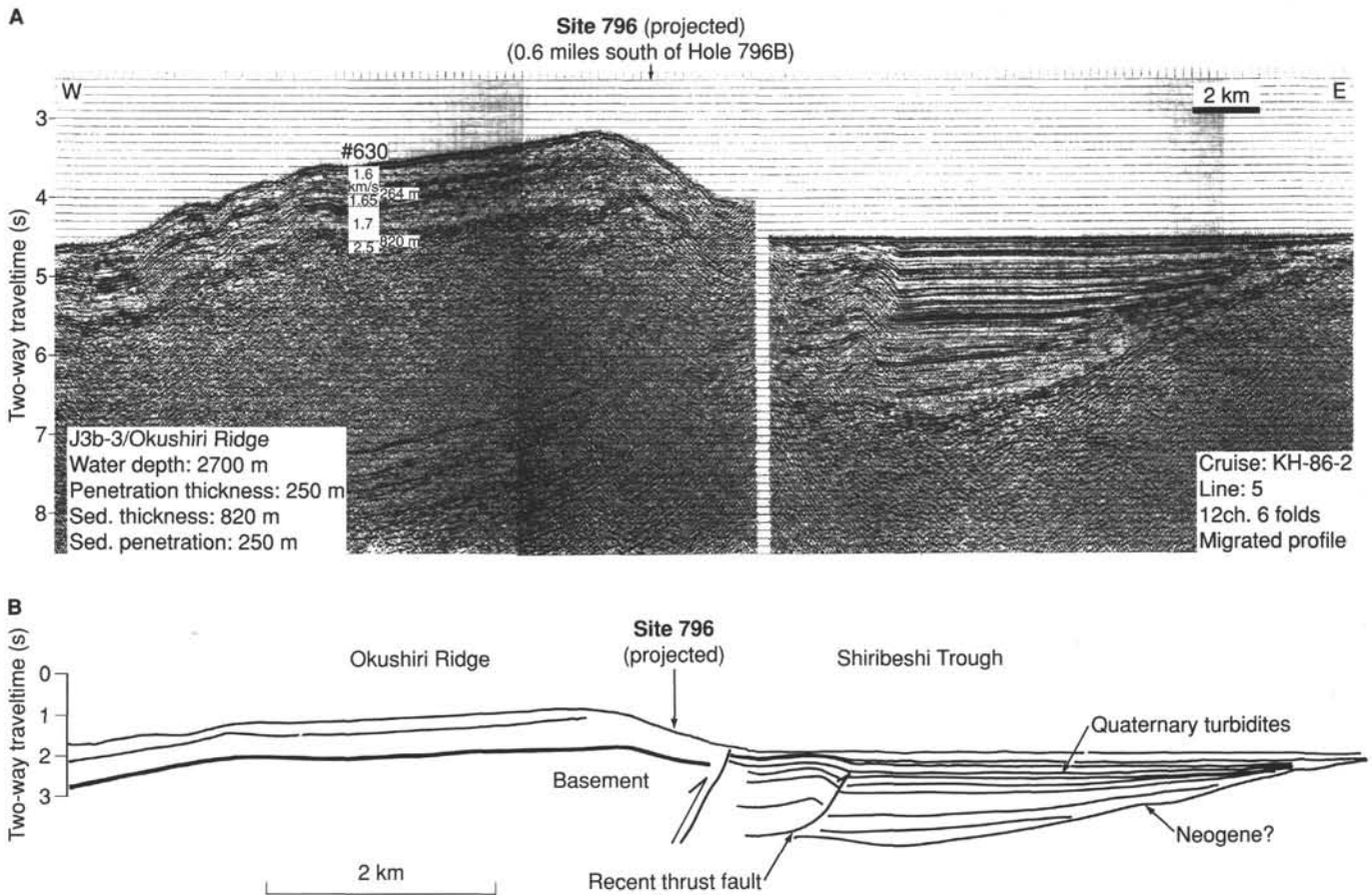


Figure 8. East-west profile south of Site 796. **A.** Ocean Research Institute multichannel seismic reflection Line 5. **B.** Line drawing interpretation of Line 5. See Figure 7 for location.

pected the definition and continuity of reflectors on this limb of the Okushiri Ridge. Nevertheless, at Site 796 we expected to encounter approximately 200 m of slumped and faulted Pliocene-Quaternary hemipelagic clays, silts, and some sands. The youngest sands were predicted to occur at about 100 mbsf in the upper Pliocene part of the section. The first occurrence of opal-CT and siliceous claystones were expected at about 200 mbsf and to extend to about 300 mbsf, coincident with the third seismic interval which is characterized by moderately well-stratified parallel reflectors. Below this, from 300 mbsf to acoustic basement at 570 mbsf, we expected mostly silty claystones.

Objectives

Timing of Uplift and Initiation of Convergence

The principal objective at Site 796 was to determine the timing of uplift of Okushiri Ridge and, by inference, the initiation of convergence and compressional tectonics in the eastern Japan Sea. The Okushiri Ridge offered one of the best sites to achieve this goal because the sedimentary section appeared to be mostly intact, albeit modified somewhat by faulting, folding, and slumping, and because dating by microfossils was expected to be good. Furthermore, this ridge typifies many of the high-standing fault blocks in this tectonic zone in terms of style. Based on seismic data and the recent seismicity of the region, the initial uplift of this ridge occurred some time during the late Pliocene, compression continuing through to the present. In or-

der to time the initial phase of uplift, we needed to document the presence and age of the youngest sandy layers, reasoning that after uplift no sands could reach the high part of the ridge. If the drilling was successful, these data would constitute one of the most precise determinations of the age of initial uplift in this region and permit comparisons with coeval tectonic events in Japan. Together these results would provide valuable constraints for tectonic reconstructions of northwestern Japan and the northeastern Japan Sea.

Style and Dynamics of Back-arc Rifting

A second goal of the drilling at Site 796 was to determine the nature and age of acoustic basement. Together with the results from additional sites drilled during Legs 127 and 128, these data would permit assessment of the style and dynamics of rifting of the Japan Sea. More specifically, if Okushiri Ridge represents an obducted block, then the basement rocks recovered from it may be typical of those flooring other parts of the Japan Basin. Comparison with the basaltic rocks recovered at Site 795 would provide the first estimate of lateral variations of this basement.

In-Situ Stress Field

An additional objective of the drilling at Site 796 was the measurement of the magnitude and direction of the present tectonic stress within an active zone of convergence. Our inability to obtain measurements at the two previous sites due to hole conditions added significance to this attempt.

Oceanographic and Sedimentation History

A further objective of the drilling at Site 796 was to characterize the history of sedimentation and water mass fluctuations in this area of the Japan Sea. As noted above, a key objective was to obtain terrigenous sand deposits within a preserved hemipelagic section which would permit dating of the uplift of the Okushiri Ridge and the initiation of convergence of the east Japan Sea tectonic zone. The compositions of these sands and sedimentary structures within them would also provide information on provenance and mode of deposition which would be useful in assessing the tectonic and sedimentary history. In addition, if the hemipelagic component was not too diluted with sandy material, the contained microfossil assemblages would provide useful data needed for temporal reconstructions of climate, water mass, subsidence, and uplift. In this regard our specific goals matched those at the previous two sites, namely: (1) the history of anoxia, circulation, and sea level in relation to climate, subsidence, and in this case, uplift; (2) fluctuations of the carbonate compensation depth; and (3) time- and temperature-controlled post-depositional processes, particularly those involving organic matter, biogenic silica, and carbonate. The integration of these data with other regional offshore and onshore data would form the basis for an understanding of the sedimentation and oceanographic history of the Japan Sea and of the western Pacific margin.

OPERATIONS

Preamble

After departing from Site 795 on 11 July, we steamed south to our next location on the Okushiri Ridge about 42 km off the west coast of Hokkaido. As a result of the transformer problems we had at Site 795, our average transit speed was only about 6 kt. We made the best of this situation by acquiring an excellent seismic record en route and by timing our arrival to coincide with a favorable GPS window. Magnetics data were also acquired during the transit. By about 1700 hr (0800 UTC) on 22 July 1989 we were in a position about 3 nmi west-northwest of the site to begin our seismic survey.

Site Approach

As for the previous sites, our seismic survey plan was to obtain several high angle crossings of the site to confirm the loca-

tion and avoid local closures. The first crossing was to be along a pre-existing east-west multichannel line. Following this, we planned to swing to the north to obtain a north-south transect parallel to the strike of the ridge, then retrace that route and drop the beacon at the best location. Special attention was to be paid to the depth profiler because we expected a rather uneven seafloor due to slumping.

We approached the primary site location from the west along Ocean Research Institute multichannel Line 5 at a speed of 4 kt (Figs. 9–11). Our first crossing line began about 3 nmi west-northwest of the planned location and continued for about a mile past it. We then turned to the north as planned and made the transit to the beginning of our north-south crossing line about 1 mi north of the location. This transect provided a valuable seafloor profile which enabled us to find a relatively flat position free from closure just north of the planned location. We continued past the original planned location for 1 mi, then returned on a reciprocal course to the identified flat area and launched the beacon. At 0755 hr (2255 hr UTC) on 22 July (21 July UTC) we slowed to pull in the gear and position the ship.

Drilling and Logging Summary

Our drilling plan for Site 796 called for two adjacent holes to achieve our scientific objectives. Hole 796A was to be an APC/XCB hole into indurated sediments. *In situ* temperature measurements, using the Uyeda probe, were scheduled after every third core until the sediments became too indurated to yield reliable information. Hole 796B was to be an RCB hole beginning at the Hole 796A total depth and carrying at least 50 m into hard basement rocks. We planned to log the complete sedimentary and basement sections of this hole and perform packer/hydrofracture experiments in the basement interval. Standard gas monitoring would be done throughout the entire sedimentary section.

Hole 796A

Hole 796A was spudded at 0330 hr on 23 July (1830 hr, 22 July UTC) with a mud-line core which established the seafloor at 2581.8 m below the rig floor. Eight oriented APC cores were taken with the polycrystalline diamond compact bit to a depth of 58.7 mbsf (Table 1). Temperature measurements were taken every third core. The sediments were firm and contained methane and hydrogen sulfide at a very shallow depth (5 mbsf). Re-

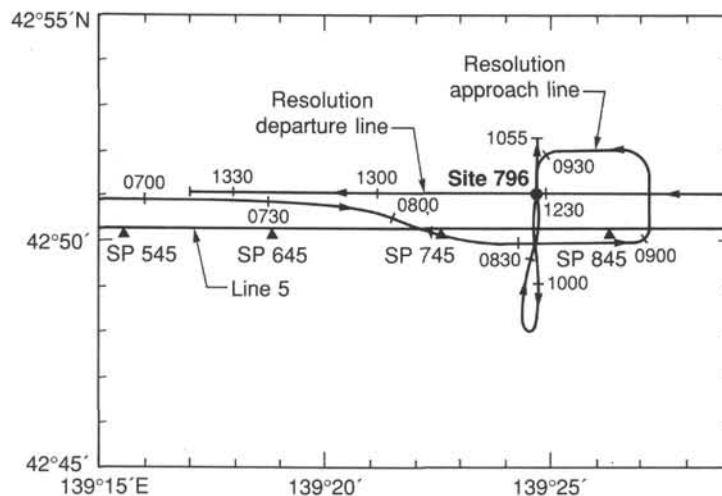


Figure 9. Chart showing JOIDES Resolution approach and departure lines and a pre-existing multichannel line for Site 796.

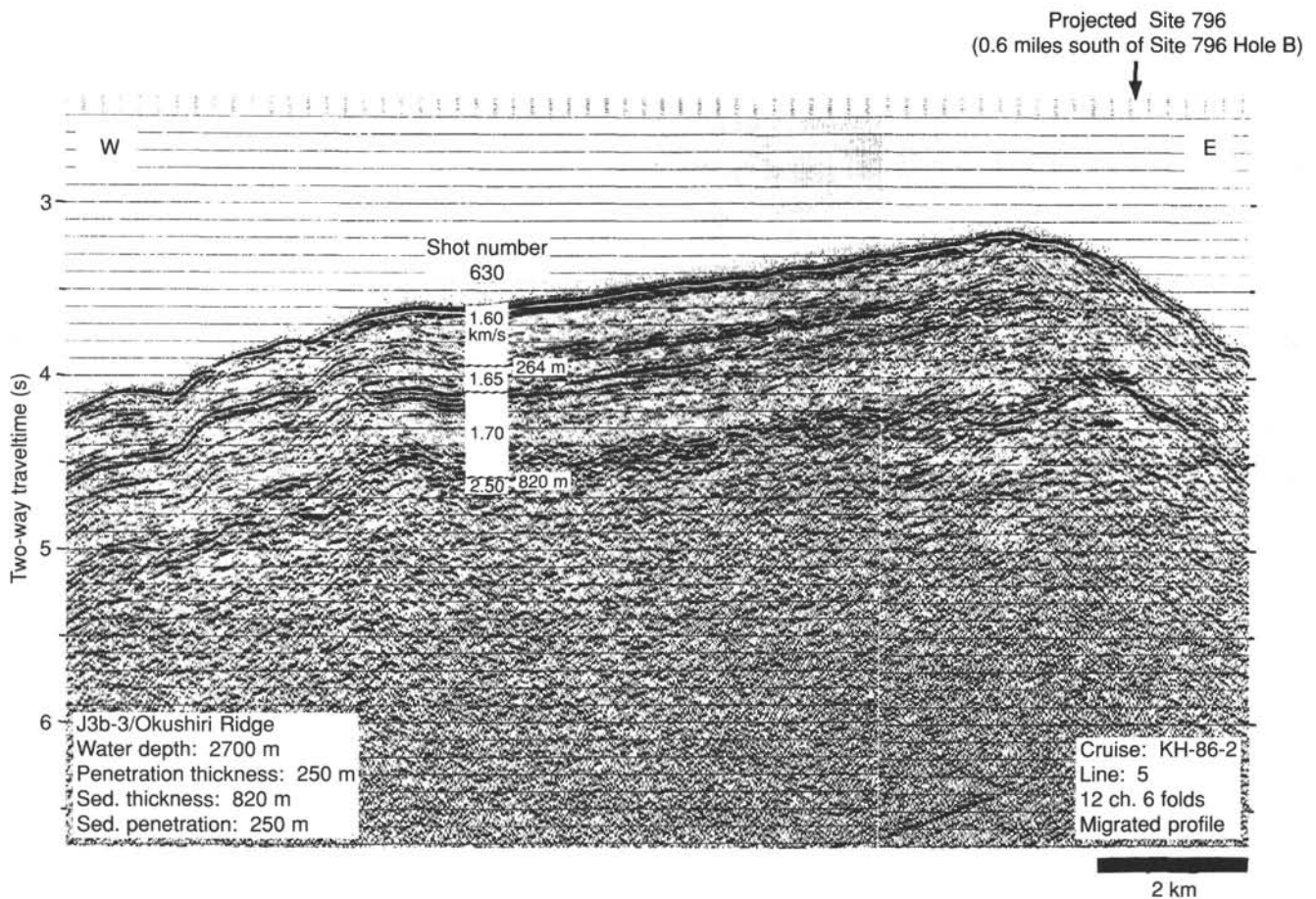


Figure 10. Ocean Research Institute multichannel seismic Line 5 south of Site 796. See Figure 9 for location.

covery was excellent down to 50.7 mbsf, but most cores contained large voids caused by gas expansion. At 50.7–51.7 mbsf, the APC encountered a hard layer and no material was recovered. A second attempt was more successful, but required considerable overpull to retrieve the core barrel.

We switched to the XCB after Core 127-796A-8H (58.7 mbsf) and took 19 cores to 242.9 mbsf. Recovery was variable over this interval, averaging about 40% (Table 1). Methane was common in the uppermost cores, including gas hydrate in Cores 127-796A-10X through -12X (68.4–97.7 mbsf), but steadily decreased with depth. We encountered some hole instability problems at about 88 mbsf, probably caused by a coarse sand layer, and flushed the hole with mud to control them. Conditions improved somewhat with further drilling, but deteriorated again at about 230 mbsf. Flushing the hole with mud did not significantly improve the situation, and we decided to terminate Hole 796A at 242.9 mbsf. We filled the hole with heavy mud, retrieved the pipe, and offset 250 m to the east in the hopes of drilling a more stable section.

Hole 796B

After a slow trip in, marred slightly by damage to the iron roughneck, we spudded Hole 796B with the RCB at 0500 hr on 25 July (2000 hr on 24 July UTC). We took one core to establish the mud line, then washed to 30.2 mbsf. Below this, we planned to take at least three cores to cover a missed interval in Hole 796A where we suspected sands and a paleontological hiatus to be present. We ended up taking seven cores (30.2–97.9 mbsf) in order to establish the stratigraphy, then washed to 243.0 mbsf, the total depth level of the first hole.

We continuously cored from 243.0 to 464.9 mbsf using the RCB and attaining variable recovery (Table 1). Hole conditions were difficult over this interval. Despite concerted efforts to keep the hole open using a combination of mud pills and wiper trips, conditions deteriorated such that it became impossible to get past a blockage at 381 mbsf without putting our last BHA at serious risk. Having already met an important part of our scientific objectives at this site, we decided to log the open section of the hole while considering our options for further drilling at this locality or proceeding to our last site following completion of the logging.

We were forced to release the bit at 367 mbsf after we were unable to lower the pipe past the blockage at this level. We then raised the pipe to 100 mbsf and filled the hole with KCl mud in preparation for logging. About this time, the first beacon failed and we were compelled to launch a second one, leaving us with two for the remainder of the leg. Given the tenuous hole conditions, we opted to log first with a nonradioactive string consisting of the sonic, dual induction, and NGT tools. If successful, we planned to follow with the FMS which would provide detailed caliper information. Pending a clean hole, the last tools would be the geochemical tool, a lithodensity and neutron string, and the borehole televiewer.

The first run into the hole with the nonradioactive string reached to a depth of 329 mbsf before encountering a blockage which stopped its progress. After several unsuccessful attempts at passing this bridge, we ceased these efforts and logged the hole. Succeeding logs were acquired without problem. Following the last log, we filled the hole with heavy mud and retrieved the drill string.

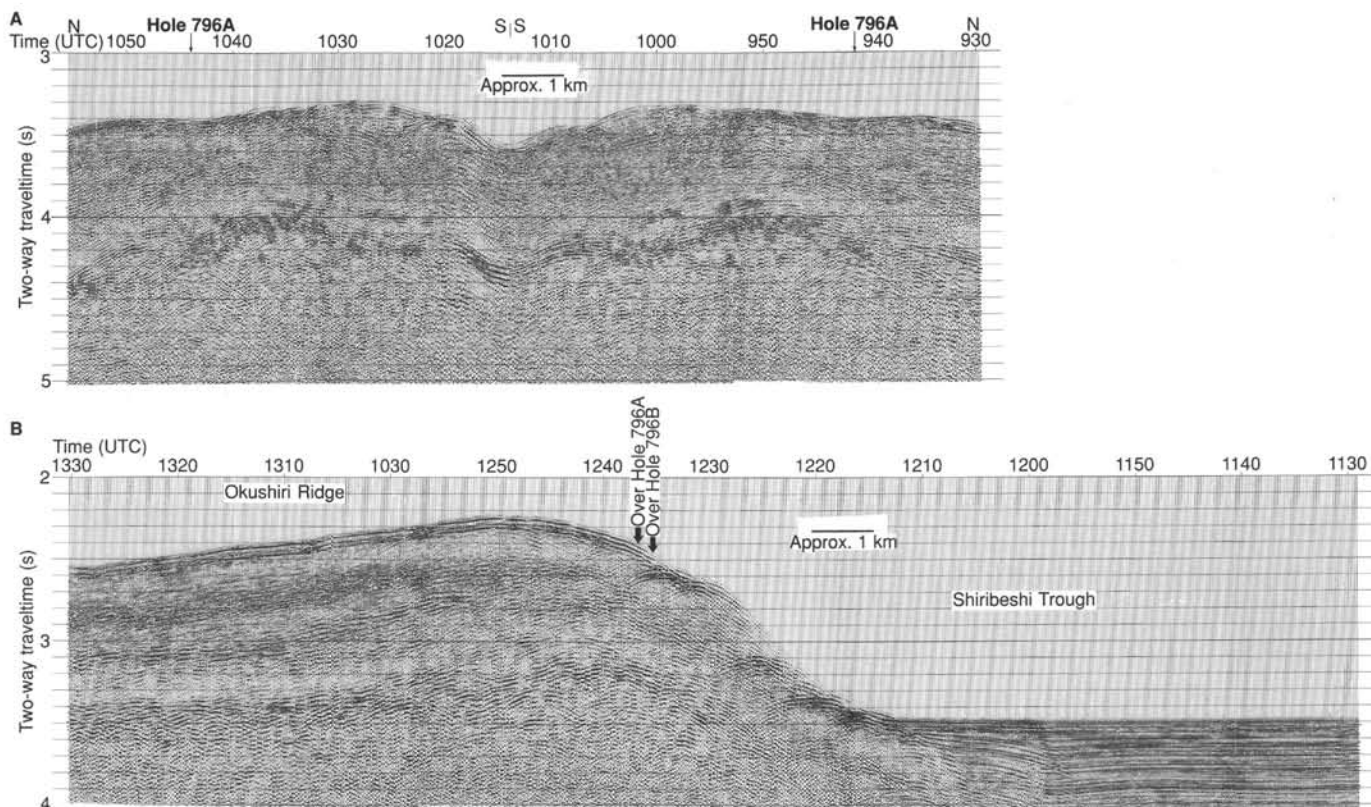


Figure 11. JOIDES Resolution single channel seismic lines for Site 796. A. Approach line. B. Departure profile. See Figure 9 for locations.

Site Departure

After the recovery of the drill string from Hole 796B at 1900 hr (1000 hrs UTC) on July 29 1989, we steamed east approximately 5 nmi and deployed the seismic gear in order to obtain an east to west crossing of the Okushiri Ridge through the site location. After making a 180° turn and adjusting our speed to 6 kt, we acquired a profile through the site and continued on a bearing due west for another 5 nmi (Fig. 11B). Following completion of this seismic line, we turned southwest, increased our speed to about 10 kt, and made for our next site near the Yamato Rise.

LITHOSTRATIGRAPHY

Lithologic Units

The sedimentary succession recovered at Site 796 (Fig. 12) consists of 465 m of silty clay and claystone, clayey diatom ooze, diatomite, and siliceous claystone. These are interbedded with sand and sandstone, pebbly mudstone, siltstone, and ash and tuff. Some units contain minor diagenetic dolomite, Mg-calcite, and glauconite. The age of the succession ranges from Quaternary to middle(?) Miocene.

We have identified five major lithologic units based on composition, structures, and textures (Fig. 12). Of these, mineral composition and grain size are the principal criteria by which units are differentiated. Figure 13 illustrates the relative abundance of major particulate components in the upper 300 m at Site 796, data which were used to help delineate the units.

Unit I (0–146.3 mbsf)

Cores 127-796A-1H through 127-796A-17X.

Unit I is dominated by diatom-bearing clay and silty clay and can be divided into two subunits based on the presence of inter-

bedded sand. Sand is not observed in Subunit IA, but first appears in Subunit IB, and has important implications for regional tectonics (discussed below).

Subunit IA (0.0–51.7 mbsf)

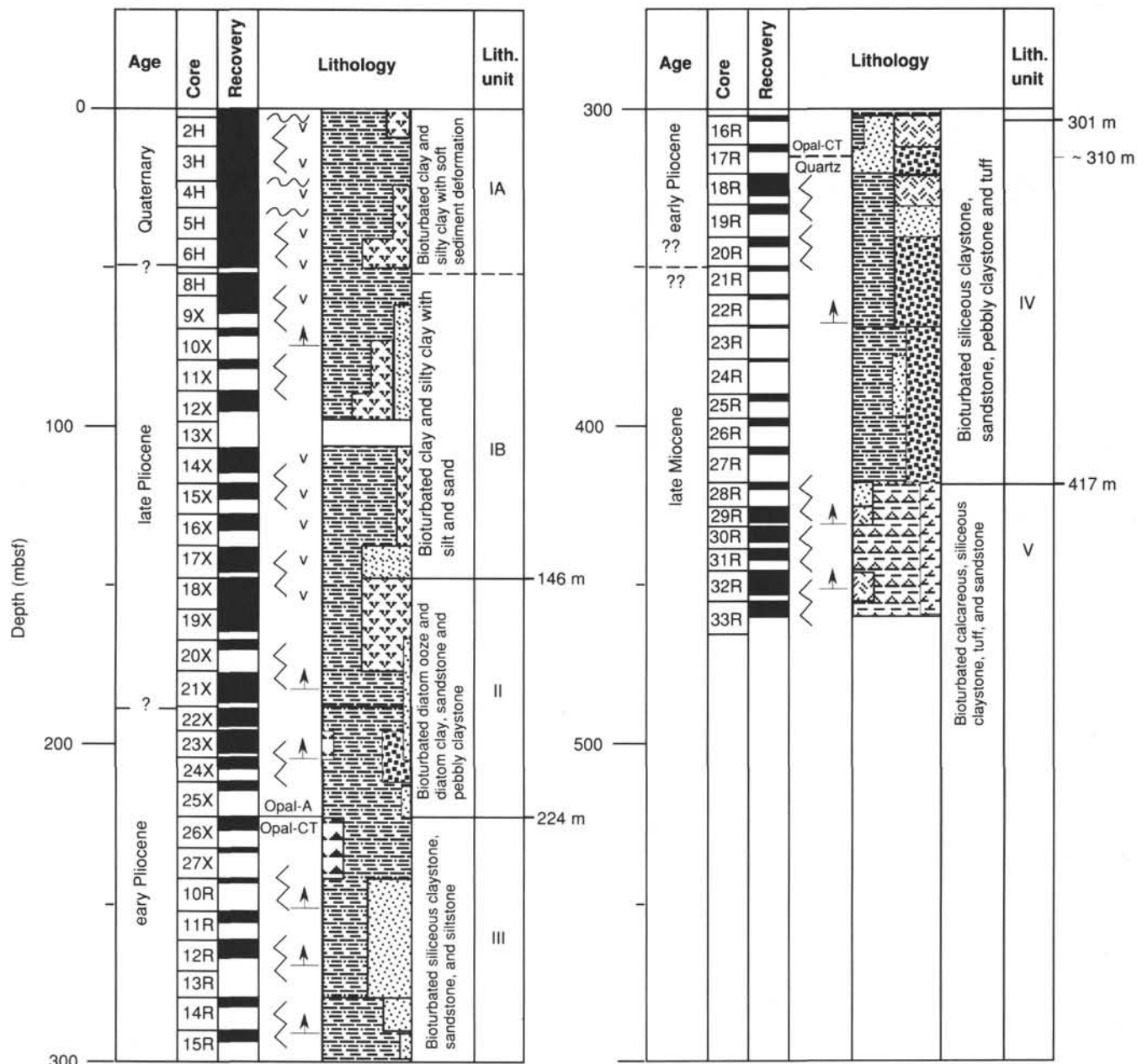
Subunit IA, Cores 127-796A-1H through 127-796A-7H, is 51.7 m thick and is dominated by diatom-bearing clay and silty clay of Quaternary age. These deposits are moderately to highly bioturbated, and show evidence of soft-sediment deformation, including both contorted and inclined beds (slump blocks?), some of which are bounded by microfaults. Diatom-bearing claystone contains scattered pyrite (in both nodular and disseminated form). Faint color banding is evident, reflecting interbedded pyrite and organic-rich zones. Glass shards are disseminated throughout the major lithologies. Subordinate lithotypes include diatom ooze and vitric ash beds. Bioturbated diatom ooze occurs only at the base of Subunit IA, interbedded with silty clay. Vitric ash beds and laminae are generally less than 2 cm thick (commonly 1 cm in thickness), are normally graded, and are locally disrupted either by bioturbation and/or by soft sediment deformation.

Subunit IB (51.7–146.2 mbsf)

Subunit IB, Cores 127-796A-8H through 127-796A-17X, late to early Pliocene in age, clay and silty clay with sand, is similar to Subunit IA, but is differentiated by the appearance of sand and silt beds. Dominant lithotypes include moderately to highly bioturbated diatom-bearing clay and silty clay. In most cases, original depositional structures are obscured. Locally, contorted and slumped beds occur, but the overall frequency of soft-sediment deformation features decreases compared to Subunit IA. Minor lithologies include sand, silt, ash, and clayey diatom ooze. Sand is first observed in Section 127-796A-9X-3 at approximately 63 mbsf, and occurs throughout the subunit as scat-

Table 1. Coring summary for Site 796.

Core no.	Date (July 1989)	Time (local)	Depth (mbsf)	Cored (m)	Recovered (m)	Recovery (%)	Age
127-796A-							
1H	22	1830	0.0-3.2	3.2	3.21	100.0	Quaternary
2H	22	1945	3.2-12.7	9.5	9.45	99.5	Quaternary
3H	22	2030	12.7-22.2	9.5	9.50	100.0	Quaternary
4H	22	2235	22.2-31.7	9.5	10.29	108.3	Quaternary
5H	22	2230	31.7-41.2	9.5	11.45	120.5	Quaternary
6H	23	0010	41.2-50.7	9.5	11.90	125.2	
7H	23	0230	50.7-51.7	1.0	0.00	0.0	
8H	23	0315	51.7-58.7	7.0	7.16	102.0	l. Pliocene
9X	23	0430	58.7-68.4	9.7	4.68	48.2	l. Pliocene
10X	23	0650	68.4-78.3	9.9	1.27	12.8	l. Pliocene
11X	23	0750	78.3-88.1	9.8	3.67	37.4	l. Pliocene
12X	23	1100	88.1-97.7	9.6	6.80	70.8	l. Pliocene
13X	23	1200	97.7-107.6	9.9	0.00	0.0	
14X	23	1330	107.6-117.2	9.6	7.12	74.1	e. Pliocene
15X	23	1530	117.2-126.9	9.7	5.93	61.1	e. Pliocene
16X	23	1745	126.9-136.5	9.6	3.56	37.1	e. Pliocene
17X	23	1815	136.5-146.2	9.7	7.21	74.3	e. Pliocene
18X	23	1900	146.2-155.8	9.6	9.79	102.0	e. Pliocene
19X	23	2000	155.8-165.3	9.5	5.72	60.2	e. Pliocene
20X	23	2045	165.3-175.0	9.7	2.42	24.9	e. Pliocene
21X	23	2120	175.0-184.7	9.7	8.95	92.2	e. Pliocene
22X	23	2215	184.7-194.4	9.7	7.43	76.6	l. Miocene
23X	23	2315	194.4-204.1	9.7	9.17	94.5	l. Miocene
24X	24	0030	204.1-213.8	9.7	2.59	26.7	
25X	24	0120	213.8-223.5	9.7	1.89	19.5	
26X	24	0310	223.5-233.2	9.7	3.27	33.7	
27X	24	0530	233.2-242.9	9.7	0.82	8.5	
Coring totals				242.9	155.25	63.9	
127-796B-							
1R	24	2100	0.0-4.2	4.2	4.04	96.2	Quaternary
2W	24	2335	4.2-30.2	26.0	4.40	(washed) 4.40	Quaternary
3R	25	0200	30.2-39.8	9.6	4.60	47.9	Quaternary
4R	25	0310	39.8-49.8	10.0	7.97	79.7	Quaternary
5R	25	0415	49.8-59.5	9.7	6.44	66.4	Quaternary
6R	25	0625	59.5-69.1	9.6	1.64	17.1	Quaternary
7R	25	0725	69.1-78.8	9.7	1.32	13.6	l. Pliocene
8R	25	0930	78.8-88.3	9.5	0.00	0.0	
9R	25	1030	88.3-97.9	9.6	0.51	5.3	l. Pliocene
10R	25	1645	243.0-252.7	9.7	0.82	8.5	l. Miocene
11R	25	1800	252.7-262.3	9.6	2.85	29.7	
12R	25	1930	262.3-271.9	9.6	4.13	43.0	
13R	25	2100	271.9-281.6	9.7	0.02	0.2	
14R	25	2315	281.6-291.3	9.7	1.85	19.1	
15R	26	0145	291.3-301.0	9.7	3.51	36.2	
16R	26	0315	301.0-310.7	9.7	0.41	4.2	l. Miocene
17R	26	0435	310.7-320.4	9.7	1.62	16.7	
18R	26	0605	320.4-330.0	9.6	6.46	67.3	
19R	26	0755	330.0-339.8	9.8	2.18	22.2	
20R	26	0930	339.8-348.7	8.9	1.32	14.8	
21R	26	1100	348.7-358.5	9.8	1.12	11.4	
22R	26	1230	358.5-368.1	9.6	1.60	16.6	
23R	26	1345	368.1-377.8	9.7	0.18	1.9	
24R	26	1500	377.8-387.4	9.6	0.19	2.0	
25R	26	1845	387.4-397.1	9.7	2.29	23.6	
26R	26	2015	397.1-406.8	9.7	2.37	24.4	
27R	26	2225	406.8-416.5	9.7	1.24	12.8	
28R	26	2340	416.5-426.2	9.7	1.79	18.4	
29R	27	0115	426.2-431.2	5.0	3.01	60.2	
30R	27	0230	431.2-435.9	4.7	4.43	94.2	
31R	27	0405	435.9-445.5	9.6	3.30	34.4	
32R	27	0535	445.5-455.2	9.7	7.47	77.0	
33R	27	0730	455.2-464.9	9.7	4.63	47.7	
Coring totals				293.8	85.31	29.0	
Washing totals				171.1	4.40		
Combined totals				464.9	89.71		



Legend: Lithology

- Silty clay/silty claystone
- Diatom ooze
- Ash / tuff tuffaceous sandstone
- Carbonate
- v Volcanic ash
- Sand / sandstone
- pebbly claystone
- Chert / Porcellanite
- Siliceous Claystone
- Bioturbation
- Graded Bedding
- Slump

Legend: Magnetics

- Normal polarity
- Reversed polarity

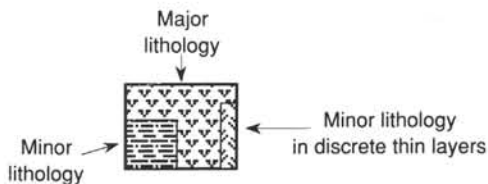


Figure 12. Lithostratigraphic summary of Site 796, Holes 796A and 796B. The uppermost cores from Hole 796B (Cores 127-796B-1R to -9R; 0.0-97.9 mbsf) are not shown, but are described in the text as Unit I, Hole 796B. These cores are nearly identical to the similar interval cored in Hole 796A.

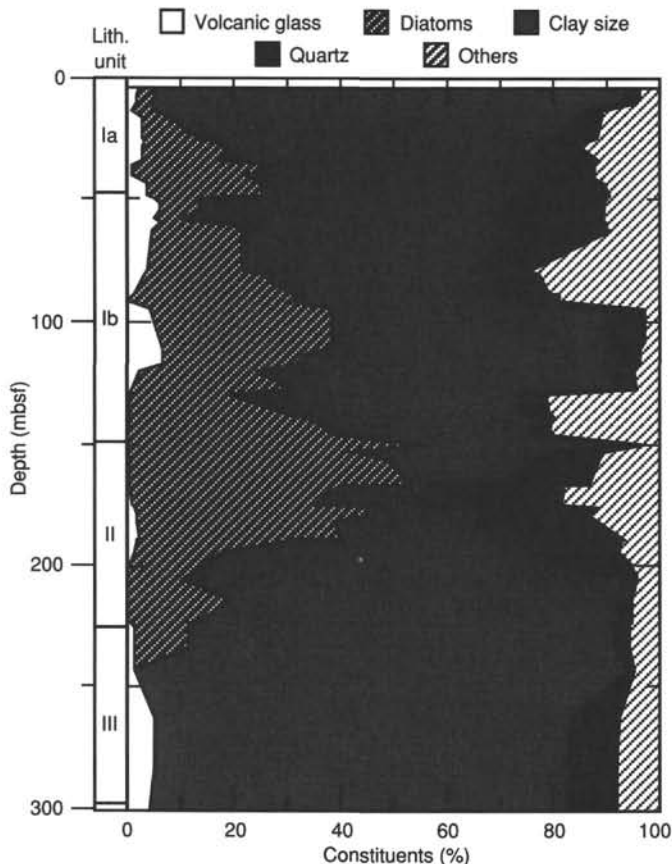


Figure 13. Plot of major components recorded in smear slides for the upper 300 m of Site 796 (from Core 127-796A-1H to Core 127-796B-15R).

tered, thin beds (typically 1–10 cm thick) that have sharp basal contacts and normal size grading to silt and silty clay. The sands are dominated by volcanic lithic fragments and pumice, with grain size ranging from silt and fine-grained sand to medium-grained sand. Thicker sand layers occur only at the base of Subunit IB in Core 127-796A-17X, which contains one sand bed 65 cm thick. Vitric ash beds, although somewhat less abundant than in Subunit IA, are present in most cores as thin (millimeter- to centimeter-scale) beds, laminae, or patches intercalated with diatom-bearing silty clay.

Unit I (0.0–97.9 mbsf)

Cores 127-796B-1R through 127-796B-9R.

The Quaternary and late Pliocene section was recored in Hole 796B to clarify the stratigraphic position of the first appearance of sand. Overall, the section in Hole 796B is similar to that cored in Hole 796A, and is dominated by diatom-bearing clay and silty clay, which are moderately bioturbated and show evidence of soft-sediment deformation. The first sand appears in Core 127-796B-7R at approximately 70 mbsf, in close agreement with the occurrence of the first sand in Hole 796A (Core 127-796A-9X at approximately 63 mbsf). Sand occurs as thin beds of fine-grained volcanic detritus, normally graded with sharp basal contacts. In both holes, the first sand appears in uppermost Pliocene strata (age 1.8–2.5 Ma).

Unit II (146.2–223.5 mbsf)

Cores 127-796A-18X through 127-796A-25X, clayey diatom ooze and diatom claystone.

This unit is dominated by clayey diatom ooze and diatom claystone and ranges in age from early Pliocene to late Miocene. Unit II is characterized by a significant increase in the abundance of diatoms compared to overlying strata (Fig. 13), while the base of the unit is defined by the last occurrence of diatoms reflecting the diagenetic transition from opal-A to opal-CT. Opal-CT first appears in Core 127-796A-25X between 213.8 and 223.5 mbsf, and becomes abundant in Core 127-796A-26X at the top of Unit III. Diatoms decrease in abundance toward the base of Unit II, while the overall detrital abundance increases as evidenced by the increasing occurrence of claystone, sandstone, and pebbly claystone at the base of the unit.

Diatom-rich sediments are typically slightly to moderately bioturbated, and homogeneous in appearance. In some cores, clayey diatom ooze is partially indurated to clayey diatomite. Overall, diatom-rich sediments are most abundant in Cores 127-796A-18X through -21X (146.2–184.7 mbsf). Below this interval, to the base of Unit II, the dominant lithology is diatom claystone interbedded with thin sandstone and pebbly claystone. Sandstone beds occur in Cores 127-796A-20X to -25X (165.3–223.5 mbsf) as thin (2–10 cm), normally graded units with sharp basal contacts. Dominant components include volcanic lithic fragments and glass or pumice. Sandstone layers grade upward to siltstone or claystone and are commonly bioturbated at the top. At the base of Unit II, pebbly claystones are interbedded with diatom claystone. This lithology is characterized by matrix-supported coarse sand- to pebble-size detritus, composed principally of volcanic lithic fragments and pumice. The matrix is dominated by silt- and clay-size grains that include glass and clay minerals. Pebbly claystone beds are generally massive, although faint lamination occurs. Vitric ash beds, generally 1–10 cm thick, occur sporadically, but are concentrated near the top of Unit II. Overall, the abundance of ash is low compared to overlying strata.

Porcellaneous zones and drilling fragments are present at the base of Unit II at the opal-A to opal-CT transition which occurs at approximately 225 mbsf. This diagenetic transition is confirmed by both X-ray diffraction and physical properties measurements which include bulk density, water content, porosity, and thermal conductivity (see “Physical Properties” section, this chapter). These data suggest that the opal-A to opal-CT transition is gradational over the interval of approximately 200–240 mbsf. This gradual change differs from the very sharp transition observed at Sites 794 and 795, and may be due in part to the overall decreased abundance of biogenic silica in Site 796 sediments.

Unit III (223.5–301.0 mbsf)

Cores 127-796A-26X through 127-796B-15R, siliceous claystone, claystone, and sandstone.

Unit III is late Miocene in age and is composed primarily of siliceous claystone. The unit lies entirely within the opal-CT diagenetic zone (Fig. 12). Claystone units are moderately to highly bioturbated with abundant compacted burrows that are aligned parallel to bedding. Induration ranges from relatively soft claystone, to moderately indurated siliceous claystone, to rare hard porcellanite with glassy texture and conchoidal fracture. Sandstone and siltstone interbeds are especially abundant in the middle of Unit III. Most sandstone beds have sharp basal contacts and are normally graded from medium- and coarse-grained sand upward to silt and clay (Fig. 14). Faint planar laminae are evident in some sandstone beds. In some cores, thin siltstone beds display normal grading and sharp basal contacts. Overall, graded sandstone beds range in thickness from a few centimeters to a maximum of 60 cm, and are dominated by volcanic lithic detritus and glass shards. Thin ash beds occur throughout Unit III.

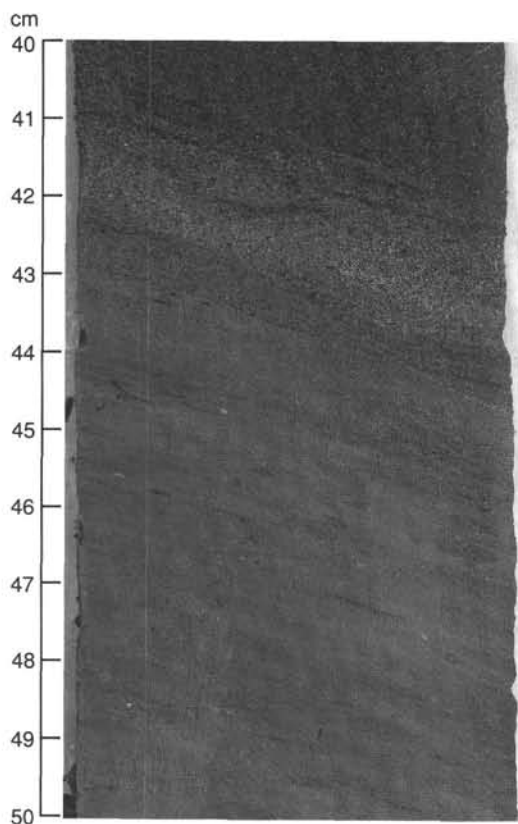


Figure 14. Close-up photograph of Core 127-796B-11R showing the sharp basal contact of a sandstone unit with underlying claystone. Note also normal-size grading in the sandstone bed.

Scattered glauconite is present in claystone in Core 127-796B-14R at approximately 282 mbsf.

Unit IV (301.0–416.5 mbsf)

Cores 127-796B-16R through 127-796-27R.

Unit IV is 115.5 m thick and is late Miocene(?) in age. The section is characterized by siliceous claystone interbedded with coarse-grained pyroclastic deposits. These include sandstone and pebbly claystone with abundant volcanic detritus, and discrete tuff beds.

Siliceous claystone and silty claystone occur throughout Unit IV, and are typically bioturbated with abundant compacted, horizontally-oriented burrows. Diagenetic silica occurs as opal-CT near the top of Unit IV, changing to quartz between Cores 127-796B-16R and -18R (approximately 301–330 mbsf). Some of the silty claystone units show faint normal size grading from silt to clay. The most distinct lithotype in Unit IV is pebbly claystone (Fig. 15). This lithotype occurs throughout Unit IV, and is characterized by matrix-supported, coarse sand- to pebble-size volcanic detritus which includes pumice, tuff, and volcanic lithic fragments. The clay- and silt-size matrix is dominated by clay, ash, and glass. Rare red chert clasts are also present. The overall fabric is disorganized; however, some units display faint planar lamination and crudely developed normal size grading. Pebbly silty claystones are further characterized by very poor sorting and angular to subangular clasts; beds range in thickness from 10–20 cm to over a meter.

Other significant lithologies in Unit IV include tuffaceous sandstone and tuff. Tuffaceous sandstone principally occurs near the top of Unit IV, but is also present as thin interbeds throughout the unit. Sandstone beds show evidence of normal size grad-

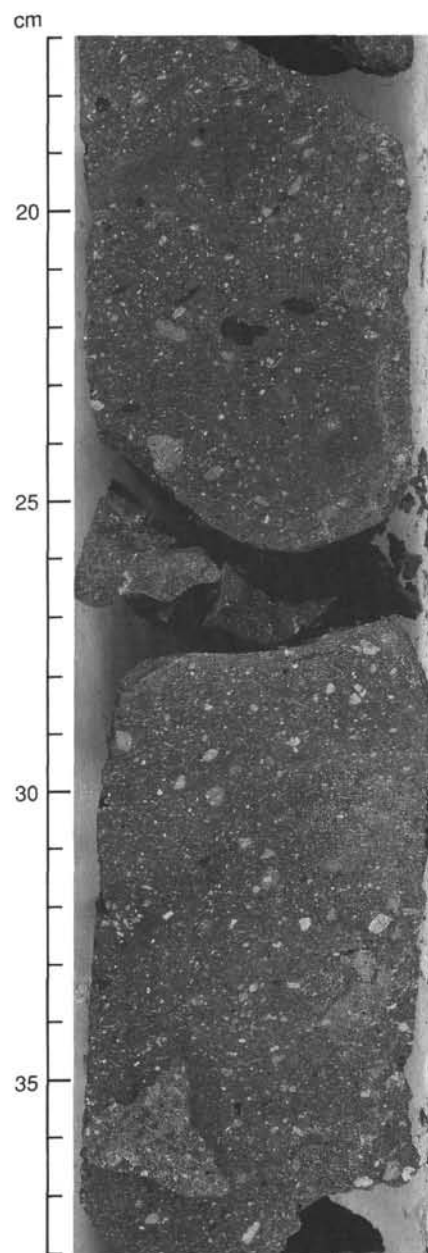


Figure 15. Close-up photograph of Core 127-796B-22R showing typical pebbly claystone with volcanic lithic fragments and pumice "suspended" in a clay- and glass-rich matrix.

ing and internal planar lamination, and range from a few centimeters to as much as a half meter in thickness. Discrete vitric tuff and crystal vitric tuff beds occur in Cores 127-796B-16R, -18R, and -26R (Fig. 12). Tuff units (some exceeding 2 m in thickness) show evidence of normal size grading from very coarse- to fine-grained volcanic detritus, with alternation of crystal-poor and crystal-rich laminations (Fig. 16).

Unit V (416.5–464.9 mbsf)

Cores 127-796B-28R through 127-796B-33R.

Only 48.4 m of Unit V was cored and this represents a minimum thickness, as drilling was halted at 464.9 mbsf. The unit is dominated by siliceous claystone, and is distinguished from overlying strata by the paucity of coarse clastic/pyroclastic de-

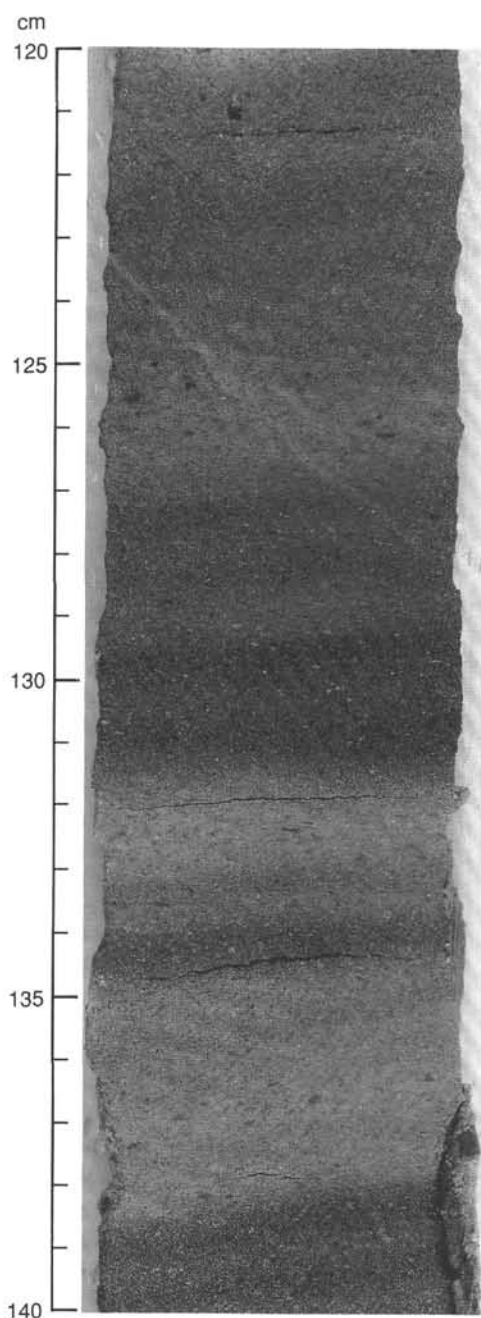


Figure 16. Close-up photograph of a tuff unit in Core 127-796B-18R.

posits (i.e., pebbly claystone, coarse-grained volcanic sandstone), and an increase in diagenetic carbonate, principally dolomite and Mg-calcite. Siliceous claystones are generally bioturbated, ranging from highly bioturbated, lighter colored intervals with abundant horizontal, compacted burrows, to slightly or moderately bioturbated darker zones with fewer burrows and increased pyrite and/or organic carbon (Fig. 17). Many silty claystone units show evidence of normal size grading from sharp basal contacts.

Diagenetic carbonates, which include dolomite, Mg-calcite, and rare ankerite, are relatively abundant throughout Unit V, occurring as small, *in situ* micronodules, lenses, and stringers in siliceous claystone (Fig. 18). Large benthic foraminifers, including both calcareous and agglutinated forms, are observed in many claystone units.

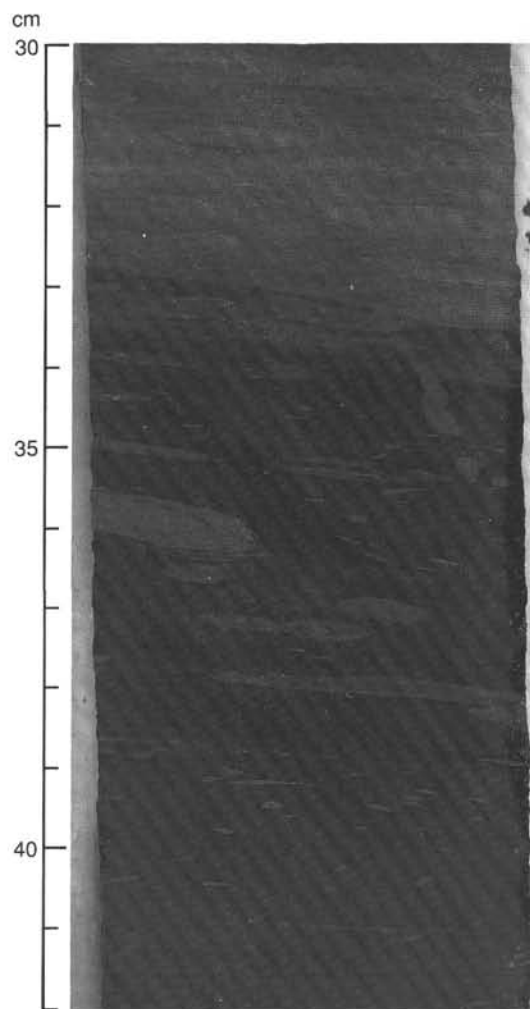


Figure 17. Close-up photograph of Core 127-796B-30R showing the style of bioturbation in Unit V: dark colored layers with small horizontal burrows (slightly bioturbated) interbedded with lighter layers with more numerous burrows (generally highly bioturbated).

Minor lithologies in Unit V include: (1) fine-grained vitric tuff, some with calcareous cement; and (2) sandstone, especially at the top of Unit V. Sandstone beds typically display sharp basal contacts and normal size grading from fine to medium sand upward to silt and clay.

Paleoceanographic and Depositional History

The sedimentary succession recovered at Site 796 accumulated under oceanographic conditions that were approximately similar to those inferred for Sites 794 and 795. There are, however, some important differences, especially regarding the more proximal location of the site relative to the inferred margin (the developing Japan arc), and the introduction of abundant coarse-grained clastic and pyroclastic detritus as sediment gravity flow deposits into a system dominated by pelagic/hemipelagic deposition.

The hemipelagic and pelagic sedimentary components at Site 796 provide insights to the paleoceanographic history at this location. Dominated by the input of abundant clay-sized detritus, and by the pelagic production of plankton (principally diatoms and radiolarians), the fine-grained sediments primarily accumulated at relatively deep water, basin floor sites. Analyses of benthic foraminifers recovered at Sites 794, 795, and 796 suggest de-

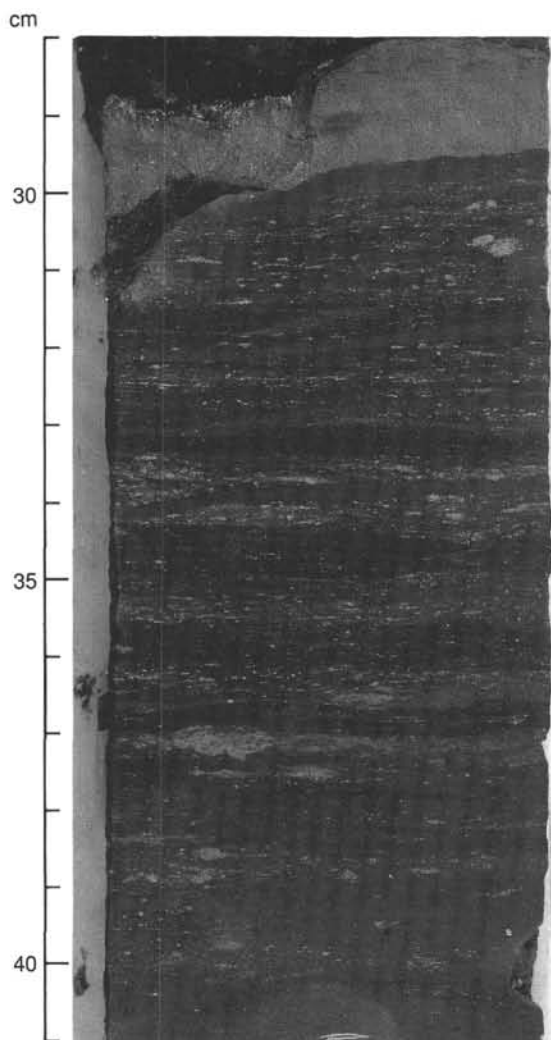


Figure 18. Close-up photograph of Core 127-796B-33R showing microconcretions, stringers, and lenses of diagenetic carbonate in dark, organic-rich claystone (middle(?) Miocene). XRD analyses reveal that most carbonate is either dolomite or Mg-calcite (ankerite is rare).

position predominantly in bathyal water depths, although depths likely varied through time from as deep as lower bathyal to as shallow as middle or upper bathyal (see "Biostratigraphy" section, this chapter).

At Site 796, recovery of benthic foraminifers is poor, and there is significant reworking. However, it is likely that most of the upper Miocene through Quaternary section was deposited at bathyal depths, probably lower bathyal. In contrast, middle(?) Miocene silty claystones accumulated at slightly shallower depths, most likely middle bathyal. Sandstones and pebbly claystones probably formed as sediment gravity flow deposits and are consistent with deposition in relatively deep water.

Conclusions regarding water depth are supported by observations of carbonate preservation. Most of the upper Miocene-Quaternary section is essentially barren of calcareous microfossils, including calcareous benthic foraminifers, suggesting deposition below the CCD. On the other hand, middle(?) Miocene claystones contain calcareous benthic foraminifers, suggesting deposition at somewhat shallower sites above the CCD, or fluctuations in the depth of the CCD. Abundant diagenetic dolomite and Mg-calcite in middle(?) Miocene claystones likewise suggest preservation of at least some original biogenic carbonate in the sediment.

Percent CaCO_3 data support the microfossil observations at Site 796. Overall, total calcium carbonate abundance is very low for most of the section, except for the lower portion below approximately 400 mbsf. This is consistent with deposition below the CCD for much of the late Miocene-Quaternary section, whereas the middle(?) Miocene succession may have been deposited, in part, above the CCD. Alternatively, low CaCO_3 values could be attributed to post-depositional dissolution processes. However, based on the present-day shallow depth of the CCD in the Japan Sea, we tentatively favor CCD-influenced dissolution of biogenic carbonate in sediments from Site 796.

The appearance in the section of diatom ooze reflects periodically enhanced productivity in the photic zone in response to increased vertical circulation (upwelling) and introduction of nutrients. This is supported by the presence of upwelling-specific diatoms (see "Biostratigraphy" section, this chapter) at scattered intervals in the upper portion of the section at Site 796 (opal-A zone: 0.0–225 mbsf). Upwelling-specific diatoms are also reported at Sites 794 and 795, and appear to fluctuate in abundance reflecting specific time periods, especially the latest Pliocene and Quaternary, where upwelling and productivity were greatly enhanced.

Overall diatom abundance, and silica abundance in the opal-CT zone below 225 mbsf, is somewhat less at Site 796 when compared to the previous sites. This is probably related to increased detrital input (see tectonic discussion below); in fact, hemipelagic clays and claystones dominate at Site 796. Increased clay and silt-size detritus likely reflects proximity to a terrestrial or volcanic source, and much of this terrigenous and pyroclastic component was likely introduced by sediment gravity processes.

Most of the sedimentary sequence at Site 796 accumulated under generally oxic conditions at the sediment-water interface as evidenced by the ubiquitous bioturbation of sediment. The striking abundance of bioturbated mudstones in the upper Miocene to Quaternary suggests well-oxygenated deep water masses, generally vigorous circulation, relatively free exchange of oxygen-rich intermediate and deep water from the Pacific, and periodically enhanced upwelling during this time. In contrast, older middle(?) Miocene sediments reflect fluctuations in the degree of oxygenation at the sediment-water interface. Based on the variability in the style and degree of bioturbation, the degree of oxygenation likely ranged from oxic to dysaerobic. In these cases, lighter-colored, highly bioturbated siliceous claystones are interbedded with darker, faintly laminated to slightly bioturbated claystones containing more organic matter and pyrite. Additionally, low-oxygen-tolerant benthic foraminifers occur in middle(?) Miocene claystones at Site 794, and are present at Site 796 in similar age deposits (see "Biostratigraphy" section, this chapter).

Organic geochemical data support the conclusion that most of the section at Site 796 was deposited under aerated conditions. Total organic carbon values are relatively low throughout the section, averaging about 0.5%, similar to those measured at Sites 794 and 795. Higher values occur in darker clay and claystone layers that are found mainly in the Quaternary and in the middle(?) Miocene, suggesting that less oxic conditions prevailed at times near the sediment-water interface.

The biogenic carbonate which occurs in middle(?) Miocene siliceous claystones (Unit V; Fig. 12) would facilitate formation of diagenetic dolomite and Mg-calcite. Its presence also argues for deposition above the CCD. In addition, the presence of diagenetic carbonate phases in middle(?) Miocene organic-rich siliceous claystones suggests that anaerobic bacterial degradation processes may have been important during early burial (sulfate reduction and/or methanogenesis). Dysaerobic conditions in the water column near the sediment-water interface would favor preservation of accumulated organic matter and subsequent genesis of carbonate phases.

Sands and Sandstones at Site 796

Sand beds in Hole 796A range from a few centimeters to tens of centimeters in thickness. Grain size is variable, ranging from very fine-grained sand to coarse-grained sand and granules. Sorting is generally poor, and grains range from angular to subangular. Several sand beds show sharp basal contacts and normal size grading, and one contains well-defined planar lamination. Some sand units appear massive, and several fine-grained beds are bioturbated near the top. Smear slide analyses of sands from Hole 796A reveal that they are composed primarily of volcanic detritus, including volcanic lithic clasts and pumice, with variable amounts of glass, plagioclase, and accessory minerals, chiefly hornblende. Quartz is present in very minor amounts. Sand units in Hole 796A were likely deposited by sediment gravity mechanisms; grading and sharp basal contacts suggest that these sediments are turbidites.

In Hole 796B, sand and sandstone units range in thickness from 5 to over 60 cm. Most have sharp basal contacts, display normal size grading, and have well-defined planar laminations that are most common near the base. Many units grade up to silt and/or clay and are bioturbated at the top. Sandstones are interbedded with either hemipelagic claystones or matrix-supported, pebbly claystones. Grain size ranges from silt to granule, and averages between fine and medium sand. Most units are poorly sorted, and grains are angular to subangular. Thin-section analyses indicate that these sandstones are composed principally of volcanic detritus. Dominant components include volcanic lithic fragments, including pumice, and plagioclase feldspar. Glass is abundant in some sandstone units, but is nearly absent in others. Some sandstones are tuffaceous based on glass content (see description of Unit IV above). Quartz is rare in all samples. Accessory minerals include hornblende, clinopyroxene, and rare celadonite replacing glass. Matrix material is generally clay-rich, or glassy. Based on the structures and textures outlined above, most sandstones in Hole 796B were likely deposited by sediment gravity flow mechanisms. Many are probably turbidites, although some of the more massive units may be grain-flow deposits. They are clearly derived from a volcanic source, and are composed principally of fresh, first-cycle material. Thus, many units are pyroclastic in origin and were likely redeposited by sediment gravity processes soon after subaqueous or subaerial volcanic eruptions. A similar origin is proposed for matrix-supported pebbly claystone beds. However, the abundance of fine-grained volcanic matrix and the disorganized fabric which characterizes these deposits suggest that these units were likely reworked as debris flows or high-density turbidity currents following subaqueous or subaerial eruption.

Tectonic Implications of the Sedimentary Sequence

Given the specific location of Site 796 on the Okushiri Ridge in the active east Japan Sea tectonic zone (see "Introduction" chapter, this volume), the occurrence of coarse clastic deposits and slumped units in the sedimentary section provide important constraints on the timing of uplift of the Okushiri ridge and the onset of compression along the east Japan Sea margin. Key observations and comparisons with other sites are summarized below.

Figure 19 shows the three sedimentary sections recovered at Sites 794, 795, and 796. Sedimentation is dominated by background hemipelagic deposition, and similar fine-grained lithologies are observed in approximately the same sequence at all three locations. Sites 794 and 795 are quite similar except for the sedimentation rate which is significantly higher at Site 795 in the Quaternary and Pliocene. At Site 796 three major differences are encountered:

1. The diatom content of the upper part of the section (above the opal-A/opal-CT transition) is lower than at the two other sites. This suggests significantly increased terrigenous clay input into the basin at this site, assuming that overall diatom productivity is similar among the different locations.

2. Sand, sandstone, and pebbly claystone, all dominated by volcanic detritus, are distributed throughout Subunit IB, Units II, III, and IV at Site 796 (Fig. 12), suggesting proximity to a source area of both terrigenous clastic and pyroclastic detritus. The first and last appearance of coarse-grained sediments in the section constrain the period during which Site 796 was not uplifted and where sediment gravity flow deposits could accumulate.

3. The opal-A/opal-CT transition occurs approximately 50–70 m shallower than at Site 794, a location which has comparable sedimentation rates. This suggests either a recent change in the local thermal gradient, or erosion of part of the uppermost section by slumping along the slope. The presence of slumps in Subunit IA favors this latter interpretation, but because no significant hiatus can be inferred from paleontological data the eroded sequence probably does not exceed a few tens of meters (see below).

These observations have significant implications for the tectonic development of the Okushiri Ridge through time. The youngest sandstones (fine- to coarse-grained, volcanic sandy turbidites) were recovered at about 63 mbsf in Hole 796A in uppermost Pliocene sediments (about 1.8 Ma). Below that depth, to the base of Unit IV (416.5 mbsf), turbidites and chaotic sediments are common. This observation suggests that turbidity currents were able to reach Site 796 during this time interval, and that the Okushiri Ridge was probably not yet uplifted. Thus, the major uplift began about 2 Ma. If the base of the reflective sequence in the Shiribeshi Basin on the seismic line (see "Seismic Stratigraphy" section, this chapter) represents the base of the Quaternary, then the total relative vertical offset on either side of the major fault is about 3 km. This estimate results in a rate of mean differential uplift of about 1.5 mm/year, beginning 2 Ma.

The occurrence of disturbed bedding in Quaternary deposits (Cores 127-796A-1H through -6H: 0.0–50.7 mbsf) suggests that slumping processes were active during uplift of the Okushiri Ridge. The oldest evidence of significant soft-sediment deformation and inclined beds is present at the base of Core 127-796A-5H to approximately 41.2 mbsf (slump structures may extend into the upper few meters of Core 127-796A-6H to approximately 45 mbsf). Based on diatom datums (See "Biostratigraphy" section, this chapter), the first sand occurs at, or just before 1.80 Ma, whereas the first slumped units occur near approximately 0.90 Ma. This gap suggests that a significant period passed between deposition of the last sand turbidite in Core 127-796A-9X and the onset of uplift of the Okushiri Ridge. Slumping processes began once the uplifting ridge reached a critical declivity.

Paleontological data suggest that no significant hiatuses are found in the Quaternary to latest Pliocene section at Site 796. In addition, disturbed sections in most cores are interbedded with noncontorted and nonrotated sediment, and slumped horizons range in thickness from approximately half a meter to several meters. Together, these suggest that the extent and magnitude of slumping was probably limited, with multiple small-scale failures enclosed in nondisturbed sediment, rather than catastrophic removal of a significant thickness of sediment. Additionally, while slump units on slopes can affect very large surface areas of sediment, the slump or slide block may only disturb sediment to a depth of several meters or tens of meters.

The oldest sandstones and coarse-grained chaotic sediments are found at about 416 mbsf near the base of Unit IV at Site

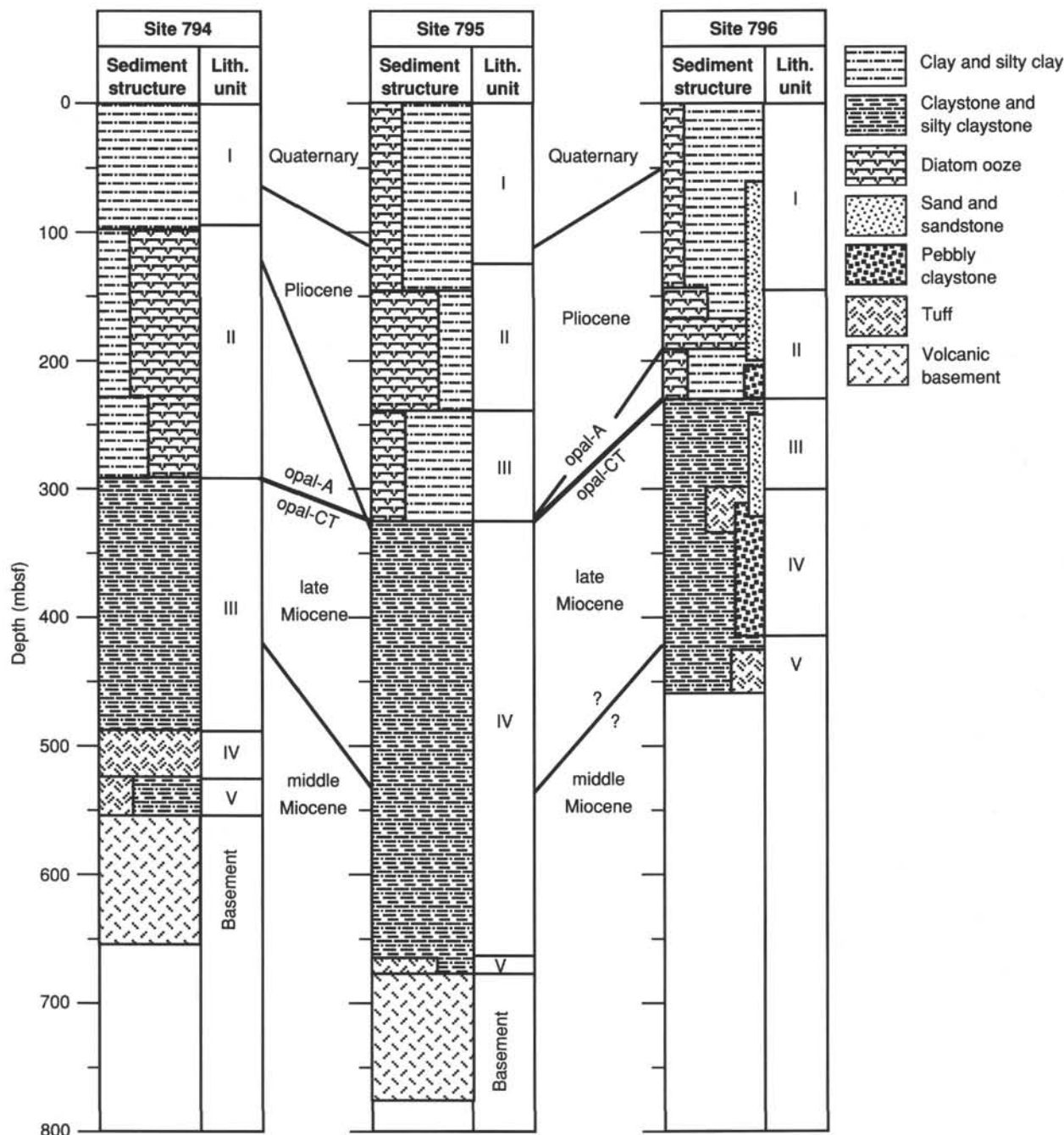


Figure 19. Comparison of the sedimentary sections recovered at Sites 794, 795, and 796.

796. The age of this horizon is not well constrained since the oldest reliable paleontological data were recovered from sediment in Core 127-796B-10R (6.4 Ma; 253 mbsf). Based on benthic foraminifers, the base of the section recovered at Site 796 may be as old as 16 Ma. Using reasonable estimates of sedimentation rates between these age extremes (Fig. 26), the age of the oldest coarse-grained detrital deposits is likely between 7 and 14 Ma. Prior to this time interval (below Unit IV; 416 mbsf), turbidite sedimentation was insignificant based on the sedimentary section recovered at Site 796 (Unit V; 416.5–464.9 mbsf). This has two possible implications: (1) either there was no significant input of terrestrial sediment at the time, or (2) the site was protected from terrigenous clastics that were trapped in basins closer to the margin.

BIOSTRATIGRAPHY

Introduction

Microfossil assemblages of diatoms, radiolarians, nannofossils, and planktonic and benthic foraminifers show variable abundance and preservation throughout the upper Miocene to Quaternary sediments of Site 796 (Tables 2 and 3). Diatoms are the most abundant microfossil group found at Site 796 and occur in all sediments above the opal-A/opal-CT boundary (at approximately 225 mbsf, late Miocene). Poorly preserved radiolarians are found in sandy claystones 100 m below the opal-A/opal-CT boundary. Infrequent occurrences and moderate preservation typify the calcareous nannofossil and foraminiferal assemblages throughout the entire sedimentary section at Site 796.

Table 2. Abundance and preservation of microfossils in Hole 796A.

Core	Diatoms		Nannofossils		Planktonic foraminifers		Benthic foraminifers		Radiolarians	
	Abundance	Preservation	Abundance	Preservation	Abundance	Preservation	Abundance	Preservation	Abundance	Preservation
1H-CC	abundant	good	barren		common	moderate	few	moderate	common	good
2H-CC	few	moderate	barren		barren		barren		rare	moderate
3H-CC	common	moderate	few	moderate	abundant	moderate	barren		common	moderate
4H-CC	common	moderate	barren		barren		barren		few	moderate
5H-CC	abundant	good	barren		barren		barren		common	good
6H-CC	abundant	good	common	good	barren		barren		common	good
7H-CC										
8X-CC	common	moderate	barren		barren		barren		rare	moderate
9X-CC	abundant	good	few	moderate	barren		barren		abundant	moderate
10X-CC	abundant	good	barren		common	good	few	good	common	moderate
11X-CC	abundant	good	barren		barren		few	moderate	abundant	moderate
12X-CC	abundant	good	barren		barren		rare	moderate	common	moderate
13X-CC										
14X-CC	abundant	good	barren		barren		barren		few	moderate
15X-CC	abundant	good	barren		barren		few	moderate	common	moderate
16X-CC	abundant	moderate	barren		barren		barren		few	moderate
17X-CC	common	moderate	barren		barren		few	moderate	few	moderate
18X-CC	abundant	good	barren		barren		rare	moderate	few	good
19X-CC	few	moderate	barren		barren		barren		rare to few	moderate
20X-CC	abundant	good	barren		barren		barren		rare to few	moderate
21X-CC	abundant	moderate	barren		rare	poor	few	moderate	few	moderate
22X-CC	common	moderate	barren		barren		barren		rare	moderate
23X-CC	rare	poor	barren		barren		barren		rare	moderate
24X-CC	common	moderate	barren		barren		barren		rare	moderate
25X-CC	few	poor	barren		barren		barren		rare	poor
26X-CC	barren		barren		barren		barren		rare	poor
27X-CC	barren		barren		rare	poor	few	moderate	few	poor to moderate

Table 3. Abundance and preservation of microfossils in Hole 796B.

Core	Diatoms		Nannofossils		Planktonic foraminifers		Benthic foraminifers		Radiolarians	
	Abundance	Preservation	Abundance	Preservation	Abundance	Preservation	Abundance	Preservation	Abundance	Preservation
1R-CC	few	poor	barren		rare	moderate	barren		common	good
2W-CC	common	good	barren		rare	moderate	barren		common	good
3R-CC	abundant	good	barren		abundant	good	few	good	abundant	moderate
4R-CC	abundant	good	barren		common	moderate	few	moderate	few	moderate
5R-CC	abundant	good	barren		barren		barren		few	good
6R-CC	abundant	good	barren		barren		barren		common	moderate
7R-CC	abundant	good	rare	poor	rare	poor	few	moderate	common	moderate
8R-CC										
9R-CC	abundant	good	barren		rare	moderate	few	moderate	common	good
10R-CC	few	moderate	barren		barren		rare	poor	few	poor
11R-CC	rare	poor	barren		barren		barren		rare	poor
12R-CC	rare	poor	barren		barren		barren		rare	poor
13R-CC	rare	poor	barren		barren		barren		rare	poor
14R-CC	rare		barren		barren		barren		rare	poor
15R-CC	barren		barren		barren		barren		rare	poor
16R-CC	common	moderate	barren		barren		barren	poor	few	poor
17R-CC	barren		barren		barren		rare	poor	rare	poor
18R-CC	barren		barren		barren		barren		barren	
19R-CC	barren		barren		barren		few	poor	barren	
20R-CC	barren		barren		barren		barren		barren	
21R-CC	barren		barren							
22R-CC	barren		barren							
23R-CC	barren									
24R-CC	barren		barren		barren		barren			
25R-CC										
26R-CC										
27R-CC										
28R-CC	barren		barren						barren	
29R-CC	barren		barren		barren		few	poor	barren	
30R-CC	barren		barren		barren		rare	poor	barren	
31R-CC	barren		barren		barren		barren		barren	
32R-CC	rare	poor	barren						barren	
33R-CC										

Middle(?) Miocene siliceous claystones and tuffs are barren of all microfossils, except rare planktonic foraminifers and common benthic foraminifers. Significant reworking in all groups and in most intervals (Figs. 20 and 21), makes biostratigraphic and paleoceanographic interpretations difficult.

Quaternary diatom assemblages are abundant, moderately well preserved, and include abundant upwelling indicators. Radiolarian, planktonic foraminiferal, and calcareous nannofossil assemblages indicate extreme variations in Quaternary oceanography probably related to northern hemisphere glaciation. Dia-

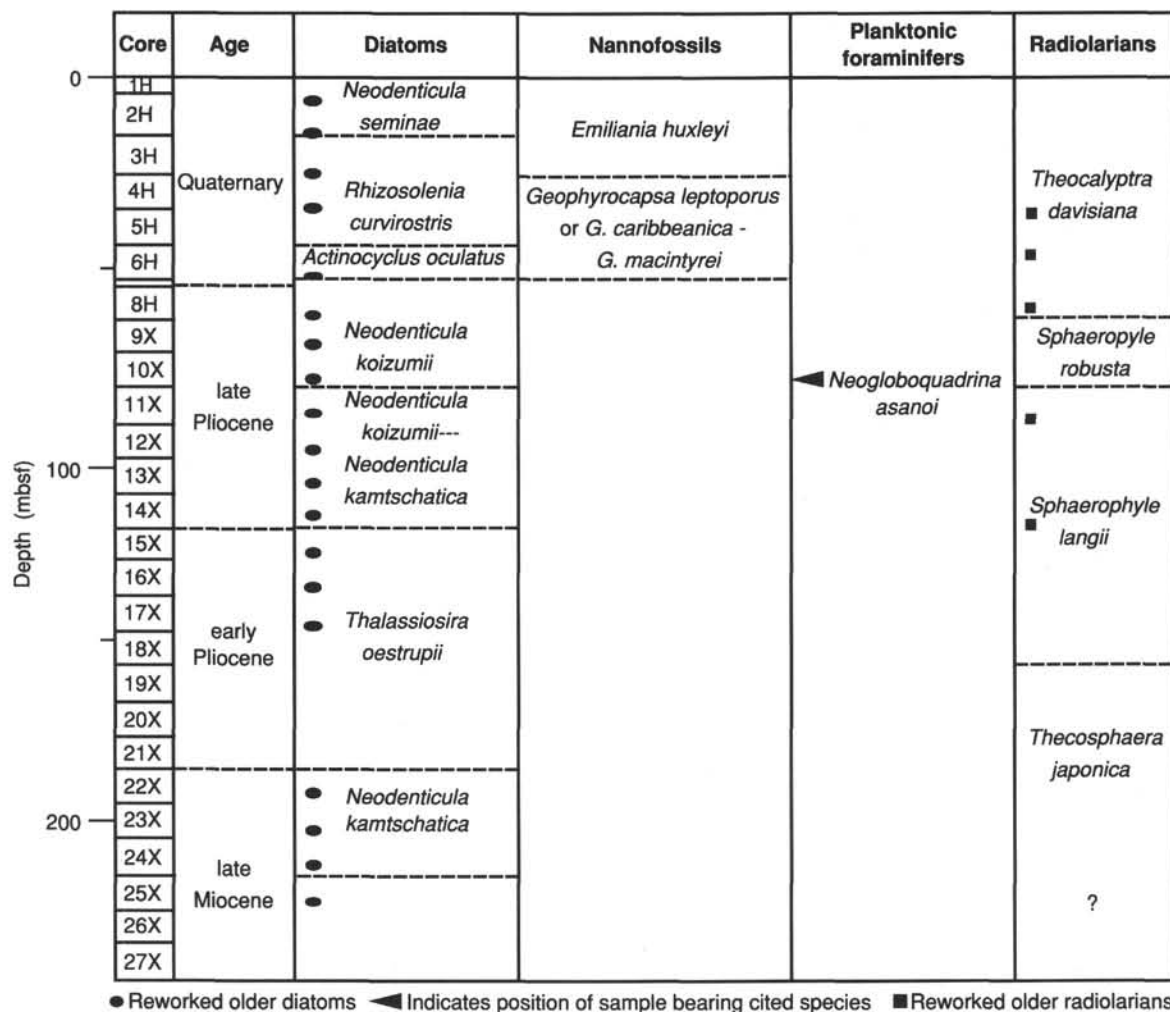


Figure 20. Planktonic microfossil zones in Hole 796A.

tom productivity was high during the deposition of diatomaceous clays and oozes in the Pliocene. Benthic foraminiferal assemblages indicate lower bathyal paleodepths in the Pliocene and late Miocene, and middle bathyal paleodepths in the middle(?) Miocene.

Age constraints for Site 796 are mainly based on diatom biostratigraphy, as no paleomagnetic reversal stratigraphy is available for this site. Where found, radiolarian, foraminiferal, and nannofossil datum levels agree with the diatom biostratigraphy. No biostratigraphically recognizable disconformities were found. Estimates of the age of the base of the sedimentary sequence at Site 796 range between 9.7 and 16 m.y. The younger estimate is based on extrapolation of the sedimentation rate determined between two late Miocene diatom markers, the base of the *Thalassiosira oestrupii* Zone (5.3 Ma, 184.7 mbsf) and the FAD of *Neodenticula kamschatica* (6.4 Ma, 252.7 mbsf) (see Fig. 26). The older estimate is based on a maximum age for the occurrence of *Globigerina bulloides* in Core 127-796B-32R (455.2 mbsf). The uncertainty in the age of the base of the sedimentary sequence makes interpretations of middle(?) Miocene ages tentative. The age of the sediments at the bottom of Hole 796B may be younger than 9.7 m.y. if the pebbly claystone between Cores 127-796B-12R and 127-796B-32R was deposited more rapidly than the overlying late Miocene unit.

Diatoms

Site 796 was the first site of Leg 127 to have abundant Quaternary diatoms with good preservation. The Quaternary sequence of Site 796 consists of clay, silty clay, and claystone with minor diatom ooze. Fossiliferous samples from this sequence include Samples 127-796A-1H-CC through 127-796A-6H-CC and Samples 127-796B-1R-CC through 127-796B-6R, (Tables 2 and 3). Samples 127-796A-1H-CC, 127-796A-2H-CC, and 127-796B-1R-CC are assigned to the *Neodenticula seminiae* Zone based on the presence of *Neodenticula seminiae* and the absence of *Rhizosolenia curvirostris* (Fig. 20). Samples 127-796A-3H-CC through 127-796A-5H-CC have *Rhizosolenia curvirostris* and are assigned to the *Rhizosolenia curvirostris* Zone. Samples 127-796A-6H-CC, and 127-796B-3R-CC through 127-796B-6R-CC are assigned to the *Actinocyclus oculatus* Zone based on the presence of *Actinocyclus oculatus*. The base of this zone indicates the Quaternary/Pliocene boundary (Fig. 20). High productivity and upwelling-related diatoms such as *Thalassionema nitzschioides*, *Thalassiothrix longissima*, and *Chaetoceros* resting spores (Burckle, 1978; Sancetta, 1982; Barron and Keller, 1983) are more abundant in the Quaternary and upper Pliocene of Site 796 than at the other sites. The upwelling may have been related to onset of northern hemisphere glaciation 2.5 m.y. ago.

10R-CC at 252.7 mbsf and constitutes the oldest (6.4 Ma) and deepest reliable diatom datum at this site. Reworked older fossil diatoms are found in a majority of the samples (Figs. 20 and 21). Miocene diatoms in particular are commonly recognized in upper Pliocene samples.

Calcareous Nannofossils

Most of the samples studied at Site 796 do not contain calcareous nannofossils. Nannofossils occur sporadically in the Pleistocene and Pliocene sediments (Tables 2 and 3). The Pliocene nannofossil assemblages consist of two or three poorly preserved species, whereas, in the Pleistocene, the assemblage is more diverse and better preserved. Due to the absence of the biostratigraphically useful taxa *Discoaster*, *Ceratolithus*, *Sphenolithus*, and *Reticulofenestra pseudoumbilica* in the Pliocene sediments, zonal assignment of the nannofossil-bearing samples was not possible.

Of the 26 cores recovered at Hole 796A, only three core-catcher samples (127-796A-3H-CC, 127-796A-6H-CC, and 127-796A-9X-CC) contain nannofossils. Core 127-796A-3H contains few to abundant nannofossils with good to moderate preservation. The assemblages above Sample 127-796A-3H-CC consist of abundant *Emiliania huxleyi* with rare small *Gephyrocapsa* and *Braarudosphaera bigelowii*. Most of the upper part of the Core 127-796A-3H is tentatively assigned to the *Emiliania huxleyi* Zone of latest Pleistocene to Holocene age (Fig. 20). This zonal assignment needs to be verified with electron microscopy. The lower boundary of this zone probably lies somewhere in the lower part of Core 127-796A-3H, because the core-catcher sample of this core does not contain the nominal species. As at Site 795, *Gephyrocapsa caribbeanica* and *Gephyrocapsa oceanica* are absent from the *Emiliania huxleyi* Zone, a condition which, once again, can be attributed to unfavorable paleoecological conditions related to northern hemisphere glaciation. Nannofossils with good preservation are common in Sample 127-796A-6H-CC. The assemblage in this sample is quite diverse and consists of *Calcidiscus leptoporus*, *Coccolithus pelagicus*, small *Reticulofenestra*, *Gephyrocapsa*, *G. caribbeanica*, *B. bigelowii*, *Helicosphaera carteri*, and *Pontosphaera* sp. Despite the diversity, the assemblage is dominated by *C. pelagicus* and *C. leptoporus*. Placoliths, with slits in their shields, resembling *Pseudoemiliania lacunosa*, rarely occur in this sample. Sample 127-796A-6H-CC belongs to the undifferentiated early Pleistocene *Calcidiscus leptoporus* Zone and *Gephyrocapsa caribbeanica*-*Calcidiscus macintyreii* Zone, based on the presence of *G. caribbeanica* and the absence of *G. oceanica*. These two zones could not be distinguished due to the absence of *C. macintyreii*, the last occurrence of which marks the boundary between the two zones. Samples 127-796A-9X-CC and 127-796A-12X-3, 20-21 cm, contain only rare to few moderately preserved nannofossils, *C. pelagicus*, small *Reticulofenestra*, and *C. leptoporus*, without any age diagnostic species.

The presence of the nearshore species *Braarudosphaera bigelowii* in Core 127-796A-3H and in Sample 127-796A-6H-CC suggests transport of sediments from a shallow sea environment. This evidence agrees with the occurrences of reworked diatoms of fresh and brackish water origin. *Coccolithus pelagicus* co-occurs with warm water diatom and radiolarian species, in Sample 127-796A-6H-CC. This suggests that the surface water temperature at this time was warm enough for diatoms and radiolarians, cold enough for the cold water species *C. pelagicus*, and probably too cold for the warm water species *Gephyrocapsa oceanica* (Roth and Coulbourn, 1982; Rahman and Roth, in press).

All the core-catcher samples of Hole 796B are barren of calcareous nannofossils, except Sample 127-796B-7R-CC which contains poorly preserved, rare nannofossils, *Calcidiscus leptoporus* and small *Reticulofenestra*, with some questionable remains

of *Sphenolithus*. At Hole 796B the diversified early Pleistocene nannofossil assemblage, as found in Sample 127-796A-6H-CC, was not recognized; this may be attributed to coarse sampling interval and incomplete recovery.

Foraminifers

Preservation of calcareous foraminifers at Site 796 is generally poor, and most samples are barren. Preservation of textularid foraminifers is generally poor, and, where textularids do occur, abundance is typically rare to few (Tables 2 and 3).

The Quaternary diatom clay and silty clay (lithologic Unit IA) contain planktonic foraminiferal assemblages with highly variable states of preservation and numbers of specimens, as has been typical of sites from Leg 31 and Leg 127 in the Japan Sea. In contrast to Quaternary sections at other sites of Leg 127, assemblages are reworked and bear species from different ages and of different states of preservation. Samples 127-796A-1H-CC and 127-796A-3H-CC contain both planktonic species typical of the Quaternary and species unique to the Pliocene such as *Neogloboquadrina asanoi*. Other indicators observed in the sand-size fraction point to extensive reworking. Samples 127-796B-3R-CC and 127-796B-4R-CC contain *Miliammina*, a benthic foraminifer that is more typical of the Pliocene than the Quaternary. All foraminiferal associations in the Quaternary section contain planktonic specimens of assorted colors ranging from white to ivory, golden brown, and rusty red. Reworked neritic diatoms, *Arachynodiscus* and *Isthmia*, are common in the interval, and monolete spores occur abundantly in Samples 127-796A-4H-CC and 127-796A-5H-CC.

Preservation and abundance of Pliocene foraminifers in the diatom clay and sand of lithologic Unit IB and the clayey diatom ooze of lithologic Unit II are generally poor and sporadic, although calcareous foraminifers occur in most fossil-bearing samples. The sporadic occurrence of foraminifers is in part due to dissolution and in part due to dilution by sand, ash, and marine diatoms. Neritic diatoms reworked from a shallow source persist in abundance throughout most of the interval.

Planktonic foraminifers are absent from the late Miocene interval, and benthic foraminifers are poorly preserved, sporadic in occurrence, and rare in abundance due in part to diagenesis below the opal-A/opal-CT boundary and in part to dilution by pebbly mudstones. In contrast, planktonic foraminifers are present and occur with abundant and moderately preserved calcareous and textularid benthic foraminifers in the calcareous, siliceous claystone of lithologic Unit V at the base of Hole 796B.

Planktonic foraminifers occur in 6 of 12 core-catcher samples of the Quaternary section of Site 796 (Table 2). The reworked assemblages contain *Neogloboquadrina kagaensis* and *Neogloboquadrina asanoi* of the Pliocene, *Neogloboquadrina pachyderma*, *Globigerina bulloides*, and *Globigerina quinqueloba* of the Miocene to Quaternary, *Globigerina umbilicata* of the late Pliocene to Holocene, and *Globigerina woodi* of the late Oligocene to late Pliocene.

Planktonic foraminifers occur in four samples of the Pliocene. Sample 127-796A-10X-CC contains common *Globigerina bulloides* and dextral *Neogloboquadrina pachyderma*, and rare *Globigerina quinqueloba* and *Neogloboquadrina asanoi*. Planktonic foraminifers occur in all four samples examined from the deepest unit of Hole 796B. Species consist of *G. bulloides*, *G. woodi*, and poorly preserved, unidentified specimens. *G. bulloides* made its first appearance in the world oceans in Zone N9 about 16 Ma. The presence of *G. bulloides* in Samples 127-796B-32R-4, 143-145 cm, and 127-796B-32R-5, 24-26 cm, indicates a maximum age of 16 m.y. for Core 127-796B-32R.

Benthic foraminifers occur in 3 of 12 Quaternary core-catcher samples and include *Quinqueloculina*, pyritized *Saccammina*, *Cassidulinoides*, pyritized *Haplophragmoides*, and *Miliammina*.

Benthic foraminifers occur in 9 of 18 Pliocene core-catcher samples (Table 2). The assemblages consist of *Miliammina* with *Eggerella*, *Elphidium*, *Martinottiella communis*, *Chilostomella*, *Cibicides*, *Discorbis*, *Fissurina*, *Fontbotia wuellerstorfi*, *Globobulimina*, *Globocassidulina*, *Melonis pompilioides*, an oolinid, *Pullenia*, *Quinqueloculina*, *Saccamina*, *Sphaeroidina bulloides*, and *Uvigerina peregrina*.

Benthic foraminifers are present in seven of seventeen core-catcher samples of late Miocene age. Assemblages consist of *Ammodiscus*, *Cassidulina*, *Cyclammina*, *Eggerella*, *Globocassidulina*, *Gyroidina soldanii*, a lagenid, *Martinottiella communis*, *Miliammina*, *Melonis pompilioides*, *Pullenia bulloides*, *Quinqueloculina*, and unidentified, poorly preserved textularids. The assemblage is similar to those found at lower middle to lower bathyal depths. The middle(?) Miocene sequence bears an abundant and moderately well-preserved assemblage of benthic foraminifers including *Bulliminella*, *Cassidulinoidea*, *Chilostomella*, *Fursenkoina*, *Globobulimina*, *Gyroidina*, *Haplophragmoides*, *Nonionella*, *Spirosigmoinella*, and poorly preserved, unidentified textularids. The assemblage is upper middle bathyal in paleodepth, and resembles that from Site 794.

Radiolarians

The radiolarians recovered at Site 796 are, in general, moderately or poorly preserved, and are found in common to rare abundances (Tables 2 and 3). Reworking of Miocene radiolarians is common in the Pliocene and Quaternary sediments (Figs. 20 and 21). Samples examined from Pleistocene sediments show the same variability in abundance and preservation as do the Pleistocene sediments recovered at Sites 794 and 795. Early Pliocene assemblages found in the diatomaceous clay and claystones of Site 796 are poorly preserved, in contrast to the well preserved, high abundance assemblages of the early Pliocene sediments recovered from Sites 794 and 795. Because of the relatively poor radiolarian record, the zonal boundaries at Site 796, (Figs. 20 and 21) are less well defined than at Sites 794 and 795.

The Pleistocene silty clays recovered at Site 796 yielded radiolarian assemblages that show drastic changes in assemblage composition and preservation reflecting climatic fluctuations that were probably caused by northern hemisphere glaciations. One sample, Sample 127-796A-6H-CC, contains a tropical or subtropical assemblage including the species *Didymocyrtis tetra-thalamus* and *Spongaster tetras*. These species have not been found at Sites 794 and 795, or in any other sample from the Site 796 cores. This sample may have been deposited during an interglacial maximum. Although samples reflecting the warmer conditions that occurred during the time of the deposition of Sample 127-796A-6H-CC were not found at Sites 794 and 795, these conditions may have existed at those sites but were not sampled. The FAD of *Lychnocanium* sp. cf. *L. grande* was observed between Samples 127-796A-1H-CC and 127-796A-2H-CC in Hole 796A, while *Lychnocanium* sp. cf. *L. grande* was not found in any sample in Hole 796B. This suggests that the uppermost Quaternary sediments may be missing at Hole 796B. The LAD of *Clathrocyclus cabrilloensis* was found between Samples 127-796A-5H-CC and 127-796A-6H-CC in Hole 796A, and between Samples 127-796A-5R-CC and 127-796A-6R-CC in Hole 796B. No other radiolarian events were found in the Pleistocene sediments of Site 796. The stratigraphic records of *Sphaeropyle robusta* and *Sphaeropyle langii* were discontinuous at Site 796 as they were at Site 795. As a result, their respective last appearance and first appearance events were poorly defined. According to the diatom zonation, these events were both confined to the Pliocene.

The Pliocene record of radiolarian stratigraphy in the silty clays and diatomaceous clays at Site 796 is poor due to low

abundance and moderate preservation. Pliocene radiolarian datum levels found at Site 796 include the FAD of *Theocalyptia davisiana* (between Samples 127-796A-10X-CC and 127-796A-11X-CC in Hole 796A, and between Samples 127-796B-6R-CC and 127-796B-7R-CC in Hole 796B), the LAD of *Sphaeropyle robusta* (between Samples 127-796A-10X-CC and 127-796A-11X-CC in Hole 796A, and between Samples 127-796B-9R-CC and 127-796B-10R-CC in Hole 796B), the FAD of *Sphaeropyle langii* (between Samples 127-796A-12X-CC and 127-796A-14X-CC in Hole 796A, and between Samples 127-796B-9R-CC and 127-796B-10R-CC in Hole 796B), the LAD of *Drupptractus acquiloni* (between Samples 127-796A-8H-CC and 127-796A-9X-CC), the FAD of *Drupptractus acquiloni* (between Samples 127-796A-18X-CC and 127-796A-19X-CC), the LAD of *Stylactonarium* sp. cf. *S. quilonarium* (between Samples 127-796A-10X-CC and 127-796A-11X-CC), and the LAD of *Thecosphaera japonica* (between Samples 127-796A-9X-CC and 127-796A-10X-CC).

Miocene sandy claystones at Site 796 have radiolarian assemblages that are rare in abundance, moderately to poorly preserved, and contain few stratigraphic indicators. Zonation of these sediments using radiolarians was difficult. Again, as at Sites 794 and 795, radiolarians survived dissolution below the opal-A/opal-CT boundary. Samples 127-796A-22X-CC through 127-796A-27X-CC are tentatively assigned to the *Thecosphaera japonica* Zone (Fig. 20); however, the main diagnostic species, *Thecosphaera japonica*, was not found in these samples. Species diagnostic of the older *Lychnocanium nipponicum* Zone are also absent from these samples. Sediments of late Miocene age recovered in Cores 796B-10R through 796B-16R are assigned to the *Lychnocanium nipponicum* Zone, based on the presence of *Lychnocanium nipponicum*. *Sethocyrtis japonica* was found in Sample 127-796B-16R-CC. Radiolarians are present in Sample 127-796B-17R-CC, but are rare, with no diagnostic species present. Below this sample, all samples examined from Hole 796B are barren of radiolarians.

Paleoenvironment

The paleodepth at Site 796 was upper middle bathyal during the middle(?) Miocene and increased to lower middle to lower bathyal by the late Miocene based on assemblages of benthic foraminifers. Further environmental interpretation of Miocene fossil assemblages is difficult due to both the presence of displaced pebbly mudstones, sands, and sandstone throughout much of the late Miocene sequence and the poor preservation of microfossils below the opal-A/opal-CT boundary.

In the early Pliocene, high productivity of diatoms, similar to that found at Sites 794 and 795, persisted in the northwestern Japan Sea from about 5.3 to 4 Ma based on the presence of diatom ooze. High productivity was sporadic in the early late Pliocene and early Quaternary based on the presence of diatom ooze in two short intervals. Throughout the late Pliocene and Quaternary, vigorous upwelling is indicated by an assemblage of diatoms, including *Thalassionema nitzschioides*, *Thalassiothrix longissima*, and *Chaetoceros* resting spores (Burckle, 1978; San-cetta, 1982; Barron and Keller, 1983), all of which are characteristic of high productivity driven by upwelling. The onset of upwelling in the region coincides with the onset of northern hemisphere glaciation. The Quaternary surface and intermediate waters of the northwestern Japan Sea varied through time between warm and cold conditions typical of Pleistocene climatic extremes, based on the variability in assemblages of planktonic foraminifers, calcareous nannofossils, and radiolarians at Site 796. Reworking of all microfossils in Pliocene and Quaternary core-catcher samples, however, makes detailed environmental interpretation of assemblages suspect.

PALEOMAGNETISM

Introduction

The NRM (natural remanent magnetization) of all except the most disturbed cores recovered at Site 796 was measured and demagnetized with peak-fields of 8 and 15 millitesla (mT) in the cryogenic magnetometer. Declination, inclination, and intensity of magnetization before and after cleaning are plotted vs. depth in Figure 22A-D.

A pilot set of 44 discrete samples (7 in Hole 796A and 37 in Hole 796B) was collected and measured before and after AF demagnetization in 5-12 steps with the spare Molspin magnetometer in peak fields up to 90 mT. We used this instrument for these measurements as the other magnetometer has a systematic offset between axial measurements that results in slightly higher uncertainties when measuring the magnetic directions of samples with low magnetic intensities.

Although the range of the NRM intensities of the sediments are similar to those observed at Sites 794 and 795, the sediments from Site 796 exhibited a slightly stronger average magnetization. The strongest magnetization was exhibited in samples from Hole 796A. Only in the lower part of Hole 796B was the intensity of magnetization regularly below 1 mA/m (Fig. 22C). The magnetic susceptibility (K) also exhibited higher values with respect to previous sites, without any apparent trend in the down-hole plot (Figs. 23A and -B). A wider range of values is distributed in the middle part of Hole 796A, where the susceptibility in several cases exceeds the value of 100 cgs units (Fig. 23A). Some spikes can be correlated with the occurrence of volcanic lithologies in the section, such as with the sands recovered at 85 and 140 mbsf in Hole 796A and the blue tuffs in Hole 796B at 323 mbsf. An increase in the terrigenous sedimentation due to the marginal position of the site could be responsible for these higher values of both remanence and magnetic susceptibility.

Results and Magnetostratigraphy

The main feature of the paleomagnetic results at this site is a predominant scattered normal polarity, especially at Site 796A (Fig. 22B and -D). These results cannot be representative of the characteristic remanent magnetization (ChRM) of the rock. Moreover, the magnetic behavior of the rock in the two holes is dissimilar and different interpretations are necessary.

Sediments recovered from Hole 796A exhibit a suspicious, scattered normal polarity after demagnetization. Monitoring of the equipment excludes the possibility that an anhysteretic remanent magnetization (ARM) was induced during the AF treatment. High quantities of gas and clathrates were present in the uppermost part of this hole (beginning in Core 127-796A-2H; see "Organic Geochemistry" and "Inorganic Geochemistry" sections, this chapter) which disrupted the cores very strongly. In contrast, Site 794 had little gas; Site 795 had larger amounts of gas than Site 794, but gross expansion of Site 795 cores was only observed in the deeper cores. The extent of disturbance at both sites was not as pronounced as in Site 796. The comparison of the magnetostratigraphic results in intervals cored using the APC from Sites 794, 795, and 796 suggests a correlation with the occurrence of gas. Apparently, the degassing causes not only an obvious disruption of the soft sediments, but also influences the magnetic fabric. We do not know the consequences of this disturbance in detail because there has been no paleomagnetic study of this phenomenon, and the mechanism and especially the amount of degassing or decompaction is unknown. Nevertheless, we assume that degassing affects the orientation of the carriers of the NRM. This could be the reason for strong noise superimposed on the magnetostratigraphic information, or for even complete remagnetization. Whether it is possible or not to remove this spurious magnetization by AF-demagnetization de-

pends on whether the disturbance of the magnetic fabric is grain-size-selective or not.

Pilot samples, from the upper part of Hole 796B (Cores 127-796B-1R through -9R) exhibited unstable magnetization without a stable end point after demagnetization (Fig. 24A). Shallow inclinations also occur in these samples (Fig. 24A, Sample 127-796A-3H, 104 cm), but cannot be explained by strong tectonic tilting of the upper part of Okushiri Ridge. It is possible that some effect was induced by the drilling, and in some cases, a spurious vertically downward component was removed from the rock (Fig. 24B; Sample 127-796B-26R, 33 cm). Alternatively, as suggested by results from the previous Sites 794 and 795, a high diatom content in the sediments is often coincident with the scattered paleomagnetic directions.

As at the previous sites, bioturbation is common in the diatomaceous sediments of Site 796. Most deep-sea sediments exhibit coherent magnetic directions (Opdike, 1972), in spite of bioturbation, as the postdepositional DRM is considered to be the process responsible for the magnetization of this kind of sediment (Kent, 1973). Nevertheless, Watkins (1968) has shown that bioturbation may indeed affect the direction of sediment magnetization. The weak and scattered magnetization of the diatomaceous sediments of Site 796 may result both from the effects of bioturbation and from the dilution of remanence-carrying components by the heavy diatom sedimentation.

Scattering of data, remagnetizations, poor recovery and limited paleontological data make it difficult to define a coherent magnetostratigraphy for this site. Without any polarity pattern, and lacking a consistent number of discrete samples, any attempt to define a reversal sequence must be considered speculative. In spite of this, magnetic behavior during demagnetization can give an indication of the polarity. Rocks with a primary reverse direction are more likely to be affected by a scattering in the results if a normal polarity remagnetization is not completely cleaned. Using the biostratigraphic data as a framework, we constructed tentative correlations between the results from Hole 796A and the GRTS (Geomagnetic Reference Time Scale).

The sediments recovered in the first 12 mbsf of Hole 796A showed a consistent normal polarity representing part of the Brunhes Chron. Below this depth, the recovered cores were highly disturbed by gas and the results are not reliable enough to define a Brunhes-Matuyama boundary, which should occur in Core 127-796A-3H according to extrapolation from the sediment accumulation rate (see "Sediment Accumulation Rates" section, this chapter). Scattered directions typify the underlying section until Core 127-796A-9X, when a consistent normal polarity is observed through Core 127-796A-12X. A correlation with the Matuyama and the Gauss chrons is only partially supported by paleontological age. Assuming that the clustering of data points between 59 and 89 mbsf is representative of a real normal polarity (Fig. 22B), the Matuyama-Gauss boundary (2.47 Ma according to Berggren et al., 1985) may be placed at 59 mbsf. In contrast, the LAD of *N. kamtschatica* (2.5 Ma) suggests that the beginning of the Gauss Chron occurs at 78 mbsf. Cleaned magnetic directions become scattered again beginning with Core 127-796A-14X at 107 mbsf. The FAD of *N. koizumii*, 3.5 Ma, occurs at 117.2 mbsf and supports a possible correlation with the Gilbert Chron.

The predominant normal polarity exhibited by the rock recovered at Hole 796B can be interpreted in terms of an uncleaned remagnetization of the rock. Magnetic inclinations are mostly positive for the NRM, attesting that a peak field of 15 mT was unable to remove an overprint with a higher coercivity. It is possible that this remagnetization is related to the observed occurrence of pyrite which indicates reducing environments (Kobayashi and Nomura, 1972). In such an environment, the oxides of iron are reduced and reprecipitated as pyrite or other iron sul-

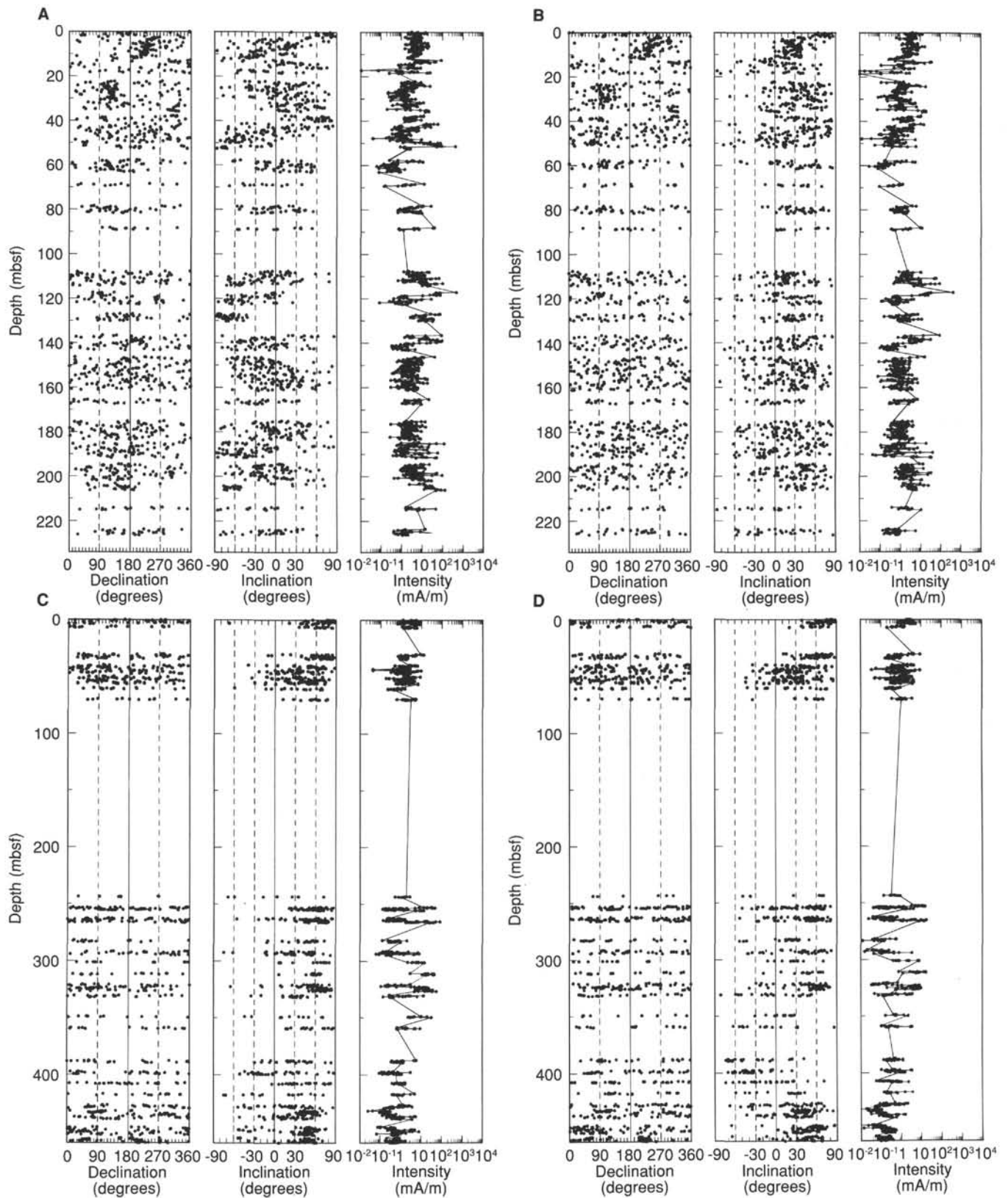


Figure 22. Downhole plots of declination, inclination, and intensity of magnetization. **A.** Hole 796A-1H-27X showing natural remanent magnetization (NRM) results. **B.** Hole 796A-1H-27X showing results from demagnetization with a peak field of 15 mT. **C.** Hole 796B-1R-33R shows results for the NRM. **D.** Hole 796B-1R-33R shows results from demagnetization with a peak field of 15 mT.

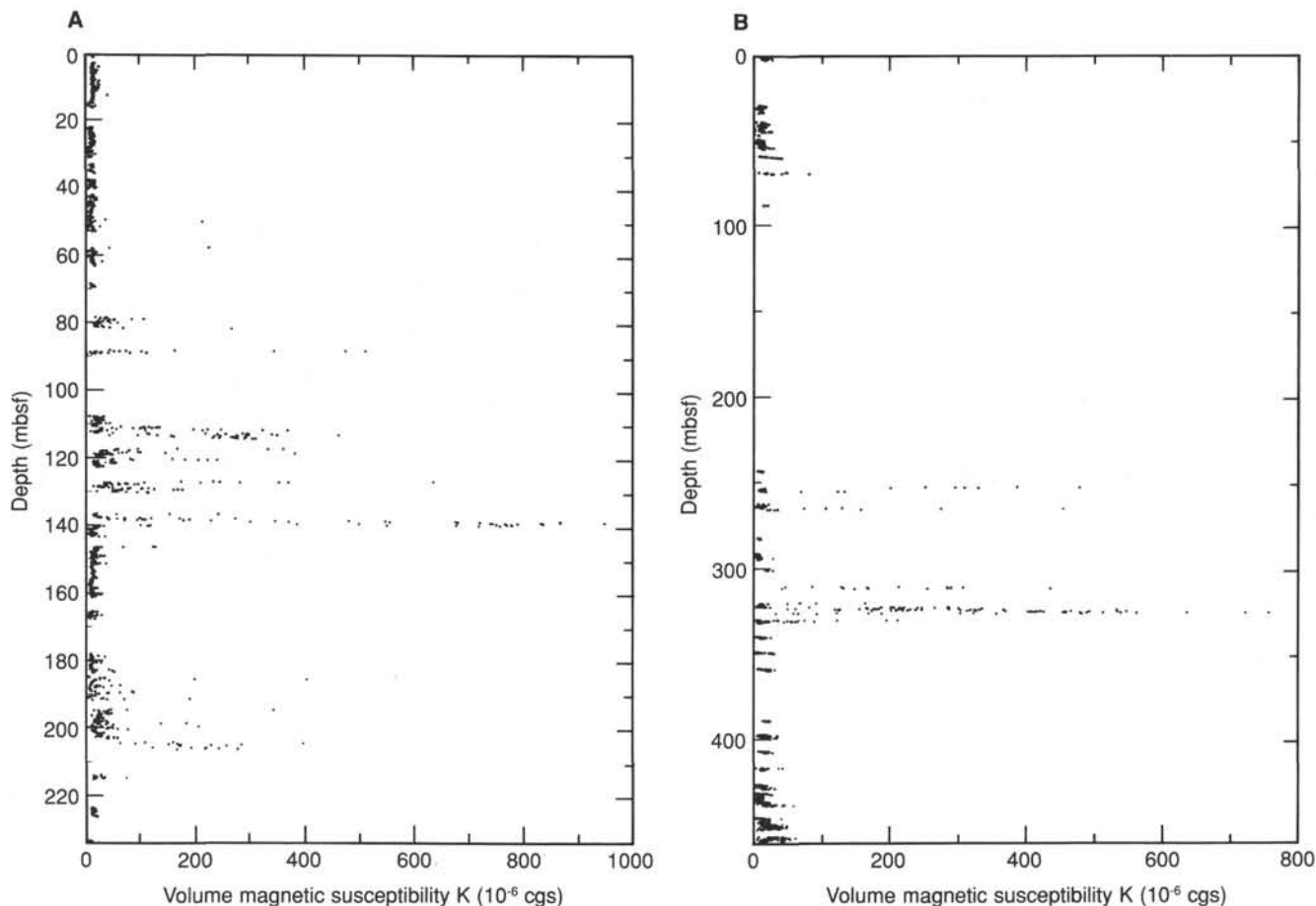


Figure 23. Magnetic susceptibility plotted vs. depth. **A.** Core 796A-1H-27X. **B.** Core 796B-1R-334.

fides that do not possess remanence or are weakly magnetized. This process could be responsible for the weak intensity of magnetization also exhibited by other rocks from previous sites.

Discrete samples measured with the Molspin magnetometer provided a different view of the polarity pattern of this hole. The rock did not always show a stable magnetization, but, on the basis of the magnetic behavior observed on the Zijderveld plots of the whole-core measurements (using the Magraph program elaborated by H. Shibuya during the Leg 124), an attempt can be made to define a reversal sequence that possibly represents the characteristic magnetization of the rock. Only Core 127-796B-17R showed very ambiguous results and so has been considered undetermined. A polarity pattern for this hole is shown in Figure 25. Unfortunately, the recovery was poor (29%), leaving large gaps in the observed magnetostratigraphy. On a paleontological basis (FAD of *N. kamtschatica*, 6.4 Ma, in Core 127-796B-10R), the normal interval observed in this core can be correlated with the normal interval of Chron 6 which starts at 6.37 Ma according to Berggren et al. (1985). The lack of datum levels below 253 mbsf make difficult any correlation with specific chrons.

SEDIMENT ACCUMULATION RATES

Estimates of sedimentation rates for Site 796 are based on seven diatom biostratigraphic datum levels and one planktonic foraminiferal datum level (Table 4). Magnetostratigraphy is poor at this site, therefore paleomagnetic reversal stratigraphy was not used in the sedimentation rate calculation. A sedimentation rate for each interval was estimated from the age vs. depth relationship (Table 4). Sediment accumulation rates ($\text{g}/\text{cm}^2/\text{k.y.}$)

are also shown in Table 4. They closely match the sedimentation rates suggesting that compaction is minimal down to the depth for which data are available (252.7 mbsf). The lack of datum levels with depth is because of dissolution of diatoms below the opal-A/opal-CT transition (225 mbsf) and the sparse recovery of carbonate nodules which often contain preserved diatom frustules.

Sedimentation rates at Site 796 range from 9 m/m.y. to 74 m/m.y. (Fig. 26). Sedimentation rates are highest in the Quaternary and in the coarse facies at the base of the section. The lowest sedimentation rate is at the base of the Quaternary, and may indicate a disconformity. In general, both core recovery and the abundance and preservation of microfossils at Site 796 samples were poor. Therefore, the sedimentation rate curve for Site 796 has fewer data points than for Sites 794 and 795 and lacks the detail of the previous curves.

The estimated age of the oldest sediment cored at Site 796 is not well constrained. The oldest and deepest age significant microfossil found is *Globigerina bulloides* at 451.8 mbsf (Table 4). *G. bulloides* ranges from approximately 16.0 Ma until the present day and indicates that the sediments at this level can be no older than 16.0 Ma (Fig. 26). Assuming that 16.0 Ma is the maximum age of the sediments at 451.8 mbsf, then the sedimentation rate between 252.7 m and 451.8 m is 21 m/m.y. Given the number of pebbly sand units below 252 m, the sedimentation rate was probably more rapid and a more realistic sedimentation rate may be closer to 62 m/m.y., which is simply the extrapolated sedimentation rate between the last two diatom datum levels (6 and 7). Extrapolating this sedimentation rate to 465 m implies that the minimum age of the sediments at this depth is ap-

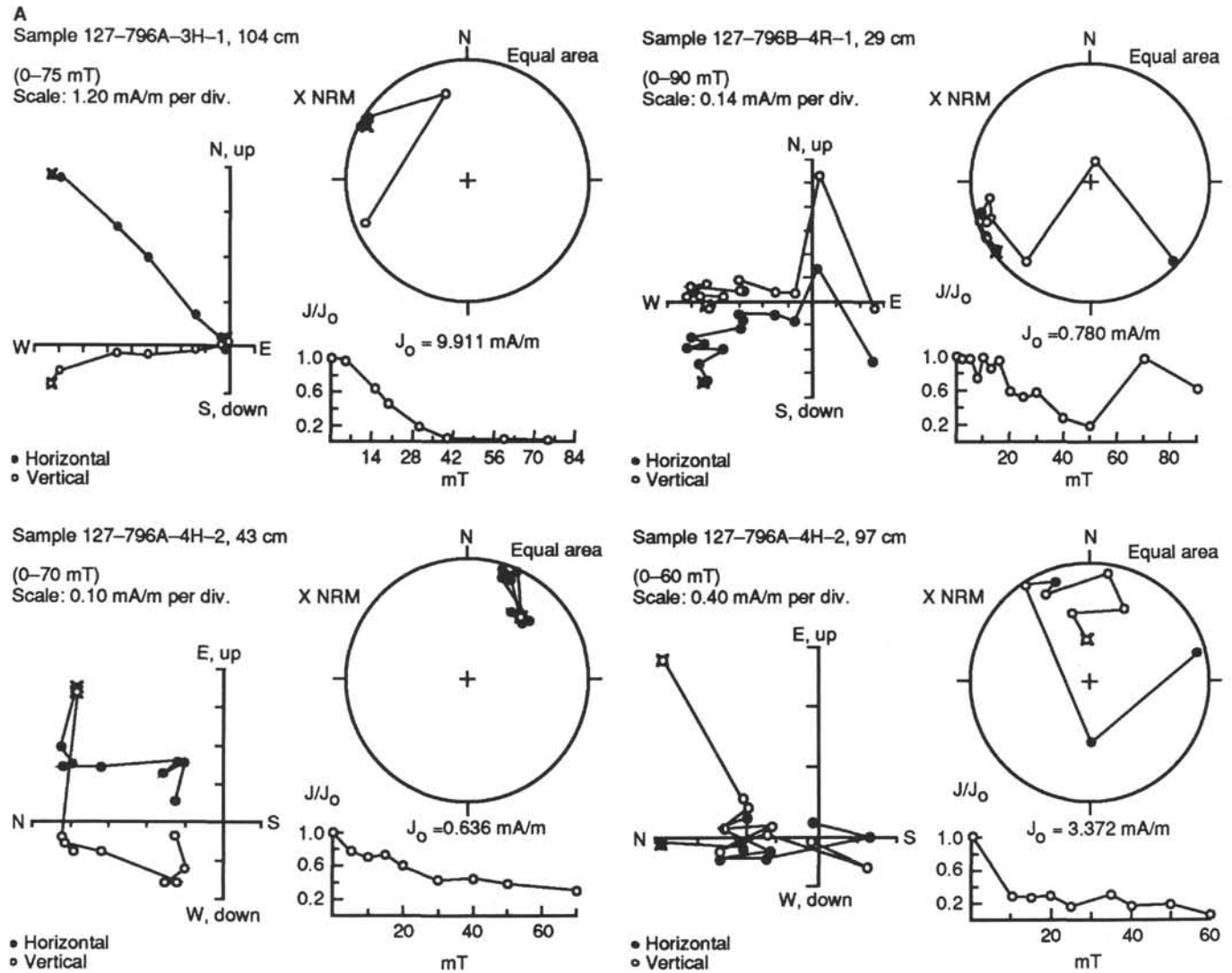


Figure 24. Zijderveld equal area and intensity decay plot as function of AF demagnetization. **A.** Pilot samples from Hole 796A. **B.** Pilot samples from Hole 796B.

proximately 9.70 Ma. The average age of the sediments at 465 mbsf is 12.9 Ma.

INORGANIC GEOCHEMISTRY

Introduction

The shipboard inorganic geochemistry program at Site 796 continued to focus on interstitial water analysis, with whole-round core samples being squeezed by both the standard stainless-steel ODP squeezer (Manheim and Sayles, 1974) and the new plastic-lined squeezer (Brumsack et al., unpubl. data). Samples were gathered from 2.0 to 294.2 mbsf (lithological Units I to III; see "Lithostratigraphy" section, this chapter). Holes 796A and 796B were drilled 250 m apart on a steep slope and therefore element profiles do not always match perfectly. Deeper downcore pore-water retrieval was not possible due to either little core recovery, intense contamination by drilling, or the hardness of the rock. Accordingly, only 16 different cores have been sampled. The Barnes *in-situ* sampler was not used. Major ion data from both squeezers are presented in Table 5.

The pore-water chemistry at Site 796 is influenced by the presence and decomposition of methane-clathrates. This was evident from the high gas pressure which lead to severe disturbance of cores upon recovery. Clathrates may be present through-

out the upper 120 m of this site. The water from one solid clathrate piece, which was recovered from 94 mbsf in Section 127-796A-12X-4, was analyzed for its chemical composition.

Salinity, Chloride, and Sodium

The salinity profile of Site 796 (Fig. 27) is characterized by a minimum centered around 50 mbsf with values as low as 28 g/kg (i.e., 20% below average seawater salinity). This minimum in salinity coincides with anomalies in Na and Cl (Fig. 27). Both elements are depleted by about 10% relative to seawater in the same depth range where the salinity minimum is situated. But since the magnitude of the anomalies is different (10% for Na and Cl vs. 20% for salinity), we conclude that the process responsible for the Na and Cl decrease is not necessarily exclusively responsible for the salinity decrease. As will be shown below, the observed decrease in Mg and sulfate alone creates a salinity decrease of approximately 9%. The anomalies in Na, Cl, and salinity are related to the occurrence of the methane-clathrates. Na and Cl are the most abundant ions in seawater and a removal process operating at such shallow depth intervals is unlikely.

Comparable anomalies could only be produced by the introduction of less saline waters from the shelf or deeper layers along fault systems. Migration through porous sand layers is the

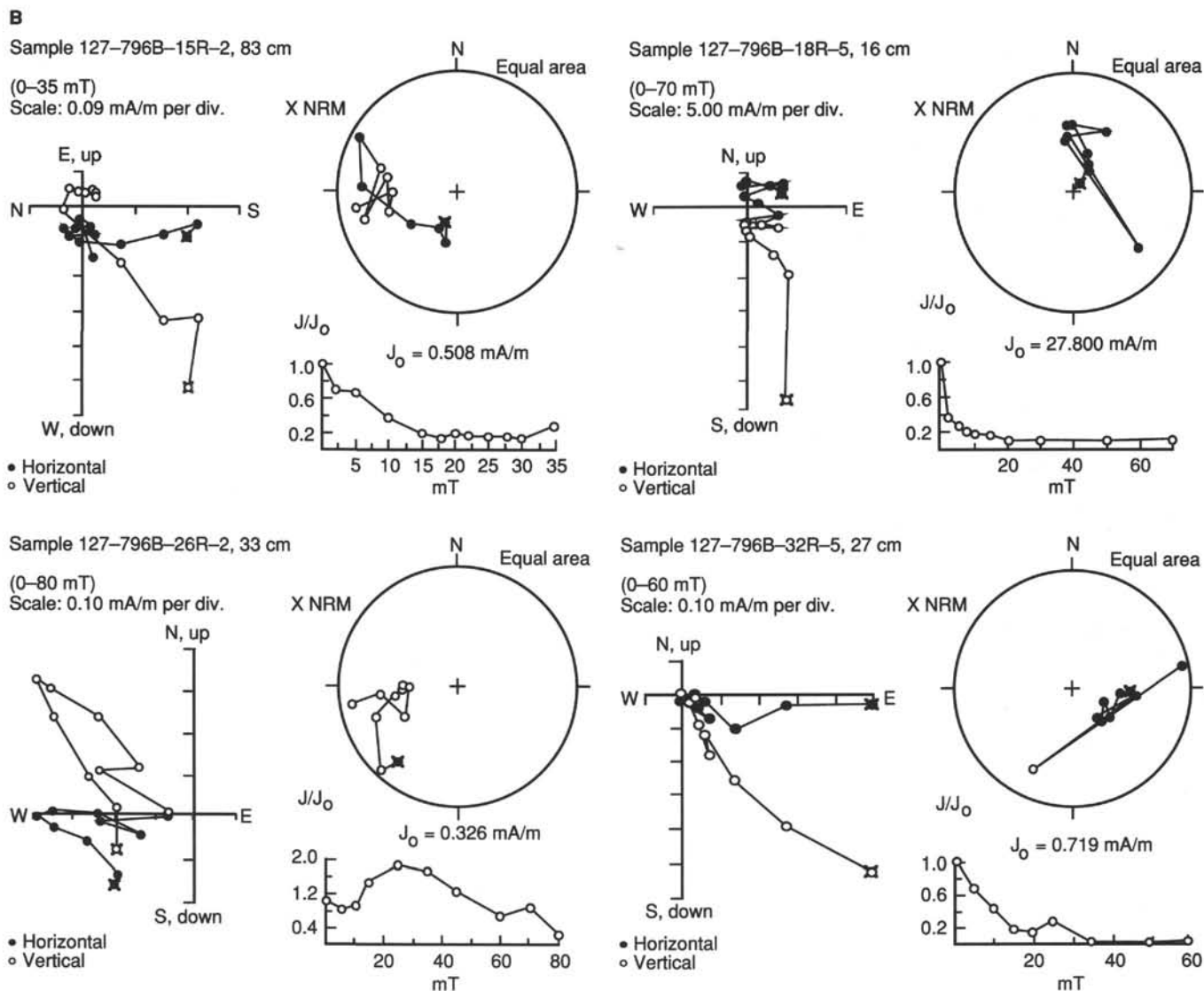


Figure 24 (continued).

least likely possibility, as the relative minimum values of Na, Cl, and salinity were not found in sandy layers, and the sand layers that were sampled (Cores 127-796A-17X and 127-796A-24X) do not exhibit anomalously low concentrations. Clathrate formation and decomposition and the related changes in pore-water chemistry are discussed in detail below.

Sulfate and Alkalinity

Bacterial sulfate reduction is an important mechanism operating in organic carbon-rich marine sediments. The smell of hydrogen sulfide in the uppermost three cores of Hole 796A and in one deeper core (Core 127-796A-14X) is closely related to the presence of sulfate in the pore waters and of organic matter in the sediments. Sulfate levels of 0 mmol/L are reached in Core 127-796A-3H (14 mbsf) and remain below detection limit (0.1 mmol/L) until Core 127-796A-9X (62 mbsf, Fig. 27). Deeper downhole sulfate levels increase until a maximum concentration of more than 20 mmol/L is attained in Core 127-796A-24X (206 mbsf). This sulfate probably represents the original sulfate which was buried during deposition of these sediments and which has not been utilized by bacteria, possibly due to lack of enough metabolizable organic matter. Furthermore, the comparably low sedimentation rate of 40 m/my (see "Sediment Accumulation Rates" section, this chapter) may have allowed significant amounts

of sulfate to diffuse downward and replenish the sulfate reservoir used by bacteria. Sulfate remains high in the two deeper samples from Hole 796B.

Alkalinity values are highest (around 15 mmol/L) in the top cores of both holes. These high values coincide with the depth interval of most intense sulfate reduction. Alkalinity starts to decrease at a comparably shallow depth (about 15 mbsf) until a minimum is reached at 80 mbsf (Core 127-796A-11X). This alkalinity minimum seems to be associated with methane production coupled with authigenic carbonate precipitation (Claypool and Threlkeld, 1983; Hesse et al., 1985). The increase in alkalinity with depth results from bacterial sulfate reduction occurring again at these depth intervals.

Ammonium and Phosphate

Ammonia increases from a near surface value of 215 $\mu\text{mol/L}$ to maximum concentrations slightly above 2200 $\mu\text{mol/L}$ at 50 mbsf (Core 127-796A-5H) (Fig. 27). Below this depth interval, ammonia concentrations decrease linearly to less than 1500 $\mu\text{mol/L}$ at 294 mbsf. The ammonia increase from the surface sediments to the maximum at 50 mbsf reflects the intensive bacterial degradation of organic matter in the surface sediments. The overall decrease from 50 mbsf downhole indicates that uptake of ammonia into clay minerals is occurring at a higher rate

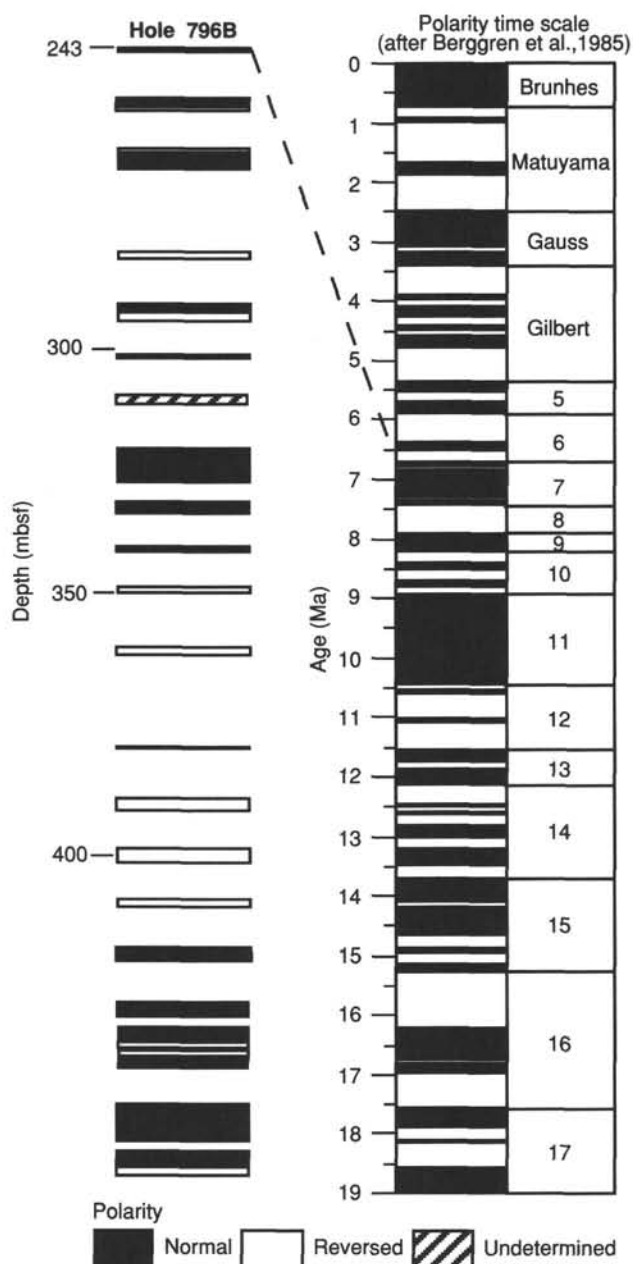


Figure 25. Polarity pattern for the lower part of Hole 796B.

than ammonia production by bacterial organic matter degradation.

Phosphate exhibits a decreasing trend from initial values of approximately $30 \mu\text{mol/L}$ near the surface of both holes to $0 \mu\text{mol/L}$ below 260 mbsf in Hole 796B, indicating strong removal into sedimentary phases (Fig. 27).

Silica

Silica increases in pore waters at Site 796A (Fig. 27) from initial values of $740 \mu\text{mol/L}$ at 2 mbsf to a maximum value of $1425 \mu\text{mol/L}$ at 181 mbsf, above the opal-A/opal-CT boundary. The two silica values obtained deeper in Hole 796B are significantly lower (265 and $385 \mu\text{mol/L}$, respectively) than those acquired for Hole 796A and are typical for siliceous sediments occurring below the opal-A/opal-CT transition zone.

The relatively large scatter of the silica data reflects the heterogeneous sediment composition at this relatively nearshore and tectonically active site. For example, the silica values at 140 mbsf (Core 127-796A-17X) and 206 mbsf (Core 127-796A-24X), which fall below the overall increasing trend, are from sand layers. The silica profile only generally indicates the position of the silicification front at below 206 mbsf. The opal-CT/quartz boundary was not reached in interstitial water sampling.

Magnesium, Calcium, and Strontium

The alkaline earth metals, in particular Mg, show large variations in the upper cores of Site 796 (Fig. 27). Magnesium decreases to values around 5 mmol/L within the upper 40 m of Hole 796A. This interval of most extreme Mg depletion coincides with the increasing frequency of ash layers (see "Lithostratigraphy" section, this chapter). Alteration reactions of these ash layers therefore represent a significant sink for pore-water Mg in the upper cores. The slight decrease of Mg in deeper sections of Hole 796B may be related to basement alteration processes in analogy to the previous sites, but a proof of this assumption cannot be given, since basement was not penetrated at Site 796. The Mg minimum also coincides with the decrease in alkalinity and the salinity minimum described above.

The strong decrease of Mg is accompanied by an increase in Ca by a factor of two (from 8.5 to 17.5 mmol/L , Fig. 27). Strontium decreases to half seawater values ($47 \mu\text{mol/L}$) in the depth range of Mg depletion and Ca increase (Fig. 27) and also seems to be removed during alteration of ash layers.

The mirror-image behavior of Ca and Mg is rather common in many ODP and DSDP drill holes and reflects either processes of dolomitization or alteration reactions of volcanic matter. In this case, the latter seems to be the primary control for the distribution of both elements in the pore waters. Carbonate precipitation is of minor importance. According to Baker and Burns (1985) several reactions of dolomitization are possible, but all dolomitization reactions involving biogenic carbonate as a precursor material should be accompanied by a release of Sr, which is not the case at Site 796.

Potassium, Lithium, and Rubidium

The alkali metals show individually distinct concentration profiles at Site 796 (Fig. 27). Potassium steadily decreases from values slightly above seawater concentrations (12 mmol/L) at the top of the hole down to 2 mmol/L at the lowermost sample in Hole 796B. Since no deviation from this steady trend is observed in the zone of ash layer alteration (upper 150 m), the ultimate K sink is probably deeper and may even be in the basement. Also, the salinity anomaly associated with the methane clathrates is not reflected in the K profile. But since the anomaly represents only a 10% decrease, it can hardly be recognized in the profile of any alkali metal, except Na.

Li and Rb exhibit pronounced nonlinear concentration changes with depth at Site 796. Li increases from initial seawater values of around $25 \mu\text{mol/L}$ to maximum concentrations of slightly greater than $70 \mu\text{mol/L}$ at 50 mbsf (Fig. 27). It then decreases to minimum values of $20 \mu\text{mol/L}$ just above the opal-A/opal-CT transition zone. The Li anomaly around 50 mbsf is definitely not associated with the decomposition of gas-hydrates since clathrate water is not enriched in this element (Table 6). In addition to the previously mentioned reactions involving biogenic silica (Gieskes, 1981), altered andesitic or rhyolitic ash layers also may represent a potential Li source (Heier and Billings, 1969). A sink for Li seems to be present close to the opal-A/opal-CT transition zone, where minimum values below seawater concentrations are observed. At greater depths, concentrations seem to slightly increase, but whether the basement rocks also

Table 4. Biostratigraphic datum levels used to determine sedimentation rates for Site 796. The depths of zonal boundaries and datums in core-catcher samples are taken from the top or bottom of the cored interval rather than from the base of the recovered sediment.

Datum	Age (Ma)	Depth (mbsf)	Sedimentation rate		Mean dry bulk density (g/cm ³)	Accumulation rate (g/cm ² k.y.)
			m/m.y.	cm/k.y.		
Seafloor	0	0				
1. LAD of <i>R. curvirostris</i>	0.30	22.2	74	7.4	1.10	8.14
2. LAD of <i>A. oculatus</i>	0.93	50.7	48	4.8	1.09	5.23
3. LAD of <i>Ne. koizumii</i>	1.80	58.7	9	0.9	1.04	0.94
4. LAD of <i>Ne. kamtschatica</i>	2.50	88.1	42	4.2	1.10	4.62
5. FAD of <i>Ne. koizumii</i>	3.50	117.2	29	2.9	1.17	3.40
6. Base of <i>T. oestrupii</i> Zone	5.30	184.7	38	3.8	1.10	4.18
7. FAD of <i>Ne. kamtschatica</i>	6.40	252.7	62	6.2	1.21	7.51
8. FAD of <i>G. bulloides</i>	16.00	451.8	21	2.1		

Note: LAD = last appearance datum. FAD = first appearance datum.

represent a final sink for Li cannot be determined since samples from deeper sections have not been investigated.

Rubidium exhibits a concentration-depth profile which is similar to Mg. Rubidium values decrease from concentrations greater than seawater (1.8 $\mu\text{mol/L}$) at the top of Hole 796A to minimum values (around 1.1 $\mu\text{mol/L}$) at 50 mbsf (Fig. 27). Rubidium then increases to higher concentrations at the opal-A/opal-CT transition zone. Below this, the two samples from Hole 796B suggest that concentrations decrease with depth. The Rb minimum at 50 mbsf cannot be related to the decomposition of methane-clathrates, since the decrease is larger than 10% relative to seawater concentrations. It is more likely that Rb is removed during alteration of volcanic ash layers in the upper cores. Sediments around the opal-A/opal-CT transition zone may act as a Rb source as well. The basement may be the final sink for Rb, as it is for K and Mg.

Clathrates

As has been mentioned above, methane-clathrates have been recovered in Section 127-796A-12H-4. One solid piece of this gas-hydrate was kept in a sealed headspace glass vial for gas analysis and the water remaining after decomposition of this material has been analyzed for major ions (Table 6). The hydrate-water was contaminated by drill water and/or pore water, as is exemplified by the comparably high salinity of 10 g/kg. Therefore some model calculations were performed in order to get a semi-quantitative estimate for the contamination of this sample by seawater and pore water.

The contribution of saline water (seawater and pore water) averages about 35% of the clathrate-water investigated, based on salinity, Na, and Cl data. The saline water component may be regarded as either contamination obtained during coring or as inclusion of pore-water droplets during growth of gas-hydrate crystals.

Table 6 lists the chemical composition of average seawater (Bruland, 1983), clathrate-water from Core 127-796A-12X, interstitial water from adjacent Core 127-796A-11X, and clathrate-water analyzed by Brooks et al. (1985). Using the concentrations of Mg, Li, and sulfate, the relative proportions of seawater and pore water can be estimated. Seawater contamination ranges in the order of 20%–40% of the saline component of the clathrate-water, whereas pore water from the same depth con-

tributes from 60% to 80% to the ion content of the water. As far as the data allow, a comparison with the analysis carried out by Brooks et al. (1985), the relative proportions of many elements range in the same order of magnitude when compared on a element/salinity basis. There is no indication for a preferential uptake of any ion species by the methane-clathrate.

The observed salinity, Na, and Cl anomalies often associated with the occurrence of gas-hydrates (Jenden and Gieskes, 1983; Hesse et al., 1985) seem to be an artifact of sample recovery, as methane-clathrates are only stable below about 1 km water depth (Kvenvolden and Barnard, 1983; Kvenvolden and McDonald, 1985). Above this depth they start decomposing upon recovery and the less saline clathrate water dilutes the corresponding pore water. The stability of gas-hydrates also depends upon temperature. Assuming a thermal gradient of 173°C/km for Site 796 (see "Downhole Measurements" section, this chapter), a temperature between 21° and 23°C should be reached at a depth of 115–135 mbsf. This temperature range would not allow the existence of gas-hydrates at greater depths (Kvenvolden and McDonald, 1985). The salinity, Na, and Cl anomalies are centered immediately above this depth range (Fig. 27).

Another prerequisite for the formation of more massive layers of methane-clathrate may be the presence of enough pore space. The sands which were recovered at this drill location represent almost ideal sites for the formation of massive gas-hydrates. The absence of sand layers at Site 795, which also had a high methane content, might explain why gas-hydrates were not encountered there.

Summary

The pore-water chemistry of the upper 100 m at Site 796 reflects the presence of gas-hydrates, which produce a salinity and NaCl anomaly centered around 50 mbsf. The occurrence of methane-clathrates results from the absence of sulfate at relatively shallow depths (14 mbsf) followed by methanogenesis. A further prerequisite for the formation of gas-hydrates may be the presence of highly porous sand layers.

The behavior of alkaline earth elements is largely controlled by alteration of the abundant ash layers in the upper 150 m of this site. In this depth range an extreme depletion in Mg is observed, associated with an increase in Ca and a minor decrease in Sr. At greater depth, basement alteration processes are proba-

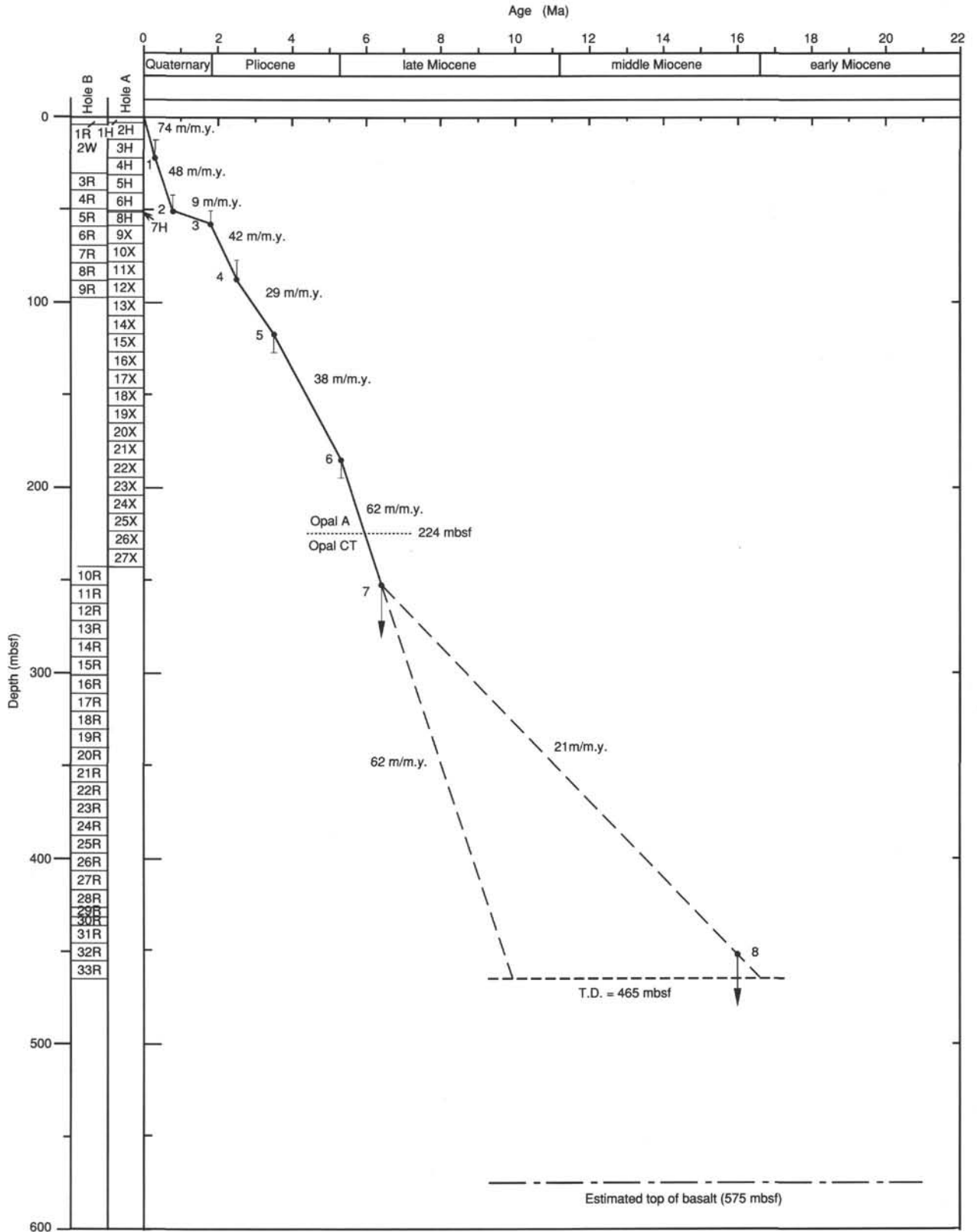


Figure 26. Age vs. depth relationship at Site 796. The error bars indicate the uncertainty in the age and precise depth of the datum levels.

Table 5. Interstitial water geochemistry data, Site 796.

Core, section, interval (cm)	Depth (mbsf)	Vol. (mL)	pH	Alk. (mM)	Sal. (g/kg)	Mg (mM)	Ca (mM)	Cl (mM)	SO ₄ (mM)	PO ₄ (μM)	NH ₄ (μM)	SiO ₂ (μM)	Mg/Ca
796A-1H-1, 50-55	0.50	10							10.1				
796A-1H-2, 55-60	2.05	72	7.95	15.15	33.3	41.1	8.6	540	9.8	29.4	215	740	4.78
796B-1R-2, 140-145	2.90	10											
796B-1R-2, 145-150	2.95	64	7.91	14.70	33.0	42.6	8.49	541	12.1	14.4	220	805	5.02
796A-2H-4, 145-150	9.15	10	8.12	14.78	31.0	18.6	11.0		2.3	30.1	1095	745	1.69
796A-2H-4, 145-150	9.15	10	8.12	14.78	31.0	18.6	11.0	510	2.3	30.1	1095	745	1.69
796A-3H-1, 140-145	14.10	10							0.4				
796A-3H-1, 145-150	14.15	46	7.92	9.85	30.0	13.0	12.5	505	0.4	14.4	1355	835	1.04
796A-4H-5, 145-150	29.65	10	7.66	7.64	29.0	6.0	16.2	508	0.0	15.7	2035	770	0.37
796A-5H-5, 145-150	39.15	10	7.71	6.71	28.5	5.2	17.0	503	0.0	16.5	2210	750	0.31
796A-6H-6, 140-145	50.10	10							0.0				
796A-6H-6, 145-150	50.15	46	7.71	6.09	28.0	4.8	17.2	490	0.0	5.7	2130	875	0.28
796A-8H-5, 93-98	58.63	10	8.19	5.86	28.2	5.7	16.0	489	0.4	6.7	2000	655	0.36
796A-9X-2, 140-145	61.60	35	7.88	6.28	28.0	5.4	17.5	495	0.0	4.3	2115	845	0.31
796A-9X-2, 140-145	61.60	10							0.0				
796A-11X-1, 145-150	79.75	10	8.22	5.03	28.5	6.2	16.4	496	0.9	2.5	2000	1005	0.38
796A-14X-2, 140-145	110.50	10											
796A-14X-2, 140-145	110.50	32	7.76	5.61	29.5	9.2	16.6	517	1.3	2.8	1800	1110	0.55
796A-17X-2, 140-145	139.40	10							4.9				
796A-17X-2, 145-150	139.45	17	7.91	6.79	30.5	17.9	13.2	532	2.8	2.0	1935	870	1.36
796A-21X-4, 140-145	180.90	10							5.4				
796A-21X-4, 145-150	180.95	37	7.87	9.36	31.7	30.6	10.5	539	4.8	7.0	1755	1425	2.91
796A-24X-1, 140-145	205.50	10							21.4				
796A-24X-1, 145-150	205.55	30	7.61	5.00	33.7	43.4	15.6	543	21.7	2.4	1715	925	2.78
796B-12R-1, 140-145	263.70	5							17.3				
796B-12R-1, 145-150	263.75	14	7.99	3.24	32.5	40.3	19.5	530	18.2	0.0	1505	265	2.07
796B-15R-2, 140-145	294.20	5							13.6				
796B-15R-2, 145-150	294.25	12	7.25	2.63	32.0	32.7	21.9	526	13.9	0.0	1470	385	1.49

bly responsible for the depletion in Mg and the increase in Ca. At Core 127-796A-24X (206 mbsf) the concentrations of Mg, sulfate, and Rb almost approach seawater values. However, ammonia, K, and Li do not follow this trend; K concentrations in particular should increase if seawater is introduced. Therefore, fluid-transport along tectonically active faults is unlikely, although it cannot be completely excluded.

Alkali metals display individually distinct concentration-depth profiles which are apparently controlled by alteration of ash-layers (Rb, Li?) or of basement rocks (K), as well as by silica transformation reactions (Li).

ORGANIC GEOCHEMISTRY

The shipboard organic geochemical analyses of sediment samples from Holes 796A and 796B included inorganic carbon; total carbon, nitrogen, and sulfur; Rock-Eval; and volatile hydrocarbon analyses. The procedures used for these determinations are outlined in the "Explanatory Notes" chapter (this volume), and background and detailed descriptions are given in Emeis and Kvenvolden (1986).

Carbon, Nitrogen, and Sulfur

The concentrations of inorganic, total, and organic carbon in the sediments recovered from Site 796 are presented in Table 7. The percentage of calcium carbonate (%CaCO₃) was calculated from the inorganic carbon concentrations by assuming that all carbonate is in the form of calcite. Nitrogen concentrations above analytical detection are also included in Table 7 for all samples analyzed for total carbon. Total sulfur is reported for most of the samples; missing values denote samples for which inconsistent quantitation was observed.

Concentration of calcium carbonate in the sediments ranges from 0.1% to 55.1%. Most of the samples contain less than 1.0% calcium carbonate, which suggests that sediment deposition occurred mostly below the CCD. The concentrations of organic carbon (%C_{org}) in the whole sediments range from 0.02% to 4.0%, with most sediments containing less than 1.0% on a dry weight basis. The total nitrogen contents range from 0.01%

to 0.32% of the whole sediments on the same basis. Total sulfur concentrations in the sediments vary between 0.09% and 2.8%. The ratios of organic carbon to total nitrogen (C/N) and total sulfur (C/S) range from 2.0 to 68 and 0.07 to 2.5, respectively.

The %CaCO₃, %C_{org}, and C/N ratio values are plotted against subbottom depth in Figure 28. The highest concentrations of carbonates (11%–55%) occur above 70 mbsf in the Quaternary and below 300 mbsf. In the section between, carbonates are present at trace levels, usually less than 0.4%, with a few exceptions (2.1%–4.7%) at approximately 70 and 180 mbsf. The sporadic occurrences of high carbonate content over narrow intervals may be authigenic in nature, although increased preservation of biogenic carbonate must also be considered.

The downhole distribution of organic carbon in the sediments at Site 796 is characterized by predominantly low values of less than 1.0%, with no apparent relationship between carbonate and organic carbon content. Low concentrations of organic carbon are especially prevalent in the sediments below 70 mbsf. These upper Miocene through upper Pliocene sediments average 0.48% C_{org}. The Quaternary sediments above 70 mbsf vary much more in organic carbon content with concentrations between 0.34% and 4.0% and with an average of 1.2%. The top 50 m of this Quaternary section are dominated by diatom-bearing clays and silty clays with variable bioturbation (see "Lithostratigraphy" section, this chapter). The occasional intervals of relatively high organic matter are correlated with the darker-colored bands and the presence of scattered pyrite in the diatom-bearing clays. The decrease in the average C_{org} at the bottom of this section may be a reflection of an increase in the abundance of thin sand beds (see "Lithostratigraphy" section, this chapter). The increased concentrations of organic carbon in the upper Quaternary sediments represent periods of increased productivity and/or preservation related to short-term anoxic events or rapid burial. Redeposition of organic-rich sediments from oxygen-deficient or more productive marginal areas upslope by slumping and turbidite flows is also suggested. The low organic carbon contents below 70 mbsf indicate deposition under well-oxygenated conditions in the bottom waters.

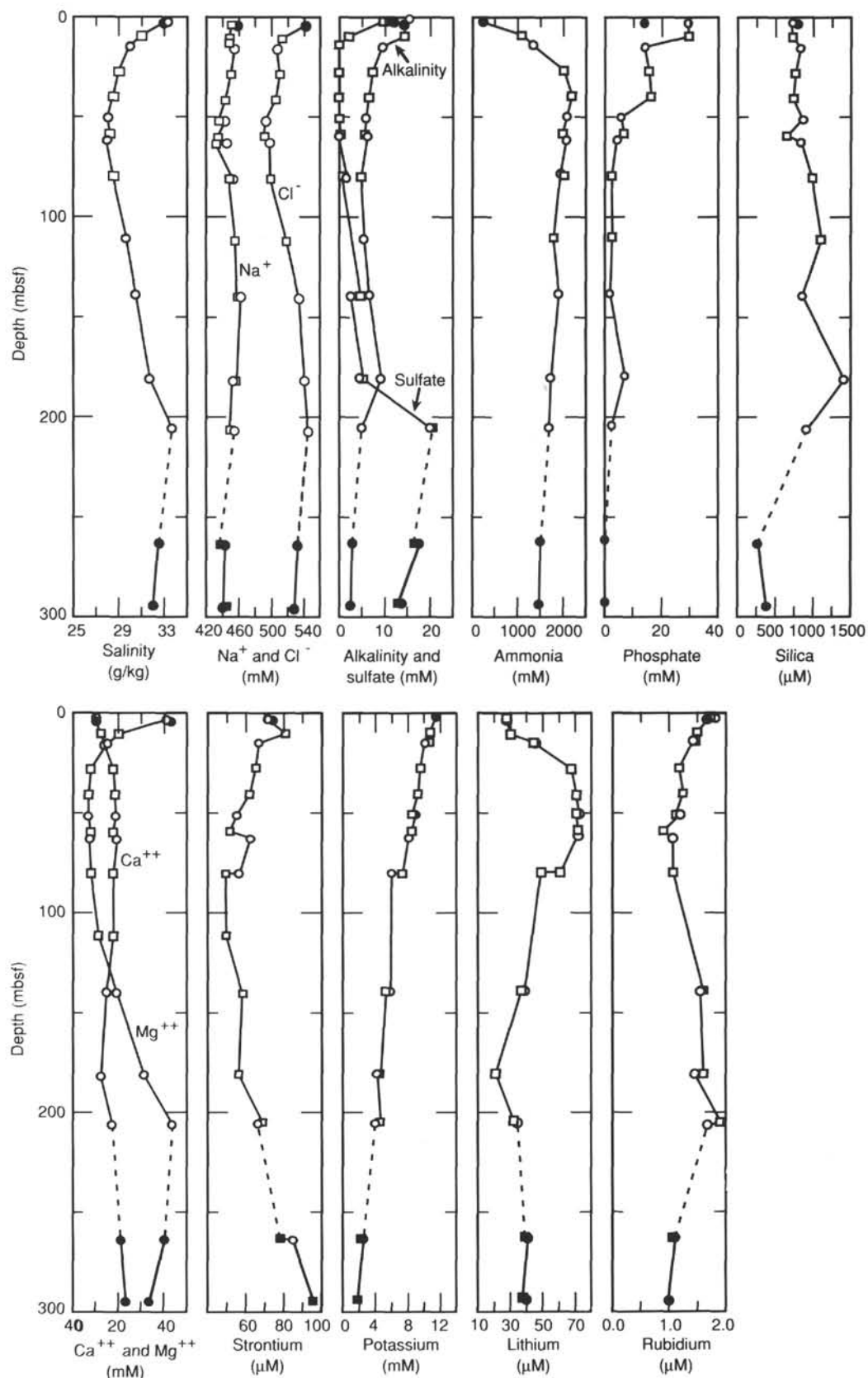


Figure 27. Depth profiles of salinity, sodium, chloride, sulfate, alkalinity, ammonia, phosphate, silica, calcium, magnesium, strontium, potassium, lithium, and rubidium. Dashed line indicates that profiles from Holes 796A and 796B may not be continuous. Circles: ODP squeezer. Squares: Brumsack squeezer. Open symbols for Hole 796A, solid symbols for Hole 796B.

Table 6. Comparison of the chemical composition of seawater, clathrate-water, and interstitial water.

Element		A	B	C	D
		Seawater Bruland (1983)	Clathrate-water Core 12X Hole 796A	Interstitial water Core 11X Hole 796A	Clathrate-water Site 540 Brooks et al. (1985)
Salinity	g/kg	35.0	10.0	28.6	2.6
Cl	mol/L	0.55	0.18	0.50	0.02
Na	mol/L	0.47	0.16	0.45	0.03
Mg	mmol/L	53.0	5.3	6.2	1.8
SO ₄	mmol/L	28.0	3.8	0.9	8.3
Ca	mmol/L	10.0	4.2	16.4	3.5
K	mmol/L	10.0	3.1	7.5	2.0
Si	mmol/L	0.10	0.56	1.00	0.20
NH ₄	mmol/L	0.00	0.88	2.00	n.d.
Li	μmol/L	25	18	62	14
PO ₄	μmol/L	2.0	2.0	2.5	n.d.
Rb	μmol/L	1.4	0.7	1.1	n.d.

The extent of downhole variability in the C/N ratio tends to mirror the fluctuations in organic carbon content in the top 350 m of sediments at Site 796 (Fig. 28). In the uppermost Pliocene through Quaternary sediments, the C/N values range between 2.9 and 68 with an average of 9.9. Below these sediments, the values drop slightly to a range between 0.60 and 7.6 with an average of 5.4. This slight trend of decreasing values with depth in this section is interrupted by a return to isolated higher values of greater than 14 below 350 mbsf. These two high ratios occur at depths with a significant carbonate component.

It is generally accepted that C/N values are higher for terrestrial- than for marine-sourced organic matter (e.g., Calvert, 1983). Except for values of 68 and 27 at about 33.8 mbsf, the C/N ratios for sediments at Site 796 are either within or below the range normally found in modern marine sediments (9–18; Müller, 1977). Since the nitrogen component of this ratio includes both organic and inorganic forms, inorganic nitrogen in clay-rich, low-organic carbon sediments can significantly decrease the ratios (Müller, 1977; Waples, 1985). Waples (1985) reported that inorganic nitrogen is the dominant form in Goban Spur (SDP Leg 80) sediments containing less than 0.50% C_{org}. Interpretations of the downhole changes in C/N ratios in Figure 28 are therefore difficult to make due to the abundance of clays and the low organic carbon contents in Site 796 sediments.

Rock-Eval Analysis

A limited number of sediments from Site 796 were analyzed for total organic carbon (TOC), source character, and thermal maturity and hydrocarbon potential using the Rock-Eval instrument. The resulting values are presented in Table 8. Interpretations of source and maturity based solely upon these parameters are unwarranted due to the instrumental instabilities and character of the sediments from the Sea of Japan, previously discussed (see "Organic Geochemistry" section, "Site 794" chapter, this volume). However, general trends in the composition of organic matter can be inferred.

Total Organic Carbon

The sediment concentrations of TOC determined by Rock-Eval range from 0.02% to 1.8%. These values compare well with the %C_{org} values determined by difference (cf., Tables 7 and 8). When results from these two methods differ, the TOC values determined by Rock-Eval are usually slightly lower. As the Rock-Eval TOC determinations are conducted by pyrolysis at only 600°C, the underestimations may be due to incomplete combustion, as can occur with very mature samples (Emeis and Kvenvolden, 1986; Peters, 1986). This inference is supported by the occasionally high T_{max} values (see following discussion and Table 8).

Source Character

The S₂ and S₃ values represent the amount of hydrocarbons and carbon dioxide, respectively, that can be released from the kerogen (i.e., insoluble organic matter) during pyrolysis or thermal maturation of whole sediments. When normalized to the amount of organic carbon in the sediments, the new parameters of hydrogen index (HI) and oxygen index (OI) provide an estimate of the organic type (Espitalié et al. 1977). For the sediments at Site 796, these indices were determined using the TOC values from the Rock-Eval analysis. Unlike Sites 794 and 795, the sediments at Site 796 are characterized predominantly by very low oxygen indices. In consideration of the inherent problems associated with measuring S₃ (see "Organic Geochemistry" section, "Site 794" chapter, this volume), replicate analyses were conducted which showed that the values tabulated in Table 8 were reproducible within the precision of the instrument.

The hydrogen and oxygen indices approximate the H/C and O/C ratios of the kerogen. A van Krevelen-type plot of the HI and OI values for sediments at Site 796 is presented in Figure 29. Based on the sample distributions in this plot, the organic contents of these sediments appear to be primarily Type I algal with a few samples of mixed marine/terrestrial origin (Type II and III). One sample has an OI above 300 and is not included in this plot. In general, the oxygen indices above 150 suggest inputs of highly oxidized and reworked/recycled organic matter to the sediments.

Thermal Maturity

The T_{max} values for the sediments from Site 796 range from 373° to 583°C. Most of the sediments are interpreted to be thermally immature, with a few near the onset of oil generation. Although T_{max} values above 500°C are often associated with highly recycled organic matter, adsorption of the pyrolysate onto clay-dominated sediments can also significantly increase the values (Peters, 1986). The pyrograms of the Site 796 samples that have high T_{max} values occasionally contain well-resolved multiple S₂ peaks, which suggest multiple inputs that include a recycled component. Other samples with high T_{max} values have pyrograms in which the S₂ peaks are broad, partially-resolved and sloping humps. This pattern suggests that the clay-induced adsorption of the pyrolysates also contributes to the erroneously high T_{max} values for some of the sediments from Site 796. Elemental analysis of purified kerogen isolates would resolve these factors and, thereby, clarify the sources and quality of the organic matter in the sediments of the Japan Sea.

Volatile Hydrocarbons

The gas contents in the shallow sediments of Site 796 were the highest found at any of the sites in the Sea of Japan during

Table 7. Concentrations of inorganic and organic carbon and total nitrogen and sulfur at Site 796.

Hole, core, section, interval (cm)	Depth (mbsf)	Total carbon (%)	Inorganic carbon (%)	Organic carbon (%)	CaCO ₃ (%)	Nitrogen (%)	Sulfur (%)	C _{org} /N	C _{org} /S
127-									
796A-1H-1, 58-61	0.58	0.47	0.08	0.39	0.7	0.07	1.90	5.60	0.21
796A-1H-1, 64-67	0.64	2.63	0.05	2.58	0.4	0.24	2.79	10.70	0.93
796A-1H-2, 40-42	1.90	1.92	0.07	1.85	0.6	0.18	2.05	10.30	0.90
796A-1H-2, 55-60	2.05	0.69	0.07	0.62	0.6	0.08	1.74	7.70	0.36
796A-1H-3, 0-5	2.10	0.44	0.08	0.36	0.7	0.06	1.27	6.00	0.28
796B-1R-2, 145-150	2.95	0.66	0.05	0.61	0.4	0.09		6.80	
796A-2H-5, 0-5	9.20	1.34	0.08	1.26	0.7	0.14	1.24	9.00	1.01
796A-2H-5, 100-101	10.20	0.70	0.05	0.65	0.4	0.09	1.34	7.20	0.49
796A-3H-1, 123-126	13.93	6.27	3.35	2.92	27.9	0.20	1.48	14.60	1.97
796A-3H-1, 145-150	14.15	2.12	0.02	2.10	0.2	0.17	2.63	12.30	0.80
796A-3H-2, 0-5	14.20	0.59	0.01	0.58	0.1	0.09	1.39	6.40	0.42
796A-3H-2, 80-81	15.00	2.44	1.40	1.04	11.7	0.11	2.21	9.45	0.47
796A-3H-3, 39-40	16.09	2.76	1.59	1.16	13.2	0.08		14.50	
796A-3H-3, 43-44	16.13	5.81	3.84	1.97	32.0	0.10		19.70	
796A-3H-3, 44-46	16.14	0.88	0.19	0.69	1.6	0.06		11.00	
796A-4H-2, 13-17	23.83	3.12	0.06	3.06	0.5	0.29	2.36	10.50	1.29
796A-4H-2, 109-111	24.79	1.25	0.91	0.34	7.6	0.07	1.09	4.80	0.31
796A-4H-4, 0-5	26.70	0.47	0.07	0.40	0.6	0.08	1.76	5.00	0.23
796A-4H-5, 109-111	29.29	0.54	0.02	0.52	0.2	0.10	0.62	5.20	0.84
796B-3R-1, 34-36	30.54	4.06	0.05	4.01	0.4	0.32	2.37	12.50	1.69
796A-4H-7, 60-62	31.80	2.83	0.04	2.79	0.3	0.19		14.70	
796B-3R-2, 99-101	32.69		0.10		0.8				
796B-3R-3, 0-3	33.20		0.11		0.9				
796A-5H-2, 53-56	33.73	0.82	0.14	0.68	1.2	0.01		68.00	
796A-5H-2, 56-60	33.76	3.64	0.12	3.52	1.0	0.13		27.10	
796A-5H-2, 100-101	34.20	1.00	0.04	0.96	0.3	0.14	0.91	6.80	1.00
796A-5H-5, 100-101	38.70	0.58	0.10	0.48	0.8	0.10	1.37	4.80	0.35
796A-5H-6, 0-5	39.20	1.55	0.28	1.27	2.3	0.14	1.48	9.07	0.86
796A-6H-1, 32-34	41.52	3.43	0.24	3.19	2.0	0.27	2.59	11.80	1.23
796A-6H-1, 44-46	41.64	2.95	0.07	2.88	0.6	0.24	1.16	12.00	2.48
796B-4R-2, 100-102	42.30	0.72	0.13	0.59	1.1	0.10	1.42	5.90	0.42
796B-4R-3, 0-5	42.80		0.12		1.0				
796A-6H-2, 99-100	43.69	0.54	0.07	0.47	0.6	0.09	0.94	5.20	0.50
796B-4R-5, 109-111	46.89		0.06		0.5				
796A-6H-5, 129-131	48.49	0.58	0.07	0.51	0.6	0.10	1.28	5.10	0.40
796A-6H-6, 145-150	50.15	0.61	0.14	0.47	1.2	0.10	0.82	4.70	0.57
796A-6H-7, 0-5	50.20	0.54	0.07	0.47	0.6	0.10	1.20	4.70	0.39
796B-5R-2, 99-101	52.29	1.34	0.10	1.24	0.8	0.15	1.29	8.26	0.96
796B-5R-4, 0-5	54.30		0.03		0.2				
796B-5R-5, 35-36	56.15		2.05		17.1				
796A-8H-5, 0-5	57.70	0.49	0.06	0.43	0.5	0.09	1.33	4.80	0.32
796A-8H-5, 49-50	58.19	0.46	0.08	0.38	0.7	0.09	1.22	4.20	0.31
796B-6R-1, 100-101	60.50		0.09		0.7				
796B-6R-1, 147-150	60.97	0.45	0.07	0.38	0.6	0.09	1.19	4.20	0.32
796A-9X-2, 140-145	61.60	0.74	0.14	0.60	1.2	0.10	1.48	6.00	0.41
796A-9X-3, 0-5	61.70	0.84	0.05	0.79	0.4	0.12	1.28	6.60	0.62
796A-9X-3, 79-80	62.49	0.80	0.25	0.55	2.1	0.10	1.59	5.50	0.35
796A-10X-1, 0-3	68.40	0.74	0.05	0.69	0.4	0.11	1.27	6.30	0.54
796A-10X-1, 60-62	69.00	0.75	0.03	0.72	0.3	0.12	1.00	6.00	0.72
796A-10X-1, 100-102	69.40	0.75	0.04	0.71	0.3	0.12	1.39	5.90	0.51
796B-7R-1, 100-101	70.10		0.25		2.1				
796B-7R-1, 120-123	70.30	1.49	0.05	1.44	0.4	0.16	1.33	9.00	1.08
796A-11X-2, 0-5	79.80	0.28	0.05	0.23	0.4	0.08	0.73	2.90	0.31
796A-11X-2, 100-101	80.80	0.89	0.03	0.86	0.2	0.13	0.76	6.60	1.10
796A-12X-5, 0-3	91.10	0.79	0.01	0.78	0.1	0.12	0.79	6.50	0.99
796A-12X-5, 80-82	91.90	0.94	0.02	0.92	0.2	0.12	0.98	7.60	0.94
796A-14X-2, 140-145	110.50	0.52	0.02	0.50	0.2	0.07		7.10	
796A-14X-3, 0-5	110.60	0.82	0.02	0.80	0.2	0.12	1.12	6.60	0.71
796A-14X-5, 50-51	114.10	0.37	0.03	0.34	0.2	0.07	0.37	4.80	0.92
796A-15X-2, 100-102	119.70	0.67	0.01	0.66	0.1	0.10	0.56	6.60	1.20
796A-15X-3, 0-3	120.20	0.13	0.02	0.11	0.2	0.03	0.32	3.60	0.34
796A-16X-2, 0-3	128.40	0.29	0.01	0.28	0.1	0.08	0.21	3.50	1.30
796A-16X-2, 98-100	129.38	0.60	0.01	0.59	0.1	0.08	0.65	7.40	0.91
796A-17X-2, 100-102	139.00	0.27	0.01	0.26	0.1	0.05	0.21	5.20	1.20
796A-17X-2, 145-150	139.45	0.17	0.04	0.13	0.3	0.04	3.20		
796A-18X-2, 99-101	148.69	0.52	0.04	0.48	0.3	0.10	0.77	4.80	0.62
796A-18X-5, 0-3	152.20	0.43	0.01	0.42	0.1	0.08	0.40	5.20	1.00
796A-19X-2, 0-3	157.30	0.75	0.01	0.74	0.1	0.10	0.70	7.40	1.00
796A-19X-2, 99-101	158.29	0.67	0.01	0.66	0.1	0.11	0.40	6.00	1.60
796A-20X-2, 0-3	166.80		0.01		0.1				
796A-20X-2, 50-51	167.30	0.70	0.02	0.68	0.2	0.10	0.39	6.80	1.70
796A-21X-2, 99-101	177.49	0.63	0.02	0.61	0.2	0.10	0.51	6.10	1.20
796A-21X-4, 145-150	180.95	1.19	0.56	0.63	4.7	0.10		6.30	
796A-21X-5, 0-3	181.00	0.84	0.25	0.59	2.1	0.09	0.94	6.50	0.63

Table 7 (continued).

Hole, core, section, interval (cm)	Depth (mbsf)	Total carbon (%)	Inorganic carbon (%)	Organic carbon (%)	CaCO ₃ (%)	Nitrogen (%)	Sulfur (%)	C _{org} /N	C _{org} /S
127- (Cont.)									
796A-22X-2, 98-101	187.18	0.39	0.01	0.38	0.1	0.06	0.73	6.30	0.52
796A-22X-2, 111-113	187.31	0.63	0.03	0.60	0.2	0.09	0.91	6.60	0.66
796A-22X-3, 0-3	187.70		0.03		0.2				
796A-23X-2, 100-101	196.90	0.85	0.04	0.81	0.3	0.12	1.51	6.70	0.54
796A-23X-5, 0-3	200.40	0.35	0.04	0.31	0.3	0.07	0.54	4.40	0.57
796A-24X-1, 145-150	205.55	0.54	0.04	0.50	0.3	0.07		7.10	
796A-24X-2, 0-3	205.60	0.57	0.03	0.54	0.2	0.08	1.11	6.70	0.49
796A-24X-2, 38-40	205.98	0.39	0.04	0.35	0.3	0.07	0.52	5.00	0.67
796A-25X-1, 99-101	214.79	0.59	0.03	0.56	0.2	0.10	0.39	5.60	1.40
796A-26X-2, 0-3	225.00	0.34	0.01	0.33	0.1	0.08	0.42	4.10	0.78
796A-26X-2, 87-88	225.87	0.49	0.02	0.47	0.2	0.09	0.61	5.20	0.77
796A-27X-1, 0-3	233.20	0.50	0.01	0.49	0.1	0.09	0.36	5.40	1.30
796A-27X-1, 40-41	233.60	0.53	0.03	0.50	0.2	0.10	0.47	5.00	1.00
796B-10R-1, 50-52	243.50	0.15	0.07	0.08	0.6	0.05	0.19	1.00	0.42
796B-11R-2, 0-3	254.20		0.02		0.2				
796B-11R-2, 93-94	255.13	0.40	0.02	0.38	0.2	0.09	0.51	4.20	0.74
796B-12R-1, 145-150	263.75	0.41	0.01	0.40	0.1	0.10		4.00	
796B-12R-3, 43-45	265.73	0.47	0.03	0.44	0.3	0.08	0.41	5.50	1.10
796B-14R-2, 25-27	283.35	0.69	0.02	0.67	0.2	0.10	1.03	6.70	0.65
796B-15R-2, 83-85	293.63	0.62	0.03	0.59	0.3	0.10	0.70	5.90	0.84
796B-15R-2, 145-150	294.25	0.50	0.02	0.48	0.2	0.10		4.80	
796B-17R-1, 142-144	312.12	1.50	1.35	0.15	11.3	0.04	0.09	3.70	1.60
796B-18R-5, 32-35	326.72	0.05	0.03	0.02	0.3	0.03	0.30	0.60	0.07
796B-19R-2, 46-48	331.96	0.44	0.04	0.40	0.3	0.08	0.95	5.00	0.42
796B-20R-1, 114-116	340.94	0.67	0.02	0.65	0.2	0.09	0.59	7.20	1.10
796B-21R-1, 26-28	348.96	0.76	0.02	0.74	0.2	0.10	0.67	7.40	1.10
796B-22R-1, 120-122	359.70	0.27	0.06	0.21	0.5	0.06	1.42	3.50	0.15
796B-23R-1, 13-15	368.23	5.95	5.52	0.43	46.0	0.03		14.00	
796B-24R-1, 15-17	377.95	0.57	0.04	0.53	0.3	0.09		5.90	
796B-25R-1, 127-129	388.67	0.53	0.05	0.48	0.4	0.08		6.00	
796B-26R-2, 44-46	399.04	0.18	0.06	0.12	0.5	0.06		2.00	
796B-27R-1, 58-60	407.38	0.76	0.04	0.72	0.3	0.12		6.00	
796B-28R-1, 25-27	416.75	7.22	6.61	0.61	55.1	0.04		15.00	
796B-29R-2, 57-58	428.27	0.15	0.06	0.09	0.5	0.05		2.00	

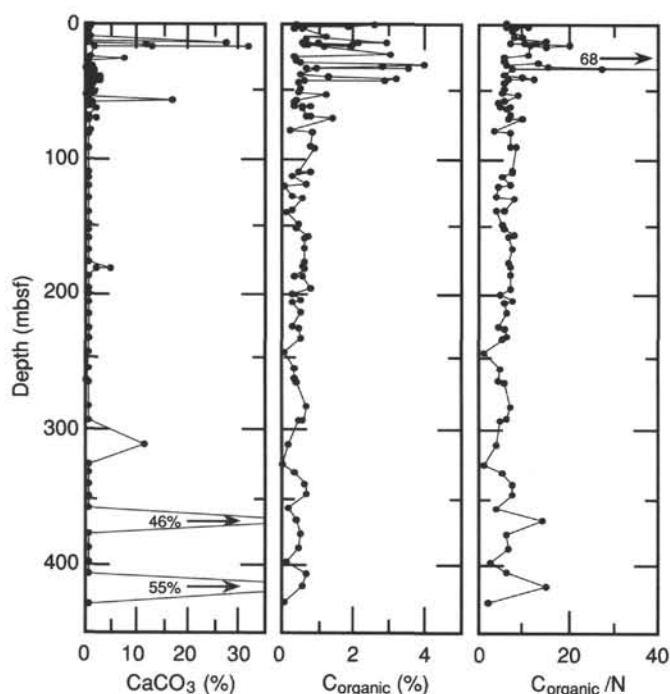


Figure 28. Downhole distribution of calcium carbonate and organic carbon concentrations as percentages of whole dry sediments, and ratio of organic carbon to total nitrogen in sediments at Site 796.

Leg 127. These high levels were readily apparent during core recovery. Extensive gas expansion in the core liners resulted in many voids, and both core liner caps and sediments were occasionally expelled onto the drill floor or core deck. As part of the shipboard safety and pollution monitoring program, the hydrocarbon contents of these gases were continuously measured in the sediments at Site 796 with the headspace technique and with sampling of gas voids by vacutainer. Significantly high levels of volatile hydrocarbons, predominantly methane, were detected. The headspace and vacutainer results are presented in Tables 9 and 10, respectively.

Methane concentrations in the headspace volumes of sediments range between 5 and 79,000 ppm, while ethane concentrations are between 1 and 12 ppm. While no propane was found in the headspace volumes, traces of ethylene and occasionally acetylene were detected; the sources of which are unknown. For headspace samples which contain ethane, the methane to ethane ratios (C_1/C_2) vary between 25 and 7,800. The low values pertain to samples with methane concentrations below 200 ppm and were not considered to be significant from a safety perspective.

The vacutainer samples are predominantly methane with concentrations between 7,300 and 820,000 ppm; ethane levels vary between 8 and 421 ppm. No higher molecular weight hydrocarbons were detected in these samples. The C_1/C_2 ratios for the vacutinners range between 1,200 and 5,400.

The concentrations of methane and ratios of C_1/C_2 in both headspace and vacutainer samples are plotted vs. depth at Site 796 (Holes 796A and 796B) in Figure 30. The concentrations of methane in the vacutinners is consistently higher than those in the comparable headspace samples, although no significant dif-

Table 8. Results of Rock-Eval analysis for Site 796.

Hole, core, section, interval (cm)	Depth (mbsf)	S ₁ (mg/g)	S ₂ (mg/g)	S ₃ (mg/g)	TOC (%)	PC	HI	OI (°C)	T _{max}	PI	S ₂ /S ₃
796A-1H-2, 55-60	2.05	0.11	2.60	0.03	0.63	0.22	412	4	458	0.04	86.66
796B-1R-2, 145-150	2.95	0.07	1.33	0.01	0.52	0.11	255	1	456	0.05	
796A-3H-1, 145-150	14.15	0.44	2.96	3.62	1.82	0.28	162	198	400	0.13	0.81
796A-6H-6, 145-150	50.15	0.02	0.87	0.21	0.39	0.07	223	53	583	0.02	4.14
796A-9X-2, 140-145	61.60	0.03	0.93	0.00	0.55	0.08	169	0	525	0.03	
796B-7R-1, 120-123	70.30	0.15	3.08	0.48	1.43	0.26	215	33	456	0.05	6.41
796A-14X-2, 140-145	110.50	0.07	1.63	0.00	0.75	0.14	217	0	581	0.04	
796A-16X-2, 0-3	128.40	0.02	1.83	0.01	0.30	0.15	610	3	522	0.01	
796A-17X-2, 145-150	139.45	0.00	0.91	0.00	0.16	0.07	568	0	541	0.00	
796A-21X-4, 145-150	180.95	0.00	0.21	1.32	0.43	0.01	48	306	395	0.00	0.15
796A-24X-1, 145-150	205.55	0.02	0.89	0.01	0.44	0.07	202	2	575	0.02	89.00
796A-26X-2, 0-3	225.00	0.00	1.03	0.00	0.29	0.08	355	0	535	0.00	
796B-12R-1, 145-150	263.75	0.03	0.22	0.02	0.30	0.02	73	6	382	0.12	11.00
796B-14R-2, 25-27	283.35	0.01	0.36	0.00	0.54	0.03	66	0	373	0.03	
796B-15R-2, 145-150	294.25	0.07	0.49	0.03	0.42	0.04	116	7	356	0.12	16.33
796B-18R-5, 32-35	326.72	0.00	0.42	0.00	0.03	0.03	1400	0	559	0.00	
796B-21R-1, 26-28	348.96	0.03	0.70	0.01	0.64	0.06	109	1	409	0.04	70.00
796B-24R-1, 15-17	377.95	0.01	0.60	0.00	0.51	0.05	117	0	411	0.02	
796B-27R-1, 58-60	407.38	0.04	1.35	0.01	0.69	0.11	195	1	417	0.03	
796B-28R-1, 25-27	416.75	0.00	0.04	0.01	0.15	0.00	26	6	458	0.00	4.00
796B-29R-2, 57-58	428.27	0.02	0.54	0.01	0.08	0.04	675	12	573	0.04	54.00

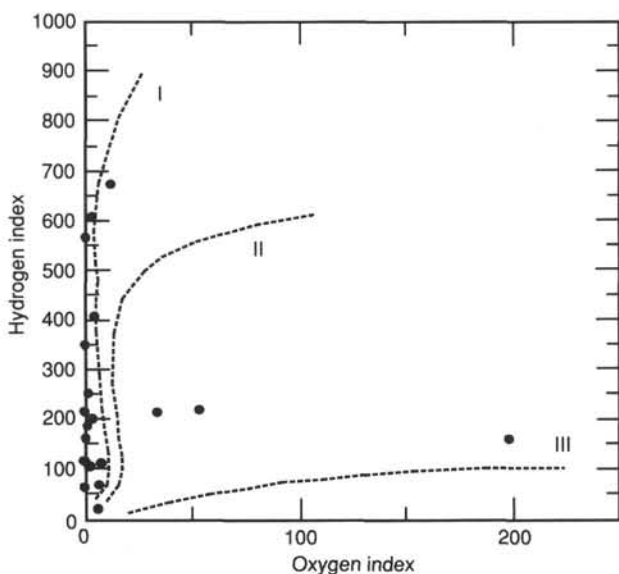


Figure 29. van Krevelen-type diagram of the hydrogen (HI) vs. oxygen (OI) indices of sediments from Site 796.

ference in the C_1/C_2 ratios between the two types of gas samples is evident. The downcore distribution of methane is highest in the top 175 m of sediment, where a C_1/C_2 ratio consistently above 1000 indicates a biogenic source. The microbial origin is also supported by pore-water sulfate profiles (see "Inorganic Geochemistry" section, this chapter) which show a rapid depletion to zero within the top 14 m of sediment. Sustained bacterial methanogenesis requires both metabolizable organic carbon and depleted sulfate levels, since methanogens are unable to effectively compete with the sulfate-reducing bacteria (Oremland and Taylor, 1978). The concentration of methane in the sediments rapidly decreases to low background levels at about 190 mbsf. A rapid increase in pore-water sulfate levels also occurs at this depth (see "Inorganic Geochemistry" section, this chapter). The low methane levels (4-33 ppm of headspace volume) between approximately 190 and 340 mbsf correspond with enhanced concentrations of sulfate, which would indicate conditions unfavor-

able for extensive methanogenesis. The organic matter in this section may have been too low in metabolizable components to sustain sulfate-reduction and the subsequent stage of methanogenesis. Alternatively, the regional uplift during the latest Pliocene (see site summary discussion at beginning of this chapter) could have resulted in an influx of seawater sulfate to the sediments in the section and a concomitant release of methane into the water column. Below this section, methane increases once again to levels comparable to those in the top 175 m. The C_1/C_2 ratios below 300 mbsf are slightly lower than those in the shallow sediments and possibly suggest a minor influx of thermogenic methane.

Gas Hydrates

Two samples of gas hydrates were recovered in sandy sediments from Hole 796B at approximately 90 mbsf. One sample was a clathrate containing sand grains and another an apparently pure white crystalline hydrate, each approximately 5 mL in volume. Both samples were immediately placed in headspace vials. After warming to room temperature and disappearance of the clathrate, headspace samples of each were analyzed. The methane and ethane data are included in Table 9 and plotted in Fig. 30.

The concentrations of methane in the headspace samples of the two hydrates are comparable and approximately four times higher than the highest concentration in headspace volumes from sediments. The C_1/C_2 ratios are also very similar (approximately 2900) and do not differ significantly from those in either the headspace or vacutainer samples.

The presence or stability of gas hydrates in sediments are a function mainly of pressure; temperature; and methane, water, and salt concentrations (Claypool and Kvenvolden, 1983). The temperature usually determines the base of the gas hydrate zone. The gas hydrates found at Site 796 appear to be very dispersed in the sediments, as no thick hydrate section was recovered and no bottom-simulating reflector (BSR) was apparent during surveying (see "Seismic Stratigraphy" section, this chapter). The gas hydrates are limited to the top 100-120 m of sediment due to the very high geothermal gradient of 178°C/km (see "Down-hole Measurements" section, this chapter) at this site. The apparently disseminated nature of the hydrates in the sandy layers above this depth results from the preferential accumulation of

Table 9. Hydrocarbon gas data for Site 796, headspace method.

Hole, core, section, interval (cm)	Depth (mbsf)	C ₁ (ppm)	C ₂ (ppm)	C ₃ (ppm)	C ₁ /C ₂
796A-1H-3, 0-3	2.10	25	1		25.00
796B-2W-3, 0-3	7.20	9100	6		1516.66
796A-2H-5, 0-3	9.20	24000	1		
796A-3H-2, 0-5	14.20	33000	1		
796A-4H-4, 0-5	26.70	7800	1		7800.00
796B-4R-3, 0-5	42.80	8900	3		2966.66
796A-6H-6, 0-5	48.70	6800	1		6800.00
796A-8H-5, 0-5	57.70	7600	1		7600.00
796B-6R-1, 147-150	60.97	8500	6		1416.66
796A-9X-3, 0-5	61.70	7400	1		7400.00
796A-10X-1, 0-3	68.40	53000	3		
796B-7R-01, 120-123	70.30	7300	6		1216.66
796A-11X-2, 0-5	79.80	7500	1		7500.00
*796A-12X-1, 0-1	88.10	370000	130		2846.15
*796A-12X-4, 147-150	91.07	290000	100		2900.00
796A-12X-5, 0-3	91.10	79000	12		6583.33
796A-14X-3, 0-5	110.60	8600	5		1720.00
796A-15X-3, 0-5	120.20	4600	1		4600.00
796A-16X-2, 0-3	128.40	10000	1		
796A-17X-3, 0-3	139.50	5800			
796A-19X-2, 0-3	157.30	43000	2		
796A-20X-2, 0-5	166.80	18000	1		
796A-21X-5, 0-5	181.00	181	1		181.00
796A-22X-3, 0-5	187.70	29	1		29.00
796A-23X-5, 0-3	200.40	9			
796A-24X-2, 0-5	205.60	33			
796A-26X-2, 0-3	225.00	5			
796A-27X-1, 0-3	233.20	4			
796B-11R-2, 0-3	254.20	29			
796B-12R-3, 0-3	265.30	6			
796B-16R-1, 0-3	301.00	6			
796B-17R-1, 0-3	310.70	13			
796B-18R-2, 0-3	321.90	13			
796B-20R-1, 0-3	339.80	1500	1		1500.00
796B-22R-1, 0-3	358.50	3600	3		1200.00
796B-31R-2, 0-3	437.40	8300	8	1	1037.50
796B-33R-3, 0-3	458.20	8200	16	1	512.50

* = headspace samples taken of the gas hydrates.

Table 10. Hydrocarbon gas data for Site 796, vacutainer method.

Hole, core, section, interval (cm)	Depth (mbsf)	C ₁ (ppm)	C ₂ (ppm)	C ₁ /C ₂
796B-2W-2, 40-40	6.10	9300	8	1162.50
796A-2H-6, 40-40	11.10	130000	3	
796A-3H-2, 30-30	14.50	750000	33	
796B-4R-3, 39-39	43.19	820000	240	3416.67
796B-5R-3, 70-70	53.50	670000	160	4187.50
796B-6R-1, 78-78	60.28	770000	420	1833.33
796A-9X-2, 10-10	60.30	810000	150	5400.00
796B-7R-1, 37-37	69.47	670000	250	2680.00
796A-12X-5, 116-116	92.26	770000	340	2264.71
796A-14X-2, 126-126	110.36	790000	180	4388.89
796A-14X-4, 80-80	112.90	830000	200	4150.00
796A-15X-3, 25-25	120.45	780000	69	
796A-16X-1, 85-85	127.75	520000	31	
796A-17X-3, 75-75	140.25	7300		

the methane in these layers as well as from the increased pore spaces available for clathrate growth.

PHYSICAL PROPERTIES

Introduction

A full program of physical property measurements was carried out for the Site 796 cores, as described in the "Explanatory Notes" chapter (this volume). The magnetic susceptibility, the

GRAPE density, and the *P*-wave velocity were measured on the multisensor track (MST). Index properties, thermal conductivity, formation factor, and the *P*-wave velocity were measured on discrete samples. All of the data from discrete samples and the processed *P*-wave logger data are sorted by depth (mbsf) and presented in Table 11 for Holes 796A and 796B. In addition, two of the index property samples from each core were analyzed for grain size, carbonate content, total organic carbon content, and X-ray diffraction (XRD) analysis. The lithology of Site 796 has some differences from the previous sites, Sites 794 and 795 (see "Lithostratigraphy" section, this chapter), which is reflected in the physical properties.

Data Quality

The *P*-wave logger on the MST has proved to be useful and important for the APC cores to correlate with the site survey seismic profiles. Unfortunately, we could not get *P*-wave data on the MST below 14 mbsf at this site because the cores had large amounts of gas that produced voids and gaps inside the liner and greatly attenuated the signal transmission. In the lithified part of the section, the *P*-wave velocity was measured on the Hamilton Frame. In addition, the *P*-wave velocity profile was obtained during downhole logging, which will fill the gaps in the shipboard data and which will be discussed below (see also "Downhole Measurements" section, this chapter).

The formation factor determinations, which involve measurements of the resistivity of the core, have far less scatter than at the previous sites. This probably stems from improvements in the technique to measure the seawater reference. At this site, the

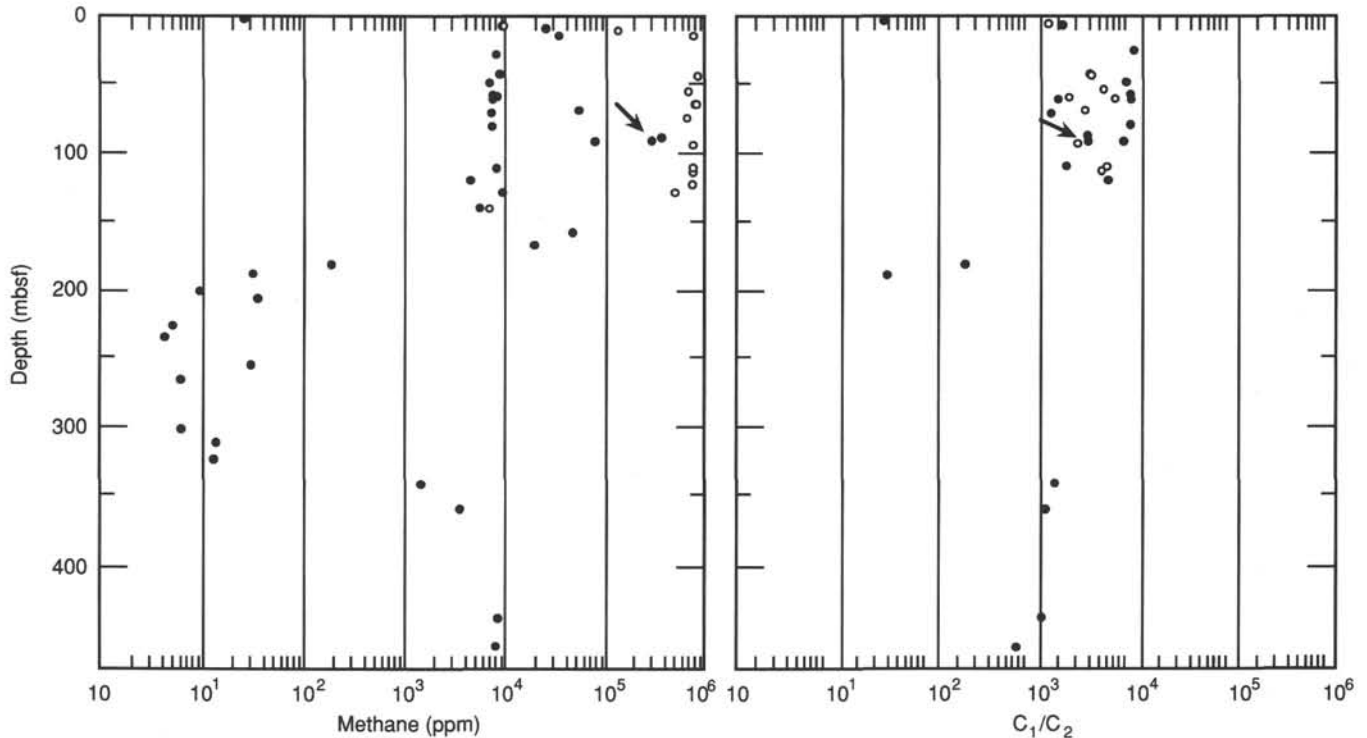


Figure 30. Downhole concentrations of methane (ppm) and ratio of methane to ethane (C_1/C_2) in both headspace and vacutainer samples. Dots refer to headspace samples and crosses refer to vacutainer samples. Arrows indicate data points for the two gas hydrate samples.

resistivity measurements were made in the undisturbed and unconsolidated cores from 0 to 161 mbsf.

As described in the Site 794 and 795 summaries, some physical properties may be altered from their *in situ* condition in the XCB section. However, it is difficult to identify the effect of the XCB disturbance from the physical properties data of this site. There are no significant changes in the physical properties around the boundary between the APC and the XCB cores. Hole 796B was drilled by rotary coring from 0 to 98 mbsf and from 243 mbsf to the bottom of hole. The data from the rotary coring show more scattering as compared with the data from the APC and the XCB cores. It is suggested that the disturbance effect of the rotary coring is slightly greater than the APC and the XCB coring for shallow drilling.

Physical Properties and Correlation with Lithostratigraphy

In this section, we describe the physical properties of all recovered sedimentary sections, and briefly discuss the correlation with the lithological units. Plots of the principal physical properties vs. depth are presented in Figures 31–37. The first order statistics for each of the major lithostratigraphic units are presented in Tables 12 through 16.

Unit I (0–146 mbsf) is divided into two subunits based on the appearance of medium- to coarse-grained volcanic sand. Unit IA (Quaternary) is unconsolidated clay and/or silty clay with diatoms. Unit IB (early to late Pliocene) is composed of an unconsolidated diatomaceous clay and volcanic sand. Overall the index properties do not show a significant change with depth in Unit I. The standard deviations, which are representative of the variations in the physical properties, are smaller than those of the other units. Figure 35 shows the relationship between the porosity and the formation factor. These two indicators are inversely correlated. This character is closely related with the lithology which is composed of ash layers and ashy silty clay.

Unit IA, however, still exhibits a high porosity because the depth is shallow, and the unit has not had sufficient time for consolidation. Wet bulk density and the grain density change little in Unit IB. Porosity and water content slightly decrease with depth, on average, due to increasing overburden pressure. Thermal conductivity decreases approximately linearly with depth from 0 to 120 mbsf. It may be concordant with the character of the porosity and the water content.

Unit II (146–224 mbsf; early Pliocene to late Miocene) is mainly composed of diatomaceous clay and/or claystone. The middle to lower part of this unit includes sand and pebbles (see “Lithostratigraphy” section, this chapter). As suggested for the Sites 794 and 795, the grain density and the wet bulk density vary with the diatom content. The mean values of bulk density, 1.60 g/cm^3 , and grain density, 2.42 g/cm^3 , are the lowest measured in the entire section. As pointed out in the Site 795 summary, the high diatom content closely relates to the strength of the sediments. Because of this, the porosity and the water content maintain relatively high values from Unit I to Unit II. The relative diatom volume has a peak at around 150–160 mbsf based on the smear slide observations (see “Lithostratigraphy” section, this chapter). Wet bulk density and grain density reach a minimum at around this depth. This behavior is very similar to that observed at Sites 794 and 795. Porosity and water content, however, maintain a high value down to approximately 200 mbsf, but at the same time decrease slightly with depth to 200 mbsf. The mean values of the porosity and the water content are approximately 15%–20% lower than at the previous two sites. Thermal conductivity gradually increases with depth below 120 mbsf. These are significant changes from the profiles at the previous two sites. At Sites 794 and 795, the physical properties were uniform almost to 300 mbsf, the opal-A/opal-CT boundary, where sharp changes then occurred.

Unit III (224–301 mbsf; late Miocene) comprises claystone and siliceous claystone with turbiditic sands. The boundary be-

Table 11. Physical properties data, Site 796.

Core, section, interval (cm)	Depth (mbsf)	Densities				Porosity (%)	Water content (%)	Void ratio	Water ratio	Velocity (m/s)			Thermal conductivity (W/m · K)	Formation factors			Anisotropy
		Wet bulk (g/cm ³)	Dry bulk (g/cm ³)	Grain (g/cm ³)						A	B	C		H	V	Mean	
127-796A-																	
1H-1, 100-102	1.00	1.60	0.84	2.54	73.6	47.2	2.79	0.89				0.879	2.30	2.21	2.25	0.98	
1H-2, 40-42	1.90	1.53	0.74	2.58	77.2	51.7	3.39	1.07				0.940	2.32	2.31	2.31	1.00	
1H-3, 50-52	2.60	1.53	0.76	2.55	75.3	50.6	3.05	1.02				0.923	2.23	2.43	2.33	1.04	
2H-1, 100-102	4.20	1.59	0.81	2.70	76.3	49.0	3.21	0.96				0.805	2.48	2.40	2.44	0.98	
2H-2, 100-102	5.70	1.64	0.78	2.59	83.8	52.3	5.18	1.10				1.060	3.25	2.86	3.05	0.94	
2H-3, 100-102	7.20	1.63	0.90	2.64	71.6	44.9	2.52	0.81				0.876	2.58	2.40	2.49	0.96	
2H-4, 100-102	8.70	1.55	0.77	2.53	76.4	50.5	3.24	1.02				0.857	2.89	2.81	2.85	0.99	
2H-5, 100-102	10.20	1.57	0.80	2.65	75.6	49.3	3.09	0.97				0.984	2.82	2.73	2.77	0.98	
2H-6, 100-102	11.70	1.70	1.04	2.67	65.0	39.1	1.86	0.64				0.907	3.04	3.66	3.34	1.10	
3H-1, 110-112	13.80	1.59	0.86	2.59	71.5	45.9	2.51	0.85				0.959	3.00	2.94	2.97	0.99	
3H-2, 80-82	15.00	1.64	0.91	2.81	71.4	44.6	2.49	0.81				0.987					
3H-3, 37-39	16.07	1.66	0.97	2.61	67.6	41.8	2.08	0.72					2.93	2.93	2.93	1.00	
4H-1, 110-112	23.30	1.57	0.81	2.62	74.5	48.7	2.92	0.95					3.33	3.28	3.30	0.99	
4H-2, 110-112	24.80	1.71	1.02	2.69	67.0	40.3	2.03	0.67			0.843	0.939	2.96	3.03	2.99	1.01	
4H-3, 100-102	26.20	1.65	0.94	2.61	69.0	42.9	2.22	0.75				0.868	2.92	2.89	2.90	0.99	
4H-4, 100-102	27.70	1.59	0.82	2.56	75.6	48.6	3.10	0.95									
4H-5, 110-112	29.30	1.62	0.90	2.50	70.3	44.4	2.37	0.80									
4H-6, 90-92	30.60	1.52	0.73	2.48	77.4	52.2	3.43	1.09									
5H-1, 104-106	32.74	1.61	0.84	2.67	75.0	47.8	2.99	0.92					2.85	3.03	2.94	1.03	
5H-2, 100-102	34.20	1.62	0.87	2.51	73.7	54.0	2.80	1.17			0.937	0.937	2.85	2.99	2.92	1.02	
5H-3, 100-102	35.70	1.50	0.69	2.39	79.0	54.0	3.75	1.17			0.780	0.780	3.04	3.17	3.10	1.02	
5H-4, 5-7	36.25	1.76	1.06	2.54	68.5	39.9	2.17	0.67									
5H-5, 100-101	38.70	1.77	1.06	2.59	69.1	39.9	2.24	0.67			0.908	0.908	3.03	3.17	3.10	1.02	
5H-6, 100-102	40.20	1.76	1.09	2.58	65.4	38.1	1.89	0.62			1.130	1.130					
6H-1, 30-32	41.50	1.59	0.84	2.52	73.1	47.2	2.71	0.90					3.08	3.36	3.22	1.04	
5H-8, 10-12	42.30	1.60	0.85	2.54	73.7	47.2	2.81	0.89					2.80	2.87	2.83	1.01	
6H-2, 100-102	43.70	1.71	1.00	2.62	69.3	41.5	2.26	0.71			1.033	1.033	3.38	3.73	3.55	1.05	
6H-3, 110-112	45.30	1.58	0.80	2.67	76.2	49.5	3.26	0.98									
6H-4, 100-102	46.70	1.61	0.83	2.81	76.0	48.3	3.17	0.93			0.918	0.918	3.51	4.05	3.77	1.07	
6H-5, 130-132	48.50	1.60	0.82	2.63	75.7	48.6	3.12	0.95									
6H-6, 100-102	49.70	1.64	0.89	2.54	73.5	45.8	2.77	0.85			0.956	0.956	3.08	3.84	3.44	1.12	
6H-7, 100-101	51.20										0.967	0.967					
6H-7, 120-122	51.40	1.64	0.92	2.51	70.5	44.2	2.40	0.79									
8H-5, 25-26	57.95										0.938	0.938					
8H-5, 49-51	58.19	1.65	0.94	2.61	68.9	42.8	2.22	0.75					3.05	2.82	2.93	0.96	
8H-5, 75-76	58.45										0.772	0.772					
9X-1, 100-102	59.70	1.56	0.77	2.65	76.5	50.4	3.26	1.02			0.799	0.799	2.77	2.54	2.65	0.96	
9X-2, 50-51	60.70										0.821	0.821					
9X-3, 79-81	62.49	1.66	0.95	2.68	69.2	42.7	2.24	0.75					3.13	3.06	3.09	0.99	
9X-3, 100-101	62.70										0.883	0.883					
10X-1, 50-51	68.90										0.891	0.891					
10X-1, 100-102	69.40	1.62	0.86	2.65	74.2	47.0	2.88	0.89					3.01	3.10	3.05	1.01	
11X-1, 100-102	79.30	1.61	0.84	2.47	75.1	47.9	3.02	0.92			0.882	0.882	2.71	2.73	2.72	1.00	
11X-2, 100-102	80.80	1.51	0.76	2.35	73.5	49.9	2.77	1.00			0.808	0.808	3.25	2.99	3.12	0.96	
12X-1, 36-38	88.46	1.76	1.13	2.72	61.7	35.9	1.61	0.56									
12X-1, 100-101	89.10										0.831	0.831					
12X-5, 80-82	91.90	1.62	0.85	2.51	75.3	47.5	3.05	0.91					3.24	3.49	3.36	1.04	
12X-5, 100-101	92.10										0.812	0.812					
12X-6, 100-102	93.60	1.47	0.69	2.50	76.5	53.2	3.25	1.14			0.801	0.801	2.92	3.09	3.00	1.03	
12X-7, 34-36	94.44	1.62	0.86	2.39	73.8	46.8	2.82	0.88									
12X-7, 50-51	94.60										0.834	0.834					
14X-1, 100-102	108.60	1.60	0.88	2.58	70.3	45.0	2.36	0.82			0.785	0.785	3.11	2.87	2.99	0.96	
14X-2, 60-62	109.70	1.56	0.81	2.57	72.8	47.8	2.67	0.92			0.919	0.919	3.33	3.54	3.43	1.03	
14X-3, 100-102	111.60	1.73	1.11	2.55	60.2	35.6	1.51	0.55			0.814	0.814	3.61	4.14	3.87	1.07	
14X-4, 110-112	113.20	1.71	1.05	2.58	64.2	38.4	1.79	0.62			0.895	0.895	4.29	4.77	4.52	1.05	
14X-5, 50-52	114.10	1.86	1.32	2.51	53.0	29.2	1.13	0.41									
15X-1, 100-102	118.20	1.60	0.89	2.60	69.7	44.5	2.30	0.80			0.767	0.767	4.86	4.64	4.75	0.98	
15X-2, 100-102	119.70	1.58	0.85	2.57	71.9	46.5	2.56	0.87			0.763	0.763	2.84	3.62	3.21	1.13	
15X-3, 100-102	121.20	1.58	0.85	2.61	70.6	45.9	2.40	0.85			0.786	0.786	4.38	3.81	4.09	0.93	
15X-4, 58-60	122.28	1.59	0.87	2.53	70.5	45.5	2.39	0.84			0.831	0.831	4.73	5.76	5.22	1.10	
16X-1, 98-100	127.88	1.54	0.81	2.49	71.4	47.6	2.50	0.91			0.838	0.838	2.96	2.89	2.92	0.99	
16X-2, 98-100	129.38	1.63	0.96	2.51	65.2	41.0	1.88	0.70			0.848	0.848	3.05	2.77	2.91	0.95	
17X-1, 100-102	137.50	1.64	0.93	2.51	68.8	43.0	2.20	0.76			0.947	0.947					
17X-2, 100-102	139.00	1.91	1.40	2.65	49.5	26.5	0.98	0.36			0.969	0.969					
17X-3, 105-107	140.55	1.57	0.84	2.51	71.0	46.4	2.44	0.87			0.774	0.774					
17X-4, 100-102	142.00	1.50	0.73	1.84	75.4	51.5	3.06	1.06			0.823	0.823					
18X-1, 99-101	147.19	1.52	0.87	2.35	70.5	45.5	2.39	0.83									
18X-2, 99-101	148.69	1.77	1.05	2.52	70.3	40.7	2.36	0.69			0.979	0.979	3.79	3.34	3.56	0.94	
18X-3, 99-101	150.19	1.56	0.81	2.46	72.9	48.0	2.68	0.92					3.42	3.74	3.58	1.05	
18X-4, 99-101	151.69	1.58	0.85	2.36	71.2	46.1	2.47	0.86			0.771	0.771	4.41	4.25	4.33	0.98	
18X-5, 99-101	153.19	1.58	0.87	2.37	69.5	45.0	2.28	0.82					2.66	2.61	2.63	0.99	
18X-6, 99-101	154.69	1.60	0.90	2.44	68.2	43.8	2.15	0.78			0.919	0.919					
19X-1, 99-101	156.79	1.50	0.76	2.31	72.6	49.5	2.65	0.98			0.775	0.775	2.43	2.51	2.47	1.02	
19X-2, 99-101	158.29	1.52	0.81	2.30	69.3	46.7	2.26	0.88			0.843	0.843	3.19	3.00	3.09	0.97	
19X-3, 99-101	159.79	1.62	0.90	2.35	70.8	44.7	2.42	0.81			0.800	0.800	4.74	4.53	4.63	0.98	
19X-4, 50-51	160.80										0.983	0.983					
19X-4, 98-100	161.28	1.62	0.93	2.43	66.8	42.3	2.01	0.73					5.82	3.97	4.81	0.83	
20X-1, 50-51	165.80										0.792	0.792					
20X-1, 100-102	166.30	1.46	0.68	2.23	75.9	53.1	3.15	1.13									
20X-2, 49-51	167.29	1.45	0.68	2.21	75.5	53.3	3.08	1.14			0.817	0.817					
21X-1, 100-102	176.00	1.99	1.48	2.66	49.4	25.5	0.98	0.34									
21X-2, 100-102	177.50	1.53	0.70	2.45	75.5	52.6	3.08	1.11			0.915	0.915					
21X-3, 100-102	179.00	1.52	0.77	2.44	73.5	49.6	2.78	0.99			0.797	0.797					

Table 11 (continued).

Core, section, interval (cm)	Depth (mbsf)	Densities				Porosity (%)	Water content (%)	Void ratio	Water ratio	Velocity (m/s)			Thermal conductivity (W/m · K)	Formation factors			
		Wet bulk (g/cm ³)	Dry bulk (g/cm ³)	Grain (g/cm ³)	A					B	C	H		V	Mean	Anisotropy	
127-796A- (Cont.)																	
21X-4, 100-102	180.50	1.68	1.03	2.56	63.5	38.7	1.74	0.63				0.920					
21X-5, 100-102	182.00	1.53	0.82	2.33	69.1	46.1	2.23	0.86				0.945					
21X-6, 50-52	183.00	1.54	0.82	2.38	70.4	46.8	2.38	0.88									
22X-1, 100-102	185.70	1.57	0.83	2.51	72.4	47.2	2.62	0.89				0.949					
22X-2, 100-102	187.20	1.85	1.31	2.54	52.7	29.1	1.11	0.41				0.867					
22X-3, 100-102	188.70	1.55	0.83	2.36	70.3	46.4	2.37	0.87									
22X-4, 100-102	190.20	1.53	0.74	2.55	77.0	51.5	3.36	1.05				0.874					
22X-5, 66-68	191.36	1.67	1.00	2.48	65.1	40.0	1.86	0.67									
23X-1, 100-102	195.40	1.66	0.97	2.45	67.1	41.5	2.04	0.71				0.913					
23X-2, 100-102	196.90	1.70	0.95	2.71	73.5	44.3	2.77	0.80									
23X-3, 100-102	198.40	1.66	0.96	2.45	68.3	42.1	2.15	0.73				0.980					
23X-4, 100-102	199.90	1.64	0.93	2.44	69.2	43.1	2.25	0.76				1.000					
23X-5, 100-101	201.40																
23X-5, 130-132	201.70	1.49	0.69	2.39	77.9	53.6	3.52	1.15	1663	1659	1644						
23X-6, 100-102	202.90	1.70	1.03	2.44	65.3	39.4	1.88	0.65									
24X-1, 100-102	205.10	1.79	1.19	2.55	58.5	33.5	1.41	0.50									
24X-2, 37-39	205.97	1.85	1.24	2.45	59.5	33.0	1.47	0.49									
25X-1, 45-46	214.25											0.953					
25X-1, 100-102	214.80	1.51	0.75	2.33	73.7	50.1	2.80	1.01				0.764					
26X-1, 80-81	224.30											1.176					
26X-1, 129-131	224.79	1.79	1.17	2.51	60.3	34.4	1.52	0.53									
26X-2, 86-88	225.86	1.84	1.25	2.41	58.1	32.3	1.39	0.48				1.091					
27X-1, 41-43	233.61	1.88	1.29	2.56	57.3	31.3	1.34	0.46									
127-796B-																	
1R-2, 60-62	2.10	1.62	0.82	2.57	77.5	49.1	3.44	0.97									
1R-3, 60-62	3.60	1.68	0.88	2.80	78.2	47.6	3.58	0.91									
3R-1, 100-102	31.20	1.59	0.80	2.39	77.0	49.7	3.34	0.99				0.833					
3R-2, 100-102	32.70	1.68	0.90	2.76	75.6	46.2	3.10	0.86				0.851					
3R-3, 100-102	34.20	1.61	0.81	2.58	78.2	49.7	3.59	0.99				0.945					
4R-1, 100-102	40.80	1.59	0.82	2.60	75.5	48.5	3.08	0.94				0.958					
4R-2, 100-102	42.30	1.55	0.76	2.51	76.8	50.8	3.30	1.03				0.827					
4R-3, 70-71	43.50											0.904					
4R-3, 92-94	43.72	1.46	0.64	2.45	80.1	56.1	4.02	1.28									
4R-4, 70-71	45.00											1.055					
4R-4, 100-102	45.30	1.72	1.03	2.60	67.5	40.1	2.08	0.67									
5R-1, 100-102	50.80	1.54	0.76	2.48	76.2	50.6	3.20	1.03				0.788					
5R-2, 100-102	52.30	1.64	0.86	2.77	75.9	47.5	3.14	0.90				0.938					
5R-3, 100-102	53.80	1.51	0.76	2.39	73.5	49.9	2.77	1.00				0.862					
5R-4, 100-102	55.30	1.64	0.87	2.55	74.6	46.7	2.94	0.88									
5R-5, 35-37	56.15	1.39	0.54	2.14	83.4	61.5	5.01	1.60									
6R-1, 100-102	60.50	1.63	0.92	2.60	69.7	43.9	2.30	0.78				0.913					
7R-1, 100-102	70.10	1.68	0.97	2.46	69.5	42.4	2.28	0.74				0.924					
10R-1, 50-52	243.50	1.79	1.16	2.57	61.9	35.4	1.62	0.55	2024	2110	2019	1.047					
11R-1, 27-29	252.97	2.59	2.38	2.73	20.3	8.0	0.25	0.09	4426	4210	4477	1.204					
11R-2, 93-95	255.13	1.94	1.43	2.47	49.8	26.3	0.99	0.36	1820	1903	1907	1.152					
12R-1, 59-61	262.89	2.00	1.49	2.57	50.0	25.7	1.00	0.35	1905	1975	1948	1.170					
12R-3, 44-46	265.74	1.86	1.33	2.44	52.1	28.7	1.09	0.40	1821	1951	1909	1.187					
12R-CC, 34-36	266.36	2.05	1.57	2.68	47.2	23.6	0.89	0.31	2359	2405	2420	1.162					
14R-1, 87-89	282.47	1.90	1.37	2.52	51.6	27.9	1.07	0.39	1857	1859	1847	1.168					
14R-2, 23-25	283.33	1.97	1.46	2.56	50.1	26.1	1.01	0.35	1834	1936	1929						
15R-1, 108-110	292.38	1.91	1.35	2.57	55.0	29.5	1.22	0.42	1837	1882	1837	1.196					
15R-2, 83-85	293.63	1.92	1.41	2.43	50.1	26.8	1.00	0.37	1974	2067	2026	1.163					
15R-2, 135-137	294.15								1954	1961	1976						
15R-3, 30-32	294.60	1.99	1.47	2.41	50.7	26.0	1.03	0.35									
16R-1, 5-7	301.05	2.07	1.39	2.90	66.3	32.8	1.97	0.49				1.025					
17R-1, 15-17	310.70											1931					
17R-1, 142-144	312.12	2.10	1.60	2.60	48.5	23.6	0.94	0.31	1868	1911	2031						
18R-1, 56-58	320.96								2126	2084	2089	1.112					
18R-1, 73-75	321.13	2.14	1.73	2.55	40.2	19.2	0.67	0.24	2278	2668	2651	1.404					
18R-2, 21-23	322.11	2.06	1.56	2.45	48.9	24.3	0.96	0.32	2024	2166	2119	1.296					
18R-3, 40-42	323.80	2.02	1.61	2.35	39.8	20.2	0.66	0.25				2592					
18R-3, 93-95	324.33	1.91	1.41	2.39	48.8	26.1	0.95	0.35		2100	2044	1.042					
18R-4, 18-20	325.08	1.98	1.43	2.52	53.5	27.6	1.15	0.38									
18R-5, 32-34	326.72	2.10	1.62	2.47	47.3	23.0	0.90	0.30	1952	1885		1.116					
19R-1, 43-45	330.43	2.66	2.53	2.68	12.7	4.9	0.14	0.05	4429	4506	4424	1.527					
19R-2, 46-48	331.96	2.16	1.70	2.66	45.2	21.5	0.83	0.27	1920	2065	2068	1.359					
20R-1, 114-116	340.94	1.94	1.43	2.58	50.2	26.5	1.01	0.36	1917	1991	1903						
21R-1, 26-28	348.96	2.10	1.65	2.58	43.8	21.4	0.78	0.27	2166	2261	2196	1.255					
22R-1, 121-123	359.71	2.06	1.54	2.73	50.3	25.0	1.01	0.33	2094	2154	2174	1.128					
23R-1, 12-14	368.22	2.55	2.34	2.79	20.0	8.1	0.25	0.09	4073	3995	3900						
24R-1, 15-17	377.95	2.12	1.66	2.75	44.4	21.5	0.80	0.27	2076	2206	2151	1.324 ^a					
24R-1, 15-17	377.95											1.385 ^b					
25R-1, 127-129	388.67	2.10	1.64	2.64	44.8	21.9	0.81	0.28	2138	2224	2185	1.678					
26R-1, 83-85	397.93	2.73	2.54	2.63	18.7	7.0	0.23	0.08	3830	3723	3682	1.347					
26R-1, 142-144	398.52	2.04	1.64	2.71	38.8	19.6	0.64	0.24	2174	2307	2218	1.225					
26R-2, 44-46	399.04	1.93	1.38	2.57	53.9	28.6	1.17	0.40	2003	2304	2210	1.095					
27R-1, 58-60	407.38	2.12	1.67	2.63	43.8	21.1	0.78	0.27	2345	2376	2347	1.289					
28R-1, 24-26	416.74	2.66	2.51	2.73	14.8	5.8	0.17	0.06	4276	4172	4131	1.669					
29R-2, 57-59	428.27	1.94	1.35	2.61	5												

Table 11 (continued).

Core, section, interval (cm)	Depth (mbsf)	Densities			Porosity (%)	Water content (%)	Void ratio	Water ratio	Velocity (m/s)			Thermal conductivity (W/m · K)	Formation factors			
		Wet bulk (g/cm ³)	Dry bulk (g/cm ³)	Grain (g/cm ³)					A	B	C		H	V	Mean	Anisotropy
127-796B- (Cont.)																
31R-2, 32-34	437.72	2.26	1.83	2.64	42.1	19.0	0.73	0.24	1972	2161	2117	1.314				
31R-2, 125-127	438.65								1995	2138	2157					
32R-1, 97-99	446.47	2.19	1.79	2.70	39.0	18.2	0.64	0.22	1989	2167	2141	1.407				
32R-2, 70-72	447.70	2.30	1.89	2.80	39.8	17.7	0.66	0.22	2037	2219	2182	1.393				
32R-3, 77-79	449.27	2.28	1.85	2.84	41.8	18.8	0.72	0.23	2000	2197	2166	1.367				
32R-4, 30-32	450.30	2.26	1.80	2.87	45.3	20.5	0.83	0.26	1932	2034	2044	1.304				
32R-5, 27-29	451.77	2.24	1.81	2.79	41.9	19.2	0.72	0.24	1879	2074	2028					
32R-5, 101-103	452.51	2.28	1.92	2.84	35.2	15.8	0.54	0.19	1999	2158	2158	1.328				
33R-1, 52-54	455.72	2.24	1.88	2.69	35.5	16.3	0.55	0.19	2103	2242	2243	1.241				
33R-2, 93-95	457.63	2.55	2.25	2.84	29.6	11.9	0.42	0.14	2895	2924	2935	1.471				
33R-3, 119-121	459.39	2.31	1.91	2.66	39.3	17.4	0.65	0.21	1955	2236	2218	1.386				

^a Reading taken parallel to bedding.
^b Reading taken perpendicular to bedding.

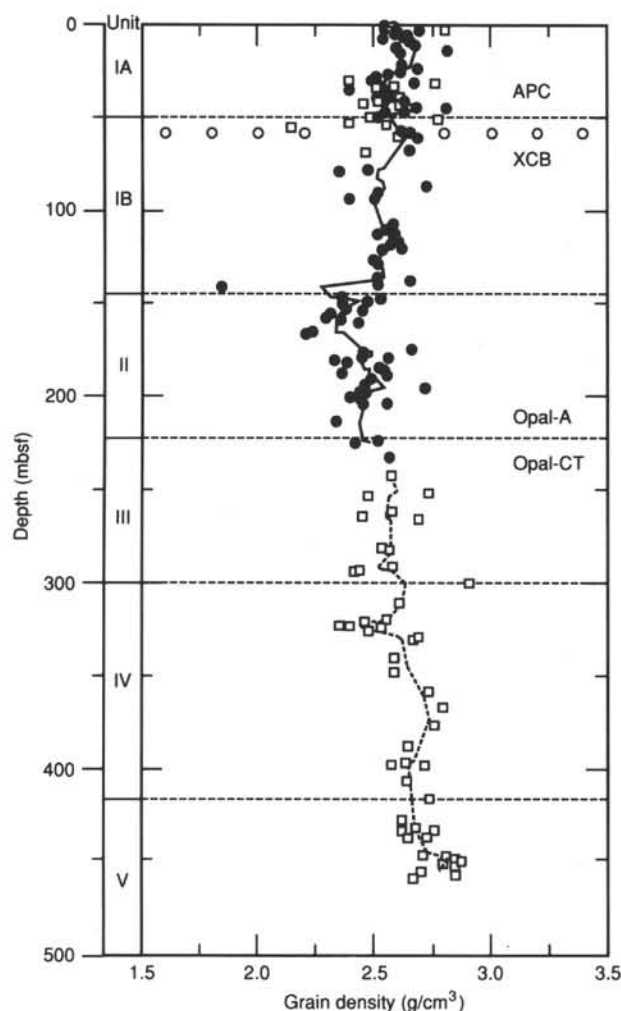


Figure 31. Wet bulk density vs. depth for Holes 796A and 796B. The circles are for Hole 796A, the squares for Hole 796B. The solid and broken lines show five-point tapered running means.

tween Units II and III at 224 mbsf is the opal-A/opal-CT diagenetic boundary within the siliceous sediments, based on XRD analyses (see also "Lithostratigraphy" section, this chapter). The bulk density, the thermal conductivity, and the P-wave velocity increase, and the other index properties decrease at the

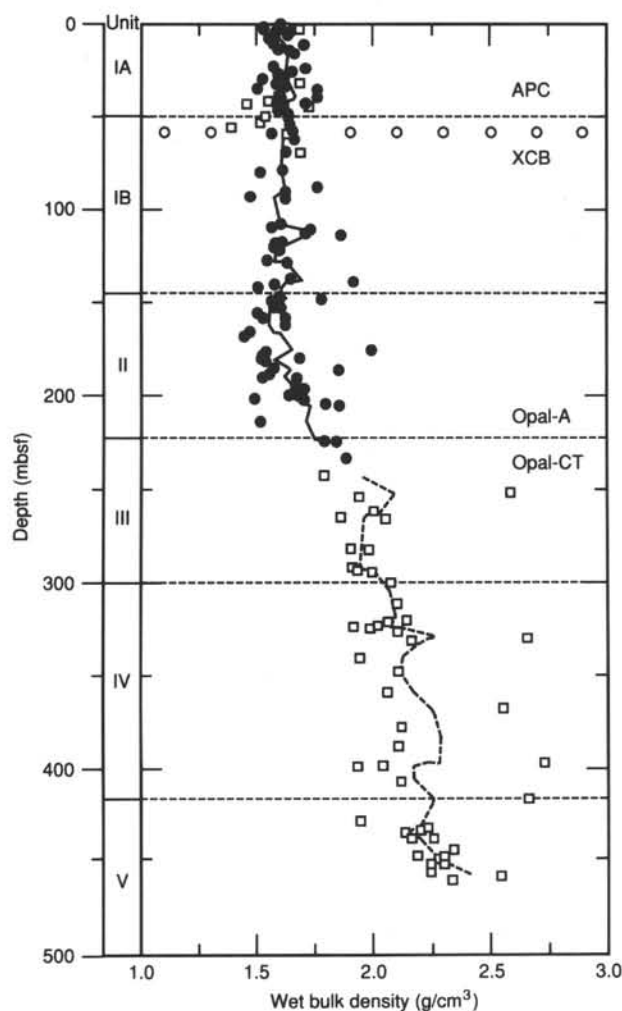


Figure 32. Grain density vs. depth for Holes 796A and 796B. The circles are for Hole 796A, the squares for Hole 796B. The solid and broken lines represent five-point tapered running means.

opal-A/opal-CT transition. At the previous sites, all of the measured physical properties with the exception of grain densities show a sharp and relatively large change at this diagenetic boundary. The changes across the opal-A/opal-CT zone at this site are more gradual rather than sharp. The mean values of

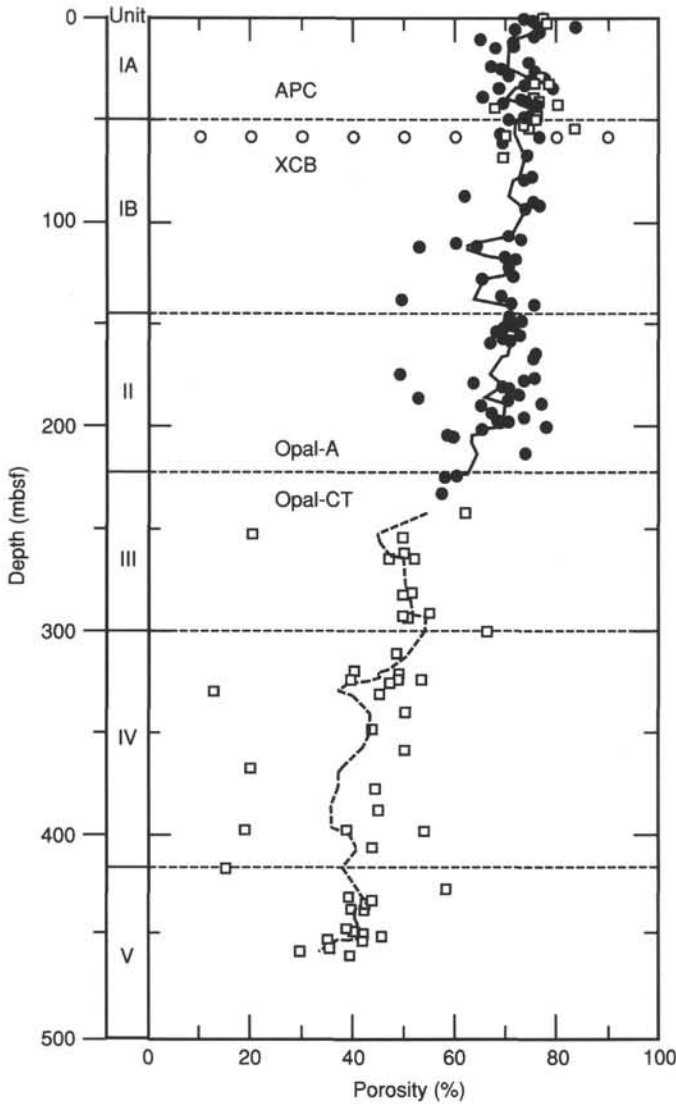


Figure 33. Porosity vs. depth for Holes 796A and 796B. The open circles are for Hole 796A, the open squares for Hole 796B. The solid and broken lines show five-point tapered running means.

physical properties change about 15%–20% or more between Unit II and Unit III. The general gradients of all index properties except grain density from 200 to 250 mbsf, through the opal-A/opal-CT transitional zone, are as follows: wet bulk density, 0.33 g/cm³/50 m; porosity, 20%/50 m; and water content, 16%/50 m. The general gradient of thermal conductivity through the same zone shows 0.19 W/m · K/50 m. Compared with the previous sites, the physical properties at Site 796 change more gradually across the opal-A/opal-CT diagenetic boundary. As at the previous sites, the wet bulk density increases linearly with depth, and the porosity and the water content decrease below the opal-A/opal-CT boundary. There is a little change in the trend of the physical properties and the velocity at the boundary from Unit III to Unit IV (approximately 275–325 mbsf). The bulk density scarcely drops, and the porosity and the water content maintain the same values or slightly increase in this interval (Figs. 31, 33, and 34). The acoustic velocity meanders between high and low values (Fig. 36), which is indicative of alternating hard and soft layers. These features are not dependent on the individual sample selection, because we usually sampled from the

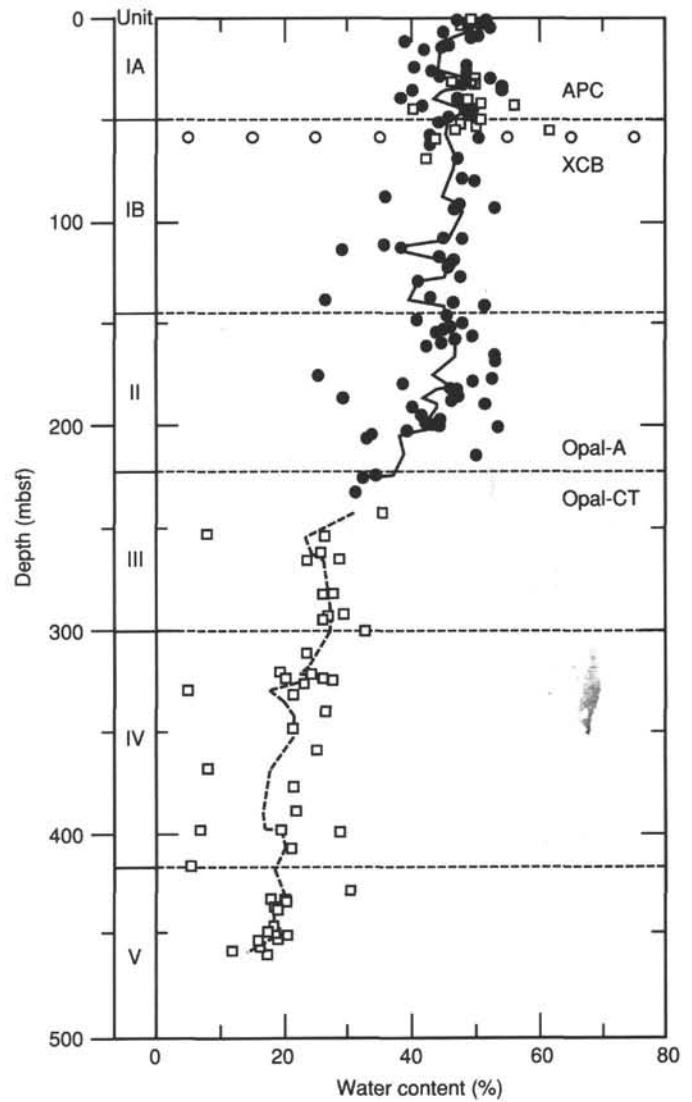


Figure 34. Water content vs. depth for Holes 796A and 796B. The circles are for Hole 796A, the squares for Hole 796B. The solid and broken curves represent five-point tapered running means.

major lithologies which always contained silt or clay. In Unit III, we measured samples of claystones, the major lithology, and infrequently made measurements in sandstone layers, of which there are only two samples. Pure sandstone shows extremely low porosity and water content, and high wet bulk density (Figs. 31, 33, and 34). There is little or no drilling disturbance, because these data plot with very low scatter (Figs. 31, 33, and 34).

Unit IV (301–417 mbsf; late Miocene) is predominantly pebbly claystone. All properties gradually change with depth in this unit except in a small anomalous zone which is a continuation from Unit III. In Figures 31, 33, and 34, the points which plot far from the trends represent sandstone samples. The other samples are claystones. There is a trend across Unit IV to Unit V of increasing wet bulk density and slightly decreasing porosity and water content.

Unit V (417–465 mbsf; middle Miocene) is a carbonate-rich siliceous claystone that is highly bioturbated. All properties show normal trends with depth; the porosity and water content decrease approximately linearly with depth, and the bulk densi-

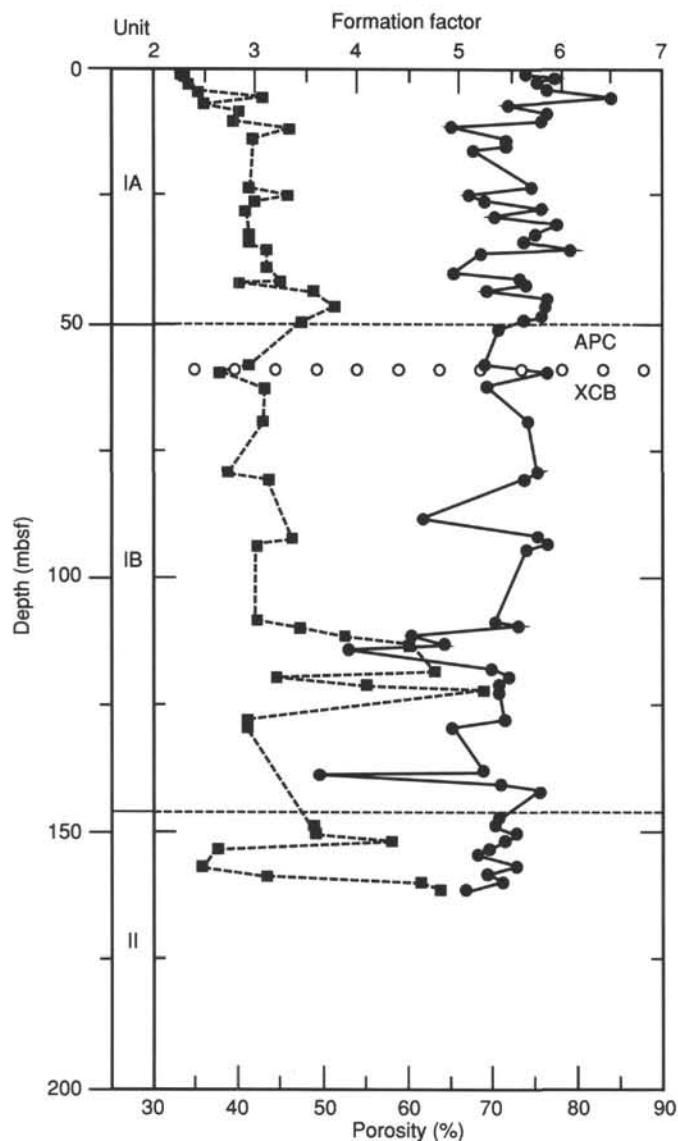


Figure 35. Formation factor and porosity vs. depth for Hole 796A. Solid squares show formation factor and circles show porosity.

ties, thermal conductivity, and acoustic velocity increase. However, without deeper samples, it is difficult to evaluate the trends of physical properties in the lowermost 50 m.

Discussion

One of the prominent features of the sediment physical properties at this site is the gradual change of physical properties across the opal-A/opal-CT diagenetic boundary as compared to the sharp change observed at previous sites. According to the available physical properties data, the top of the diagenetic boundary between opal-A and opal-CT is around 205 mbsf. At this depth, there are relatively large changes in the wet bulk density, porosity, and water content (Figs. 31, 33, and 34). The opal-A/opal-CT transition zone is obviously different from that at the previous sites in terms of the width of the zone and the change in relative values of index properties across the boundary. The change in index properties across this zone is significantly smaller at this site, partially because the wet bulk density is 10%–15% higher, the porosity is about 10% lower, and the

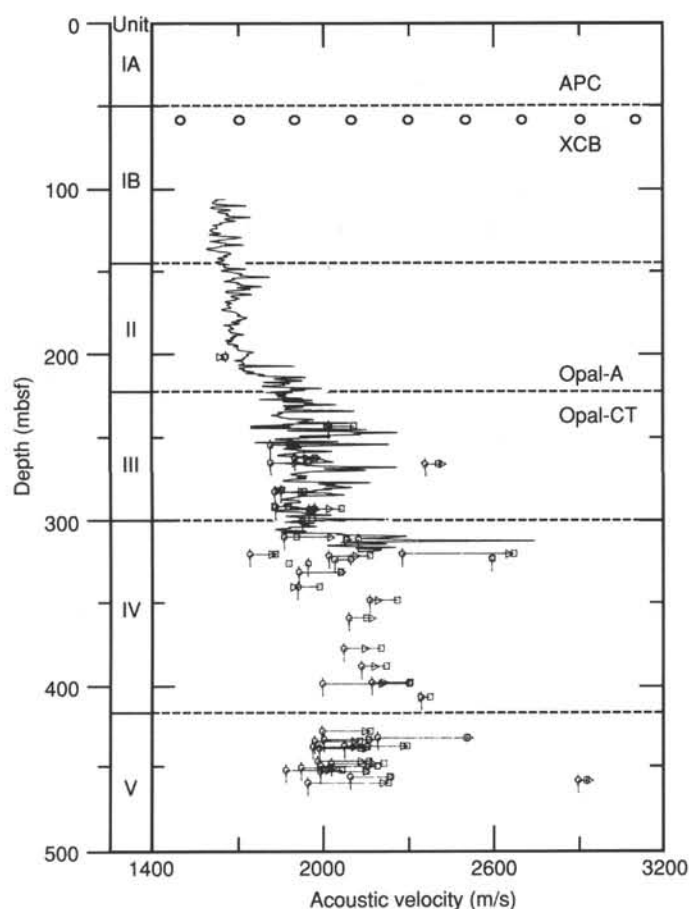


Figure 36. Compressional wave velocities vs. depth for Holes 796A and 796B. The data from 0 to 13 mbsf are results of the *P*-wave logger on MST (thin solid line). The Hamilton Frame velocities are shown for the A (circle and vertical tick mark), B (square), and C (triangle) directions in the samples. The lines denote the range of velocity values for a given sample. Thick solid line shows sonic velocity data from logging.

water content is 10%–15% lower above the transition than at the previous sites. Grain density shows almost the same values. The lower water content at Site 796 may relate to the lithology (e.g., lower diatom content, coarse grain size, and/or higher carbonate content) or to a greater degree of lithification, but the exact cause of the difference is uncertain. These differences in the physical properties in the upper section of Site 796 as compared to Sites 794 and 795 account for the smaller change in the physical properties across the opal-A/opal-CT boundary, but cannot explain the gradual nature of the opal-A to opal-CT transition. The diagenetic boundary may be migrating upward because of the recent tectonism and the related high thermal gradient at Site 796.

We will briefly mention the possibility of water flow at 175–200 mbsf. The water content is maintained at a high value over this interval despite a decrease in the diatom content (Fig. 38). At Sites 794 and 795, the water content decreased with decreasing diatom content. As one possibility, this high water content may reflect water flow, similar to the seepage at accretionary prisms in subduction zones. Okushiri Ridge is obducting toward the Japanese arc along large thrust faults at this site (Tamaki and Honza, 1985; Kuramoto, in press) and the faults may serve as conduits for fluid flow.

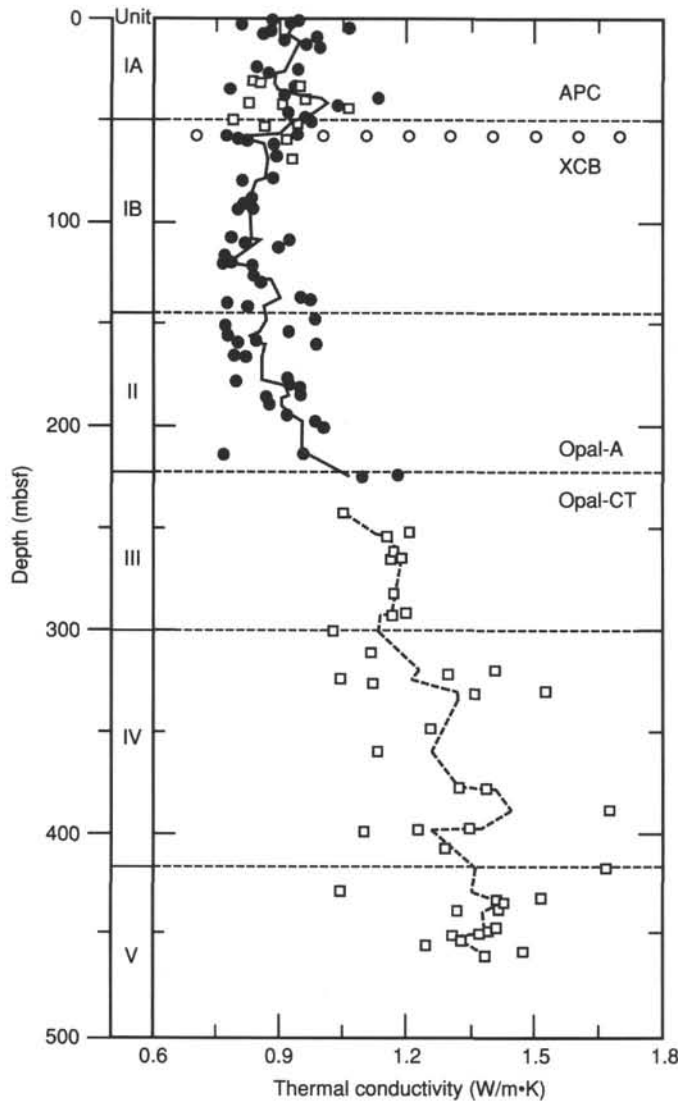


Figure 37. Thermal conductivity vs. depth for Holes 796A and 796B. The circles are for Hole 796A, the squares for Hole 796B. The solid and broken lines represent five-point tapered running means.

Table 12. Physical properties of Unit I, Site 796; (0–146 mbsf, Quaternary to early Pliocene).

	Units	Mean	Standard deviation	Maximum	Minimum
Wet bulk density	g/cm ³	1.62	0.09	1.91	1.39
Dry bulk density	g/cm ³	0.88	0.14	1.40	0.54
Grain density	g/cm ³	2.56	0.14	2.81	1.84
Water content	%	46.2	5.5	61.5	26.5
Porosity	%	72.4	5.8	83.8	49.2
Thermal conductivity	W/m · K	0.885	0.080	1.130	0.763
Mean formation factor		3.16	0.61	5.22	2.25
Formation anisotropy		1.01	0.05	1.13	0.93

DOWNHOLE MEASUREMENTS

Operations

Downhole measurements were made in two of the holes drilled at Site 796. In Hole 796A, five measurements of temperature ahead of the bit were made using the Barnes/Uyeda probe. In Hole 796B, three temperature measurements ahead of the bit were made. Unfortunately, drilling in Hole 796B was terminated

Table 13. Physical properties of Unit II, Site 796; (146–223.5 mbsf, early Pliocene to late Miocene).

	Units	Mean	Standard deviation	Maximum	Minimum
Wet bulk density	g/cm ³	1.60	0.10	1.99	1.45
Dry bulk density	g/cm ³	0.91	0.17	1.31	0.68
Grain density	g/cm ³	2.42	0.11	2.71	2.21
Water content	%	43.7	7.6	53.6	15.6
Porosity	%	67.9	9.7	77.9	23.3
Thermal conductivity	W/m · K	0.886	0.075	1.000	0.771
Acoustic velocity, A	m/s	1663	—	—	—
Acoustic velocity, B	m/s	1659	—	—	—
Acoustic velocity, C	m/s	1644	—	—	—
Mean formation factor		3.64	0.83	4.81	2.47
Formation anisotropy		0.99	0.03	1.05	0.94

Table 14. Physical properties of Unit III, Site 796; (223.5–301 mbsf, late Miocene).

	Units	Mean	Standard deviation	Maximum	Minimum
Wet bulk density	g/cm ³	1.96	0.19	2.59	1.79
Dry bulk density	g/cm ³	1.44	0.29	2.38	1.16
Grain density	g/cm ³	2.53	0.09	2.73	2.41
Water content	%	27.3	6.3	35.4	8.0
Porosity	%	51.0	9.5	61.9	20.3
Thermal conductivity	W/m · K	1.110	0.121	1.204	0.764
Acoustic velocity, A	m/s	1939	156	2359	1820
Acoustic velocity, B	m/s	2005	152	2405	1859
Acoustic velocity, C	m/s	1982	158	2420	1837

Table 15. Physical properties of Unit IV, Site 796; (301–416.5 mbsf, late Miocene).

	Units	Mean	Standard deviation	Maximum	Minimum
Wet bulk density	g/cm ³	2.14	0.22	2.73	1.91
Dry bulk density	g/cm ³	1.70	0.34	2.54	1.38
Grain density	g/cm ³	2.61	0.13	2.90	2.35
Water content	%	21.2	7.0	32.8	4.9
Porosity	%	43.0	12.4	66.3	12.7
Thermal conductivity	W/m · K	1.290	0.172	1.678	1.042
Acoustic velocity, A	m/s	2055	154	2345	1749
Acoustic velocity, B	m/s	2163	208	2668	1837
Acoustic velocity, C	m/s	2155	188	2651	1827

Table 16. Physical properties of Unit V, Site 796; (416.5–465 mbsf, middle Miocene).

	Units	Mean	Standard deviation	Maximum	Minimum
Wet bulk density	g/cm ³	2.26	0.16	2.66	1.94
Dry bulk density	g/cm ³	1.86	0.24	2.51	1.35
Grain density	g/cm ³	2.73	0.08	2.87	2.61
Water content	%	18.0	4.8	30.6	5.8
Porosity	%	39.2	8.5	57.8	14.8
Thermal conductivity	W/m · K	1.379	0.132	1.669	1.039
Acoustic velocity, A	m/s	2064	226	2895	1879
Acoustic velocity, B	m/s	2239	204	2924	2034
Acoustic velocity, C	m/s	2227	212	2935	2028

before reaching basement due to deteriorating conditions. Logging operations, including the full suite of Schlumberger logs and the Lamont-Doherty Geological Observatory's Borehole Televier, were run in the interval available for logging. The planned basement packer/hydrofracture experiment was abandoned because the basement was not penetrated at this site.

Temperature Measurements

The Uyeda probe was used to make temperature measurements at the bottom of Holes 796A and 796B at Site 796. Of the

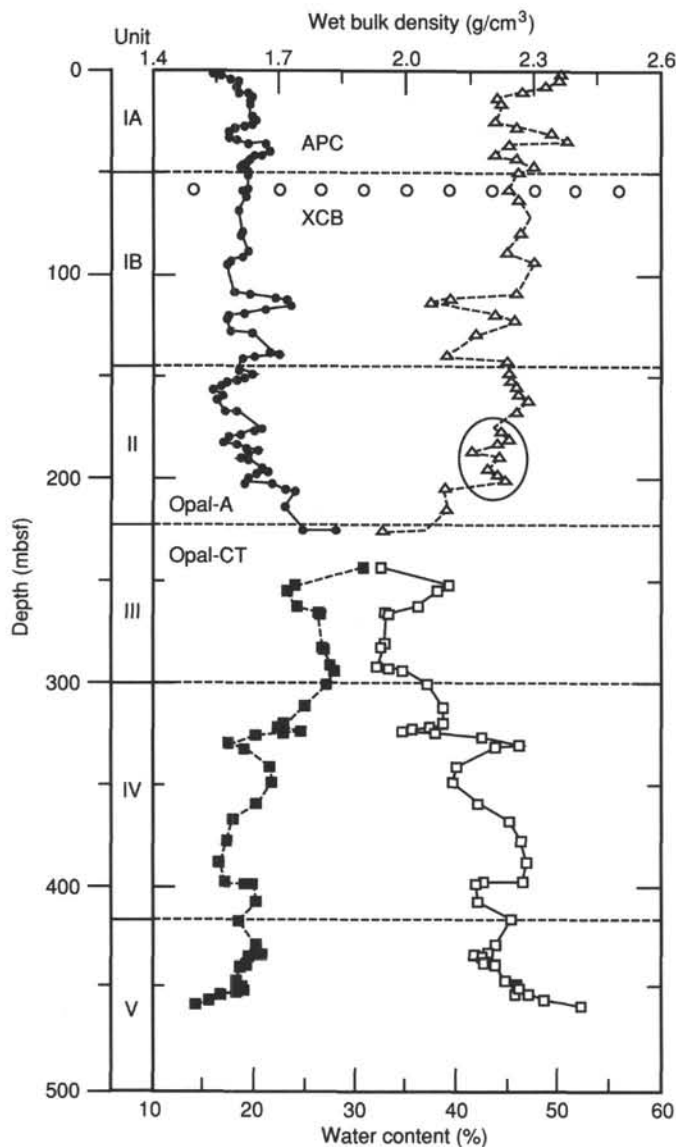


Figure 38. Wet bulk density and water content vs. depth for Holes 796A and 796B. Solid circles and squares represent smoothed water content using a five-point tapered running mean. Open triangles and squares represent smoothed wet bulk density using a five-point tapered running mean. The large circle shows an anomalous high water content area, which may indicate positive fluid flow.

five measurements made in Hole 796A, two (Runs #1A and #4A) meet the usual criteria for valid measurements and a third (run #2A) appears to be only slightly disturbed. In Hole 796B, two of the three measurements attempted (runs #2B and #3B) gave valid temperatures. Holes 796A and 796B are only 250 m apart on the eastern slope of Okushiri Ridge, yet the profiles of temperature vs. depth in the two holes (Fig. 39) are very different. If both are valid, the difference would be very difficult to reconcile. The three best measurements in Hole 796A indicate a gradient that decreases significantly with depth. The gradient defined by the three sub-seafloor points is about 80°C/km, whereas the gradient defined by the seafloor temperature and run #1A defines a gradient of 158°C/km. The two good temperature determinations at Hole 796B combined with the seafloor temperature define a nearly uniform gradient of 178°C/km

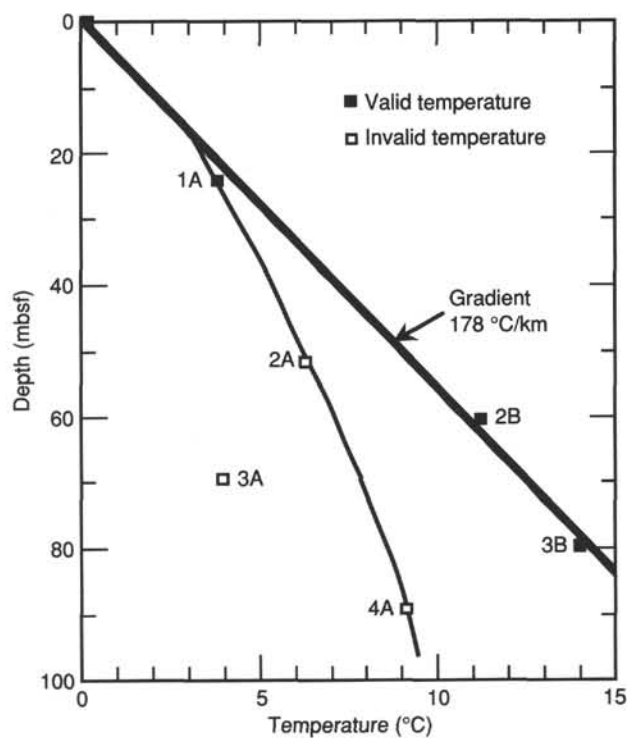


Figure 39. Estimated formation temperatures for six of the Site 796 downhole temperature measurements vs. depth. Values believed to represent virgin formation temperatures are shown as solid squares.

km. Our current opinion is that the measurements #1A in Hole 796A and #2B and #3B in Hole 796B are valid and provide a representative measurement of the *in situ* thermal gradient, whereas the measurements made on runs #2A, #3A, and #4A in Hole 796A (see Fig. 40) are not valid measurements of the virgin formation temperatures. The reasons for this conclusion are summarized below.

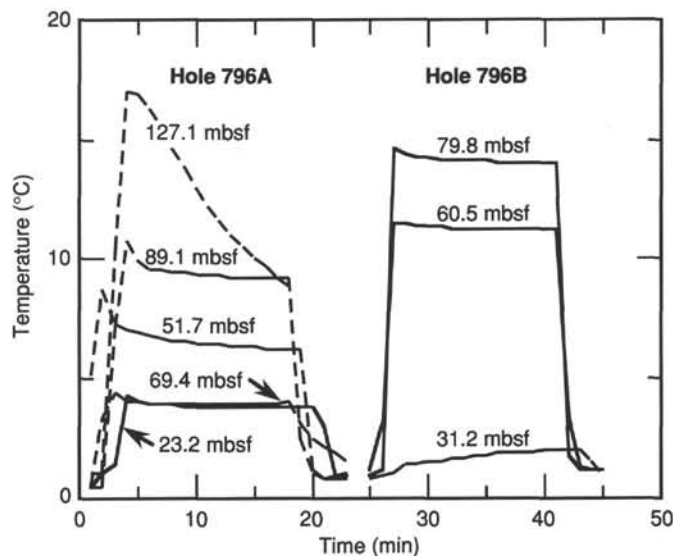


Figure 40. Temperature histories for all of the Uyeda probe runs at Site 796. Traces that are dashed apparently equilibrated to false, low formation temperatures.

Assessing Bottom Hole Temperature Measurements

Hyndman et al. (1987) give as the main criterion for a valid downhole temperature measurement that the temperature history in the sediment should closely follow the theoretically expected decay curve for a probe with the dimension and properties of the Uyeda probe. After the probe has been in the sediment for 5 min the decay curve should be closely approximated by a function of the simple form:

$$T(t) = A/t + T_{eq}, \tag{1}$$

where A is a constant and T_{eq} is the equilibrium or virgin formation temperature.

According to eq. 1, temperature should decrease linearly with the reciprocal of time after it has been in the sediment for 5 min. A departure from linearity usually means a disturbance of

some kind and therefore the validity of the temperature measurement is questionable.

The temperature histories for all of the runs are shown in Figure 40. The traces for Hole 796B have been displaced about 25 min to the right for clarity. Four of the traces from Hole 796A look normal, as a heat pulse associated with penetration into the sediment was followed by a smooth decay. However, the measurement at 69.4 m (run #3A) decays to a temperature nearly equal to the measurement at 23.2 m. In Figure 41A we show the runs #1A to #4A at Hole 796A plotted vs. 1/time (a cycle equals 1 min). Runs #1A and #4A define nearly linear decays with respect to 1/t, but Run #2A tails off anomalously and Run #3A is disturbed near the end of the time in the sediment. With no other evidence at hand we would probably accept runs #1A and #4A as good, since they meet the Hyndman et al. (1987) criterion.

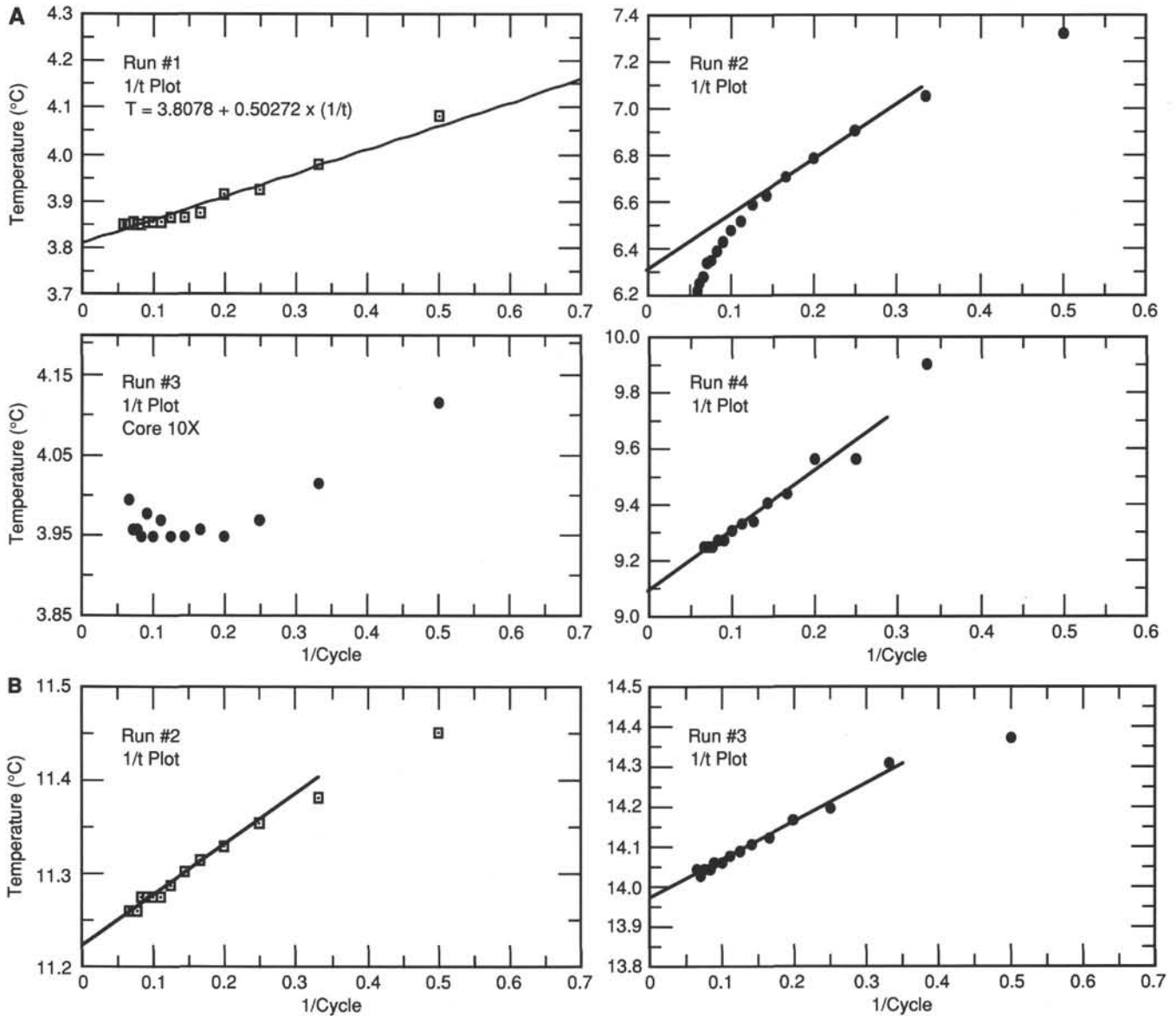


Figure 41. A. Plots of temperatures after penetration vs. 1/time for four runs in Hole 796A (a cycle equals 1 min). A thermal equilibration of a cylindrical probe should plot as a straight line on this type of plot after about 5 cycles. The intercept at 1/time = 0 is the equilibrium temperature. B. Plots of temperatures after penetration vs. 1/time for two runs in Hole 796B.

The $1/t$ plots for runs #2B and #3B in Hole 796B are presented in Figure 41B. Both runs describe a linear decay with respect to $1/t$, and therefore meet the criterion for good measurements. In Hole 796A, some measurements decay normally, but other evidence suggests that they equilibrate to a false low value. The most likely cause of this result is the cooling of a large volume of the formation ahead of the bit by circulating fluid. Circulation at rates of 150–250 gallons per minute are maintained during coring to clear cuttings from the bit face. This water is at a temperature close to that of the bottom water, i.e., close to 0°C. If the formation ahead of the bit is permeable, (e.g., loose sand or gravel), or is made permeable by fracturing of sediments ahead of the bit while coring, then cold water will mix into the sediments and reduce their temperature.

Significant thicknesses of sand and silt were cored in both holes. On run #3A the temperature tool came back with the telescoping mechanism filled with silt and sand. This is the run that yielded an equilibrium temperature nearly equal to run #1A, 58 m above it. In Table 17 we summarize the contents of the first section of the core taken following each of the downhole temperature measurements. This section should contain material in which the measurement was made. The frequent occurrence of sand in the section suggests that there is a high probability that permeable sediments lie just below the bit when the probe is inserted. Consequently, we conclude that flooding permeable formations ahead of the bit with cold circulation is the most likely cause of the apparently low temperatures at many of the runs at Site 796.

If this explanation is correct, it raises a general concern about measuring downhole temperatures in alternating permeable and impermeable sub-seafloor beds, since probe measurements in sandy or silty layers would give occasionally invalid results even though the decay curves may look perfectly normal. The best approach to obtaining valid gradient measurements in such alternating sequences is to make as many measurements as possible, and to apply the knowledge that operational disturbances to downhole measurements in the deep sea are always in a direction that reduces the temperature. Thus, the measurements that define the a maximum gradient are most likely to be correct. We have applied this simple rule to the Site 796 observations.

Temperature Gradient and Heat Flow

The temperature data are presented in Table 18. The temperatures from runs #1A, #2B, #3B, and the seafloor yield a least square fit gradient of 178°C/km (Fig. 39). The thermal conductivity measurements adjusted to *in situ* conditions are plotted vs. depth in Figure 42, and are used to calculate the thermal resistance between the seafloor and each temperature measurement. Linear regression of the valid downhole temperatures vs. thermal resistance yields a heat flow of 156 mW/m² (Fig. 43). This is one of the highest values of heat flow observed in the Japan Sea.

Table 17. Contents of cores that follow downhole temperature measurements.

Hole	Run #	Next core no.	Contents 1st section
796A	1	4H	Clay 85%, silt 12%, sand 3%
	2	7H	No recovery, possibly sand
	3	10X	Silt 20%, clay 80%
	4	12X	Sand 75%, silt 15%, clay 10%
796B	1	3R	Clay 50%, silt 40%, sand 10%
	2	6R	Clay 80%, silt 20%
	3	8R	No recovery, possibly sand

Table 18. Downhole temperature data from Site 796.

Hole	Run no.	Depth (mbsf)	Thermal resistivity (m ² ·°C)/W	Temperature (°C)
796A	1A	23.2	28.1	3.81
	2A	51.7	58.9	^a 6.30
	3A	69.4	—	^a 3.95
	4A	89.1	103.0	^a 9.10
	5A	127.1	—	—
796B	1B	—	—	—
	2B	60.5	69.4	11.22
	3B	79.8	91.0	13.98

^a Judged not to be a valid virgin formation temperature determination.

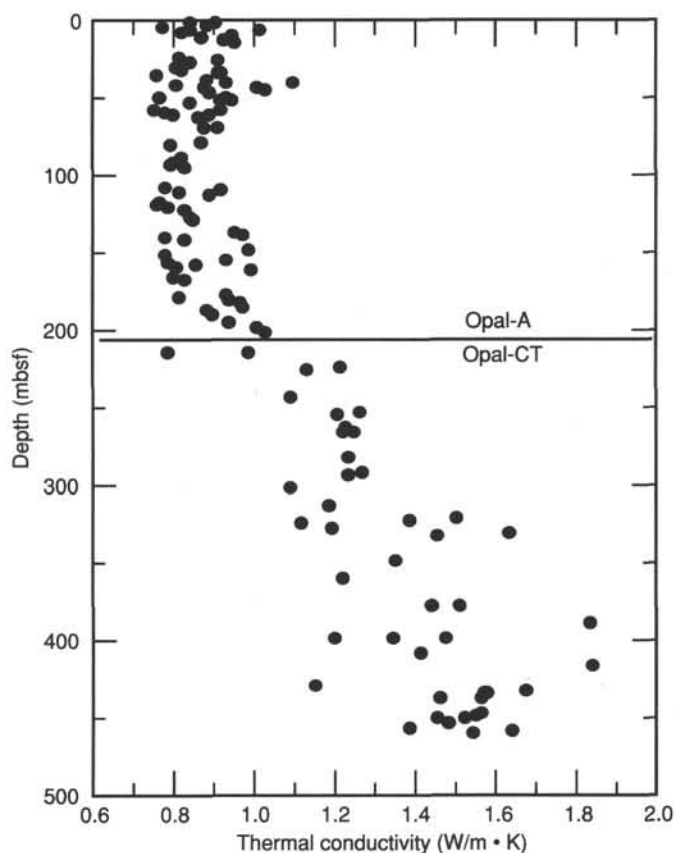


Figure 42. Thermal conductivity values corrected to *in situ* condition of temperature and pressure vs. depth. Notice nearly constant values in the upper 200 m and the significant change at the opal-A/opal-CT front.

The heat flow and the thermal conductivity data can be combined to estimate the temperature profile deeper in the section. The resulting profile is shown in Figure 44. Hydrates were recovered in some of the cores. Methane hydrates should be stable in fresh water to about 22°C at the ambient pressures in Holes 796A and 796B (Kvenvolden and MacDonald, 1985). Methane hydrates in seawater should be stable to somewhat lower temperatures. The temperature profile in Figure 44 indicates that the maximum depth at which hydrates are stable is about 120 mbsf at Site 796. The temperature estimated for the opal-A/opal-CT transition is 38°C. This temperature is about the same as that found at Sites 794, 795, and 797, which lends credence to

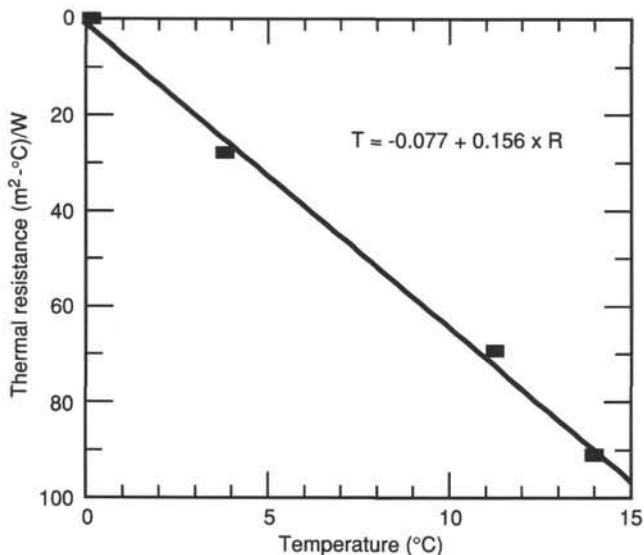


Figure 43. Formation temperatures vs. thermal resistance of the sedimentary section between the seafloor and each measurement location (see Table 18). The slope of the line, 0.156 W/m², is the best estimate of the heat flow.

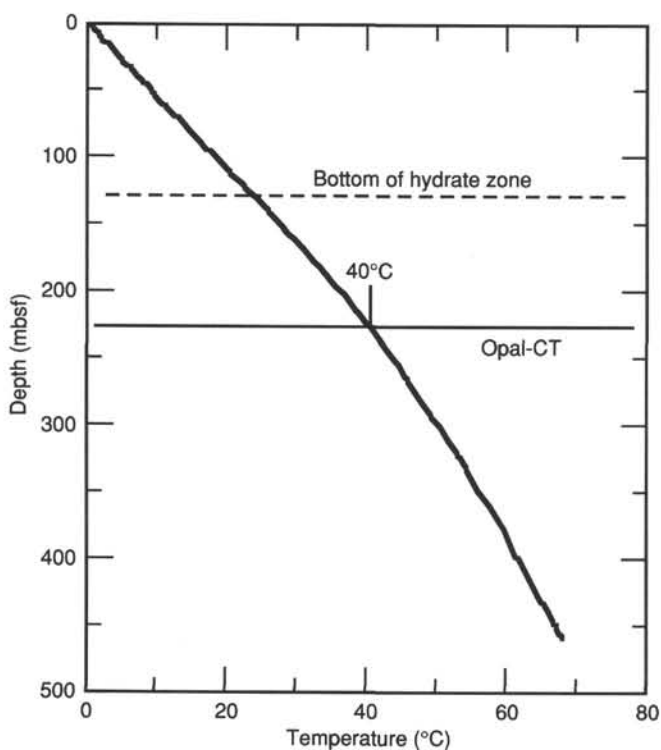


Figure 44. Estimated temperatures to the bottom of the hole based on a heat flow of 156 mW/m² and the conductivity values in Figure 42.

our gradient determination using the highest temperature values measured.

Possible Causes of the Anomalous Heat Flow Observed on Okushiri Ridge

The seafloor topography and the basement topography of Okushiri Ridge will have a significant effect on the lateral varia-

tion of seafloor heat flow over the feature. In this report, the discussion will be limited to a qualitative assessment of topographic effects to show the sense of the disturbances and to make a rough estimate of their magnitude.

Heat flow will decrease near the crest of a ridge due to the spreading of isotherms in the crust to conform with the nearly isothermal seafloor. For similar reasons, heat flow will increase near the base of a ridge where there is a break in slope and isotherms pinch together (see Fig. 45A). For slopes less than 15°, the magnitude of the effects are not large, on the order of 10% near the break in slope at the crest or base of the ridge. Since Holes 796A and B are close to the crest of Okushiri Ridge, the effect of seafloor topography alone will tend to reduce the seafloor heat flow relative to that flowing up from the mantle. The effect will be somewhat larger at Hole 796A since it is closer to the crest. It is possible that local topography with steeper slopes may be superimposed on the large scale shape of the ridge and could have a major effect on shallow sub-bottom measurements.

The basement escarpment associated with the eastern slope of Okushiri Ridge combined with the insulating effect of the sediment-filled basin east of the ridge will cause focusing of heat flow from the basin toward the ridge. This edge effect will be opposite to the reduction in heat flow that results from the seafloor topography, consequently the net disturbance to the heat flow may be small. Experience suggests a correction on the order of ± 10%. A more detailed analysis is obviously required but is beyond the scope of this preliminary report. In our opinion, topographic effects will not explain the large positive anomaly revealed by the heat flow measurements at Site 796.

Any interpretation of the 40–50 mW/m² anomaly on Okushiri Ridge is premature until we have a better definition of the scale of the anomaly and its relation to the structure of the ridge, and

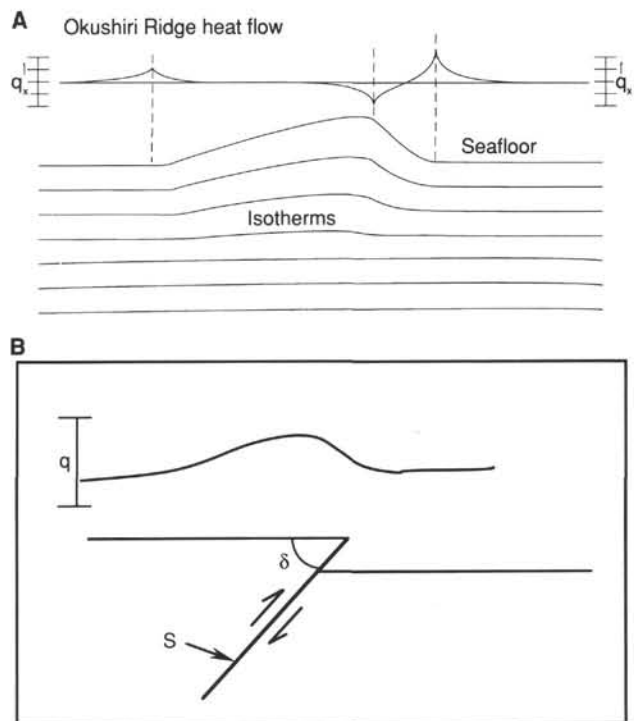


Figure 45. A. Qualitative sketch of the variation of heat flow due to topography over the Okushiri Ridge. B. Sketch of a simple model of thrust faulting associated with the obduction of the Okushiri Ridge. See equation in text for explanation.

until we have made topographic corrections. However, it seems certain that additional sources of heat in the lithosphere, or strong focusing of the flux, are required to explain the anomaly. Two potential sources are frictional heating on the thrust faults on the eastern edge of the ridge, and heat transport by fluid flow along faults through the crust and/or sediment. It is possible that both mechanisms are acting simultaneously.

A crude estimate of the heat produced by frictional heating along the faults that bound Okushiri Ridge can be made with the simple relation:

$$\text{Heat generated/unit area} = \text{normal stress on fault} \times \text{rate of slippage.}$$

This assumes that all of the work done on the fault plane goes toward generating heat. Referring to the sketch in Figure 45B, if δ is the dip of the fault and the heat generated on the fault flows vertically upward from the fault,

$$\text{Stress} = \text{Excess heat flow} \times \cos(\delta)/\text{slip rate.} \quad (2)$$

Assuming the excess heat flow is $0.04 \text{ N}/(\text{m} - \text{s})$, $\delta = 75^\circ$, and the slip rate is $1000 \text{ m}/\text{Ma}$, then by eq. 2 the stress is about 320 MPa or 3.2 kbar . This is about an order of magnitude higher than stresses reported from other studies on major faults. Thus, it would be difficult to argue that the anomalous heat flow is due to frictional heating unless the heat flow is focused into a small area of the seafloor. As a caveat, if significant translational motion has recently occurred on the fault in addition to thrust motion, then the rate of slippage assumed above would be too low, leading to a lower calculated stress.

Transport of heat flow by fluid flow along the fault or associated fractured zones in the crust is one way that frictional heat generated along the fault could be focused near the outcrop of the fault. Fluid flow along faults in compressive tectonic regimes has been observed at several active accretionary wedges (e.g., Mascle, Moore, et al., 1988). Transport of heat by fluid flow has also been proposed to explain heat flow anomalies associated with thrust faults in the central Indian Ocean (Geller et al., 1983).

The large gradients in pore-water chemistry (see "Inorganic Geochemistry" section, this chapter) would be hard to explain if there was a thermally significant vertical flux of water through the sedimentary section. On the other hand, nearly horizontal flow along permeable beds cannot be ruled out. Flow that is confined to igneous units below the sedimentary section can effectively focus the heat generated on faults into a relatively small area.

Summary of Temperature Measurements

The downhole temperature measurements at Site 796 led to more anomalous temperature records than normal ones. This is in sharp contrast to the other three sites where valid measurements were the rule. We believe that the anomalies are caused by flooding of permeable layers (turbiditic sands and silts) ahead of the drill by cold water circulated during drilling. The best temperature measurements indicate a gradient of about $178^\circ\text{C}/\text{km}$ and a heat flow of $156 \text{ mW}/\text{m}^2$, one of the highest values observed in the Japan Sea, and $40\text{--}50 \text{ mW}/\text{m}^2$ higher than the average heat flow for the Japan or Yamato Basins. This excess heat flow is probably associated with the rapid obduction and deformation of Okushiri Ridge. Frictional heating along the thrust faults is one potential source of excess heat, but crude calculations suggest that a process to concentrate the heat flow is required to match the magnitude of the anomaly. Further geothermal investigations of Okushiri Ridge would be very rewarding.

Logging

Three Schlumberger tool strings were run at Hole 796B: the geophysical/lithodensity tool string, the geochemical tool string, and the formation microscanner (FMS). The geophysical/lithodensity tool was run twice, the first time without nuclear sources due to concerns of possible tool sticking. This tool included the long-spaced sonic tool (LSS), the induction tool (ILDIT) for measuring resistivity, and the natural gamma ray tool (NGT) for measuring clay content. The geophysical/lithodensity tool was run for a second time with nuclear sources after proof that the hole was in satisfactory condition, and for this run included the lithodensity tool (HLDT) and the neutron porosity log (CNL) as well. We were unable to run the temperature tool at this site because of software problems. An LDGO borehole televiwer (BHTV) tool was run to investigate whether hard sandstone beds, having sonic velocities greater than $4 \text{ km}/\text{s}$, contained fractures (see "Physical Properties" section, this chapter).

The logging operations in Hole 796B were conducted in the open hole between 103 and 330 mbsf, except for the geochemistry tool string which was recorded both in the open hole and through pipe between the seafloor and 100 mbsf. Both upgoing and downgoing measurements were made for the geophysical tool string runs, but due to a slower logging speed the upgoing logs are of higher quality and are the only logs displayed in this report. A summary of intervals logged for each tool string is presented as Table 19.

Log Quality and Processing

The quality of the acquired logging data was variable. The data from the geochemistry and the FMS tool strings are of high quality. In contrast, the caliper of the geophysical tool string malfunctioned during its first run, but this problem was not present on the second run. No depth shifts were applied to the logs because the log values closely coincided with many key horizons.

The LSS tool showed significant noise problems between 120 and 140 mbsf and more intensely in the intervals 210–255 mbsf, 275–285 mbsf, and 300–320 mbsf. Sonic data are shown as a collection of microseismograms recorded by receivers. The source is an impulse generated a fixed distance away from the receivers. For purposes of calculating velocities, the first break in the microseismogram or waveform, representing the *P*-wave arrival and called the travelttime, is detected. This first break is measured in microseconds. Noise in the aforementioned intervals can be attributed to several causes. One possibility is that low amplitudes of the waveforms caused spurious spikes to be recognized as first break travelttimes. A second possibility is that the tool was disturbed due to the tool contacting the well bore; this is commonly referred to as "road noise." Each bump would correspond to a large amplitude spike, often mistakenly identified as travelttime.

An algorithm to process this noise in sonic data (Srivastava, Arthur, et al., 1987) was applied. This algorithm computes mean and median travelttimes by combining eight different source-receiver travelttime pairs and by editing poor values. In processing this sonic log, we removed approximately 10% of the travelttimes. The sonic log before and after processing-out noise information is displayed in the left and right columns of Figure 46.

The short spacing electron density log (RHOB) malfunctioned because the number of electrons counted at various energy levels was too low by a factor of 20. As a result, the measurements displayed wild gyrations and gave meaningless data. At Sites 794 and 795, there was close agreement in the results from the short and long spacing electron density logs. Therefore, at Site 796, we decided to accept the long spacing measurement as the bulk density measurement.

Table 19. Summary of logging intervals for each tool string. Logging depths at Hole 796B.

Seafloor ^a (m)	Seafloor measured from rig floor (m)	Rig floor height (m)	Total depth drilled (mbsf)	Deepest log (mbsf)	Basement depth
2622.6	2633.8 (8641.1 ft)	11.3	464.9	332.0	n/a

Tool	Depths				Upgoing (y/n)	Hole condition	Side-entry		
	Shallowest (mbsf)	(fbrf)	Deepest (mbsf)	(fbrf)			KCL	mud	sub
Geophysical	-39.2	8512.5	328.9	9720.0	y	open hole drill pipe 0-101 mbsf	4%		n
FMS ^b	101.1	8972.8	332.0	9730.3	y	open hole		n/a	n
Geochemistry	-7.6	8616.0	329.3	9721.5	y	open hole drill pipe 0-101 mbsf	4%		n
Geophysical	-2.8	8632.0	330.5	9725.5	y	open hole drill pipe 0-101 mbsf	4%		n
BHTV	240.0	9428.5	330.0	9723.8	y	open hole		n/a	n

^a From "Introduction/Objectives" chapter, this volume, Table 1.

^b Drill pipe raised 30 m for FMS run.

Four percent KCl drilling fluid was used in Hole 796B to help combat anticipated clay swelling problems. This represents a higher content of KCl than is typically used by ODP. The high KCl value significantly increased the potassium counts determined from the natural gamma ray tool. Therefore, a correction was applied to the potassium log. This correction was too high, as the logs showed much lower (even negative) counts for potassium at Site 796 than at the earlier sites, despite the similarity of the sedimentology between the Leg 127 sites. This overcorrection was likely caused by assuming that the hole volume was too small.

Density, Sonic, Resistivity

The results of the density, sonic, and resistivity logs are presented in Figure 47, along with lithostratigraphic and chronostratigraphic information from Table 1. The density log is from the long spacing of the HLDT, the resistivity log is from the deep resistivity measurement plotted on a linear scale, and the sonic velocity log has been processed as discussed above. We consider the responses of these logs in each of the lithologic units below.

Lithologic Unit I consists of silty clay with minor diatom ooze and interbeds of ash. The unit extends from 0 to 148 mbsf. Sonic, density, and resistivity logging was performed from the end of drill pipe at 103-148 mbsf. The density log is characterized by an average density of about 1.6 g/cm³ and a few intervals with higher densities. The resistivity log is broadly sinuous ranging from 0.6 to 0.8 ohm-meters. Bulbous increases in resistivity disrupt the sinuosity at 130 and 133 mbsf. The sonic log is also broadly sinuous but shows increases at 130 and 133 mbsf.

Lithologic Unit II consists of diatom ooze interbedded with clays and pebbly claystone. Minor lithologies are thin interbeds of sand and pebbly claystone. The unit extends from about 150 to 224 mbsf, the opal-A/opal-CT transition zone (see "Lithostratigraphy" section, this chapter). The logging measurements show roughly three subdivisions of this unit. From 150 to 168 mbsf the density, resistivity, and sonic logs show high variability and zones of high velocity, density, and resistivity. These zones of high velocity, density, and resistivity are usually quite thin, on the order of 10-50 cm and are commonly referred to as hard streaks because of the relative hardness of the constituent minerals. With the lithologies encountered here, these hard streaks

would most likely be layers of dolomite or chert. The hard streaks might also be calcite-cemented zones. This lithologic identification is based on core recovery that is often sporadic because these hard streak zones are more difficult to drill.

From 168 to 210 mbsf, which corresponds to an interval of diatom ooze with sands in discrete thin layers, the resistivity log is remarkably uniform at 0.5 ohm-meters. The density and sonic logs are also very stable throughout this interval. However, this uniformity is punctuated by another thin hard streak having a high velocity at 208 mbsf. All three logs show a large change in properties at 215 mbsf which corresponds to the top of the opal-A/opal-CT transition zone. Because of the high geothermal gradient, varying silica content, and shallow depth, the opal-A/opal-CT transition zone is very complex at this site. It extends to a depth of 225 mbsf (see "Lithostratigraphy" section, this chapter). This complexity is reflected in Figure 48, which shows the high amount of variation in the porosity log for this interval. There is a major change in porosity at 213 mbsf and another minor change to a minimum porosity value of 40 percent at 226 mbsf.

Lithologic Unit III consists dominantly of clay and silty clay interbedded with thin layers of sand. It extends from 224 to 300 mbsf. Figure 47 shows that the density, sonic velocity, and resistivity are highly variable in this unit. Broadly, the density log is characterized by a sinuous character, but at a small scale it is highly variable. The resistivity log is characterized by an average value of 1 ohm-meter, but it is highly variable as well. The sonic log at this site shows an average value of about 1800 m/s from 224 to 240 mbsf and then increases to about 1925 m/s below this depth. Noise in the sonic log was a serious problem in this unit; we believe that this is primarily due to the presence of hard streaks. In intervals not punctuated by hard streaks, such as 248-253 mbsf and 259-268 mbsf, the sonic and resistivity logs are characterized by a ramp-like gradients.

A prime example of a hard streak is seen at 253 mbsf. A very sudden increase in density from 1.8 to 2.2 g/cm³ is seen here along with a resistivity and sonic velocity increase. Unfortunately, this zone was not recovered at Site 796. Because of the large, abrupt change in properties, this hard streak is most likely dolomite or chert. A less obvious hard streak occurs from 243 to 248 mbsf with a thicker section of increased values in the resistivity and sonic log, but a lower increase in the density. This

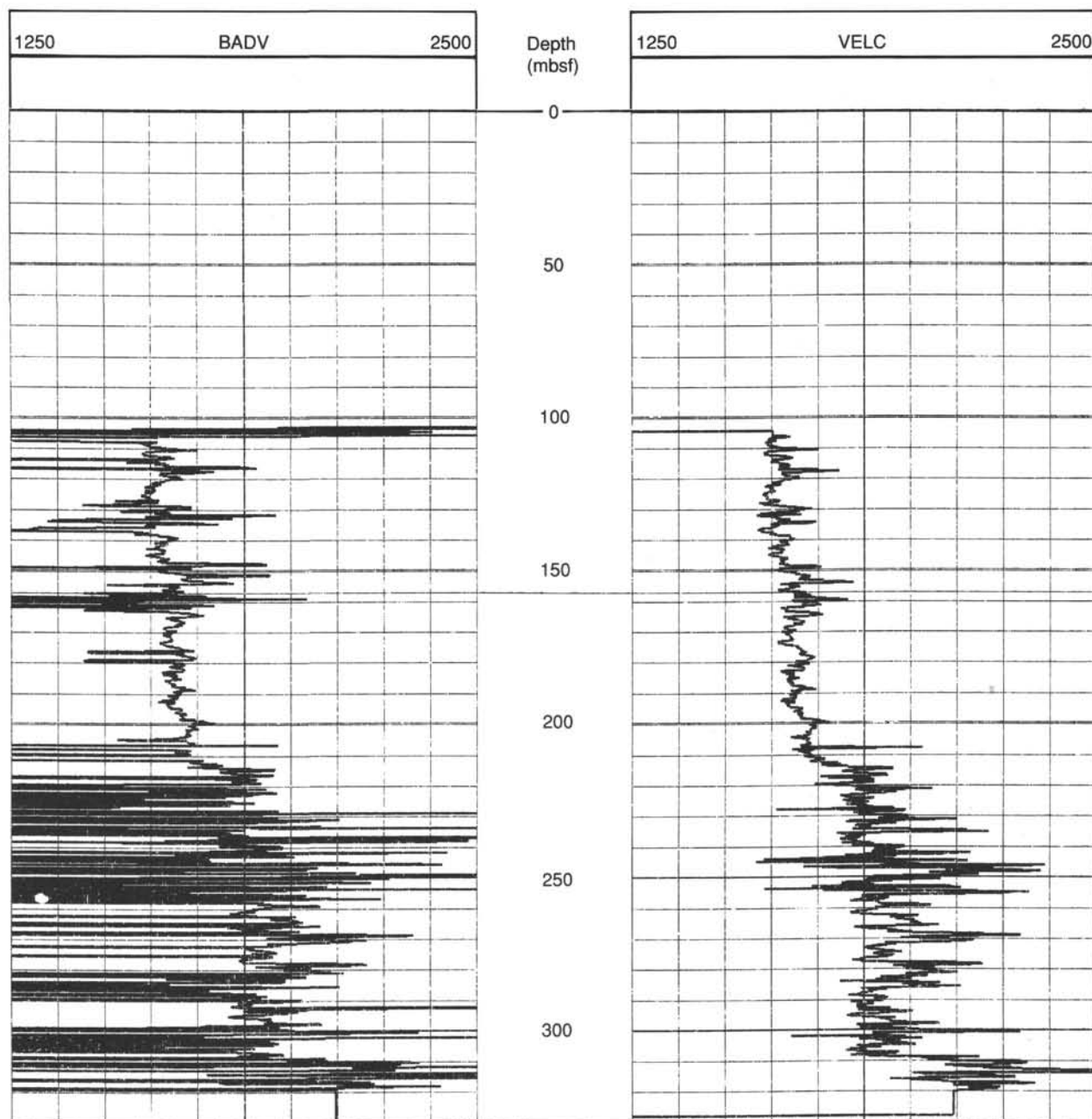


Figure 46. Sonic log displayed before and after noise removal algorithm (Srivastava, Arthur, et al., 1987) has been applied. Left-hand curve (BADV) is the sonic log before noise removal and is measured in m/s. Right-hand curve (VELC) is the sonic log after noise removal also measured in m/s.

might be a calcite-cemented zone. Again it is hard to confirm this lithologic speculation because of poor core recovery. More examples of these hard, cemented zones occur at 268–271 mbsf.

Lithological Unit IV extends from 301 to 417 mbsf and consists of tuffs and pebbly claystones. We were only able to acquire logs over 29 m of this unit to a total depth of 330 mbsf in this unit. A decrease in the density log measurement from 1.8 to 1.5–1.6 g/cm³ indicates that a tuff unit extends from 301 to 310 mbsf. A decrease in the sonic velocity and resistivity over this interval supports this observation. Beginning at about 309 mbsf, just below the tuff, the transition from opal-CT to quartz begins. The density increases to 1.8 g/cm³ and the resistivity in-

creases to 0.9 ohm-meters. The sonic velocity increases to just above 2000 m/s. A high velocity zone is also seen at 313 mbsf.

Porosity, Caliper, Gamma Ray

Neutron porosity (PORS, neutron porosity percentage divided by 100), caliper (CALI, inches) and gamma ray (CGR, compensated gamma ray, API (American Petroleum Institute) units) curves are plotted in Figure 49. The CGR measurement shows a most interesting profile. From 103 mbsf in Unit I to about 210 mbsf in Unit II there is a ramp-like increase in the gamma ray log until the average value of 35 API units is reached for Units III and IV. This increase does not correlate well with

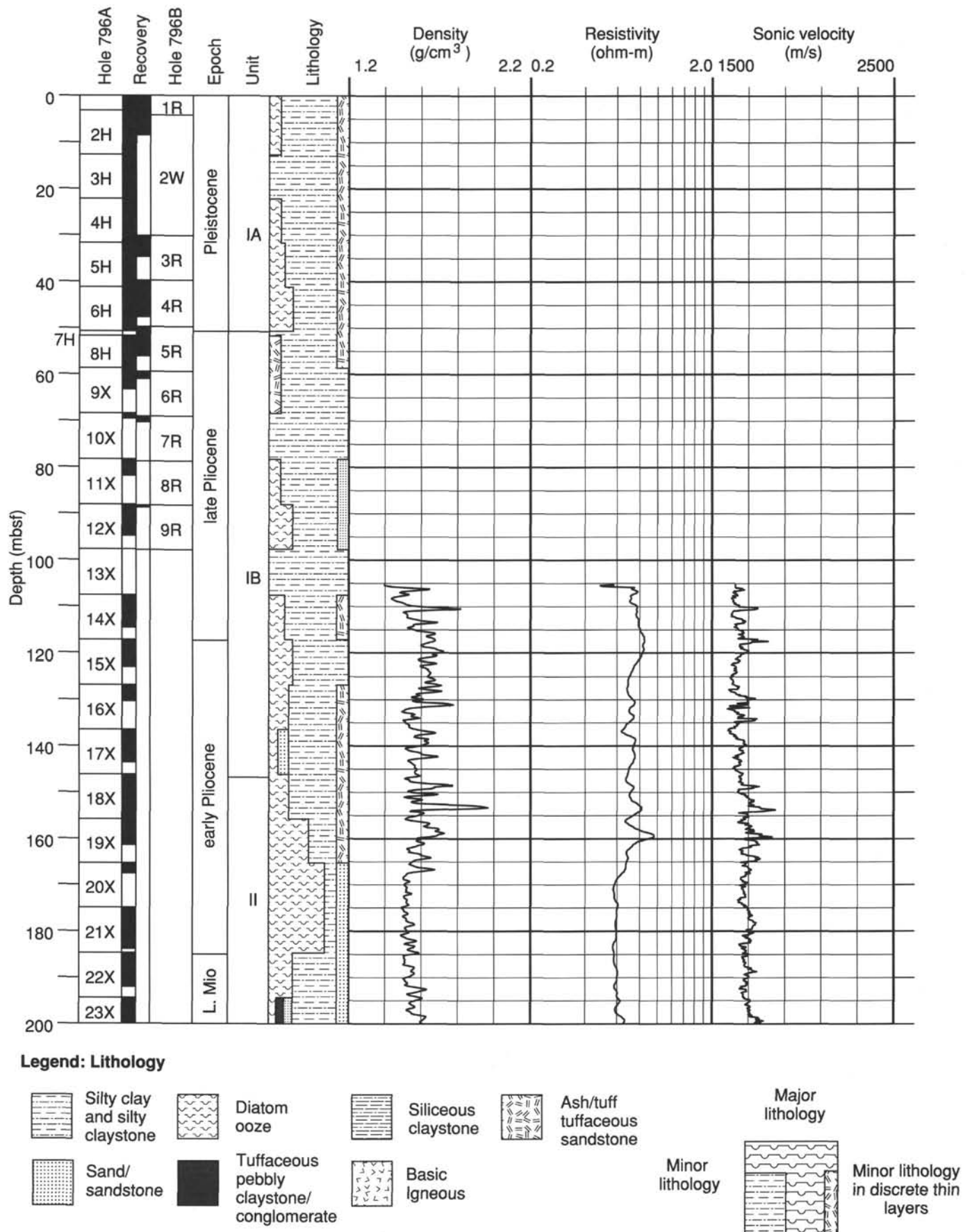
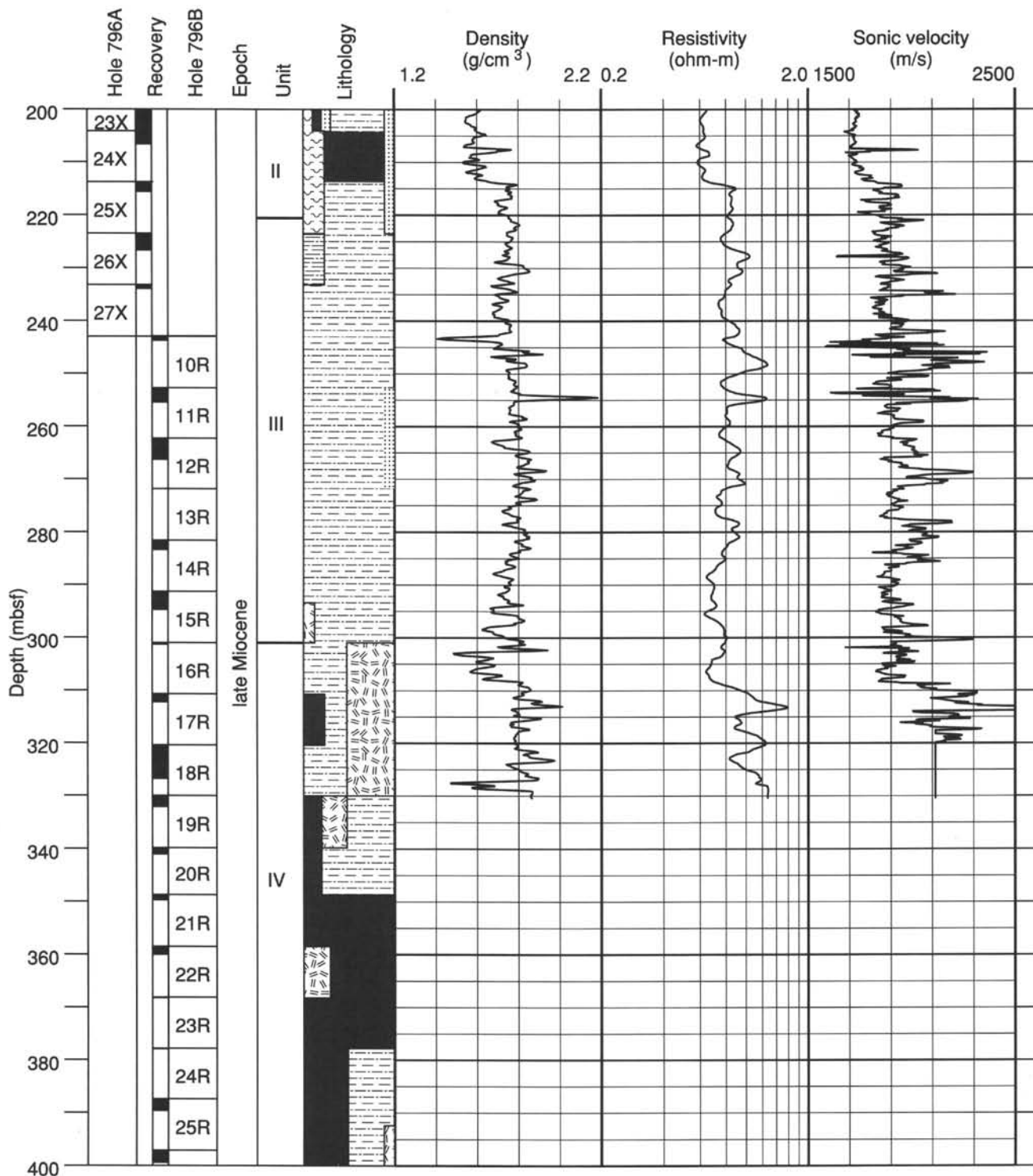


Figure 47. Modified lithostratigraphic column from Figure 1 with logs of density, resistivity, and sonic velocity plotted vs. depth.



Legend: Lithology

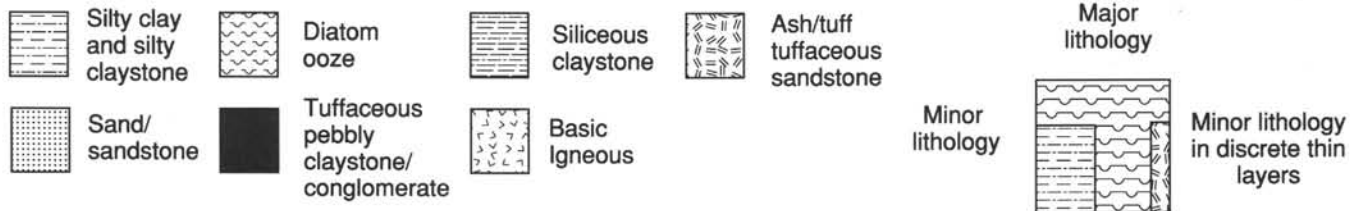


Figure 47 (continued).

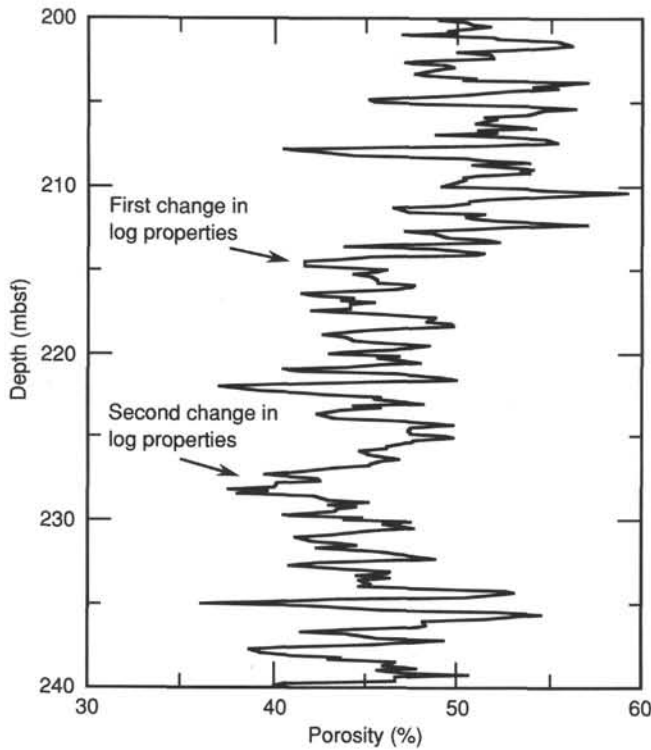


Figure 48. Plot of porosity log vs. depth for interval from 200 to 240 mbsf. Five-point smoothing has been applied.

lithology; Unit I, a clay unit, is shown by the gamma ray log to have significantly less clay than Unit II, a diatom ooze unit.

The caliper log reflects changes in borehole shape. In Unit I, the caliper averages 13 in., but decreases at 130 m to 11 in. corresponding to the top of a claystone unit which is interbedded with tuff. In Unit II, the borehole diameter expands to almost 15 in. before returning to an average of 12 in. just above the opal-A/opal-CT transition zone. The caliper log below Unit II is only slightly variable, averaging about 12 in.

Figure 49 shows that the neutron porosity in Units I and II averages 53% from 103 to 213 mbsf. The porosity averages about 45% for the subsequent sequences of Units II, III, and IV.

Geochemistry

The geochemistry tool string measures the concentrations of aluminum, iron, calcium, chlorine, hydrogen, silicon, sulfur, potassium, thorium, and uranium. The most complete analysis of these data depends on onshore processing, but we display the uncorrected data here (Fig. 50). This figure displays the uncorrected aluminum reading plus the uncorrected but normalized counts of silicon, calcium, iron, sulfur, hydrogen, and chlorine. The elemental percentages were normalized by dividing each element by the total number of counts.

The largest effects exhibited on the geochemistry log are those by drill collars and the pipe. Below the base of the drill pipe, a large decrease in the iron reading and a large increase in the aluminum are readily apparent. A large increase is also seen in the aluminum reading below 138 mbsf where the first interbeds of sand occur in Unit I. Below this level, aluminum is roughly constant through Unit II. The aluminum concentration is higher in Unit II than in Unit I even though Unit II is a diatom ooze and Unit I is a clay. Since aluminum ions are primarily associated with clay mineralogy, this association of increased

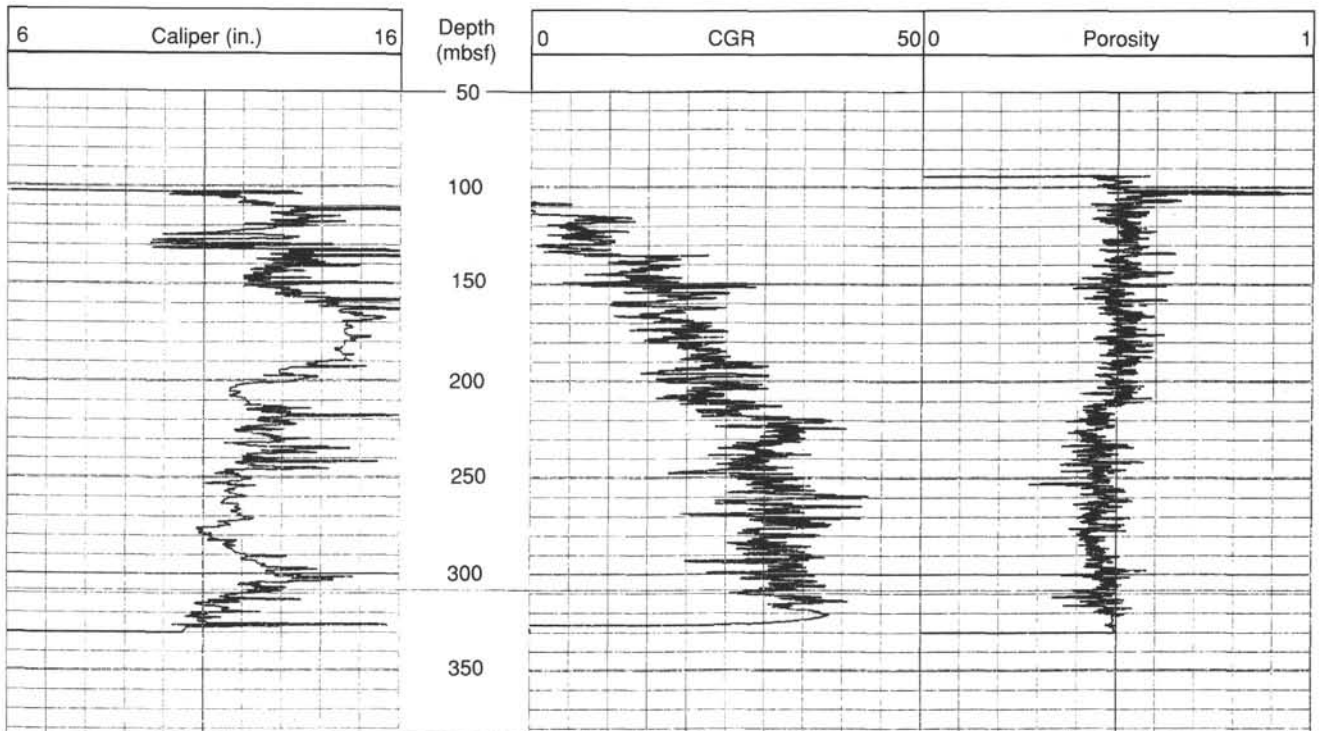


Figure 49. Logs from Hole 796B. Caliper (CALI, inches) (left), plot of gamma ray (CGR, API units) (center), and porosity (PORS, %) (right) plotted vs. depth.

aluminum counts with the appearance of diatom ooze is curious and, as yet, unexplained. This observation is similar to the gamma ray log result showing increasing clay content through Unit II.

A roughly bell-shaped aluminum decrease characterizes Unit III below the opal-A/opal-CT transition zone. Other decreases in aluminum are noted from 270 to 290 mbsf and again from 300 to 309 mbsf. This last interval corresponds to the first claystone interbedded with tuff and sandstone of Unit IV. This decrease in aluminum may reflect a deficiency in clay content due to the presence of the sands.

Normalized silicon increases at 310 mbsf corresponding to the silty clay and claystone of Unit III and the opal-CT/quartz transition. Iron is nearly constant beyond the pipe. Sulfur shows an increase from 140 to 200 mbsf. There exists a strong inverse correlation between calcium and silicon. This correlation is a consequence of calcium and silicon being the most abundant elements in the formation.

Formation Microscanner (FMS)

FMS images span the entire logging interval from 101 to 330 mbsf. The preliminary onboard image analysis shows that features of less than 5 to 10 cm in thickness can be resolved.

The measurements of hole direction show a general hole inclination or deviation (DEVI) between 3° and 4° (Figs. 51A and B). Two orthogonal caliper readings, which supply information about hole shape and diameter, characterize the logged hole as predominantly elliptical in shape with minor and major axes averaging 10 and 14 in., respectively (Fig. 51B). There is a strong preferred orientation of the major axis for thick intervals. From 101 to 200 mbsf, the major axis was north-northeast trending. From 200 mbsf to 330 mbsf, the major axis was north-northwest trending.

The hole conditions determined from these caliper readings range from very rough borehole walls (e.g., 101–167 mbsf, 218–250 mbsf (Fig. 51A), and 305–317 mbsf) to intervals with smooth features (e.g., 167–197 mbsf, 201–218 mbsf, and 286–305 mbsf). The interval of 218–250 mbsf is corrugated due to the presence of more competent dolomitic and cherty layers sandwiched between clays.

This corrugated interval coincides with a general increase of resistive, and therefore better imaged material below the opal-A/opal-CT transition zone. Below this zone, horizontal layers with thicknesses ranging from about 10 to 30 cm (246–251 mbsf, Fig. 51C) and 10 to 60 cm (304–308 mbsf) are present on this log. These horizontal layers most likely correspond to the dolomitic and cherty layers.

Borehole Televiewer

The LDGO BHTV logged upward from 330 to 240 mbsf in order to investigate the high velocity sandstone beds in this interval. Although the BHTV is generally most effective in hard basement rocks, fractures, and breakouts were anticipated in the well-lithified sandstones.

The data obtained were stored in two different ways. The raw data were recorded from an oscilloscope using a VCR beta tape for further digital processing. In addition, Polaroid images were taken simultaneously for onboard analysis. These real-time amplitude Polaroid photographs display the borehole image in 5-ft segments. The images were sometimes distorted by vertical striping, indicating tool sticking problems. This distortion obscures any information for these intervals.

The Polaroid photographs show small fractures from 2 to 5 cm in length, both in horizontal and vertical orientations. These photographs further show an ellipticity of the borehole which was confirmed by the two-armed caliper measurements from the previous FMS run. No other dominant features were observed.

Our preliminary interpretation is that the high velocity sandstone beds show a few small fractures, but that these fractures do not dominate the rock fabric. Further processing of the BHTV data at the Lamont-Doherty Geological Observatory was not completed in time for this publication.

SEISMIC STRATIGRAPHY

Available Data

The original proposal for Site 796 was made on the basis of single channel seismic reflection data of the Geological Survey of Japan (Tamaki et al., 1985). The data were obtained by systematic single channel seismic reflection surveys that were carried out in 1978 at an interval of 15 nmi over a wide area of the Japan Sea (Honza, 1979). Two site survey cruises for Site 796 were carried out since the proposal was submitted. Two east-west seismic reflection survey lines (12-channel digital seismics) were obtained by the KH86-2 research cruise in 1986 by the *Hakuho-maru* of Ocean Research Institute, University of Tokyo (Kuramoto et al., 1988), and an additional north-south single track of seismic reflection line (six-channel digital seismics) was acquired during the KT87-6 research cruise in 1985 by the *Tan-sei-maru* of Ocean Research Institute, University of Tokyo (Tamaki et al., 1988). Two single-channel digital seismic reflection profiles were obtained during the approach of the *JOIDES Resolution* to Site 796, and one east-west single channel seismic line located exactly over Holes 796A and 796B was obtained as the *JOIDES Resolution* left the site (see "Operations" section, this chapter).

Seismic Stratigraphy

Site 796 is located on the upper part of the eastward slope of Okushiri Ridge. The seismic stratigraphy of Okushiri Ridge is continuous with that of the Japan Basin to the west of the ridge (Fig. 6). As Okushiri Ridge is an upthrust feature formed since 1.8 Ma (see site summary discussion at beginning of chapter), the seismic stratigraphy of the ridge should be identical with that of the Japan Basin. The upper part of the sedimentary sequence in the eastern margin of the Japan Basin is far more opaque than it is at Site 795 in the northern margin of the Japan Basin. This character suggests more abundant input of terrigenous components into the sedimentary units of this part of the basin than at Site 795.

Obvious dense stratifications are observed in the upper opaque unit on the western slope of Okushiri Ridge, while the stratification in the sedimentary units is poorly developed on the eastern slope of the ridge where Site 796 is situated. As Okushiri Ridge is an eastward obducted feature along a westward-dipping thrust fault (Tamaki and Honza, 1985), the eastern slope is steeper than the western slope. The poor development of stratification in the sedimentary units of the eastern slope is probably a result of tectonic deformation of this part of the sedimentary units by slumping and faulting.

Shiribeshi Trough lies immediately east of Okushiri Ridge and is filled with thick, stratified sediments reaching 2.0 s in thickness (two-way traveltime; hereafter, this unit is used for the thickness of seismic unit). The sedimentary sequence of Okushiri Ridge is mostly continuous with the lowermost part of the sedimentary units of the Shiribeshi Trough. This stratigraphic relationship suggests that the middle-upper sedimentary units of the Shiribeshi Basin were deposited after uplift of Okushiri Ridge so that the ridge acted as a barrier behind which the terrigenous deposits shed from Hokkaido were trapped.

The possible opal-A/opal-CT reflector is better observed in the multichannel seismic profile (Fig. 52) than in the single channel seismic profile (Figs. 53 and 54). The opal-A/opal-CT reflector is well traced over Okushiri Ridge from the western slope to the eastern slope. The depth of the opal-A/opal-CT is

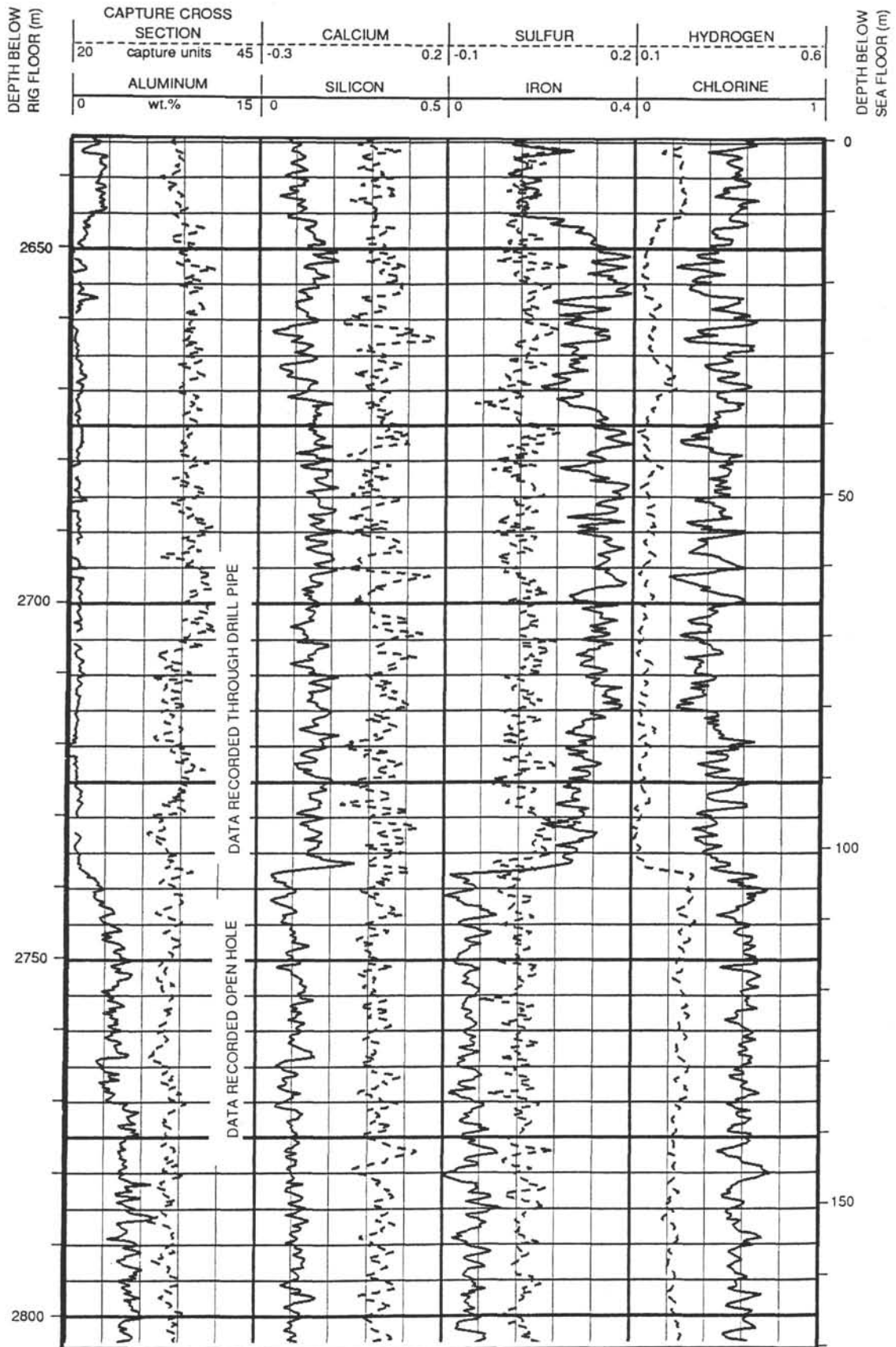


Figure 50. Geochemical logs from Hole 796B. Uncorrected elemental readings, capture cross section, and aluminum weight percent are plotted vs. depth.

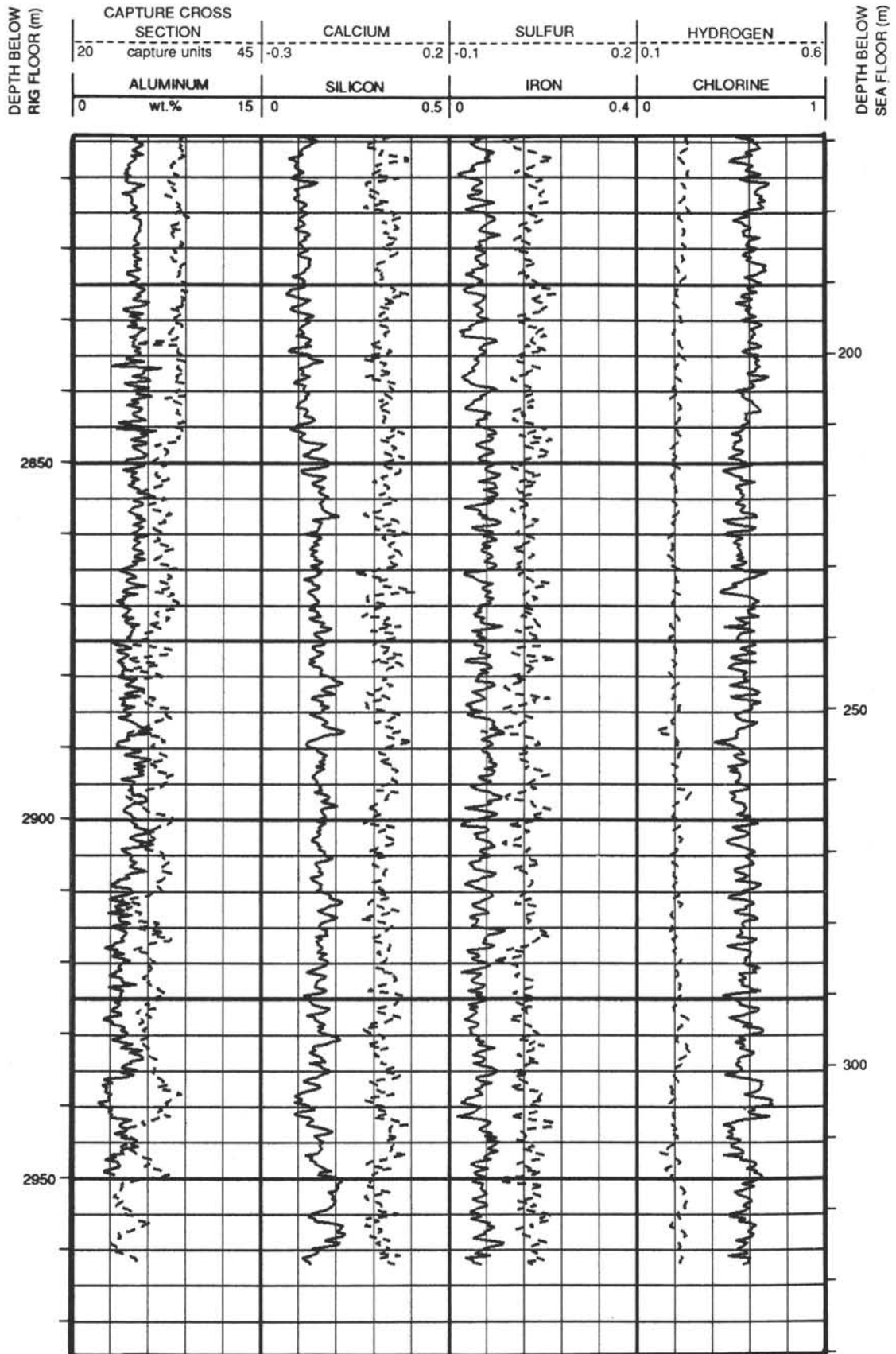


Figure 50 (continued).

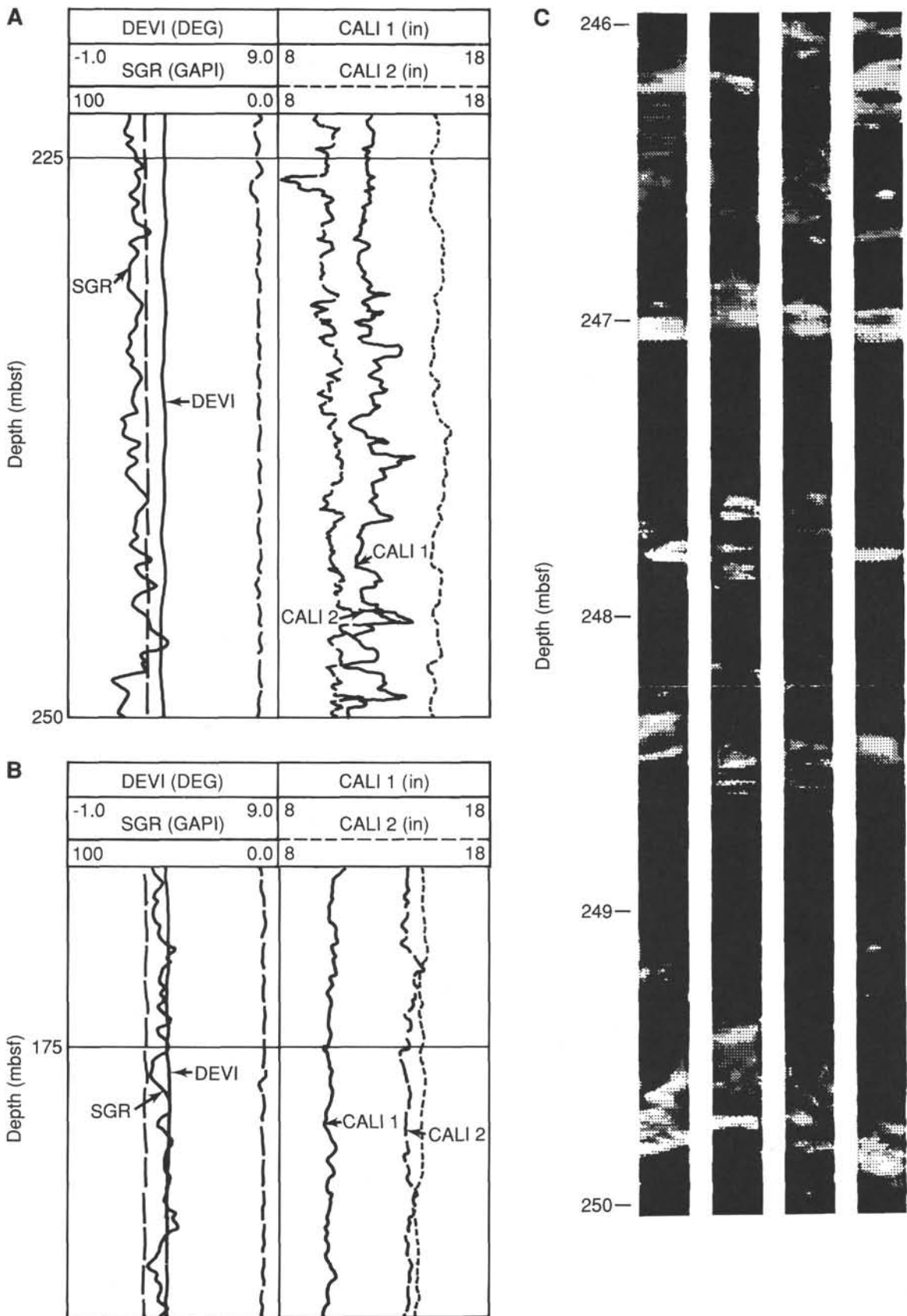


Figure 51. Formation microscanner data. A. General Purpose Inclination Tool (GPIT—part of FMS) measurement 225–250 mbsf. B. General Purpose Inclination Tool (GPIT—part of FMS) measurement 170–190 mbsf. C. Images from 246–250 mbsf.

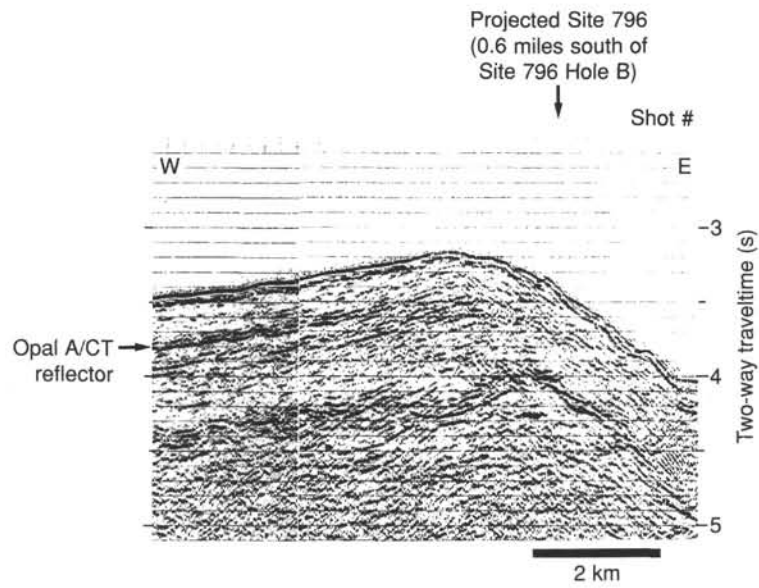


Figure 52. Twelve-channel seismic reflection record of Line 5 (KH86-2 research cruise). See Figure 9 for track lines.

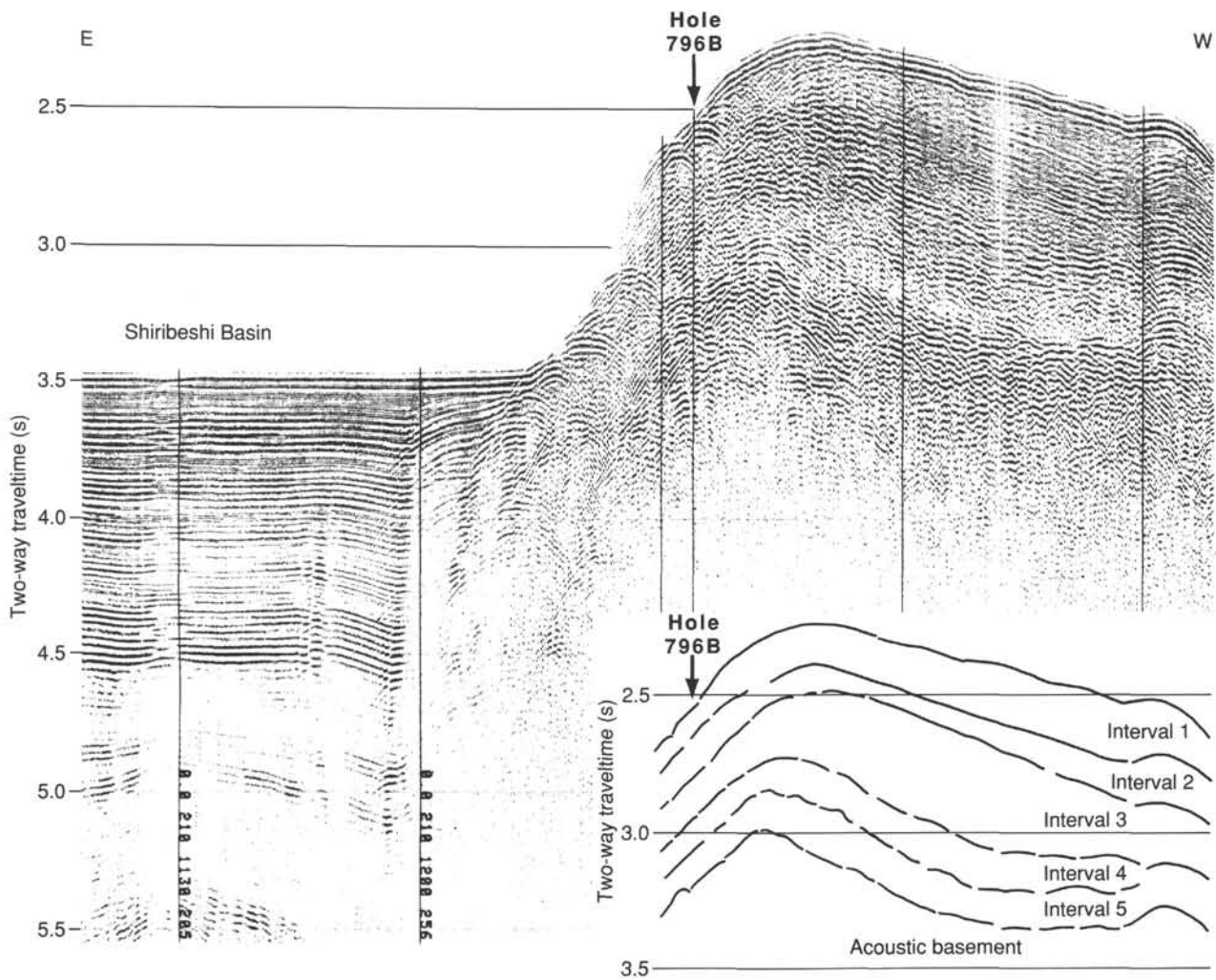


Figure 53. East-west single channel *JOIDES Resolution* seismic reflection record obtained during the departure from Site 796, with an assignment of acoustic intervals and the site location. See Figure 9 for track lines.

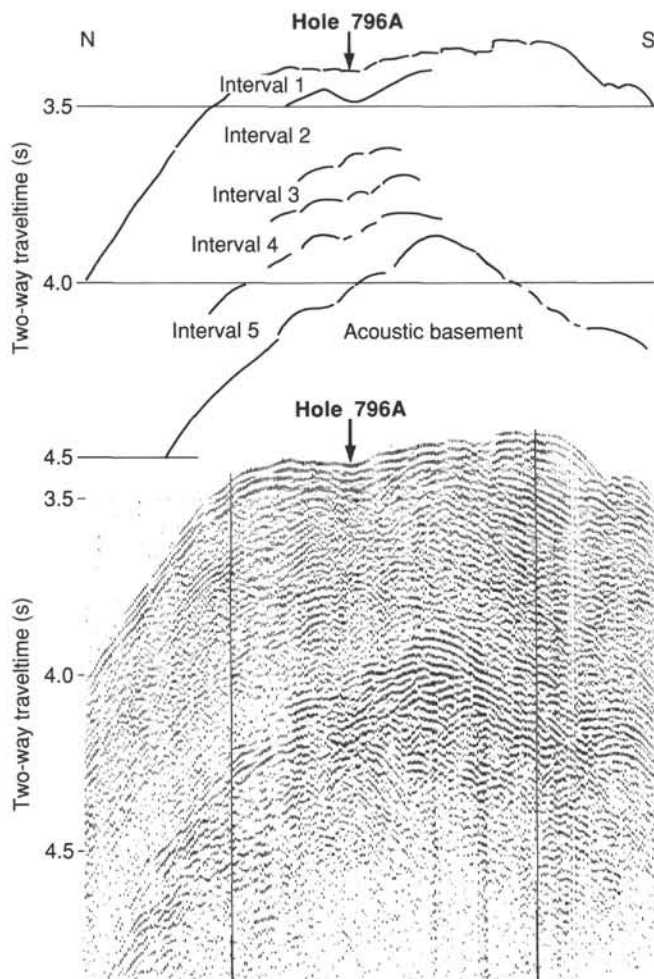


Figure 54. North-south single channel *JOIDES Resolution* seismic reflection record obtained during the approach to Site 796, with an assignment of acoustic intervals and the hole location. See Figure 9 for track lines.

generally deeper on the western slope than on the crest and the eastern slope. The variation is from 0.30 s to 0.20 s. This variation of the depth of the opal-A/opal-CT reflector may reflect the variation of heat flow over Okushiri Ridge (see "Downhole Measurements" section, this chapter). The possibility of erosion of the uppermost part of the sediments by slumping, however, should be accounted for in the detailed analyses of the depth of opal-A/opal-CT reflector.

Five major seismic intervals (Intervals 1–5) and acoustic basement are recognized in the area around Site 796 (Figs. 53 and 54). From top to bottom they are: Interval 1, an uppermost weakly stratified interval; Interval 2, an upper stratified interval; Interval 3, a middle densely stratified interval; Interval 4, an irregularly stratified interval; Interval 5, a lowermost non-stratified interval; and an acoustically opaque zone, with some stratification in its upper part, corresponding to acoustic basement. The opal-A/opal-CT reflector correlates to the boundary between Interval 2 and Interval 3. These seismic intervals are typically observed on the single channel analog monitor records of the western slope but are less clear on the eastern slope of Okushiri Ridge and on the multichannel records. Seismic intervals of the sedimentary section at Site 796 differ from those of the previous two sites (Sites 794 and 795) by their characteristic strong stratification through Intervals 1–4. Each seismic interval

does not necessarily correlate to the seismic intervals of previous sites, although the same nomenclature is used.

The thickness of Interval 1 in the area around Site 796 varies between 0.15 and 0.20 s. The thickness of Interval 1 increases downslope on the western slope of Okushiri Ridge. The boundary between Interval 1 and Interval 2 is unconformable, especially on the eastern slope. The thickness of Interval 2 is highly variable from 0.10 to 0.30 s, with a decreasing tendency toward the crest of the ridge. Interval 3 is the most densely stratified layer in the sedimentary column of Okushiri Ridge and is characterized by parallel stratification. The stratification of Interval 3 is parallel on the western slope but loses its parallelism at the ridge crest and on the eastern slope. The thickness of this interval is also highly variable from 0.15 and 0.45 s. The thickest part is observed on the upper part of the western slope. Interval 4 is characterized by irregular, subparallel stratification. The thickness of Interval 4 is between 0.10 and 0.15 s. Interval 5 is nonstratified or acoustically semi-transparent. The thickness is 0.10 s or less and covers the acoustic basement rather uniformly. The acoustic basement of the Okushiri Ridge is characterized by abundant stratification in its upper part (Fig. 52). Side echoes increase the ambiguity in the eastern slope. The stratified interval in the acoustic basement reaches 0.3 s in many places.

The thicknesses of each interval at Site 796 were determined from the seismic reflection data acquired by the *JOIDES Resolution* during the site approach and the site departure. They are: 0.08 s for Interval 1; 0.19 s for Interval 2; 0.10 s for Interval 3; 0.11 s for Interval 4; and 0.15 s for Interval 5 (Fig. 54).

Correlation between Seismic Stratigraphy and Lithology of Site 796

Correlation between seismic stratigraphy and lithostratigraphy was done using physical property velocity data and logging sonic velocity data. Results of the correlation between the seismic stratigraphy and the lithostratigraphy are summarized in Figure 55.

The opal-A/opal-CT reflector is diffuse at Site 796. The reflector was first identified in the multichannel seismic profile of the western slope (Fig. 52), was subsequently correlated with a reflector on the single channel seismic profile of the western slope (Fig. 53), and finally was traced to Site 796. The reflector, which correlates to the opal-A/opal-CT boundary, is identified at 0.27 s bsf at Site 796. The opal-A/opal-CT transition is identified at 215 mbsf by logging data, and this depth differs slightly from that determined by lithologic data (224 mbsf). As the logging data is more reliable in terms of depth below seafloor, the opal-A/opal-CT transition at 215 mbsf is cited here and is correlated to the most plausible reflector at 0.27 s bsf.

The most prominent reflector in the sedimentary section at Site 796 is observed at 0.38 s bsf and is correlated to a horizon at 310 mbsf where a sharp increase in logging sonic velocity occurs (see "Downhole Measurements" section, this chapter). This horizon is very close to the boundary between Units III and IV at 301 mbsf.

The drilling was terminated midway in the sediments, so there is no distinct constraint on the depth of the acoustic basement. We estimated the depth of the acoustic basement by extending the physical properties velocity data of Interval 5. Based on this approach, the estimated depth of the acoustic basement is about 575 mbsf and the bottom of Hole 796B (total depth 464.4 mbsf) is at about 110 m above the acoustic basement.

Interval 1 correlates to the clay and silty clay of Unit IA. The boundary between Intervals 1 and 2 represents a prominent unconformity on the north-south seismic profile along the strike of the slope (Fig. 54). This unconformity correlates well to the boundary between Units IA and IB. The age of this boundary corresponds to the initiation of the uplift of Okushiri Ridge at

	Seismic interval	Acoustic character	Interval velocity (m/s)	Thickness (two-way traveltime) (s)	Thickness (distance) (m)	Simplified lithology	Lith. unit	Age	
0	1	Weekly stratified	1520	0.08	60	Clay and silty clay without sand	IA	Pleistocene	0
0.08	2	Densely stratified	1630	0.19	155	Clay and silty clay with frequent sand	IB	Pliocene	60
0.27					Diatom ooze and diatom claystone	II	215		
0.38	3	Well stratified	1900	0.10	95	Opal-A/CT Siliceous claystone, claystone, and sandstone	III	late Miocene	310
0.38	4	Irregularly stratified	2100	0.11	105	Siliceous claystone, pebbly claystone, tuffaceous sandstone, and tuff	IV		415
0.63	5	Nonstratified	2150	0.15	160	Siliceous claystone and silty claystone	V		Approx. 575
	Acoustic basement	Stratified in upper part	?	?	?	?		?	

Figure 55. Summary of the seismic stratigraphy of Site 796 and its correlation with lithostratigraphy. The depth of opal-A/opal-CT transition is based on the logging sonic velocity data.

1.8 Ma (see site summary discussion at beginning of chapter). This unconformity is probably related to the initial uplift of Okushiri Ridge. The interval velocity of Interval 1 (1520 m/s) is an estimation based on *P*-wave logger velocity data and is comparable with the interval velocity of Interval 1 of Site 794. Gas hydrate is observed at the upper part of Interval 2 but no correlatable bottom-simulating reflector is observed.

Interval 2 correlates to the clay and silty clay of Unit IB and diatomaceous ooze and diatom clay of Unit II. Units IB and II include frequent sand layers of fine to medium grain size. The frequent occurrence of sand beds may be correlated to more dense stratification of Interval 2 than that of Interval 1. The lithologic boundary between Units I and II cannot be identified with a boundary between the seismic intervals. The interval velocity of Interval 2 is estimated to be 1630 m/s, based on the assumption that the reflector at 0.27 s bsf is assigned as the opal-A/opal-CT transition. This velocity is consistent with the logging sonic velocity data.

Interval 3 corresponds to Unit III. Unit III consists of siliceous claystone, pebbly claystone, and sandstone. The top of Interval 3 is coincident with the opal-A/opal-CT transition at 215 mbsf. The well-stratified character of Interval 3 reflects the abundant occurrence of hard siliceous layers and sandstone layers within this unit. Dense stratification of Interval 3 is consistent with the logging velocity data which shows correspondingly high variability in this interval. The interval velocity of Interval 3 is 1900 m/s, which is estimated on the basis of the logging velocity data and on the physical properties velocity data in this interval. This interval velocity is higher than the comparable intervals beneath the opal-A/opal-CT boundary at Site 794 (1750 m/s) and Site 795 (1750 m/s), suggesting abundant input of terrigenous components into this interval.

Interval 4 corresponds to the siliceous claystone, pebbly claystone, tuffaceous sandstone, and tuff of Unit IV. This interval is characterized by rather rugged, unorganized stratification. This type of stratification may be correlated to the rapidly deposited massive pebbly claystone. The interval velocity of Interval 4 is

estimated to be 2100 m/s based on the logging velocity data and on the physical properties velocity data. The velocity of 2100 m/s is the highest interval velocity of any of the sedimentary rocks recovered at this site or at Site 794 and Site 795, again reflecting the strongly terrigenous nature of the sediments in this interval.

Interval 5 corresponds to Unit V. Unit V is the lowermost unit at Site 796 and the penetration of this unit was not completed. Unit V consists of siliceous claystone and silty claystone, and it is characterized by a smaller amount of terrigenous components. This character is consistent with the nonstratified or semi-transparent acoustic character of this seismic interval. As sonic logging did not reach Unit V, only physical properties velocity data from the uppermost cored part of this interval are used for the estimation of the interval velocity of this seismic interval. Based on these data, we assigned an interval velocity of 2150 m/s to Interval 5. If this estimation is valid, the acoustic basement is at 575 mbsf.

The acoustic basement of Okushiri Ridge is characterized by well-developed stratification in its upper part. This stratification may reflect another sedimentary unit or alternation of igneous sills and sediments. The abundant occurrence of side echoes in the acoustic basement on the eastern slope of Okushiri Ridge may represent displacements by faults.

Discussion

The total thickness of the sediments is explicitly different between on the western slope and on the eastern slope of Okushiri Ridge. The thickness of the sediments on the western slope is a constant 0.9 s in the east-west section crossing the site and is apparently thicker than that on the eastern slope (0.6–0.65 s in general). The difference between the two thickness values is 0.25–0.30 s. The intervals that are mainly responsible for the difference in these thicknesses are Interval 2 and Interval 3, although Interval 1 is partly responsible for the difference. Intervals 4 and 5 are rather constant in thickness throughout on the western slope to the eastern slope and do not contribute to the

difference. The boundary between Interval 2 and Interval 3 is the opal-A/opal-CT boundary. This diagenetic front shows some intersection with the original depositional structure on the western slope as observed at Site 795 and accounts for the variation of the thickness of Intervals 2 and 3 within each interval. Here we consider the combined thicknesses of Intervals 2 and 3 to eliminate the clutter effect of the opal-A/opal-CT reflector and in order to interpret original depositional strata. The combined thickness of Intervals 2 and 3 on the eastern slope is about 0.3 s and that on the western slope reaches 0.50–0.55 s. The apparent difference between these two thicknesses is 0.20–0.25 s. This value is close to the difference of the total thickness between the sedimentary column on the western and eastern slope (0.25–0.30 s). An additional difference of 0.05 s appears to be due to Interval 1, suggesting some erosion by submarine sliding or constant smaller sedimentation rates on the eastern slope than on the western slope.

Intervals 2 and 3 correlate to the upper Miocene to Pliocene lithologic Units IB, II, and III which include abundant terrigenous components. The larger thicknesses of Intervals 2 and 3 on the western slope as compared to the eastern slope suggests that the depositional center in the late Miocene to Pliocene was situated in the present western slope area or more westward. Further areal analyses of sediment thickness will provide critical constraints needed to reconstruct the original depositional environment and topography before the uplift of Okushiri Ridge.

The opal-A/opal-CT reflector is usually apparent on single analog seismic profiler records. The reflector, however, is not clear at Site 796 on the single seismic reflection records. The depth of the opal-A/opal-CT reflector at Site 796 (0.27 s) is much shallower than at the other three sites (Sites 794 and 795, 0.38 s; Site 795, 0.40 s). This shallow opal-A/opal-CT reflector is consistent with the unusually high heat flow at Site 796 (see "Downhole Measurements" section, this chapter) and the gradual change of physical properties at this horizon (see "Physical Properties" section, this chapter). As this high heat flow is probably related to recent tectonics of Okushiri Ridge that were initiated at 1.8 Ma, the diffuse opal-A/opal-CT reflector may reflect ongoing upward migration of this diagenetic front.

Summary

The Site 796 seismic stratigraphy is characterized by dense stratification of the sedimentary section. The abundant terrigenous component of the sedimentary column accounts for this well-developed stratification. The opal-A/opal-CT reflector is observed in this dense stratification, but the reflector is less conspicuous on the eastern slope than at the previous sites on the single channel seismic profiles, suggesting the possibility of ongoing upward migration of the diagenetic front since 1.8 Ma. The appreciable difference of the sediment thickness (0.9 s) between the western slope and the eastern slope (0.60–0.65 s) depends mainly on the difference of the thickness of Intervals 2 and 3 and partly on that of Interval 1. The former difference suggests different depositional environments in the late Miocene to Pliocene between the western slope and eastern slope areas. The latter difference may reflect erosion by slumping of soft sediments during the uplift of Okushiri Ridge which is evident by the unconformity between Intervals 1 and 2. Although gas hydrate was observed in some cores at about 90 mbsf, no bottom-simulating reflector corresponding to the bottom of the gas hydrate is observed on the seismic profile at Site 796. The acoustic basement, which was not attained by drilling because of bad hole conditions caused by coarse sediments and probable faults or fractures, is estimated to lie 110 m below the bottom of Hole 796B.

CONCLUSIONS

We accomplished two of our four main objectives at Site 796. These four objectives were: (1) to determine the age and history of uplift of Okushiri Ridge; (2) to measure the direction of the present stress field; (3) to gain information on the style and dynamics of rifting through a determination of the age and nature of basement; and (4) to characterize the sedimentation and oceanographic evolution of the area. Unfortunately, penetration of the acoustic basement was not attained (total depth 464.9 mbsf, 110 m above basement) because of unstable hole conditions caused by shallow coarse sand beds and fractured rocks in the lower levels. As a result, we were unable to reach our second and third goals, a measurement of the magnitude and direction of the present stress field and to determine the age and nature of the basement. The age of the acoustic basement is estimated to be 17 Ma by simple extrapolation of the sediment accumulation curve to the acoustic basement reflector. The detailed summary of the results and conclusions for Site 796 can be found at the beginning of this chapter. For emphasis, we highlight the key findings as they relate to our principal objectives in the sections below.

Uplift of Okushiri Ridge

The age of the initiation of the uplift of Okushiri Ridge was inferred by the shallowest occurrence of a sand bed. The age of the shallowest sand bed is 1.8 Ma, based on its occurrence near the boundary between the *Actinocyclus oculatus* and *Neodenticula koizumii* Diatom Zones. Below this, abundant fine- to coarse-grained sand beds (1–10 cm thick) with sharp basal contacts and graded bedding suggesting a turbiditic origin were observed in the upper Pliocene unit as well as in the underlying lower Pliocene to upper Miocene units. These data suggest that turbidites were able to reach Site 796 during this time interval, and that Okushiri Ridge did not yet exist. The shallowest appearance of these sand beds in strata deposited at 1.8 Ma indicates that Okushiri Ridge (water depth 2300 m) was uplifted 1300 m above the Japan Basin floor (water depth 3600 m) in 1.8 Ma at a rate of 0.7 mm/yr. Several lines of evidence indicate an unconformity which may be caused by uplift of the ridge. The seismic stratigraphy shows an unconformity in the uppermost Pliocene that extends some distance around the site. The sedimentation rates are very slow (9 m/m.y.) in the sequence that includes the uppermost sand. As the uplift of Okushiri Ridge is caused by thrust activity along the eastern margin of the Japan Sea (a possible new Eurasia-North America plate boundary), these results provide the first direct age data bearing on the initiation of the convergence along this margin and are crucial to address the tectonics of this possible new plate boundary.

The highest heat flow ever obtained in the Japan Sea (156 mW/m²) was measured at Hole 796B. The associated high temperature gradient (178°C/km) is quite consistent with the shallow, indistinct opal-A/opal-CT transition zone (215 mbsf, 38°C). Seismic stratigraphy shows that the depth of opal-A/opal-CT reflector is generally shallower than that of the adjacent Japan Basin itself, suggesting that anomalous high heat flow is widespread over the Okushiri Ridge. Frictional heating along the thrust faults is one potential source of excess heat, but frictional heat alone cannot account for this high heat flow. A mechanism to concentrate the heat flow, such as fluid flow along faults, is required to match the magnitude of the anomaly. The possibility of vertical flux, however, was not confirmed by the interstitial water geochemical data, physical property data, and log data, although all of them show many anomalous vertical profiles of elements and physical properties.

Sedimentary History of the Eastern Margin of the Japan Sea

The lithology at Site 796 below the uppermost Pliocene is quite different from the previous two sites and is characterized by abundant input of coarse-grained clastic and pyroclastic detritus as sediment gravity flow deposits, suggesting a marginal facies of a basin. These clastic deposits provide unique information about the basin margin sedimentary history in the eastern Japan Sea.

Paleoceanographic conditions that are suggested by the sedimentary sequences and paleontological data, however, are approximately similar to those inferred at Sites 794 and 795 with some temporal variations. The calcium carbonate abundance in the sediments and the microfossil preservation show that the site was above the CCD during the middle(?) Miocene and below it through the late Miocene to the Quaternary. The ubiquitous bioturbation observed throughout the sedimentary column shows that the sediments at Site 796 accumulated under oxic conditions.

The interstitial water geochemistry shows elemental depth variation that is much different from the previous two sites. These variations are explained by correlation with lithology, especially with ash beds and sand beds. No vertical fluid transport was suggested by the interstitial water geochemical data, whereas physical property data may suggest the occurrence of some vertical fluid flux.

High methane concentrations, including gas-hydrate, were observed at 10–140 mbsf, with the concentrations ranging from 7,300 to 830,000 ppm in the vacutainer samples. This high concentration may be due to the abundant occurrence of coarse sedimentary deposits and to the structurally high position of Site 796 on Okushiri Ridge.

REFERENCES

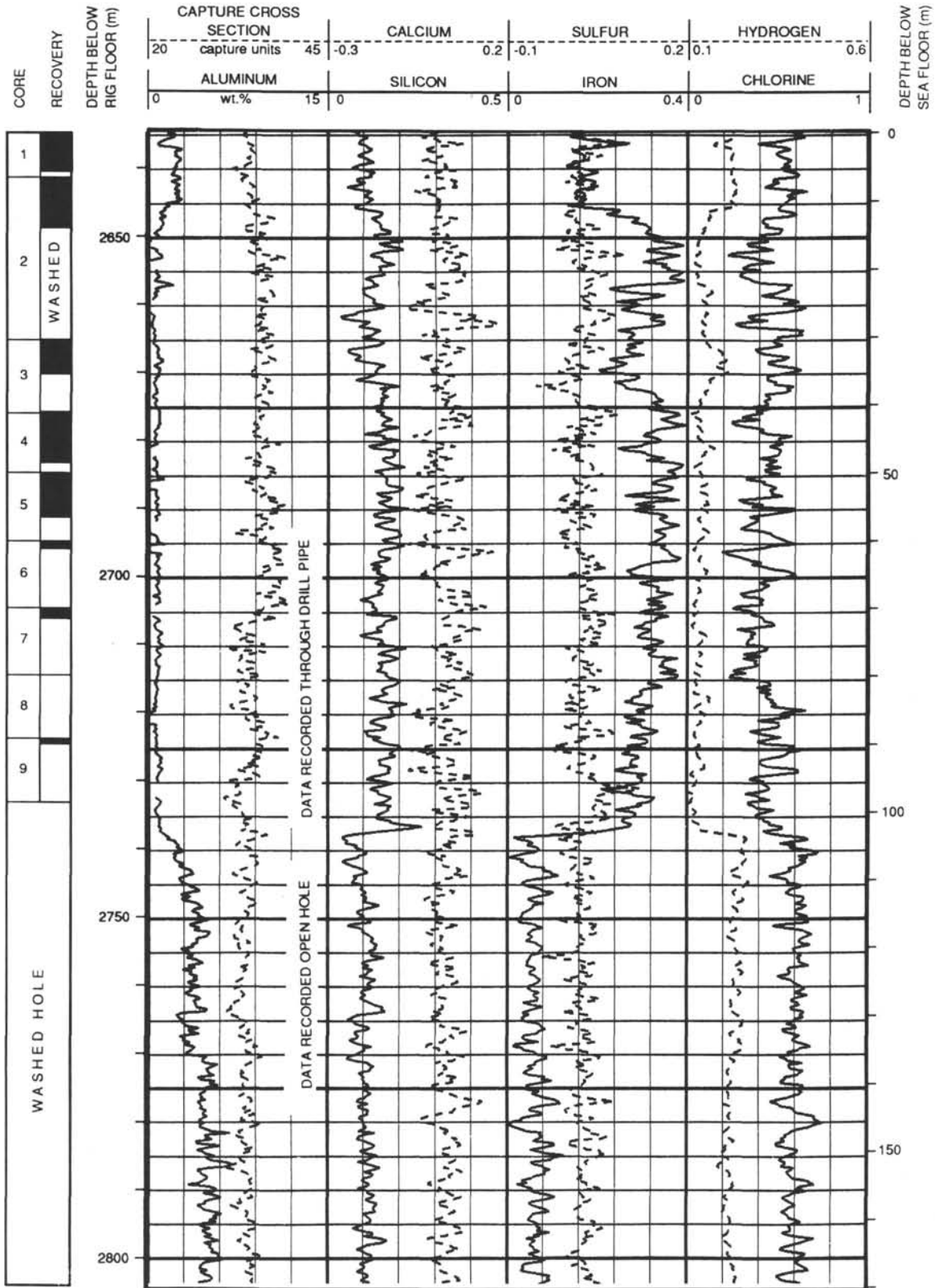
- Abe, K., and Kanamori, H., 1970. Mantle structure beneath the Japan Sea as revealed by surface waves. *Tokyo Daigaku Jishin Kenkyusho Iho*, 48:1011–1021.
- Baker, P. A., and Burns, S. J., 1985. Occurrence and formation of dolomite in organic-rich continental margin sediments. *AAPG Bull.*, 69: 1917–1930.
- Barron, J. A., and Keller, G., 1983. Paleotemperature oscillations in the middle and late Miocene of the northeastern Pacific. *Micropaleontology*, 29:150–181.
- Berggren, W. A., Kent, D. V., Flynn, J. J., and Van Couvering, J. A., 1985. Cenozoic geochronology. *Geol. Soc. Am. Bull.*, 96:1407–1418.
- Brooks, J. M., Jeffrey, A. W. A., McDonald, T. J., Pflaum, R. C., and Kvenvolden, K. A., 1985. Geochemistry of hydrate gas and water from Site 570, Deep Sea Drilling Project Leg 84. In von Huene, R., Aubouin, J., et al., *Init. Repts. DSDP*, 84: Washington (U.S. Govt. Printing Office), 699–703.
- Bruland, K. W., 1983. Trace elements in seawater. In Riley, J. P., and Chester, R. (Eds.), *Chemical Oceanography* (Vol. 8): London (Academic Press), 157–220.
- Burckle, L. H., 1978. Diatom biostratigraphy of Unit 2 (Tripoli) of the neostatotype Messinian. *Riv. It. Paleontol.*, 84:1037–1050.
- Calvert, S. E., 1983. Geochemistry of Pleistocene sapropels and associated sediments from the Eastern Mediterranean. *Oceanol. Acta*, 6: 255–267.
- Claypool, G. E., and Threlkeld, C. N., 1983. Anoxic diagenesis and methane generation in sediments of the Blake Outer Ridge, Deep Sea Drilling Project Site 533, Leg 76. In Sheridan, R. E., Gradstein, F. M., et al., *Init. Repts. DSDP*, 76: Washington (U.S. Govt. Printing Office), 391–402.
- Emeis, K.-C., and Kvenvolden, K. A., 1986. Shipboard organic geochemistry on JOIDES Resolution. *ODP Tech. Note*, 7.
- Espitalié, J., Madec, M., Tissot, B., Mennig, J. J., and Leplat, P., 1977. Source rock characterization method for petroleum exploration. *Proc. 9th Annu. Offshore Technol. Conf.*, 3:439–448.
- Fukao, Y., and Furumoto, M., 1975. Mechanism of large earthquakes along the margin of the Japan Sea. *Tectonophysics*, 25:247–266.
- Geller, C. A., Weissel, J. K., and Anderson, R. N., 1983. Heat transfer and intraplate deformation in the central Indian Ocean. *J. Geophys. Res.*, 88:1018–1032.
- Geological Survey of Japan, 1982. Geologic atlas of Japan. *Geol. Surv. Jpn.*
- Gieskes, J. M., 1981. Deep-sea drilling interstitial water studies: implications for chemical alteration of the oceanic crust, layers I and II. In Warne, J. E., Douglas, R. G., and Winterer, E. L. (Eds.), *The Deep Sea Drilling Project: A Decade of Progress*. SEPM Spec. Publ., 32:149–167.
- Gnibidenko, H., 1979. The tectonics of the Japan Sea. *Mar. Geol.*, 32: 71–87.
- Heier, K. S., and Billings, G. K., 1969. Lithium. In Wedepohl, K. H. (Ed.), *Handbook of Geochemistry* (Vol. 2), 3-E.
- Hesse, R., Lebel, J., and Gieskes, J. M., 1985. Interstitial water chemistry of gas-hydrate-bearing sections on the Middle America Trench slope, Deep-Sea Drilling Project Leg 84. In von Huene, R., Aubouin, J., et al., *Init. Repts. DSDP*, 84: Washington (U.S. Govt. Printing Office), 727–736.
- Honza, E., (Ed.), 1979. Geological investigation of the Japan Sea. April–June 1978 (GH78-2 Cruise). *Cruise Rep.—Geol. Surv. Jpn.*, 13:1–99.
- Hyndman, R. D., Langseth, M. G., and Von Herzen, R. P., 1987. Deep Sea Drilling Project geothermal measurements: a review. *Rev. Geophys.*, 25:1563–1582.
- Ichikawa, M., 1971. Reanalysis of mechanism of earthquakes which occurred in and near Japan, and statistical studies on the nodal plane solutions obtained, 1929–1968. *Geophys. Mag.*, 35:207–273.
- Isezaki, N., 1986. A magnetic anomaly map of the Japan Sea. *J. Geomagn. Geoelectr.*, 38:403–410.
- Ishikawa, Y., Takeo, M., Hamada, N., Katsumata, M., Satake, K., Abe, K., Kikuchi, M., Sudo, K., Takahashi, M., Kashiwabara, S., and Mikami, N., 1984. Mechanism of the central Japan Sea earthquake, 1983. *Chikyū*, 6:11–17.
- Jenden, P. D., and Gieskes, J. M., 1983. Chemical and isotopic composition of interstitial water from Deep Sea Drilling Project Sites 533 and 534. In Sheridan, R. E., Gradstein, F. M., et al., *Init. Repts. DSDP*, 76: Washington (U.S. Govt. Printing Office), 453–461.
- Jolivet, L., Huchon, P., Brun, J. P., Le Pichon, X., Chamot-Rooke, N., and Thomas, J. C., in press. Arc deformation and marginal basin opening: Japan Sea as a case study. *J. Geophys. Res.*
- Kent, D. V., 1973. Post-depositional remanent magnetization in deep-sea sediment. *Nature*, 246:32–34.
- Kimura, G., Miyashita, S., and Miyasaka, S., 1983. Collision tectonics in Hokkaido and Sakhalin. In Hashimoto, M., and Uyeda, S. (Eds), *Accretion Tectonics in the Circum-Pacific Regions*: Tokyo (Terra Publ.), 69–88.
- Kobayashi, K., and Nomura, M., 1972. Iron sulfides in the sediment cores from the Sea of Japan and their geophysical implications. *Earth Planet. Sci. Lett.*, 16:200–208.
- Kuramoto, S., in press. Back-arc ophiolite emplacement: an example of Okushiri Ridge, Japan Sea. *Chigaku Zasshi*.
- Kuramoto, S., Tokuyama, H., Asanuma, T., and Suemasu, M., 1988. Multichannel and single-channel seismic reflection survey. In Kobayashi, K. (Ed.), *Preliminary Report of the Hakuho Maru Cruise KH86-2*, Ocean Res. Inst., Univ. Tokyo, 92–109.
- Kvenvolden, K. A., and Barnard, L. A., 1983. Gas hydrates of the Blake Outer Ridge, Site 533, Deep Sea Drilling Project Leg 76. In Sheridan, R. E., Gradstein, F. M., et al., *Init. Repts. DSDP*, 76: Washington (U.S. Govt. Printing Office), 353–365.
- Kvenvolden, K. A., and McDonald, T. J., 1985. Gas hydrates of the Middle America Trench—Deep Sea Drilling Project Leg 84. In von Huene, R., Aubouin, J., et al., *Init. Repts. DSDP*, 84: Washington (U.S. Govt. Printing Office), 667–682.
- Lallemand, S., and Jolivet, L., 1985. Japan Sea: a pull apart basin? *Earth Planet. Sci. Lett.*, 76:375–389.
- Ludwig, W. J., Murauchi, S., and Houtz, R. E., 1975. Sediments and structure of the Japan Sea. *Geol. Soc. Am. Bull.*, 86:651–664.
- Manheim, F. T., and Sayles, F. L., 1974. Composition and origin of interstitial waters of marine sediments based on deep sea drill cores. In Goldberg, E. D. (Ed.), *The Sea* (Vol. 5): New York (Wiley), 527–568.

- Masle, A., Moore, J. C., et al., 1988. *Proc. ODP, Init. Repts.*, 110: College Station, TX (Ocean Drilling Program).
- Müller, P. J., 1977. C/N ratios in Pacific deep-sea sediments: effect of inorganic ammonium and organic nitrogen compounds sorbed by clays. *Geochim. Cosmochim. Acta*, 41:765-776.
- Opdike, N. D., 1972. Paleomagnetism of deep-sea cores. *Rev. Geophys. Space Phys.*, 10:213-249.
- Oremland, R. S., and Taylor, B. F., 1978. Sulfate reduction and methanogenesis in marine sediments. *Geochim. Cosmochim. Acta*, 42: 209-214.
- Peters, K. E., 1986. Guidelines for evaluating petroleum source rock using programmed pyrolysis. *AAPG Bull.*, 70:318-329.
- Rahman, A., and Roth, P. H., in press. Late Neogene paleoceanography and paleoclimatology of the Gulf of Aden region based on calcareous nannofossils. *Paleoceanography*.
- Roth, P. H., and Coulbourn, W. T., 1982. Floral and solution patterns of coccoliths in surface sediments of the North Pacific. *Micropaleontology*, 7:1-52.
- Sancetta, C., 1982. Distribution of diatom species in surface sediments of the Bering and Okhotsk Seas. *Micropaleontology*, 28:221-257.
- Schlumberger, 1987. *Log Interpretation Principles/Applications*: New York (Schlumberger).
- Shipboard Scientific Party, 1987. Site 645. In Srivastava, S. P., Arthur, M., et al., *Proc. ODP, Init. Repts.*, 105: College Station, TX (Ocean Drilling Program), 61-418.
- Tamaki, K., 1986. Age estimation of the Japan Sea on the basis of stratigraphy, basement depth and heat flow data. *J. Geomagn. Geoelectr.*, 38:427-446.
- _____, 1988. Geological structure of the Japan Sea and its tectonic implications. *Chishitsu Chosasho Geppo*, 39:269-365.
- Tamaki, K., and Honza, E., 1985. Incipient subduction and obduction along the eastern margin of the Japan Sea. *Tectonophysics*, 119: 381-406.
- Tamaki, K., Kobayashi, K., Isezaki, N., Sayanagi, K., Nakanishi, N. and Park, C. H., 1988a. Measurement of geomagnetic total force by a proton precession magnetometer. In Kobayashi, K. (Ed.), *Geophysical and Geological Investigation of the Northeastern Part of the Japan Sea and Japan Trench. Preliminary Report of the Hakuho Maru Cruise KH 86-2 (April 21-May 15, 1986)*, Ocean Res. Inst., Univ. Tokyo, 7-9.
- Tamaki, K., Tokuyama, H., Miyashita, S., Tsukui, M., Furukawa, K., Sayanagi, K., Kuramoto, S., Nakanishi, M., Uno, I., Yamashita, S., and Itoda, C., 1988b. An annex for Preliminary report of the Tansei maru cruise KT87-6 (ODP site survey). In Kobayashi, K. (Ed.), *Preliminary Report of the Hakuho Maru Cruise KH86-2*. Ocean Res. Inst., Univ. Tokyo, 112-130.
- Waples, D. W., 1985. Organic and inorganic nitrogen in sediments from Leg 80, Deep Sea Drilling Project. In de Graciansky, P. C., Poag, C. W., et al., *Init. Repts. DSDP*, 80 (Pt. 2): Washington (U.S. Govt. Printing Office), 993-997.
- Watkins, N. D., 1968. Short period geomagnetic polarity events in deep-sea sedimentary cores. *Earth Planet. Sci. Lett.*, 4:341-349.
- Yoshii, T., and Yamano, M., 1983. Digital heat flow data file around the Japan islands. Unpublished Data Files, Ocean Res. Inst., Univ. Tokyo.

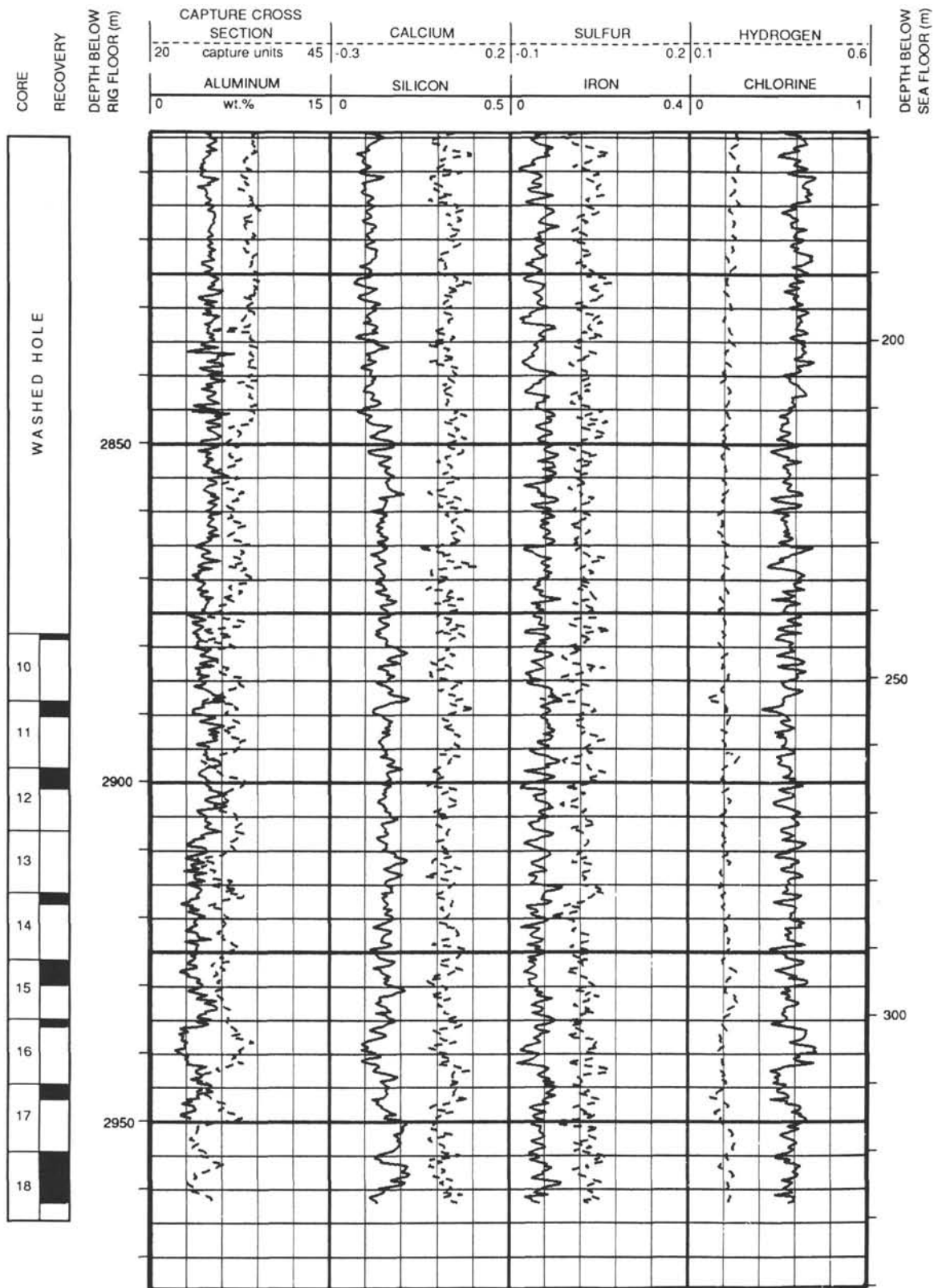
Ms 127A-106

NOTE: All core description forms ("barrel sheets") and core photographs have been printed on coated paper and bound as Section 3, near the back of the book, beginning on page 425.

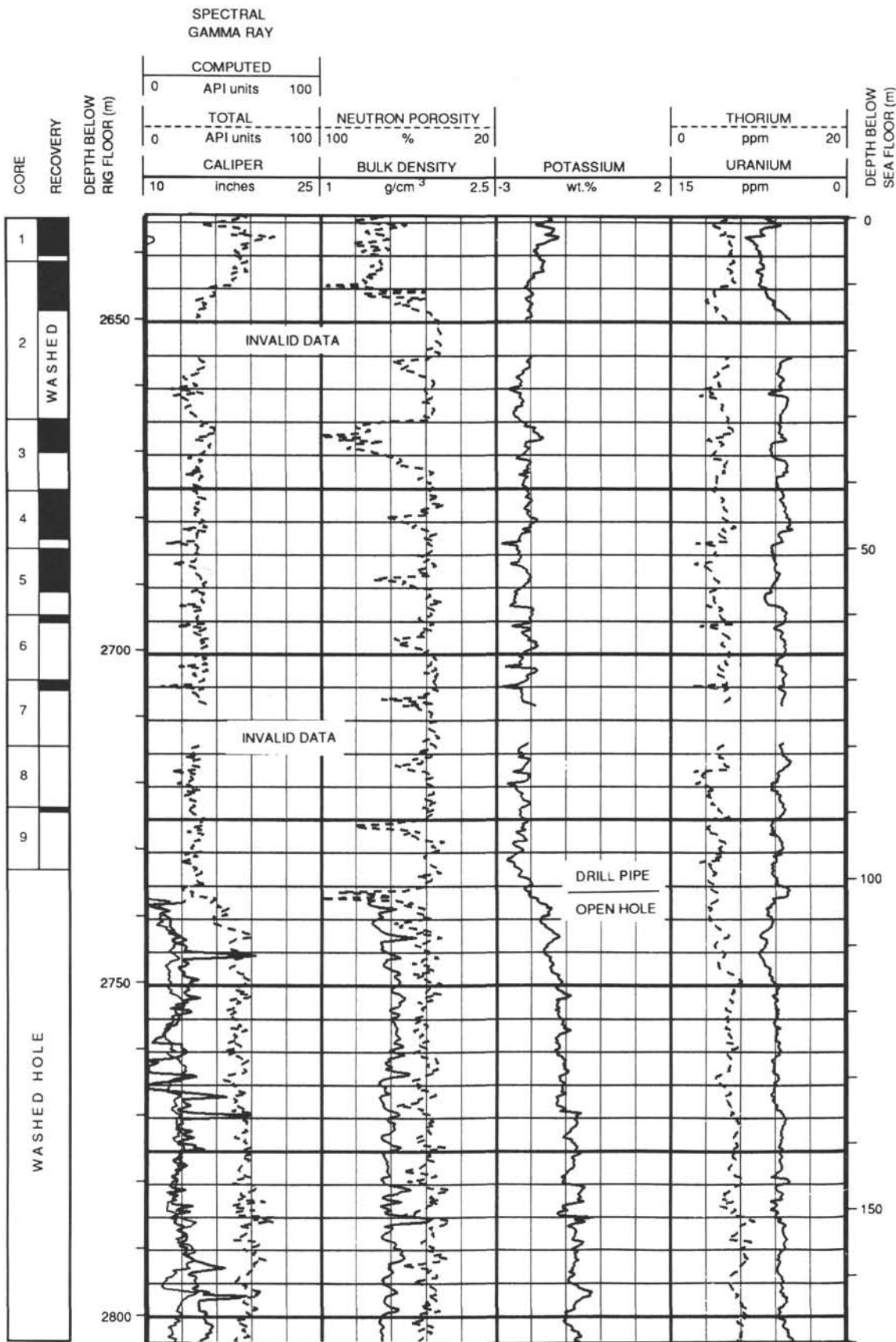
Summary Log for Site 796



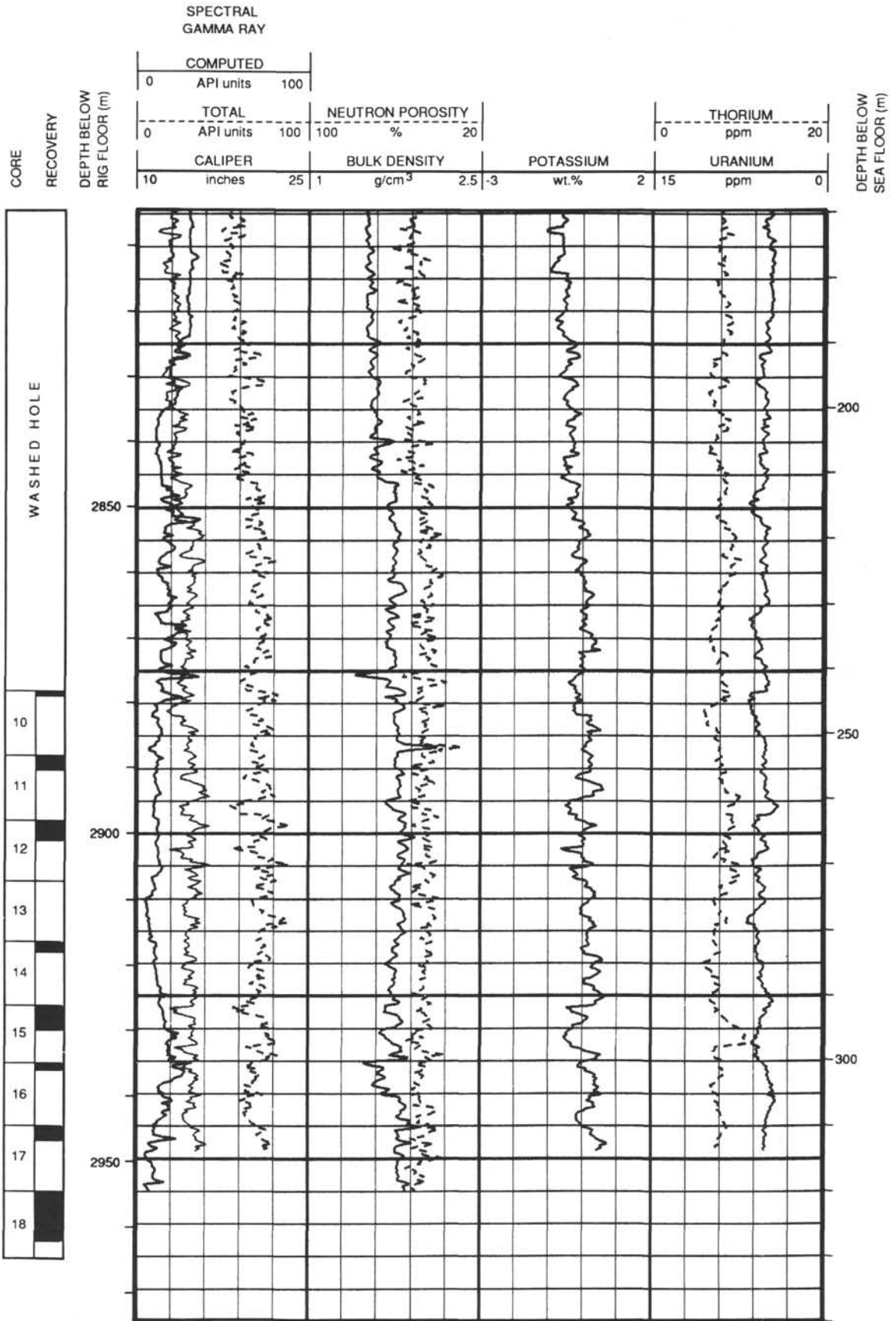
Summary Log for Site 796 (continued)



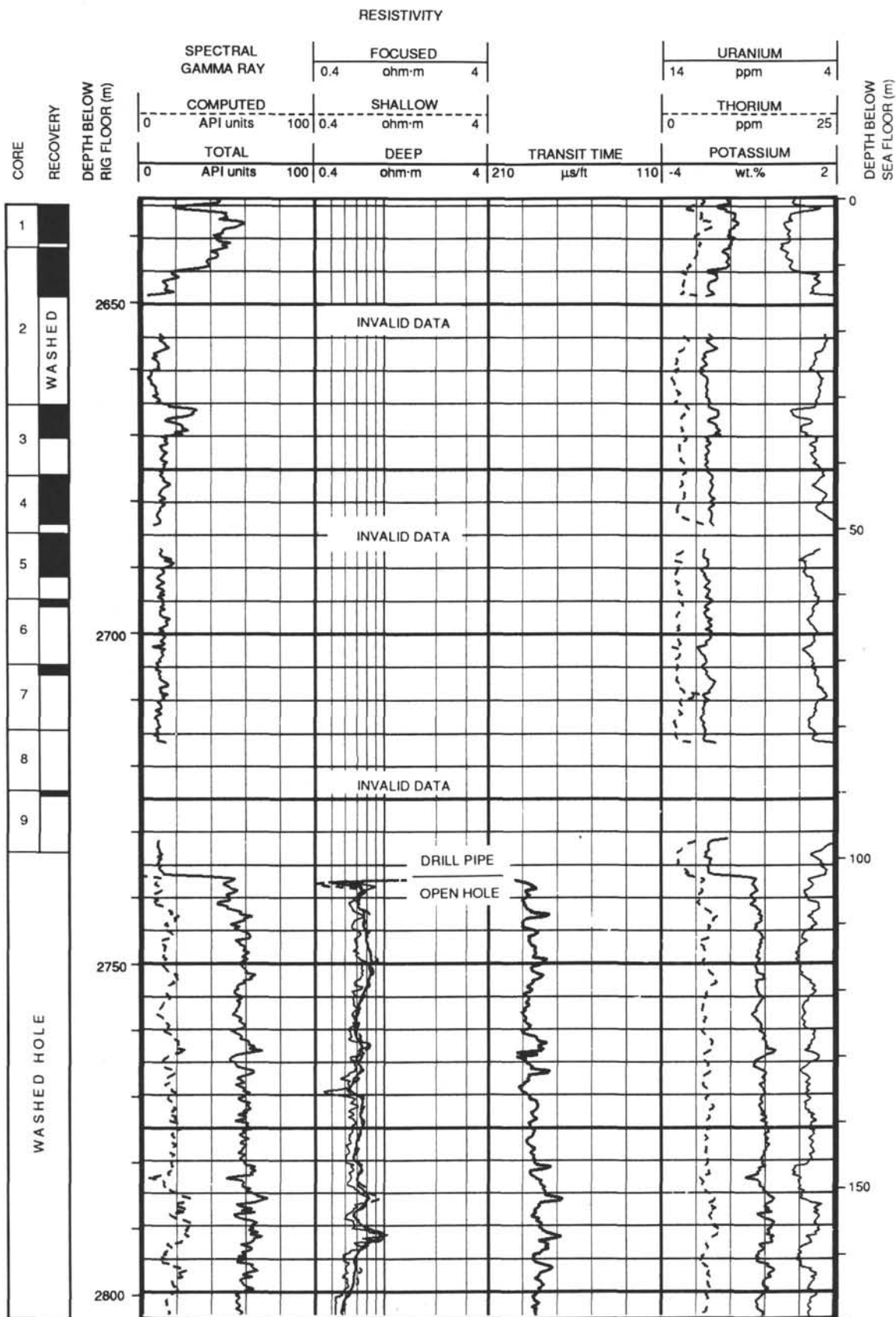
Summary Log for Site 796 (continued)



Summary Log for Site 796 (continued)



Summary Log for Site 796 (continued)



Summary Log for Site 796 (continued)

